

# Hydrogen-Enriched Methane Flames in a Swirl Stabilized Combustor with Axial Air Injection

MSc Thesis in Aerospace Engineering

Vittorio De Lauso

# Hydrogen-Enriched Methane Flames in a Swirl Stabilized Combustor with Axial Air Injection

MSc Thesis in Aerospace Engineering

by

Vittorio De Lauso

Student Number

5833000

Supervisor:	Dr.I. Ivan Langella
Project Duration:	January, 2024 - September, 2024
Faculty:	Faculty of Aerospace Engineering, Delft
Track:	Flight Performance and Propulsion
Profile:	Power and Propulsion

The background image has been retrieved on Freepik and it is attributable to rawpixel.com

# Acknowledgments

I want to express my deepest gratitude to my supervisor, Professor Ivan Langella, for his continuous support, guidance, and invaluable advice throughout my research journey. His expertise and encouragement have been instrumental in completing this work. Above all, I want to thank him for believing in me when he assigned me this research project, which has been a crucial part of my academic development.

I am also profoundly grateful to my PhD supervisor, Gioele Ferrante, whose insights, mentorship, and unwavering support have greatly contributed to this work. I truly appreciated his guidance, not only on an academic level but also on a personal level, where his approach made our interactions both productive and enjoyable.

My sincere thanks extend to the entire combustion research group. Their collaborative spirit and stimulating discussions have made this experience both enlightening and enjoyable.

I would like to thank Professor Arvind Gangoli Rao for his continued support, which began during my internship project and has extended throughout my research. His guidance and expertise have been greatly appreciated.

I want to extend my heartfelt thanks to the entire Ergon Research group. Even though they did not directly contribute to this thesis, every skill I applied during this effort originated from my questions to Dr. Lorenzo Mazzei and Dr. Lorenzo Palanti. Their guidance had a far greater impact on my personal and academic growth than they might realize, helping me become a better engineer and a better person, and making my internship a truly enjoyable experience.

I must also thank the people I've lived with during these two years, starting with those who welcomed me in the Netherlands, in Rotterdam—Bianca, Sasha, and Sophie—who made me feel at home right away, like we had known each other forever. I am also grateful to everyone at TSH Delft, where I found not just a place to stay, but a welcoming group of friends that made my time there truly enjoyable, and to Marianna and Carmenrita, the girls from Florence, with whom I always looked forward to coming back home. Their warmth, companionship, and shared moments of laughter and support made our home a comforting and joyful place, reminding me of the importance of friendship and the feeling of belonging, no matter how far from home we were.

Finally, I want to thank my colleagues, Vaclav, Teresa, and Pietro, who, more than anyone, endured two years of my complaints without losing patience. In particular, I am especially grateful to Pietro, who consistently responded with the calmness I needed to navigate the challenges we faced—here's to the endless nights spent together in the library.

Lastly, I must thank my lifelong friends, Marco, Silvia, Irene, and Imma, who have always kept me connected to the child I once was, reminding me of what truly matters to me in life.

I am deeply thankful to my parents and my sister, whose endless love, patience, and encouragement have been crucial to the completion of this work. I want to especially thank my mother for the long talks, even when I was just venting; they had a much greater impact than she could have imagined. My sister's unwavering belief in me has been a constant source of strength and motivation. And last but not least, I owe a special thanks to my father for his invaluable insights and for being the hero I look up to every day, even though he often sings, "*che mondo sarà se ha bisogno di chiamare Superman*"—he doesn't realize that he is Superman to me.

For the mind does not require filling like a bottle, but rather, like wood, it only requires kindling to create in it an impulse to think independently and an ardent desire for the truth.

---

*Plutarch*



# Abstract

This thesis explores the dynamics of hydrogen-enriched methane flames in a swirl-stabilized combustor with axial air injection, a configuration crucial for advancing low-emission combustion technologies. The study focuses on enhancing the understanding of flame behaviour under varying hydrogen enrichment levels, with particular attention to the effects of heat loss and strain on flame shape, mixing, and emissions. Utilizing computational methods, the research investigates key operating scenarios from the APPU project, refining thermal boundary predictions through an improved Heat Resistance Tuning approach. Additionally, it assesses the performance of a necessary flashback-prevention method, Axial Air Injection, quantifying its impact on mixing and flame shape, including their effects on temperature and pollutant formation, with varying results based on the level of hydrogen enrichment in the fuel. The results offer valuable insights that could inform control strategies for the stable and efficient operation of hydrogen-enriched combustion systems, supporting the development of fuel-flexible and environmentally sustainable propulsion technologies.

**Keywords:** Hydrogen, Swirl-Stabilized Combustion, Axial Air Injection, Flame Shape Transition, POD, PVC, NO<sub>x</sub>, LES

# Contents

<b>1</b>	<b>Introduction</b>	<b>1</b>
1.1	Addressing Global Warming: the Challenge of the 21st Century . . . . .	1
1.2	Assessing the Aviation Industry Contribution to Climate Change . . . . .	4
1.3	Hydrogen for net zero carbon emissions . . . . .	7
1.3.1	Production . . . . .	7
1.3.2	Storage and Transportation . . . . .	8
1.3.3	Consumption . . . . .	8
1.4	Organization of the thesis . . . . .	11
<b>2</b>	<b>Theoretical Background</b>	<b>12</b>
2.1	Reactive Flows . . . . .	12
2.2	Laminar Premixed Combustion . . . . .	17
2.2.1	Flame Structure . . . . .	18
2.2.2	Flame Thickness . . . . .	19
2.2.3	Flame Speed . . . . .	20
2.3	Turbulence Description . . . . .	20
2.4	Turbulent Premixed Combustion . . . . .	21
2.4.1	Turbulent Premixed Combustion Regimes . . . . .	22
2.5	Flame/Wall Interactions . . . . .	25
2.5.1	Laminar Flame/Wall Interaction . . . . .	26
2.5.2	Turbulent Flame/Wall Interactions . . . . .	28
2.6	Emissions . . . . .	29
2.6.1	NO <sub>x</sub> . . . . .	29
2.6.2	CO . . . . .	30
2.6.3	UHC . . . . .	30
2.6.4	Soot . . . . .	31
2.7	Swirling Flows . . . . .	32
2.7.1	Swirling Flows and Emissions . . . . .	35
2.7.2	An Operating Limit of Swirl-Stabilized Combustors: Flashback . . . . .	36
<b>3</b>	<b>Literature Review</b>	<b>39</b>
3.1	State of the Art in Land-Based Gas Turbines . . . . .	39
3.1.1	Aerodynamically Stabilized Combustion . . . . .	40
3.1.2	Stabilized Combustion for Self-Ignition . . . . .	42
3.1.3	Staged Combustion . . . . .	43
3.2	State of the Art in Test Rigs . . . . .	44
3.2.1	TD Combustor . . . . .	44
3.2.2	EM2C Combustor . . . . .	46
3.2.3	PRECCINSTA Combustor . . . . .	50
3.2.4	TU Berlin AHEAD Combustor . . . . .	57
3.2.5	TU Delft APPU Combustor . . . . .	62
3.3	Knowledge Gap and Objectives of the Thesis . . . . .	65
3.3.1	Knowledge Gap . . . . .	65

3.3.2	Objectives of the Thesis . . . . .	65
<b>4</b>	<b>Modeling and Methodology</b>	<b>67</b>
4.1	Discretization of the Transport Equations . . . . .	67
4.1.1	Iterative Algorithms . . . . .	67
4.2	Turbulence Modeling in Computational Fluid Dynamics . . . . .	69
4.2.1	Large Eddy Simulations . . . . .	70
4.2.2	Turbulence Modeling . . . . .	72
4.3	Turbulent Combustion Models . . . . .	74
4.3.1	TFM . . . . .	75
4.4	1D Simulations: A framework for 3D interpretation . . . . .	76
4.5	3D Simulations . . . . .	78
4.5.1	Computational Domain . . . . .	78
4.5.1.1	Mesh Characterization . . . . .	79
4.5.2	Simulation Matrix . . . . .	82
4.5.3	Heat Resistance Tuning . . . . .	84
4.5.3.1	HRT: Workflow . . . . .	85
4.5.4	POD . . . . .	87
<b>5</b>	<b>Results</b>	<b>89</b>
5.1	1D Simulations . . . . .	89
5.2	HRT Results . . . . .	92
5.3	Baseline Simulation: H2-25% with 0% AAI . . . . .	95
5.3.1	Averaged fields . . . . .	95
5.3.2	V-to-M Flame Shape Transition . . . . .	99
5.3.3	PVC, Mixing and Flame Interaction . . . . .	101
5.4	The Effect of AAI: H2-25% with 20% AAI . . . . .	110
5.4.1	Observations on PVC . . . . .	113
5.4.2	Observations on Mixing . . . . .	113
5.4.3	Observations on NO Emissions . . . . .	115
5.5	The Effect of H2 Enrichment: H2-60% with 20% AAI . . . . .	119
5.5.1	Observations on Mixing - Effect of Fuel Momentum . . . . .	121
5.5.2	Observations on NO Emissions . . . . .	123
<b>6</b>	<b>Conclusions and Next Steps</b>	<b>127</b>
6.1	Next Steps . . . . .	128
<b>A</b>	<b>Appendix A: Mechanism Reduction</b>	<b>129</b>
A.1	Mechanism reduction methodology . . . . .	129
A.2	Validation Across Operating Conditions . . . . .	129
	<b>References</b>	<b>132</b>

# List of Figures

1.1	The causal chain from emissions to resulting warming of the climate system. Courtesy of [1]	2
1.2	Global GHG emissions of modelled pathways (funnels in Panel a), and projected emission outcomes from near-term policy assessments for 2030 (Panel b). Courtesy of [1]	3
1.3	Schema showing the principal emissions from aviation operations and the atmospheric processes that lead to changes in radiative forcing components. Radiative forcing changes lead to climate change as measured by temperatures and sea levels, for example. Climate change creates impacts on human activities and ecosystems and can lead to societal damages. From [8], adapted from [9] and [10]	4
1.4	Best-estimates for climate forcing terms from global aviation from 1940 to 2018. The bars and whiskers show ERF best estimates and the 5–95% confidence intervals, respectively. Red bars indicate warming terms and blue bars indicate cooling terms. Numerical ERF and RF values are given in the columns with 5–95% confidence intervals along with ERF/RF ratios and confidence levels. RF values are multiplied by the respective ERF/RF ratio to yield ERF values. ERF/RF values designated as [1] indicate that no estimate is available yet. Courtesy of [11]	5
1.5	Aviation market growth. Courtesy of [11]	6
1.6	Comparison of new technologies and sustainable aviation fuels. From [19]	7
1.7	Estimated costs of hydrogen production in 2030 for various technology options, retrieved from [20]. Renewable electricity price = USD 40/MWh at 4,000 full load hours in best locations. Sensitivity analysis based on $\pm 30\%$ variation in OPEX (Operating EXpense), CAPEX (CAPital EXpenditure), and fuel costs; $\pm 8\%$ change in default WACC (Weighted Average Cost of Capital); and a USD40/tCO <sub>2</sub> price variation to USD0/tCO <sub>2</sub> and USD100/tCO <sub>2</sub> levels.	8
2.1	Structure of a laminar plane premixed flame. From [36]	18
2.2	The combustion time (the time needed to reach the maximum pressure in a closed vessel) for a methane/air flame with and without turbulence, plotted as a function of the proportion of CH <sub>4</sub> in the reactant mixture, corresponding to the equivalence ratio $\phi$ (stoichiometric proportions correspond to about 10 % of methane). Time units correspond to 10 <sup>-2</sup> seconds. Adapted from [39]	22
2.3	Borghi diagram (turbulent combustion diagram): combustion regimes are identified in terms of length ( $l_t/\delta_l$ ) and velocity ( $u'/s_L^0$ ) ratios in a log-log diagram. [42]	24
2.4	Interactions between walls, flame and turbulence.	26
2.5	Laminar flame interacting with a cold wall. Temperature profiles at four consecutive instants $t_1$ to $t_4$ . The fresh gases temperature $T_1$ is equal to the wall temperature $T_W$ . Quenching occurs at $t = t_3$ .	27
2.6	The three configurations for flame/wall interaction in laminar flows.	27
2.7	Schematic diagram of processing leading to CRZ formation: (1) tangential velocity profile creates a centrifugal pressure gradient and sub-atmospheric pressure near the central axis; (2) axial decay of tangential velocity causes decay of radial distribution of centrifugal pressure gradient in axial direction; (3) thus, an axial pressure gradient is set up in the central region towards the swirl burner, causing reverse flow.	32

2.8	Swirl effect on flames. (1) Low $SN$ , (2) Intermediate $SN$ , (3) High $SN$ . . . . .	33
2.9	Sketch of instantaneous (a) azimuthal and (b) axial velocity inside the vortex breakdown bubble showing precessing vortex core (PVC) [59] . . . . .	34
2.10	Flashback in the core flow. The red shaded area indicates the region of burned gases, red arrows correspond to flame propagation and black arrows to the flow. The size of the arrow is drawn relative to the speed (flow or flame). [67] . . . . .	36
2.11	oundary-layer flashback. The shading and arrows are the same as in Figure 2.10 . . . .	37
2.12	Flashback- combustion instability-induced. The shading and arrows are the same as in Figure 2.10. . . . .	37
2.13	Flashback- combustion-induced vortex breakdown (CIVB).The flow enters from the mixing tube on the left into the combustion chamber. The shading and arrows are the same as in Figure 2.10. . . . .	38
2.14	Flame stability diagram for different equivalence ratios, with the Lower and Upper limit Flashback (LLF and ULF) indicated. . . . .	38
3.1	Qualitative representation of NO <sub>x</sub> and CO emissions and normalized pressure fluctuation, as a function of the equivalence ratio. The nominal equivalence ratio and its stable range are purely qualitative. The pollutant emission limits refer to the Industrial Emissions Directives (IED) on natural gas combustion of November 2010. It should be noted that the limits may be lower than those shown here, depending on what is agreed in the relevant Best Available Technologies (BAT) reference document (BREF). Permission levels for individual sites can also be lower. From [27]. . . . .	40
3.2	A schematic diagram showing an EV burner [33] . . . . .	41
3.3	Schematic of the FLOX® combustion principle implemented in [77] . . . . .	42
3.4	Top: OH* chemiluminescence measurement using a swirl burner in a square section non-adiabatic combustor [82]. Bottom: Scheme for the shear layers and recirculation zones. . . . .	44
3.5	CFD geometry with the TD burner. From [83] . . . . .	45
3.6	Reaction source term at cross plane from CFD simulations. (a) Original TFC model, (b) Extended TFC model with $S_L$ without heat loss effects, (c) Extended TFC model with $S_L$ with effects of strain and heat loss. From [83]. . . . .	46
3.7	Schematic of the test-rig. Dimensions are in mm. The reference computational domain for both non-reacting and reacting cases is delimited by the blue dashed line. The red dashed line represents the preliminary computational domain used to extract the velocity boundary conditions for the reference domain. The yellow dot at the tip of the central rod indicates the origin of the numerical frames. From [88] . . . . .	47
3.8	Comparisons of the mean flame position for the case $X_{H_2} = 0.6$ . Experiments, adiabatic (S1) and non-adiabatic (S2) simulations results are shown. From [88]. . . . .	48
3.9	Comparisons of the mean flame position for the case $X_{H_2} = 0.9$ . Experiments and non-adiabatic simulation results are shown. From [88]. . . . .	49
3.10	Computed geometry of the PRECCINSTA burner. From [96]. . . . .	50
3.11	Normalized progress variable iso-contour $c = 0.7$ , conditioned to heat release rate values exceeding 1% of its maximum value, colored by the temperature. From [96] . .	52
3.12	Scatter plot of the heat release rate against the velocity gradient norm, for points with $0.75 \leq c \leq 0.8$ , colored by the enthalpy defect for NAD4 simulation. From [96]. . . .	52
3.13	Validation of the LES simulations with HRT approach for case $P_{th} = 10kW$ . Comparison of experimental normalized time-averaged LOS OH* chemiluminescence image with LOS of predicted heat release rate $\bar{q}$ . From [100]. . . . .	54

3.14	(a) Instantaneous field of solid temperature and iso-contour of heat-release rate $\dot{q}$ at 10% of maximum value; (b) cut-plane showing the time-averaged temperature $\bar{T}$ and heat release rate $\bar{\dot{q}}$ predicted by CHT simulations. The added red iso-contour line corresponds to a temperature of 450 K, showing the pre-heating of the fresh gases by the solid walls. A zoom showing the temperature field with a different colorbar helps visualize the pre-heating of the gases and the temperature gradient in the solid. The fluid domain is delimited by a white line to visualize the separation between solid and fluid parts. From [100]. . . . .	55
3.15	Validation of CHT simulations. (a) Comparison of experimental normalized time-averaged Line of Sight (LOS) OH* chemiluminescence image with LOS predicted heat release rate $\bar{\dot{q}}$ . (b) Comparison of experimental normalized time-averaged OH-PLIF signal with predicted OH mass fraction. The arrows are tangential to the experimental and numerical time-averaged velocity field in the PIV plane. Their length and color indicate the velocity magnitude. Case B: 20% H <sub>2</sub> . From [100] . . . . .	56
3.16	Validation of CHT simulations. (a) Comparison of experimental normalized time-averaged Line of Sight (LOS) OH* chemiluminescence image with LOS predicted heat release rate $\bar{\dot{q}}$ . (b) Comparison of experimental normalized time-averaged OH-PLIF signal with predicted OH mass fraction. The arrows are tangential to the experimental and numerical time-averaged velocity field in the PIV plane. Their length and color indicate the velocity magnitude. Case C: 50% H <sub>2</sub> . From [100]. . . . .	57
3.17	(a) Experimental configuration (Reichel and Paschereit [71]) and (b) Computational domain. From [109]. . . . .	58
3.18	Instantaneous fields of HRR and equivalence ratio $\phi$ in a vertical cut plane for the LES-CHT case, with an isocontour of HRR at $2 \times 10^9 \text{ W/m}^3$ . Representation of the concave and convex parts around the flame front (defined with respect to the fresh gasses). From [111]. . . . .	60
3.19	(a–d) Instantaneous fields of O, NO, H mass fractions and temperature in a vertical cut plane close to the chamber inlet for the LES-CHT case. Iso-contour of HRR at $2 \times 10^9 \text{ W/m}^3$ indicating the flame front (black/red lines). From [111]. . . . .	61
4.1	Solution order of the transport equations. In most cases, the turbulence equations are outside of the iterative algorithm loop for efficiency reasons. . . . .	68
4.2	Reactants-to-products counterflow flame configuration, with temperature symbols annotation. Adapted from [135] . . . . .	77
4.3	Fluid computational domain of the APPU combustor, with annotations on main dimensions. Given the long chamber, compared to the length of the prechamber (inlets, swirler and mixing tube), only the first 200 mm of chamber are shown. . . . .	78
4.4	Section of the fluid computational domain of the APPU combustor. Inlets are highlighted, main dimensions are annotated. . . . .	79
4.5	Detail of relevant solid domain of the APPU combustor, with annotations on main dimensions . . . . .	79
4.6	Visualization of the velocity subgrid scale across the computational domain. The upper limit of the contour values has been clipped to the threshold embedding value. . . . .	80
4.7	Ratio of the velocity subgrid scale to the velocity magnitude, providing a normalized view of the subgrid scale velocity across the domain. . . . .	81
4.8	Illustration of the Thickened Flame Model (TFM) efficiency across the mesh. . . . .	81
4.9	Depiction of the thickening factor throughout the computational domain. . . . .	82
4.10	Heat Resistance Circuit . . . . .	86

5.1	Peak Heat Release Rate in counterflow premixed R2P CHEM1D simulations across various levels of Heat Loss parameters ( $HL = 1$ corresponds to the adiabatic case). The rows represent increasing equivalence ratios, while the columns show increasing hydrogen enrichment. . . . .	90
5.2	Peak NO Source term in counterflow premixed R2P CHEM1D simulations across various levels of Heat Loss parameters ( $HL = 1$ corresponds to the adiabatic case). The rows represent increasing equivalence ratios, while the columns show increasing hydrogen enrichment. . . . .	90
5.3	Inner Wall Temperature profile convergence . . . . .	92
5.4	Heat Transfer Coefficient (HTC) profile convergence . . . . .	92
5.5	Thermocouple placement. TC1 was introduced to estimate the plate temperature, while TC2, TC3 and TC4 tried to report the main points of the quartz, respectively the ORZ, the stagnation point of the swirled hot products and the outlet temperature. . . . .	93
5.6	This comparison between numerical expected value and thermocouple measured value shows the difficulty in retrieving the temperature of the metal plate, which has a high thermal inertia. . . . .	94
5.7	The figure shows a reasonable agreement of the numerically expected value compared to the thermocouple diagnosed value. The last abrupt increase in temperature is due to the detachment of the sensor, which came into contact with the hotter plate. . . . .	94
5.8	In this figure the accuracy of the prediction shows its best performance, as the predicted stagnation point of the swirling hot products is maintained at almost a constant temperature of 600 K. . . . .	94
5.9	The poor agreement on the outlet temperature prediction is to be attributed to a main reason, and it is a too coarse mesh on the outlet region, which unfortunately could not be resolved more due to compromises in the computational expense and relevance of the zone. . . . .	94
5.10	Averaged axial velocity field. An isoline is showed at $V = 0m/s$ to distinguish the recirculation zones. . . . .	95
5.11	Averaged radial velocity field. . . . .	95
5.12	Axial velocity RMS field. . . . .	96
5.13	Radial velocity RMS field. . . . .	96
5.14	OH* chemiluminescence image from experimental campaign. . . . .	96
5.15	HRR averaged value. . . . .	96
5.16	OH PLIF image from experimental campaign. . . . .	97
5.17	OH mole fraction averaged value. . . . .	97
5.18	Axial velocity field at $t = 269$ ms. . . . .	98
5.19	HRR instantaneous value at $t = 269$ ms. . . . .	98
5.20	OH mole fraction instantaneous value at $t = 269$ ms. . . . .	98
5.21	Instantaneous temperature field extracted at 150 ms after ignition - 1/2 Flow Through Time (FTT). <i>Note:</i> only the first 200 mm of the chamber are shown. . . . .	99
5.22	Instantaneous temperature field extracted at 600 ms after ignition - 2 Flow Through Time (FTT). <i>Note:</i> only the first 200 mm of the chamber are shown. . . . .	99
5.23	Temporal evolution of the flame Lift-Off Height (LOH). The data acquisition started from $0.3 s = 1$ FTT and finished at $0.6 s = 2$ FTT. . . . .	100
5.24	Non Reactive S1 case - Spatial POD modes on $z = 0m$ slice. POD is conducted on the azimuthal component of the velocity using as sampling period $t = 1e - 4s$ and as overall sampling time $T = 100ms$ . . . . .	101

5.25	Non Reactive S1 case - FFT applied to the POD modes time coefficients on $z = 0m$ slice. POD is conducted on the azimuthal component of the velocity using as sampling period $t = 1e - 4s$ and as overall sampling time $T = 100ms$ . . . . .	102
5.26	Reactive S1 case - Spatial POD modes on $z = 0m$ slice. POD is conducted on the azimuthal component of the velocity using as sampling period $t = 1e - 4s$ and as overall sampling time $T = 100ms$ . . . . .	102
5.27	Reactive S1 case - FFT applied to the POD modes time coefficients on $z = 0m$ slice. POD is conducted on the azimuthal component of the velocity using as sampling period $t = 1e - 4s$ and as overall sampling time $T = 100ms$ . . . . .	103
5.28	Reactive S1 case - TKE of the first 10 POD modes on $x = 0m$ slice. POD is conducted on the azimuthal component of the velocity using as sampling period $t = 1e - 4s$ and as overall sampling time $T = 100ms$ . . . . .	104
5.29	Reactive S1 case - First three POD modes time coefficients on $x = 0m$ slice. POD is conducted on the azimuthal component of the velocity using as sampling period $t = 1e - 4s$ and as overall sampling time $T = 100ms$ . . . . .	104
5.30	Reactive S1 case - Spatial POD modes on $x = 0m$ slice. POD is conducted on the azimuthal component of the velocity using as sampling period $t = 1e - 4s$ and as overall sampling time $T = 100ms$ . . . . .	105
5.31	Reactive S1 case - FFT applied to the POD modes time coefficients on $x = 0m$ slice. POD is conducted on the azimuthal component of the velocity using as sampling period $t = 1e - 4s$ and as overall sampling time $T = 100ms$ . . . . .	106
5.32	Equivalence Ratio Histogram. In order to acquire relevant data for the description of the flame, the datapoints $\vec{x}$ are conditioned to satisfy $HRR(\vec{x}) \geq 0.9HRR_{max}$ . . . . .	107
5.33	Equivalence ratio contour with HRR isosurface at time $t = 0.3202s$ . . . . .	107
5.34	Equivalence ratio contour with HRR isosurface at time $t = 0.3221s$ . . . . .	107
5.35	Planar view at $x = 0.0m$ of planar velocity vector field at time $t = 0.3202s$ . . . . .	108
5.36	Planar view at $x = 0.0m$ of planar velocity vector field at time $t = 0.3221s$ . . . . .	108
5.37	Planar view at $x = 0.0m$ of equivalence ratio field at time $t = 0.3202s$ . Isosurfaces of nominal and LBO equivalence ratio are shown. . . . .	108
5.38	Planar view at $x = 0.0m$ of equivalence ratio field at time $t = 0.3221s$ . Isosurfaces of nominal and LBO equivalence ratio are shown. . . . .	108
5.39	Reactive S1 case - Spatial POD modes on $x = 0m$ slice. POD is conducted on the equivalence ratio using as sampling period $t = 1e - 4s$ and as overall sampling time $T = 100ms$ . . . . .	109
5.40	Reactive S1 case - FFT applied to the POD modes time coefficients on $x = 0m$ slice. POD is conducted on the equivalence ratio using as sampling period $t = 1e - 4s$ and as overall sampling time $T = 100ms$ . . . . .	109
5.41	Reactive S1 case - Spatial POD modes on $x = 0m$ slice. POD is conducted on the heat release rate using as sampling period $t = 1e - 4s$ and as overall sampling time $T = 100ms$ . . . . .	110
5.42	Reactive S1 case - FFT applied to the POD modes time coefficients on $x = 0m$ slice. POD is conducted on the heat release rate using as sampling period $t = 1e - 4s$ and as overall sampling time $T = 100ms$ . . . . .	110
5.43	Averaged axial velocity field. An isoline is showed at $V = 0m/s$ to distinguish the recirculation zones. . . . .	111
5.44	Averaged radial velocity field. . . . .	111
5.45	Axial velocity RMS field. . . . .	112
5.46	Radial velocity RMS field. . . . .	112
5.47	OH* chemiluminescence image from experimental campaign. . . . .	113



5.48	HRR averaged value. . . . .	113
5.49	Averaged OH molar fraction . . . . .	113
5.50	Equivalence Ratio Histogram for simulation S1. In order to acquire relevant data for the description of the flame, the datapoints $\vec{x}$ are conditioned to satisfy $HRR(\vec{x}) \geq 0.9HRR_{max}$	114
5.51	Equivalence Ratio Histogram for simulation S2. In order to acquire relevant data for the description of the flame, the datapoints $\vec{x}$ are conditioned to satisfy $HRR(\vec{x}) \geq 0.9HRR_{max}$	114
5.52	Averaged equivalence ratio contour with HRR isosurface for case S1 . . . . .	114
5.53	Averaged equivalence ratio contour with HRR isosurface for case S2 . . . . .	114
5.54	Volume-averaged NO molar fraction in the first 10 cm of the combustion chamber. Sampling starts 100 ms after the ignition. . . . .	115
5.55	Volume-averaged Temperature in the first 10 cm of the combustion chamber. Sampling starts 100 ms after the ignition. . . . .	116
5.56	Equivalence ratio field in the flame region. The current flame shape is an M, with suppressed PVC in the chamber, but not in the mixing tube, resulting in richer reactant pockets. . . . .	116
5.57	NO molar fraction field in the flame region. The richer reactant pockets result in higher flame temperatures, and on the same location higher levels of NO molar fraction are present. . . . .	116
5.58	Equivalence ratio field in the flame region. A white isoline highlights the points at the stoichiometric equivalence ratio. . . . .	117
5.59	NO molar fraction field in the flame region. The higher concentration is present at the tip of the axial air flow, where high temperatures, N2 and O2 are both present in high quantity. . . . .	117
5.60	Temperature field in the flame region. High temperature combustion can be seen at the lip of the burner, where the flame is stabilized, but the hot products are convected to the center of the chamber, resulting in a higher average temperature of the flame region. . .	117
5.61	Simulation S2 - Heat Release Rate vs Strain scatterplot, coloured with temperature, to resemble the levels of Heat Loss parameters employed in CHEM1D. The strain magnitude is estimated following an approximation common in literature, retrieved in the Ansys theory manual [146]. . . . .	118
5.62	Simulation S2 - NO Mass Source vs Strain scatterplot, coloured with temperature, to resemble the levels of Heat Loss parameters employed in CHEM1D. <i>Note: only positive contribution are considered for this study.</i> . . . . .	118
5.63	Averaged axial velocity field. An isoline is showed at $V = 0m/s$ to distinguish the recirculation zones. . . . .	119
5.64	Averaged radial velocity field. . . . .	119
5.65	Axial velocity RMS field. . . . .	120
5.66	Radial velocity RMS field. . . . .	120
5.67	OH* chemiluminescence image from experimental campaign. . . . .	120
5.68	HRR averaged value. . . . .	120
5.69	Averaged OH molar fraction . . . . .	121
5.70	Equivalence Ratio Histogram for simulation S2. In order to acquire relevant data for the description of the flame, the datapoints $\vec{x}$ are conditioned to satisfy $HRR(\vec{x}) \geq 0.9HRR_{max}$	121
5.71	Equivalence Ratio Histogram for simulation S3. In order to acquire relevant data for the description of the flame, the datapoints $\vec{x}$ are conditioned to satisfy $HRR(\vec{x}) \geq 0.9HRR_{max}$	122
5.72	Averaged equivalence ratio contour with Lean Blow Off Limit and nominal equivalence ratio isosurface for case S2 . . . . .	122
5.73	Averaged equivalence ratio contour with Lean Blow Off Limit and nominal equivalence ratio isosurface for case S3 . . . . .	122

5.74	Averaged equivalence ratio contour with Lean Blow Off Limit and nominal equivalence ratio isosurface for case S2 . . . . .	123
5.75	Averaged equivalence ratio contour with Lean Blow Off Limit and nominal equivalence ratio isosurface for case S3 . . . . .	123
5.76	Averaged equivalence ratio contour with Lean Blow Off Limit and nominal equivalence ratio isosurface for case S2 . . . . .	123
5.77	Averaged equivalence ratio contour with Lean Blow Off Limit and nominal equivalence ratio isosurface for case S3 . . . . .	123
5.78	Volume-averaged NO molar fraction in the first 10 cm of the combustion chamber. Sampling starts 100 ms after the ignition. . . . .	124
5.79	Volume-averaged Temperature in the first 10 cm of the combustion chamber. Sampling starts 100 ms after the ignition. . . . .	124
5.80	Equivalence ratio field in the flame region. A white isoline highlights the points at the stoichiometric equivalence ratio. . . . .	125
5.81	NO molar fraction field in the flame region. The higher concentration is present at the tip of the axial air flow, where high temperatures, N <sub>2</sub> and O <sub>2</sub> are both present in high quantity. Comparing it with Figure 5.59, however, a higher NO concentration can be seen also close to the flame. . . . .	125
5.82	Temperature field in the flame region. High temperature combustion can be seen at the lip of the burner, where the flame is stabilized, but the hot products are convected to the center of the chamber, resulting in a higher average temperature of the flame region. . .	125
5.83	Schematic representation of the pathways, reactions and molecules involved in the NO formation for H <sub>2</sub> /air combustion. Adapted from [111]. . . . .	126
A.1	Comparison of the laminar flame speed for the original GRI 3.0 and reduced GRI 3.0 mechanisms at varying equivalence ratios. The results are shown for different hydrogen fractions in the fuel mixture. The reduced mechanism closely matches the original mechanism across the range of equivalence ratios, indicating good performance in predicting flame speeds. . . . .	130
A.2	Comparison of ignition delay times for the original GRI 3.0 and reduced GRI 3.0 mechanisms across various equivalence ratios and hydrogen fractions. The reduced mechanism demonstrates similar predictive capability to the original mechanism, maintaining accuracy in ignition delay times. . . . .	131
A.3	Comparison of NO emission indices between the original GRI 3.0 and reduced GRI 3.0 mechanisms for different equivalence ratios and hydrogen fractions. The reduced mechanism provides a reliable estimation of NO emissions, closely following the trends observed in the original mechanism, validating its effectiveness for emissions prediction.	131

# List of Tables

1.1	Properties of H <sub>2</sub> compared with Methane (CH <sub>4</sub> ) and Jet-A, adapted from [27], [25], [28], [29]	9
2.1	Simple classification of flame speeds	20
3.1	Resolution parameters for the LES computational grids. From [96].	51
3.2	Hydrogen-enriched operating points	56
3.3	Operating conditions and results from freely propagating flames computed from the solver CHEM1D [114] with the GRI3.0 chemical kinetics mechanism. From [113].	62
3.4	Section-averaged mean mass fractions of main emissions species and CO <sub>2</sub> from LES at the combustor exit. From [113].	63
4.1	Range of operating conditions explored in CHEM1D simulations	77
4.2	Operating conditions and key parameters for the simulation setups.	83
4.3	Estimation of bulk velocity at characteristic points of the APPU combustor.	84
4.4	Computed properties from preliminary 1D freely propagating flames.	84
A.1	Summary of the reduction in species and reactions achieved in the GRI 3.0 mechanism through the application of DRG, DRGEP, and DRGSA techniques.	130

# Introduction

This chapter will serve to introduce the *burning* environmental issues, examined and analyzed through the lens of prominent literature studies on climate change. Within this exploration, the specific role of combustion will be elucidated, as the chapter will delve into the compelling necessity for a transformative overhaul in combustion science, highlighting its significance in the broader context of sustainability and environmental stewardship. Finally, the structure of this thesis will be outlined.

## 1.1. Addressing Global Warming: the Challenge of the 21st Century

In order to accurately capture the current state of climate change assessment and potential outcomes, efforts were made to procure the most recent source available, without compromising on reliability and accuracy. As such, the primary studies considered span from the Assessment Report 6 (AR6) [1] of the Intergovernmental Panel on Climate Change (IPCC) [2]. This report comprises three Working Group contributions: "Climate Change 2021: The Physical Science Basis" [3], "Climate Change 2022: Impacts, Adaptation, and Vulnerability" [4], and "Climate Change 2022: Mitigation of Climate Change" [5]. These assessments draw upon scientific literature accepted for publication by January 31, 2021, September 1, 2021, and October 11, 2021, respectively.

From AR6, it is shown how emissions of greenhouse gases (GHGs) have increased rapidly over recent decades, as portrayed in panel (a) of Figure 1.1. In that same panel, it is possible to distinguish the different sources of global net anthropogenic GHG emissions:

- CO<sub>2</sub> from fossil fuel combustion and industrial processes (CO<sub>2</sub>-FFI) (dark green)
- net CO<sub>2</sub> from land use, land-use change and forestry (CO<sub>2</sub>-LULUCF) (grey)
- non-CO<sub>2</sub> emissions: CH<sub>4</sub>, N<sub>2</sub>O and fluorinated gases (HFCs, PFCs, SF<sub>6</sub>, NF<sub>3</sub>) (light blue)

These emissions have led to increases in the atmospheric concentrations of several GHGs including the three major well-mixed GHGs CO<sub>2</sub>, CH<sub>4</sub> and N<sub>2</sub>O, shown in panel (b), using annual values.

To indicate their relative importance each subpanel's vertical extent for CO<sub>2</sub>, CH<sub>4</sub> and N<sub>2</sub>O is scaled to match the assessed individual direct effect (and, in the case of CH<sub>4</sub> indirect effect via atmospheric chemistry impacts on tropospheric ozone) of historical emissions on temperature change from 1850–1900 to 2010–2019. This estimate arises from an assessment of effective radiative forcing and climate sensitivity.

The global surface temperature (shown as annual anomalies from a 1850–1900 baseline) has increased by around 1.1°C since 1850–1900, as portrayed in panel (c). The vertical bar on the right shows the estimated temperature (very likely range) during the warmest multicentury period in at least the last 100,000 years, which occurred around 6500 years ago during the current interglacial period (Holocene), caused by slow (multi-millennial) orbital variations.

Formal detection and attribution studies synthesise information from climate models and observations and show that the best estimate is that all the warming observed between 1850–1900 and 2010–2019 is caused by humans. Panel (d) shows temperature change attributed to:

- Total human influence
- Its decomposition into changes in GHG concentrations and other human drivers (aerosols, ozone and land-use change (land-use reflectance))
- Solar and volcanic drivers
- Internal climate variability.

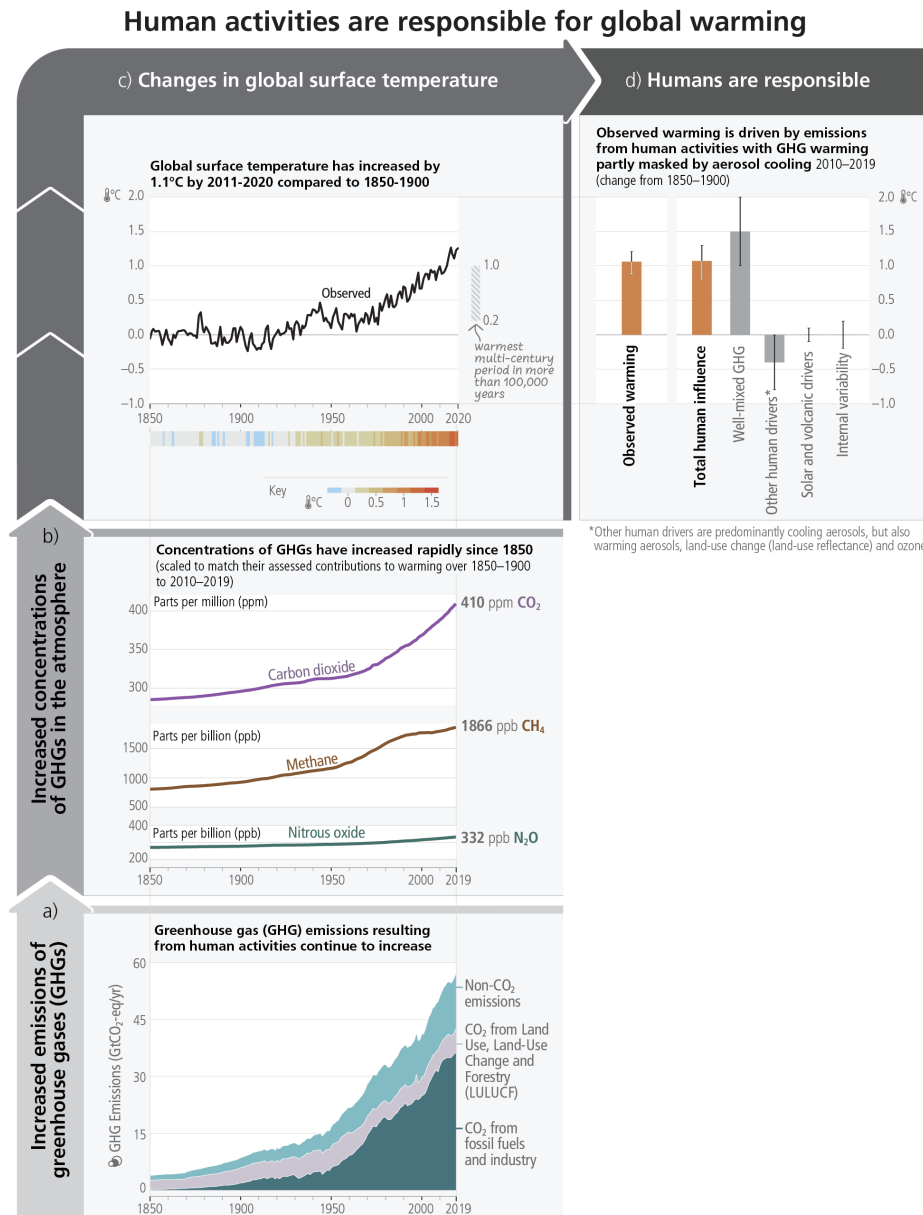


**Figure 1.1:** The causal chain from emissions to resulting warming of the climate system. Courtesy of [1]

At the time of the AR6 there are gaps between global ambitions and the sum of declared national ambitions, further compounded by gaps between declared national ambitions and current implementation for all aspects of climate action. For mitigation, global GHG emissions in 2030 implied by Nationally Determined Contributions (NDCs) announced by October 2021 would make it likely that warming will exceed 1.5°C during the 21st century and would make it harder to limit warming below 2°C. Despite progress, adaptation gaps persist, with many initiatives prioritising short-term risk reduction,

hindering transformational adaptation. Hard and soft limits to adaptation are being reached in some sectors and regions, while maladaptation is also increasing and disproportionately affecting vulnerable groups. Systemic barriers such as funding, knowledge, and practice gaps, including lack of climate literacy and data hinders adaptation progress.

Panel (a) in Figure 1.2 shows global GHG emissions over 2015–2050 for four types of assessed modelled global pathways:

- Trend from implemented policies: Pathways with projected near-term GHG emissions in line with policies implemented until the end of 2020 and extended with comparable ambition levels beyond 2030 (red line)
- Limit to 2°C (>67%) or return warming to 1.5°C (>50%) after a high overshoot, NDCs until 2030: Pathways with GHG emissions until 2030 associated with the implementation of NDCs announced prior to COP26, followed by accelerated emissions reductions likely to limit warming to 2°C or to return warming to 1.5°C with a probability of 50% or greater after high overshoot (blue line)
- Limit to 2°C (>67%) with immediate action: Pathways that limit warming to 2°C (>67%) with immediate action after 2020 (green line)
- Limit to 1.5°C (>50%) with no or limited overshoot: Pathways limiting warming to 1.5°C with no or limited overshoot (cyan line)

Panel (b) shows a snapshot of the GHG emission ranges of the modelled pathways in 2030 and projected emissions outcomes from near-term policy assessments in 2030.

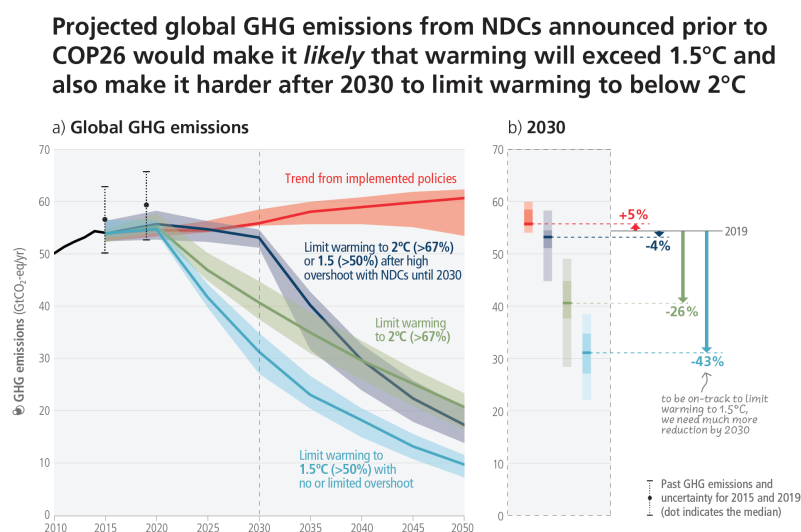


**Figure 1.2:** Global GHG emissions of modelled pathways (funnels in Panel a), and projected emission outcomes from near-term policy assessments for 2030 (Panel b). Courtesy of [1]

## 1.2. Assessing the Aviation Industry Contribution to Climate Change

In 1999, following a European assessment on the atmospheric impact of aviation in 1998 [6], the IPCC released a report titled "Aviation and the Global Atmosphere" [7]. This report marked the first comprehensive evaluation of aviation's influence on climate using the metric of radiative forcing (RF).

RF measures the alteration in the Earth-atmosphere energy balance since 1750, typically expressed in watts per square meter ( $W/m^2$ ) at the top of the atmosphere. Aviation-related RF components stem from various processes, listed here and showed in Figure 1.3:

- Emission of CO<sub>2</sub> (positive RF)
- Emission of NO<sub>x</sub>, which comprises three component terms: production of tropospheric O<sub>3</sub> (positive RF), a longer-term reduction in ambient methane (CH<sub>4</sub>) (negative RF), and a further small decrease in O<sub>3</sub> (negative RF)
- Emissions of H<sub>2</sub>O (positive RF)
- Formation of persistent linear contrails (positive RF)
- Aviation-Induced Cloudiness (AIC, potentially positive RF)
- Emission of sulfate particles (negative RF)
- Emission of soot particles (positive RF)

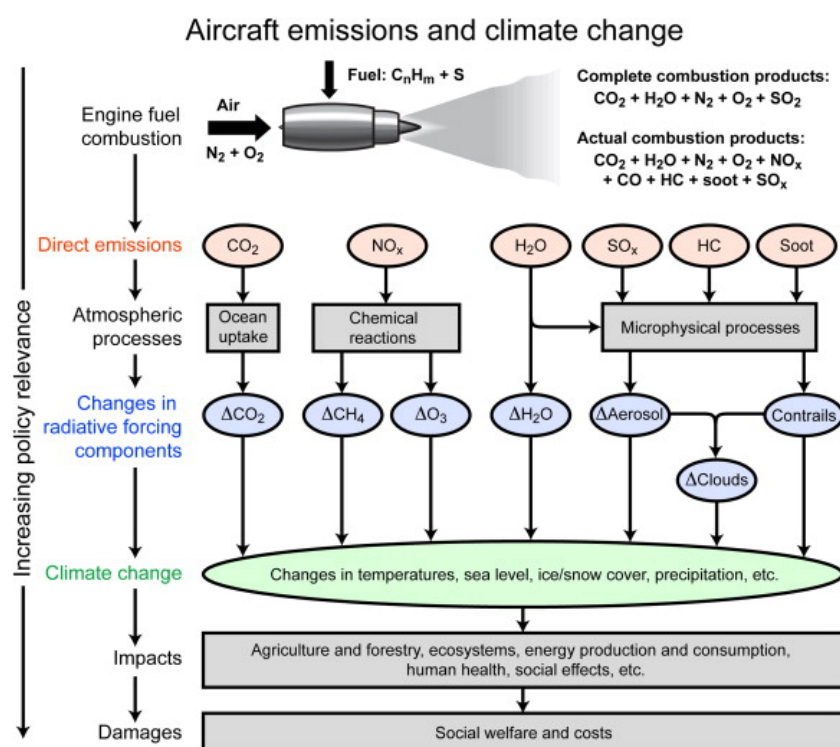


**Figure 1.3:** Schema showing the principal emissions from aviation operations and the atmospheric processes that lead to changes in radiative forcing components. Radiative forcing changes lead to climate change as measured by temperatures and sea levels, for example. Climate change creates impacts on human activities and ecosystems and can lead to societal damages. From [8], adapted from [9] and [10]

The IPCC report concluded that while aviation represented a small portion of total anthropogenic RF in 1992 (estimated at 3.5%, excluding AIC), it could become a more significant and increasing contributor to climate forcing, primarily due to its non-CO<sub>2</sub> effects. Following the analysis outlined in [8], by 2050, under a mid-range emission scenario, aviation's contribution to total anthropogenic RF was

projected to increase to 5%.

This last comprehensive and meticulous emission accounting effort has been followed by another improved and updated analysis [11], where calculations of radiative forcing have been expanded to include values for Effective Radiative Forcing (ERF) in addition to the traditional Radiative Forcing (RF) values.

The distinction between ERF and RF is outlined here, although a comprehensive description of the two quantities is described in [11]: ERF is considered the preferred metric for comparing the expected impacts of climate forcing terms, as it exhibits a stronger correlation with changes in the equilibrium global-mean surface temperature for certain forcing agents compared to RF.

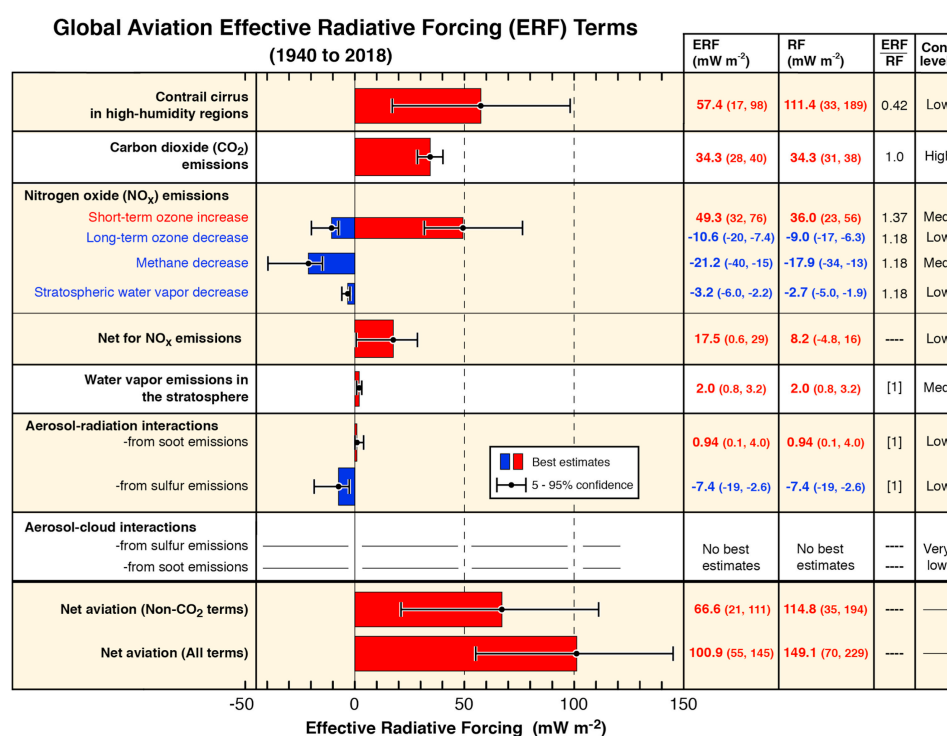


**Figure 1.4:** Best-estimates for climate forcing terms from global aviation from 1940 to 2018. The bars and whiskers show ERF best estimates and the 5–95% confidence intervals, respectively. Red bars indicate warming terms and blue bars indicate cooling terms. Numerical ERF and RF values are given in the columns with 5–95% confidence intervals along with ERF/RF ratios and confidence levels. RF values are multiplied by the respective ERF/RF ratio to yield ERF values. ERF/RF values designated as [1] indicate that no estimate is available yet. Courtesy of [11]

To put these estimates into perspective, it is necessary to highlight the high rate of increase of the entire aviation industry: global aviation fuel use and CO<sub>2</sub> emissions have exhibited substantial growth over the past four decades, particularly in Asia and other developing regions, driven by the rapid expansion of civil aviation [12][13]. This growth trend is expected to continue, with projections indicating significant orders from the Asia-Pacific region in the coming years. However, the COVID-19 pandemic has introduced uncertainty into these projections, leading to a slowdown in aviation operations in early 2020.

The sustained multi-decade growth in CO<sub>2</sub> emissions is a notable feature, with the average growth rate increasing significantly in recent years. In 2018, global aviation CO<sub>2</sub> emissions surpassed 1000 million tonnes per year for the first time, with approximately half of the cumulative emissions occurring in the last 20 years [14]. Current CO<sub>2</sub> emissions from aviation represent around 2.4% of anthropogenic CO<sub>2</sub> emissions, including those from land use change.



Despite this growth, aviation efficiency has improved substantially over time, as evidenced by increases in available seat kilometers (ASK) and revenue passenger kilometers (RPK) while fuel usage and CO<sub>2</sub> emissions have grown at a lesser rate. However, future aviation growth is expected to remain heavily reliant on kerosene fossil fuel, resulting in continued CO<sub>2</sub> emissions. Renewable biofuels offer a partial solution, but challenges remain in scaling up production and addressing uncertainties surrounding their life-cycle emissions.

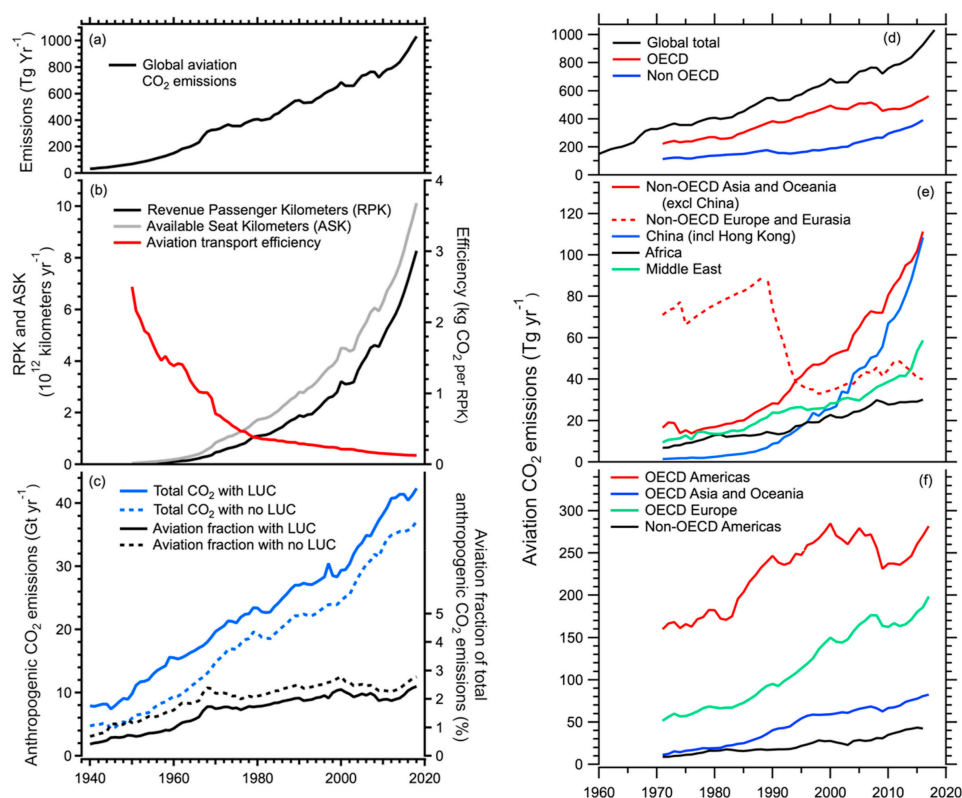


**Figure 1.5:** Aviation market growth. Courtesy of [11]







In Figure 1.5 it is possible to analyze data related to the growth of aviation traffic and CO<sub>2</sub> emissions from 1940 to 2018:

- Panel (a): Global aviation CO<sub>2</sub> emissions. Underlying fuel usage data for 1940 to 1970 are derived from [15] and for 1970–2016 from International Energy Agency [14] data, which include international bunker fuels. The average annual increase of global emissions from 1960 to 2018 is 15 Tg of CO<sub>2</sub> per year and the corresponding decadal average growth rates are 8.0, 2.2, 3.0, 2.3 and 1.1% per year, yielding an overall average of 3.3% per year.
- Panel (b): Global aviation traffic in RPK and ASK from airlines.org [16], and the transport efficiency of global aviation in kg CO<sub>2</sub> per RPK. The passenger load factor defined as RPK/ASK increased from about 60% in 1960 to 82% in 2018.
- Panel (c): Total anthropogenic CO<sub>2</sub> emissions and the aviation fractions of this total with and without the inclusion of CO<sub>2</sub> emissions from land use change (LUC) from the Global Carbon Budget 2018 [17].
- Panel (d)–(f): Additional aviation emissions data by region and year. The yearly sums of OECD (Organisation for Economic Co-operation and Development) and non-OECD values in (d) equal the respective global total values. The regional values in (e) and (f) also sum to equal the yearly global total values. Note different vertical scales [18]

## 1.3. Hydrogen for net zero carbon emissions

To address this challenge, various fuels and technologies are being considered, including sustainable aviation fuels (SAF), synfuels, and hydrogen. SAF, derived from biomass or waste, are environmentally friendly but may not significantly reduce CO<sub>2</sub> emissions, as shown in Figure 1.6. Synfuels, produced from hydrogen and captured carbon, offer compatibility with existing infrastructure but have limited reduction of non-CO<sub>2</sub> effects.

Hydrogen emerges as a promising option for decarbonizing aviation, whether used in fuel cells or combustion engines. Hydrogen fuel cells have been identified as suitable for commuter and regional aircraft, while hydrogen turbines are considered for medium-range aircraft. However, challenges remain, particularly in developing lightweight and safe hydrogen tanks, improving fuel cells' reliability and efficiency, and addressing safety concerns related to hydrogen combustion.

Comparison vs. kerosene	 Biofuels	 Synfuels	 Battery-electric	 Hydrogen
<b>Commuter</b> <19 PAX	No limitation of range	No limitation of range	Maximum ranges up to 500-1,000 km due to lower battery density	No limitation of range
<b>Regional</b> 20-80 PAX				
<b>Short-range</b> 81-165 PAX			Not applicable	Revolutionary aircraft designs as efficient option for ranges above 10,000 km
<b>Medium-range</b> 166-250 PAX				
<b>Long-range</b> >250 PAX				
<b>Main advantage</b> 	Drop-in fuel – no change to aircraft or infrastructure	Drop-in fuel – no change to aircraft or infrastructure	No climate impact in flight	High reduction potential of climate impact
<b>Main disadvantage</b> 	Limited reduction of non-CO <sub>2</sub> effects	Limited reduction of non-CO <sub>2</sub> effects	Change to infrastructure due to fast charging or battery exchange systems	Change to infrastructure

**Figure 1.6:** Comparison of new technologies and sustainable aviation fuels. From [19]

Hydrogen, a promising fuel alternative, possesses unique characteristics that set it apart from traditional hydrocarbons. Despite being the most abundant element in the universe, hydrogen is not readily available in its pure form on Earth, necessitating specific production processes. Its high Lower Heating Value (LHV) and reactivity present challenges in handling and utilization, distinguishing it from conventional fuels and requiring a comprehensive analysis of the entire value chain.

However, Hydrogen possesses also a unique set of issues, spanning from its production until the consumption, and a small review has been outlined here:

### 1.3.1. Production

Production of hydrogen is achieved through various methods, with Steam Methane Reforming (SMR) being the most common for commercial bulk production. This process, however, emits carbon dioxide and often requires Carbon Capture and Storage (CCS) technologies to mitigate environmental impact.

Alternative methods such as electrolysis offer a cleaner approach but are currently more expensive. Despite its higher costs, as shown in Figure 1.7, there is ongoing research to reduce the expense of producing green hydrogen, which could significantly impact global emissions.

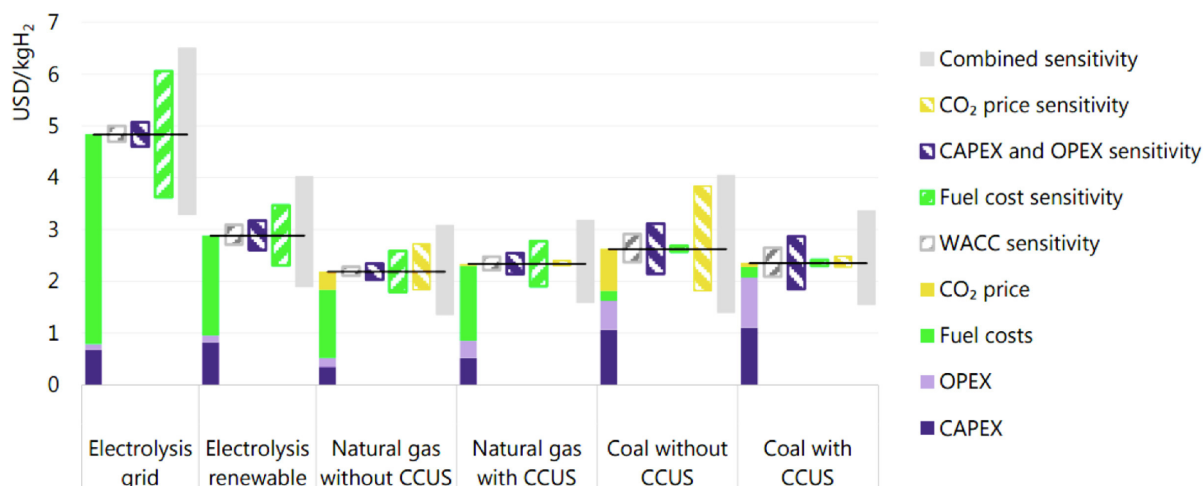


**Figure 1.7:** Estimated costs of hydrogen production in 2030 for various technology options, retrieved from [20]. Renewable electricity price = USD 40/MWh at 4,000 full load hours in best locations. Sensitivity analysis based on  $\pm 30\%$  variation in OPEX (Operating EXpense), CAPEX (CAPital EXpenditure), and fuel costs;  $\pm 8\%$  change in default WACC (Weighted Average Cost of Capital); and a USD40/tCO<sub>2</sub> price variation to USD0/tCO<sub>2</sub> and USD100/tCO<sub>2</sub> levels.

### 1.3.2. Storage and Transportation

Storage and transportation of hydrogen present unique challenges compared to hydrocarbon fuels due to its low volumetric energy density and safety hazards. To mitigate this, hydrogen can be compressed to high pressures or liquefied at cryogenic temperatures. Compressed hydrogen is stored in robust tanks, while liquefaction requires special cryogenic storage tanks. Additionally, hydrogen can be stored chemically in metal hydrides or compounds like ammonia, though this method requires chemical processing for extraction.

Despite technical storage solutions, hydrogen poses safety risks due to its high flammability and ability to form explosive mixtures with air. Its low molecular weight and high diffusivity make leakage detection difficult, and it can cause material failure through hydrogen embrittlement [21]. Special safety protocols and training are necessary to handle hydrogen safely.

Hydrogen is transported using various methods, including high-pressure gas cylinders for smaller quantities, tube trailers for larger volumes, and cryogenic liquid tankers, although the latter is energy-intensive. Bulk movement can be achieved through pipelines, with existing liquid methane pipelines potentially repurposed for hydrogen transport. The European Hydrogen Backbone initiative aims to expand hydrogen pipeline infrastructure significantly [22].

### 1.3.3. Consumption

Consumption of hydrogen energy can be achieved through fuel cells or combustion. Fuel cells offer a clean and efficient method, converting chemical energy into electricity with water as the only emission. However, their specific power output limits their applications. Alternatively, hydrogen combustion, though less efficient, can generate power outputs comparable to traditional gas turbines, presenting a viable option for various applications, including aviation.

Despite its potential, the implementation of hydrogen as a fuel faces challenges, particularly in aviation where commercial hydrogen-powered aircraft are not yet a reality. Here is a list of the specific issues regarding hydrogen combustion:

- **High reactivity**, attributed to its simple bond-breaking process and the small size of hydrogen atoms, which accelerates combustion by facilitating radical formation.  
The ignition delay time decreases with H<sub>2</sub> addition [23]. Designing the premixer to preclude autoignition requires knowledge of the fuel mixture ignition delay time and the local conditions relative to a premixing time scale.  
The higher flame speed (due to the increased production of OH, H, O radicals and the higher molecular diffusivity of H<sub>2</sub> [24]) increases the risk of dynamic instabilities (i.e., flashbacks where turbulent flame speed exceeds the flow velocity, typically in the flow boundary layer, allowing flame propagation inside the mixer, with obvious problems of material resistance and safety). Furthermore, H<sub>2</sub> enrichment increases the critical strain rate and minimizes the quenching possibilities of the flame.
- **High diffusivity**, caused by its small molecular size and weak intermolecular forces, leads to faster flame speeds compared to hydrocarbons. This difference in flame speed necessitates careful consideration in combustor design to ensure both efficiency and safety.  
Hydrogen's unique diffusive properties may also lead to thermo-diffusive instabilities, affecting flame behavior and local reaction rates. Managing these instabilities requires careful attention to factors like combustion chamber geometry and operating conditions to prevent issues like flashback or blow-off.
- **Higher flame temperature**, resulting from its high Lower Heating Value (LHV) and reactivity, poses challenges for NO<sub>x</sub> production. Mitigation techniques such as lean-burn technology can lower flame temperatures to reduce NO<sub>x</sub> emissions, leveraging hydrogen's properties to operate under lean conditions without lean blow-off.  
However, in that case, working with a blend of C<sub>n</sub>H<sub>m</sub>/H<sub>2</sub> with an excessively lean mixture, the temperature decrease could increase the CO emissions [25], as in not so excessive lean conditions the oxidation of CO to CO<sub>2</sub> is increased by the higher concentration of OH and H radicals [26]
- **Low Density**, the lower calorific value of hydrogen, on a volumetric basis, is approximately 1/3 of that of natural gas; therefore, fuel supply systems capable of providing a higher volumetric flow rate are required.

	<b>H<sub>2</sub></b>	<b>CH<sub>4</sub></b>	<b>Jet-A</b>
Molar mass [ <i>g/mol</i> ]	2.016	16.04	168
Density at NTP [ <i>kg/m<sup>3</sup></i> ]	0.0838	0.6512	775–840
Self Ignition T [ <i>K</i> ]	845–858	813–905	483
Minimum Ignition energy [ <i>mJ</i> ]	0.02	0.29–0.33	20
Flammability range in Air [ <i>vol%</i> ]	4–75	5–15	0.6–7
Flammability range [ <i>φ</i> ]	0.1–7.1	0.4–1.6	-
Stoich. Composition in air [ <i>vol%</i> ]	29.53	9.48	15
Adiabatic Flame Temperature [ <i>K</i> ]	2318–2400	2158–2226	2366
Lower Heating Value [ <i>MJ/kg</i> ]	118.8–120.3	50	43
Higher Heating Value [ <i>MJ/kg</i> ]	141.75	55.5	46.2
Lower Heating Value [ <i>MJ/m<sup>3</sup></i> ]	10.78	35.8	34400
Higher Heating Value [ <i>MJ/m<sup>3</sup></i> ]	12.75	39.72	36960

**Table 1.1:** Properties of H<sub>2</sub> compared with Methane (CH<sub>4</sub>) and Jet-A, adapted from [27], [25], [28], [29]

To effectively utilize hydrogen in aircraft engines, a model capable of capturing these differences and handling typical gas turbine combustor conditions is essential. Such a model would enable engineers to design combustors that harness hydrogen's advantages while mitigating potential risks, ensuring safe and efficient operation in the aviation industry.

Research and innovation efforts are underway to overcome these challenges and develop hydrogen propulsion technologies that can significantly reduce aviation's climate impact. International research projects funded by organizations like the European Union are focused on understanding hydrogen combustion and its integration with existing aircraft systems to achieve the ambitious goal of net zero carbon emissions.

A growing number of land-based gas turbines are embracing H<sub>2</sub> as either their primary or secondary fuel source, leveraging the fact that its low volumetric lower heating value poses no issue for terrestrial applications, unlike in aircraft where it could significantly hamper performance.

A comprehensive review of some examples has been reported in section 3.1, following the main review papers published on this topic, such as [27], [30], [31], [20], [29], [32], [33] and [34].

## 1.4. Organization of the thesis

To comprehensively tackle the challenges highlighted in this introduction chapter, this thesis is structured following this organizational framework:

- **Theoretical Foundation:** This segment furnishes an exhaustive overview of the theoretical underpinnings that underlie our investigation. Topics addressed encompass a mathematical description of reactive flows, some qualitative aspects of turbulent combustion, combustion dynamics, flame stabilization mechanisms, particularly swirling flows, and the main traits of hydrogen incorporation on flame characteristics.
- **Literature Review:** This chapter undertakes a comprehensive review of pertinent literature about swirl-stabilized flames involving methane, hydrogen and their blends. Through critical analysis of prior studies, lacunae in understanding or young first approaches are identified, underscoring the significance of our research contributions and stating the research questions that this research effort will answer.
- **Modeling and Methodology:** Herein, we expound upon the computational methodologies deployed in our research endeavours. This encompasses the integration of theoretical frameworks into reactive LES simulations, with a particular emphasis on elucidating heat loss, flame morphology, mixing dynamics, and emissions behaviour. Moreover, simulation setup details, post-processing techniques, and evaluation criteria are described.
- **Results and Discourse:** Findings from our reactive LES simulations are elucidated and deliberated upon in this segment. We scrutinize the implications of hydrogen addition on flame attributes, expound upon the repercussions of heat dissipation, and gauge the fidelity of modeling approaches.
- **Conclusion and Next Steps:** The thesis culminates with a succinct summation of key findings, coupled with a discourse on prospective avenues for future investigations. Insights obtained from our research are contextualized within the broader landscape of low-carbon combustion technologies, paving the way for continued scholarly inquiry and technological advancement.

# 2

## Theoretical Background

Quelli che si innamorano della pratica senza scientia sono come nocchieri che entrano in naviglio senza timone o bussola, che mai hanno certezza dove si vadano.

---

*Leonardo da Vinci*

This chapter serves to provide a foundational understanding of the theoretical framework necessary for comprehending the methodologies employed in this thesis endeavour, detailed in chapter 4. The discussion begins with the description of reactive flows and then transitions to laminar premixed flames. Then, it offers qualitative insights into turbulence, and the interaction between turbulence and chemistry is addressed. Notably, considerable attention is directed towards flame/wall interactions, given their significance in this study. Furthermore, a section is dedicated to emissions, outlining their characteristic reaction mechanisms and models utilized for their evaluation. Finally, the chapter concludes with a description of a specific type of flow known as swirling flow, which exhibits distinct characteristics which are of particular interest to the combustors studied in this research.

### 2.1. Reactive Flows

This section presents the conservation equations for reacting flows and highlights the three main differences between these equations and the usual Navier-Stokes equations for non-reacting cases:

1. A reacting gas is a non-isothermal mixture of multiple species (hydrocarbons, oxygen, water, carbon dioxide, etc.) which must be tracked individually. Thermodynamic data are also more complex than in classical aerodynamics because heat capacities in a reacting gas change significantly with temperature and composition.
2. Species react chemically and the rate at which these reactions take place requires specific modeling.
3. Since the gas is a mixture of gases, transport coefficients (heat diffusivity, species diffusion, viscosity, etc.) require specific attention.

The basic set of balance equations for a reactive flow comprises the classical Navier-Stokes, species and energy transport equations, which can be derived by applying the Reynolds transport theorem and the Divergence theorem to the conservation laws for a material volume  $V(t)$ , defined as a volume with mass  $M$  and always made of the same set of material points.

First of all, it is necessary to assume that continuum mechanics is applicable, which is the case for

most reactive flows: this can be proved by checking the Knudsen number  $Kn$ , a dimensionless number defined as the ratio of the molecular mean free path length to a representative physical length scale:

$$Kn = \frac{l_{mfp}}{L} \quad (2.1)$$

For  $Kn \ll 1$ , continuum mechanics is applicable, resulting in these instantaneous local balance equations:

**Mass:**

$$\frac{\partial \rho}{\partial t} + \vec{\nabla} \cdot (\rho \vec{u}) = 0 \quad (2.2)$$

**Momentum:**

$$\frac{\partial \rho \vec{u}}{\partial t} + \vec{\nabla} \cdot (\rho \vec{u} \vec{u}) - \rho \vec{f} + \vec{\nabla} p - \vec{\nabla} \cdot \underline{\underline{\tau}} = 0 \quad (2.3)$$

**Species:**

$$\frac{\partial \rho Y_k}{\partial t} + \vec{\nabla} \cdot (\rho \vec{u} Y_k) + \vec{\nabla} \cdot (\rho Y_k \vec{V}_k) = \dot{\omega}_k \quad (2.4)$$

**Enthalpy:**

$$\frac{\partial \rho h^s}{\partial t} + \vec{\nabla} \cdot (\rho \vec{u} h^s) = \left( \frac{\partial p}{\partial t} + \vec{u} \cdot \vec{\nabla} p \right) - \vec{\nabla} \cdot \vec{q} + \Phi + \sum_{k=1}^N \rho Y_k \vec{V}_k \cdot \vec{f}_k + \sum_{k=1}^N h_{f,k}^0 \vec{\nabla} \cdot (\rho Y_k \vec{V}_k) - \sum_{k=1}^N h_{f,k}^0 \dot{\omega}_k \quad (2.5)$$

Where  $k = 1, \dots, N$ , and  $N$  is the number of species.

Apart from the typical thermodynamic properties, such as density, temperature, etc., the following list explains the additional terms that appear in the above-mentioned equations:

- $\vec{f}$  represents the vector of **body forces** per unit mass:  $\vec{f} = \sum_{k=1}^N Y_k \vec{f}_k$
- The **viscous stress tensor**  $\underline{\underline{\tau}}$  is divided into its isotropic and deviatoric components:

$$\underline{\underline{\tau}} = -p \underline{\underline{I}} + \underline{\underline{\tau}} \quad (2.6)$$

Where  $\underline{\underline{I}}$  is the **identity tensor**,  $p$  is the **pressure** and  $\underline{\underline{\tau}}$  is the **viscous stress tensor**, which elements are the viscous stresses  $\tau_{ij}$ , that can be expressed, assuming that the fluid is Newtonian, as follows:

$$\underline{\underline{\tau}} = 2\mu_m \underline{\underline{S}} + \left( k - \frac{2}{3}\mu_m \right) \cdot \vec{\nabla} \cdot \vec{u} \cdot \underline{\underline{I}} \quad (2.7)$$

Where:

- $\underline{\underline{S}}$  is the **strain rate tensor**  $\underline{\underline{S}} = \frac{1}{2} \left( \vec{\nabla} \vec{u} + \left( \vec{\nabla} \vec{u} \right)^T \right)$
- $\mu_m$  is a suitable **mixture averaged dynamic viscosity**
- $k$  is the **bulk viscosity** (also called **dilatational viscosity**). The usual practice is to employ the following hypothesis made by Stokes in 1845:

$$k = 0 \quad (2.8)$$

Physically, the nonzero values of  $k$  for polyatomic gases are caused by relaxation effects between the translational motion and the various internal degrees of freedom.



The constitutive relation for Newtonian fluids is still valid but a suitable mixture averaged viscosity  $\mu_m$  is needed. This can be computed using the Wilke formula which is valid for diluted polar and non-polar gases:

$$\mu_m = \sum_{k=1}^N \frac{X_k \mu_k}{\sum_{j=1}^N X_j \phi_{kj}} \quad (2.9)$$

With:

$$\phi_{kj} = \frac{1}{\sqrt{8}} \left( 1 + \frac{M_k}{M_j} \right)^{-1/2} \left[ 1 + \left( \frac{\mu_k}{\mu_j} \right)^{1/2} \left( \frac{M_j}{M_k} \right)^{1/4} \right]^2 \quad (2.10)$$

- $\vec{V}_k$  is the **diffusion velocity** of the species  $k$ .  
It is defined as  $\vec{V}_k = \vec{v}_k - \vec{u}$ , where  $\vec{v}_k$  is the local velocity of the species  $k$  and  $\vec{u} = \sum_{k=1}^N Y_k \vec{v}_k$  is the mass averaged local velocity of the mixture.

A property of the diffusion velocity, coming from mass conservation, is the following:

$$\sum_{k=1}^N Y_k \vec{V}_k = 0 \quad (2.11)$$

- $\dot{\omega}_k$  is the **net rate of production** of the species  $k$  per unit of volume that is the source term that needs to be taken into account because of the occurrence of chemical reactions, that conserve the mass but not each species.

The conservation of mass, therefore, implies:

$$\dot{\omega} = \sum_{k=1}^N \dot{\omega}_k = 0 \quad (2.12)$$

The reaction rate of species  $k$  can be expressed following the Arrhenius form:

$$\dot{\omega}_k = \sum_{i=1}^L \left( \nu''_{k,i} - \nu'_{k,i} \right) A_i T^{n_i} \exp \left( \frac{E_i}{RT} \right) \prod_{j=1}^N [M_j]^{\nu'_{j,i}} \quad (2.13)$$

Where:

- $L$  is the **number of reactions** that occur, paying attention that direct and reverse reactions count as two different reactions for what concerns the number  $L$ .
- $\nu'_{k,i}$  and  $\nu''_{k,i}$  are the **stoichiometric coefficient** of the species  $k$  of, respectively, the reactants and the products of the reaction  $i$ .
- $M_j$  is the symbol of species  $j$ .
- $A_i$  is the **pre-exponential factor** of Arrhenius kinetic, and in this mass basis expression it is needed to be taken into account also the molecular weight  $W_k$  of species  $k$ .
- $n_i$  is the **global order of chemical reaction**  $i$
- $E_i$  is the **activation energy** of chemical reaction  $i$ .
- $\vec{q}$  is the **generalized heat flux**:

$$\vec{q} = -\lambda_m \vec{\nabla} T + \rho \sum_{k=1}^N h_k Y_k \vec{V}_k + RT \sum_{i=1}^N \sum_{j=1}^N \frac{X_j D_i^T}{M_i D_{ij}} \left( \vec{V}_i - \vec{V}_j \right) + \vec{q}_r \quad (2.14)$$

The single terms are:

- $-\lambda_m \vec{\nabla} T$ : **Conduction heat transfer** in the presence of a temperature gradient (Fourier's law). The thermal conductivity  $\lambda_m$  is a mixture averaged property and, as for the viscosity, it can be calculated from the thermal conductivity of pure species.
- $\rho \sum_{k=1}^N h_k Y_k \vec{V}_i$ : **Heat transfer through mass diffusion** due to the different enthalpy (i.e. total enthalpy, that is sensible plus chemical) content of the various species.
- $RT \sum_{i=1}^N \sum_{j=1}^N \frac{X_j D_{ij}^T}{M_i D_{ij}} (\vec{V}_i - \vec{V}_j)$ : **Dufour effect**, that takes into account the heat transfer due to concentration gradients.
- $\vec{q}_r$ : **Radiative heat transfer** and it is an integral function accounting for the radiation effect in all directions. It depends on the gas temperature as well as the molecular structure because the efficiency of molecular radiation absorption and emission is sensitive to the wavelength of the radiation.

This last term is important for flames with heavy soot loading because, in such cases, the radiative heat loss can be so substantial that the flame temperature is significantly reduced.

- $\vec{\Phi}$ : **Dissipation function** representing the dissipation of mechanical energy into heat due to viscous stresses. This term comes, together with  $-p \vec{\nabla} \cdot \vec{u}$  in the derivation of the energy equation, from the double dot-product between the stress tensor and the gradient of the velocity field  $\underline{\underline{T}} : \vec{\nabla} \vec{u}$ .

Highlighting the two contributions:  $\underline{\underline{T}} : \vec{\nabla} \vec{u} = -p \underline{\underline{I}} : \vec{\nabla} \vec{u} + \underline{\underline{\tau}} : \vec{\nabla} \vec{u}$ , where  $-p \underline{\underline{I}} : \vec{\nabla} \vec{u}$  represents the reversible work of the surface forces acting on the boundaries of the control volume  $V(t)$  and  $\vec{\Phi} = \underline{\underline{\tau}} : \vec{\nabla} \vec{u}$  is the viscous dissipation term, or the irreversible work of the surface forces (i.e. of the viscous stresses) acting on the boundaries of the control volume  $V(t)$ . The reversible work did not survive as was taken out of the energy equation by applying the local conservation of mass.

- $\sum_{k=1}^N h_{f,k}^0 \dot{\omega}_k$ : **Heat release** term due to the chemical reaction that occurs in the system. It is negative for exothermic reactions.

Considering Equation 2.2 and Equation 2.4, they are  $N + 1$  balance equations, that will close the  $N + 1$  unknowns  $[\rho, Y_k]$ . One must be aware that only  $N - 1$  of the  $N$  species equations are linearly independent: the mass fraction of the species not accounted for by the above system is given by the following constraint:  $\sum_{k=1}^N Y_k = 1$ . The determination of the further  $3N$  unknown given by the components of  $\vec{V}_k$  for each species has now to be addressed.

The diffusion velocities  $\vec{V}_k$  are obtained by solving the system:

$$\vec{\nabla} X_p = \sum_{k=1}^N \frac{X_p X_k}{D_{pk}} (\vec{V}_k - \vec{V}_p) + (Y_p - X_p) \frac{\vec{\nabla} p}{p} + \sum_{k=1}^N \frac{X_p X_k}{\rho D_{pk}} \left( \frac{D_k^T}{Y_k} - \frac{D_p^T}{Y_p} \right) \frac{\vec{\nabla} T}{T} + \frac{\rho}{p} \sum_{k=1}^N Y_p Y_k (\vec{f}_p - \vec{f}_k) \quad (2.15)$$

For  $p = 1, 2, \dots, N$ , where  $D_{pk} = D_{kp}$  is the **binary mass diffusion coefficient** of species  $p$  into species  $k$  and  $X_k$  is the **molar fraction** of species  $k$ :  $X_k = Y_k W / W_k$ .

The following is a description of the terms of the right-hand-side of the equation, which contributes to the  $\vec{\nabla} X_p$ :

- $\sum_{k=1}^N \frac{X_p X_k}{D_{pk}} (\vec{V}_k - \vec{V}_p)$  represents the difference between diffusion velocities.
- $(Y_p - X_p) \frac{\vec{\nabla} p}{p}$  takes into account the **pressure gradient** term.
- $\sum_{k=1}^N \frac{X_p X_k}{\rho D_{pk}} \left( \frac{D_k^T}{Y_k} - \frac{D_p^T}{Y_p} \right) \frac{\vec{\nabla} T}{T}$  is the contribution to the mass diffusion given by the temperature gradients, and it is called **Soret diffusion**.
- $\frac{\rho}{p} \sum_{k=1}^N Y_p Y_k (\vec{f}_p - \vec{f}_k)$  takes into account the difference between the **body forces** acting on each species.

The system provides concentration gradients in terms of diffusion velocities. The diffusion velocity  $\vec{V}_k$  is given implicitly and depends on all the diffusion velocities and all the concentrations. This aspect adds complexity to the numerical solution of the balance equations and for this reason two simplifications are common:

1. **Fick's law**, for theoretical and analytical flame studies, which is an exact, though simplified, approach.
2. **Hirschfelder and Curtiss approximation**, used in most numerical tools.

If pressure gradients are small (i.e.  $\vec{\nabla}p/p \ll 1$ ), volume forces are neglected (i.e.  $\vec{f}_k \approx 0$ ), and the Soret effect is considered to be negligible (which is not always true when dealing with combustion, however, it is often neglected for simplicity), the system can be solved exactly in two cases: first if the mixture contains only two species (i.e.  $N = 2$ ), leading to Fick's law for binary mixture; second is multispecies diffusion ( $N > 2$ ) with all the binary diffusion coefficients are equal ( $D_{jk} = D$ ), leading again to Fick's law.

Most flame theories assume that all species have identical diffusion coefficients so that Fick's law is a common choice in theoretical flame studies. As soon as a more detailed description of transport is required (i.e. to describe complex kinetics), Fick's law can not be used and in most codes the rigorous (and computationally expensive) inversion of system in a multispecies gas is often replaced by the Hirschfelder and Curtiss approximation, which is the best first-order approximation to the exact resolution of the system [35].

**Simplifying Assumptions of the Instantaneous Balance Equations** With regard to non-reacting problems, combustion adds complexity because species react and their rate of reaction  $\dot{\omega}_k$  must be modeled, species and heat coefficients change within the solution, and transport coefficients are species-dependent. In this section the simplifying assumptions that are often used in literature, and their effect on the governing equations, are shown:

- For subsonic flow the  $\vec{\Phi}$  **term can be neglected**, being the dissipation function much smaller than the heat release
- $\vec{q}_r$  **is generally neglected**, although it is relevant for certain applications with sooty flames.
- $\vec{f}_k$  **are generally neglected**
- **Dufour effect and Soret effect are generally not taken into account**, the former is in fact typically negligible in most combustion problems whereas the latter is typically neglected for simplicity.
- In low-speed subsonic flow (deflagrations) the **low Mach approximation can be made** ( $M \ll 1$ ): this implies that  $\vec{\nabla}p \approx 0$  hence both the momentum and energy equation result to be simplified. In comparison to their compressible counterparts, LES, DNS, and RANS simulations can use greater time steps thanks to this approximation. As a result, more complex kinetics can be used, which can improve predictions of the flame and its interactions with turbulence. On the other hand, in exchange, the acoustics are ignored. The interest in this work is for deflagration flames, where the pressure is nearly constant throughout the flame and the speed of the flame front  $s_L$  (i.e., the speed with which it advances into the reactants field) is substantially slower than the speed of sound.
- The diffusion velocities can be modeled using the Hirschfelder approximation, thus one can write  $V_k X_k = -D_k \vec{\nabla} X_k$ , where  $D_k$  is related to the thermal diffusivity  $D_{th}$  through the Lewis number of species  $k$ :  $Le_k D_k = D_{th}$  where  $D_{th}$  is the thermal diffusivity defined as  $D_{th} = \frac{\lambda_m}{\rho c_p}$ , where  $c_p$  is the averaged specific heat at a constant pressure of the mixture:  $c_p = \sum_{k=1}^N c_{p,k} Y_k$

- The assumption of  $Le_k = 1$  for all the  $k$  species is generally made to simplify turbulent flame modeling, especially in premixed flames when species mass fractions and temperature are assumed to be equivalent variables. Nevertheless, thermodiffusive instabilities occur in premixed systems when the Lewis number is lower than unity (e.g. for hydrogen). One direct consequence of these instabilities is an increase in the premixed flame area and in the reaction rate, which is non-negligible, therefore a mixture-averaged approach is preferable when these low  $Le$  species are present.
- **The fluid mixture is considered to be Newtonian**, with zero bulk viscosity allowing to express  $\underline{\tau}$  as:  $\underline{\tau} = 2\mu_m \left( \underline{S} - \frac{1}{3} \vec{\nabla} \cdot \underline{\vec{u}} \underline{I} \right)$
- It is assumed the validity of the equation of state of the ideal gas, since the temperatures with which the combustion deals are much higher than the critical temperature of the mixture of reactants and products:

$$p = \rho \frac{R}{M_m} T \quad (2.16)$$

## 2.2. Laminar Premixed Combustion

The elementary case of a one-dimensional laminar flame propagating into a premixed gas (fuel mixed with air for example) is a basic problem in combustion, both for theory and for numerical techniques. Numerically solving for laminar premixed flames is of interest because:

- It is one of the few configurations where detailed comparisons between experiments, theory and computations can be performed.
- It may be used to validate chemical models
- Many theoretical approaches may be used for laminar flames, not only to study their one-dimensional structure but also the various instabilities which can develop on such fronts
- Laminar flames are viewed in many turbulent combustion models as the elementary building blocks of turbulent flames (flamelets models)

For laminar one-dimensional premixed flames, the conservation equations derived before can be simplified, considering only one spatial dimension:

**Mass:**

$$\frac{\partial \rho}{\partial t} + \frac{\partial \rho u}{\partial x} = 0 \quad (2.17)$$

**Momentum:**

Neglecting the viscous terms, the momentum equation is decoupled, meaning that it can be used to compute the pressure field after all fields have been computed by applying:

$$p(x) = p_1 - \rho_1 s_L (u(x) - u_1) \quad (2.18)$$

**Species:**

$$\frac{\partial \rho Y_k}{\partial t} + \frac{\partial}{\partial x} (\rho(u + V_k) Y_k) = \dot{\omega}_k \quad (2.19)$$

**Sensible Entalphy:**

$$\rho c_p \left( \frac{\partial T}{\partial t} + u \frac{\partial T}{\partial x} \right) = - \sum_{k=1}^N h_k \dot{\omega}_k + \frac{\partial}{\partial x} \left( \lambda \frac{\partial T}{\partial x} \right) - \rho \frac{\partial T}{\partial x} \left( \sum_{k=1}^N c_{p,k} Y_k V_k \right) \quad (2.20)$$

Where  $k = 1, \dots, N - 1$ , and  $N$  is the number of species. These equations describe a wave propagating from the burnt to the fresh gas at a speed which reaches a

constant value  $s_L$  when transients are ignored. Solving for the structure of this flame is still a research task for complex chemistry descriptions even when the flame has reached a constant velocity. When the flame is steady, writing Equation 2.17, Equation 2.19 and Equation 2.20 in the reference frame of the flame (moving at speed  $s_L$ ) leads to:

$$\rho u = \rho_1 s_L \quad (2.21)$$

This set of equations is closed if a model is given for the reaction rate  $\dot{\omega}_k$  (Arrhenius law) and for the diffusion velocities  $V_k$  (Fick's law with a correction velocity, for example) and if proper boundary conditions are provided. For premixed flames, these boundary conditions may raise some difficulties. Typical inlet conditions (at location  $x = 0$ ) correspond to a cold premixed gas flow:  $u(x = 0) = u_1$ ,  $Y_k$  imposed for reactants (in proportions imposed by the code user),  $T(x = 0) = T_1$  imposed.

### 2.2.1. Flame Structure

The structure of a laminar premixed flame is shown in Figure 2.1. Fresh gases and burnt gases are separated by a thin reaction zone, where a strong temperature gradient is observed.

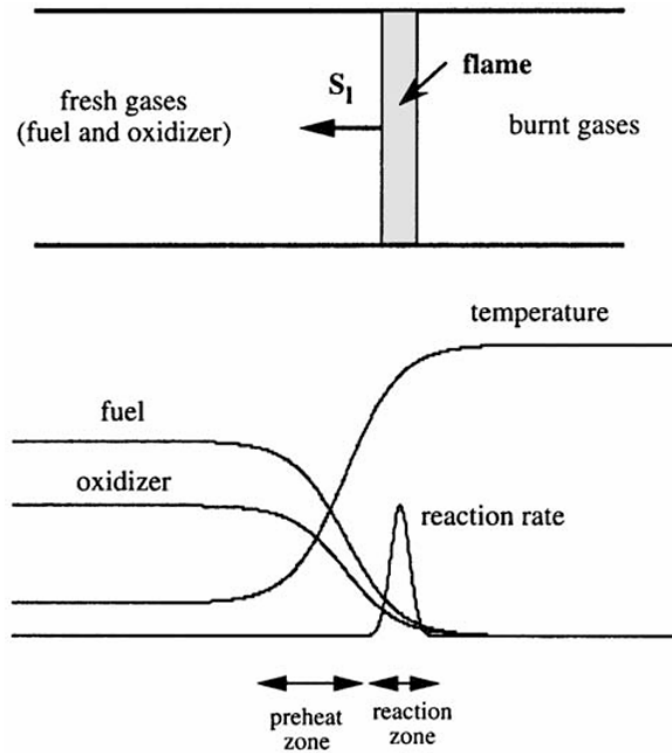
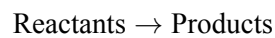


**Figure 2.1:** Structure of a laminar plane premixed flame. From [36]

Because of the temperature gradient and the corresponding thermal fluxes, fresh gases are preheated and then start to burn. The local imbalance between diffusion of heat and chemical consumption is what leads to the propagation of the front with a particular speed, as further explained in subsection 2.2.3. For a simple one-step irreversible chemical scheme:



the flame is described using a progress variable  $c$ , such as  $c = 0$  in the fresh gases and  $c = 1$  in the fully

burnt ones, using a reduced temperature or a reduced mass fraction:

$$c_T = \frac{T - T_u}{T_b - T_u} \quad (2.22)$$

$$c_F = \frac{Y_F - Y_F^u}{Y_F^b - Y_F^u} \quad (2.23)$$

Where  $T$ ,  $T_u$  and  $T_b$  are the local, unburnt gas and the burnt gas temperatures, while  $Y_F$ ,  $Y_F^u$  and  $Y_F^b$  are the local, unburnt gas and burnt gas fuel mass fractions.

### 2.2.2. Flame Thickness

Defining and estimating a flame thickness before computation is an obvious requirement for many numerical combustion problems because this thickness controls the required mesh resolution: in most combustion approaches, the flame structure must be resolved and enough points must be localized within the flame thickness. There are many ways to define thicknesses for premixed flames. Some of them require a first computation of the flame front (for example in a one-dimensional configuration) while others are based only on scaling laws and can be performed before computations start. It is also necessary to distinguish between thicknesses defined for variables such as temperature, which are useful in simple chemistry approaches, and thicknesses corresponding to radicals, which raise very different problems.

A flame thickness  $\delta$  can be introduced from scaling laws:

$$\delta = \frac{\lambda_1}{\rho_1 c_p s_L} = \frac{D_{th}^1}{s_L} \quad (2.24)$$

Where all quantities with index 1 are evaluated in the fresh gases. The thickness  $\delta$  (called here “**diffusive**” **thickness**) may be evaluated easily before any computation as soon as the flame speed is known. In practice, this thickness may be too approximate to be used for mesh determination (it is usually too small by a factor of order 5). A more useful thickness is obtained by using the temperature profile and computing:

$$\delta_L^0 = \frac{T_2 - T_1}{\max \left( \frac{\partial T}{\partial x} \right)} \quad (2.25)$$

Another thickness (“**total thickness**”)  $\delta_L^t$  may be constructed by defining the distance over which the reduced temperature  $\theta = \frac{T - T_1}{T_2 - T_1}$  changes from 0.01 to 0.99.

$\delta_L^t$  is always larger than  $\delta_L^0$  and not very useful for computations: in real flames, slow reactions taking place in the burnt gases usually create a long temperature “tail” leading to large values for  $\delta_L^t$  which can be misleading if this thickness is used to determine the grid resolution.

Since it measures temperature gradients,  $\delta_L^0$  is the most appropriate thickness to consider for mesh resolution. This thickness, however, requires a first flame computation. Being able to evaluate it before computation is useful to determine mesh constraints. This can be achieved with correlations.

The previous section provides useful estimates of flame thicknesses when computations are performed for simple chemistry schemes (Fuel to Products) in which the computation does not have to account for any intermediate radical. In real flames and in all computations using complex chemistry descriptions, many radicals are found within the flame front. These radicals may exist over distances much smaller than  $\delta_L^0$ . Defining mesh resolution in such flows is an open question at the moment for which no a priori mesh estimations may be obtained. In one-dimensional stationary flames, adaptive meshes are used; but in multi-dimensional flames, a trial and error technique is still used by many researchers

### 2.2.3. Flame Speed

The “speed” of a flame is a central element in combustion theory. It is also the source of many difficulties because there are multiple definitions for flame speeds and multiple ways to measure them.

The notion of a flame speed  $s_L$  was used up to now without further precision, by first stating that this velocity measured the speed at which the flame front was moving with respect to the fresh gases in a one-dimensional geometry. This definition is used intuitively by most researchers and corresponds to a description of the flame as an interface moving at speed  $s_L$  against the local flow. Later it was also shown that this flame speed may also be defined from the integral of the burning rate across the flame brush:

$$s_L = -\frac{1}{\rho_1 Y_F^1} \int_{-\infty}^{+\infty} \dot{\omega}_F dx \quad (2.26)$$

These notions, one based on kinematic properties of the flame and the other based on the integral of the reaction rate, must be connected to understand many of the recent concepts used in premixed combustion theories.

First, it is necessary to introduce three flame speed definitions and to distinguish between local and global speeds:

Identification	Definition
Absolute	Flame front speed relative to a fixed reference frame
Displacement	Flame front speed relative to the flow
Consumption	Speed at which reactants are consumed

**Table 2.1:** Simple classification of flame speeds

Even though these definitions may seem equivalent or, at least, directly connected, it is not always the case and multiple differences between these definitions are evidenced in [35].

An important difference between these speeds is that  $s_d$  or  $s_a$  are local quantities depending on the isosurface  $\theta_f$  where they are evaluated while  $s_c$  is a quantity resulting from an integral over all  $\theta_f$  values across the flame front. The speed used intuitively by experimentalists is the displacement speed measured on the fresh reactant side:  $s_d(\theta = 0)$ .

## 2.3. Turbulence Description

This section describes some basic concepts of turbulence relevant to understand turbulent combustion approaches. Most results are given without any proof but the reader will find more information in textbooks such as [37]. Turbulence may be characterized by fluctuations of all local properties and occurs for sufficiently large Reynolds numbers, depending on the system geometry. Any property  $f$  is usually split into mean ( $\bar{f}$ ) and fluctuating ( $f'$ ) contributions:

$$f = \bar{f} + f' \quad (2.27)$$

The turbulence strength is generally characterized by the turbulence intensity  $I$  which is the ratio between the root mean square of the fluctuations  $f'$  and the mean value  $\bar{f}$ :

$$I = \frac{\sqrt{\overline{f'^2}}}{\bar{f}} \quad (2.28)$$

In some situations, the local value  $\bar{f}$  may be replaced by a relevant reference mean value  $\bar{f}_0$ . For example, in boundary layers, the turbulence intensity is usually determined as the ratio of velocity fluctuations

divided by the mean free stream velocity. Typical values of the turbulence intensity  $I$  go from 0 (in a laminar flow) to tens of percent in typical wall-bounded flows: the local velocity in a turbulent flow may deviate from its mean value by tens of percent.

An important issue is the distribution of turbulence over the different length scales present in the flow field. Turbulent fluctuations are associated with different scales ranging from the largest, the integral length scale  $l_t$ , to the smallest one, the Kolmogorov length scale  $\eta_k$ . The integral scale is usually close to the characteristic size of the flow.

A Reynolds number  $Re(r)$  is introduced for each turbulent scale as:

$$Re(r) = u'(r)r/\nu \quad (2.29)$$

Where  $u'(r)$  is the characteristic velocity of the motion of size  $r$  and  $\nu$  is the flow kinematic viscosity. When  $r$  corresponds to the integral scale  $l_t$ , the corresponding Reynolds number is the integral Reynolds number:

$$Re_t = Re(l_t) = u'l_t/\nu \quad (2.30)$$

Which is usually high (100 to 2000 in most combustion devices). Since the Reynolds number represents the ratio of inertia to viscous forces, the largest scales in a turbulent flow are mainly controlled by inertia and are not affected by viscous dissipation.

For homogeneous isotropic turbulence, the energy of the large scales flows to the smaller scales through the Kolmogorov cascade [38]. The energy flux from one scale to another (due to non-linear terms  $u_i u_j$ ) is constant along scales and is given by the dissipation  $\epsilon$  of the kinetic energy  $k$ . This dissipation  $\epsilon$  is estimated as follows:

$$\epsilon = \frac{u'^2(r)}{r/u'(r)} = \frac{u'^3(r)}{r} \quad (2.31)$$

Along the cascade, the Reynolds number  $Re(r)$  goes down from  $Re_t$  to values close to unity, where inertia and viscous forces balance. This limit determines the smallest scale found in the turbulent flow, the Kolmogorov scale  $\eta_k$ , controlled by viscosity and by the dissipation rate  $\epsilon$  of the turbulent kinetic energy  $k$ :

$$\eta_k = (\nu^3/\epsilon)^{1/4} \quad (2.32)$$

Corresponding to a unity Reynolds number:

$$Re_k = \frac{u'_k \eta_k}{\nu} = 1 \quad (2.33)$$

The ratio of the integral length scale,  $l_t$ , to the Kolmogorov length scale,  $\eta_k$ , comparing the largest and smallest turbulence eddies, is then expressed as:

$$\frac{l_t}{\eta_k} = Re_t^{3/4} \quad (2.34)$$

## 2.4. Turbulent Premixed Combustion

Based on the turbulence characteristics detailed in the preceding section, a key issue is the description of the qualitative interaction between turbulence and the laminar premixed combustion features outlined earlier. Understanding this interplay is crucial for a comprehensive analysis of turbulent combustion processes.

Starting from a simple, but effective and validated result, the main effect of turbulence on combustion



is to increase the combustion rate.

Consider a statistically one-dimensional premixed flame propagating in a turbulent flow field.

In this situation, the “mean” flame brush is a planar flame, moving relatively to the flow field with a turbulent displacement speed  $s_T$ .

Experimentalists have known for a long time that changing the turbulence level before starting combustion in a vessel may change the time needed for total combustion and, accordingly the turbulent flame speed.

Proof of these qualitative trends is given by Laffitte [39], which presents combustion times measured in a stirred vessel in 1918 showing that the combustion rate is maximum (the combustion time is minimum) when the reactants are mixed in stoichiometric proportions and increases when the flow becomes turbulent:

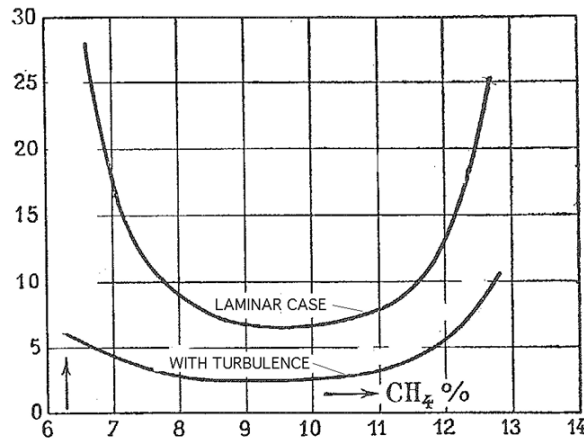


**Figure 2.2:** The combustion time (the time needed to reach the maximum pressure in a closed vessel) for a methane/air flame with and without turbulence, plotted as a function of the proportion of  $CH_4$  in the reactant mixture, corresponding to the equivalence ratio  $\phi$  (stoichiometric proportions correspond to about 10 % of methane). Time units correspond to  $10^{-2}$  seconds. Adapted from [39]

At that time, Laffitte noted that “the turbulent flame speed was always larger than two times the laminar flame speed.” The factor of two is not generic to all turbulent flames and more precise measurements lead to empirical relations such as the one proposed by Abdel-Gayed et al. [40]:

$$s_T \approx s_L \left( 1 + \frac{u'}{s_L} \right) \quad (2.35)$$

Where  $u'$  is the rms (root mean square) of the velocity fluctuations (or the square root of the turbulent kinetic energy  $k$ ). This approximate expression shows that premixed combustion is enhanced by turbulent motions. For large values of the velocity fluctuations, the turbulent flame speed  $s_T$  becomes roughly independent of the laminar flame speed  $s_L$ , meaning that  $s_T \approx u'$ . Experiments also show that the mean turbulent flame brush thickness  $\delta_T$  is always larger than the laminar flame thickness  $\delta_L^0$ .

### 2.4.1. Turbulent Premixed Combustion Regimes

Deriving models for turbulent combustion requires a physical approach because the mean (or filtered, as it will be explained later) burning rate  $\bar{\omega}_k$  cannot be determined from a filtered Arrhenius law, according to [36]. Different length scales, velocities, and time scales are used to describe the turbulent flow field and chemical reactions in turbulent combustion. Comparing these scales is the primary method of physical analysis, as already pointed out in section 2.3, where the turbulent flow is characterized by a Reynolds number that compares turbulent transport to viscous forces.

The **Damköhler number** compares the turbulent ( $\tau_t = l_t/u'$ ) and the chemical ( $\tau_c$ ) time scales:

$$Da = \frac{\tau_t}{\tau_c} \quad (2.36)$$

In the limit of high Damköhler numbers ( $Da \gg 1$ ), the chemical time is short compared to the turbulent time, corresponding to a thin reaction zone distorted and convected by the flow field. The internal structure of the flame is not strongly affected by turbulence and may be described as a laminar flame element called a 'flamelet' (from here the name 'Flamelet model'). The turbulent structures wrinkle and strain the flame surface.

On the other hand, a low Damköhler number ( $Da \ll 1$ ) corresponds to a slow chemical reaction. Reactants and products are mixed by turbulent structures before reaction. In turbulence, as long as quenching does not occur, most practical situations correspond to high or medium values of the Damköhler. Obviously, various chemical time scales may be encountered: fuel oxidation generally corresponds to short chemical time scales ( $Da \gg 1$ ) whereas pollutants production or destruction such as CO oxidation or NO formation are slower. These different time scales among different species are the reason for the stiffness problem when dealing with the reaction rate of different species: some are really slow (i.e. low reaction rates) whereas some are really fast (i.e. high reaction rates).

By comparing turbulence and chemical characteristic length and time scales, it is possible to provide a combustion diagram showing various regimes for different values of two dimensionless numbers: Damköhler and Karlovitz. In premixed flames, the chemical time scale can be expressed as  $\tau_c = \delta_l/s_L^0$  where  $\delta_l$  is the laminar flame thickness and  $s_L^0$  is the laminar flame speed;  $\tau_c$  corresponds to the time required for the premixed flame to propagate over a distance equal to its own thickness.

Thus, the Damköhler results to be:

$$Da = \frac{\tau_t}{\tau_c} = \frac{l_t s_L^0}{\delta_l u'} \quad (2.37)$$

The Karlovitz number  $Ka$  compares the chemical time scale with the time scale of the smallest turbulence scales (i.e. the Kolmogorov scales):

$$Ka = \frac{\tau_c}{\tau_k} = \frac{\delta_l u_k}{\eta_k s_L^0} \quad (2.38)$$

where the velocity of the Kolmogorov structures  $u_k$  is given by  $u_k = (\nu\epsilon)^{1/4}$ .

Some considerations based on the values of the couple ( $Da, Ka$ ) are:

- For  $Da \gg 1$  the flame front is thin and its inner structure is not affected by turbulence motions which only wrinkle the flame surface. This is called the 'flamelet regime' and occurs when the smallest turbulence scales have a turbulent time  $\tau_k$  larger than  $\tau_c$  (i.e. turbulent motions are too slow to affect the flame structure), meaning that at the same time, as a condition of existence of the 'flamelet regime', also  $Ka < 1$  must be satisfied.

On the other hand, when  $Da \ll 1$ , the chemical time is larger than turbulent times and the overall reaction rate is therefore controlled by chemistry whereas reactants and products are mixed by turbulence motions. This limit case is the so-called 'perfectly stirred reactor'.

- The Karlovitz number is used to define the Klimov-Williams criterion, corresponding to  $Ka = 1$ . This criterion was first interpreted as the transition between the 'flamelet regime' ( $Ka < 1$ ) and the so-called 'distributed combustion regime', where the flame inner structure is strongly modified by turbulence motions. A recent analysis [41] has shown that for Karlovitz numbers larger than unity ( $Ka > 1$ ), turbulent motions become able to affect the flame's inner structure but not necessarily the reaction zone, hence extending the validity of the flamelet regime (and consequently the validity of the flamelet model that is used for this work) to higher Karlovitz number's values (approximately  $Ka = 100$ , up to  $Ka = 1000$ ).

The reaction zone, where heat is released, has a thickness  $\delta_r$  much lower than the thermal thickness  $\delta_l$  of the flame ( $\delta_r \approx 0.1\delta_l$ ).

Then, the following turbulent premixed flame regimes are proposed [36], not taking into account [41]:

- $Ka < 1$ : **Flamelet regime**. The chemical time scale is shorter than any turbulent time scale and the flame thickness is smaller than the smallest turbulent scale. In this regime the flame front is thin, has an inner structure close to a laminar flame and is wrinkled by turbulence motions. Two subdivisions of this regime may be proposed depending on the velocity ratio  $u'/s_L^0$ :
  - $(u'/s_L^0) < 1$ : **Wrinkled flame**. As  $u'$  may be viewed as the rotation speed of the larger turbulent motions (i.e. integral scale), turbulent structures are unable to wrinkle the flame surface up to flame front interactions. The laminar propagation is predominant and turbulence/combustion interactions remain limited
  - $(u'/s_L^0) > 1$ : **Wrinkled flame with pockets**. In this situation, larger structures become able to induce flame front interactions leading to pockets of fresh and burnt gases (i.e. structures that are richer or leaner in fuel).
- $1 < Ka < 100$ : **Thickened wrinkled flame**. In this case, turbulent motions are able to enter and modify (thicken) the flame preheat zone, but cannot modify the reaction zone which remains thin and close to a wrinkled laminar reaction zone.
- $Ka > 100$ : **Thickened flame regime or well-stirred reactor**. In this situation, preheat and reaction zones are strongly affected by turbulent motions and no laminar flame structure may be identified.

These various regimes are generally displayed on a log-log diagram ( $u'/s_L^0$  vs  $l_t/\delta_l$ ), called 'Borghi diagram':

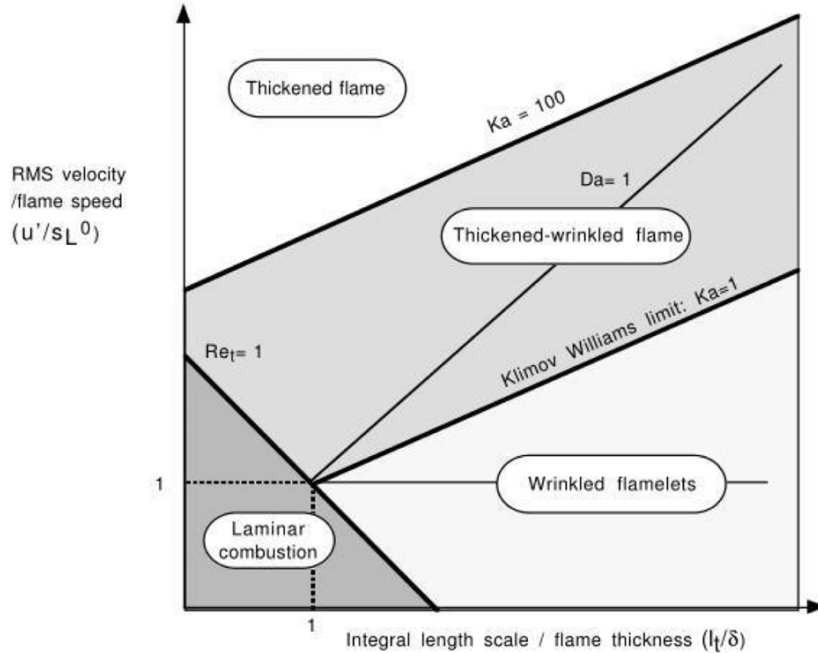


**Figure 2.3:** Borghi diagram (turbulent combustion diagram): combustion regimes are identified in terms of length ( $l_t/\delta_l$ ) and velocity ( $u'/s_L^0$ ) ratios in a log-log diagram. [42]

The list above, which is a rough classification of combustion regimes as a function of characteristic numbers, has been developed as a support to choose turbulent combustion models. Most practical

applications correspond to flamelet or thickened wrinkled flame regimes.

Nevertheless, as already mentioned with [41], such analyses are only qualitative and should be used with care, also because all these analyses are based on a single-step irreversible reaction (i.e. Reactants  $\rightarrow$  Products) but in actual turbulent combustion a large number of chemical species and reactions are involved (several hundred species and several thousand reactions for most hydrocarbons/air mixture). These reactions may correspond to a large range of chemical time scales.

For instance, it is reasonable to suppose that the oxidation of propane is fast in comparison to the turbulent time scale, yet the formation of CO<sub>2</sub> from CO is much slower and has a chemical time of the same order as turbulent times. Another crucial feature is that the analysis is based on the assumption that the turbulence is homogeneous and isotropic frozen (i.e. unaffected by heat release)

## 2.5. Flame/Wall Interactions

To produce power, combustion must take place in a vessel in which flames develop in the vicinity of walls and interact with them.

Phenomena taking place during flame/wall interaction are not well understood: this interaction, however, is very strong. It influences combustion and wall heat fluxes in a significant manner and constitutes a difficult challenge for combustion studies.

Most flame/wall interaction studies have been performed for premixed combustion: this section focuses on this combustion mode even though non-premixed devices are also submitted to similar phenomena. In most combustion devices, burnt gases reach temperatures between 1500 and 2500 K while wall temperatures remain between 400 and 600 K because of active/passive cooling. The temperature decrease from burnt gas levels to wall levels occurs in a near-wall layer which is less than 1 mm thick, leading to very large temperature gradients.

Studying the interaction between flames and walls is extremely difficult from an experimental point of view because all interesting phenomena occur in a very thin zone near the wall: in most cases, the only measurable quantity is the unsteady heat flux through the wall, which is an “indirect” measurement of phenomena taking place in the gas phase.

Moreover, flames approaching walls are dominated by transient effects. They do not usually touch walls: they quench a few micrometres before because the low temperature of most walls inhibits chemical reactions. At the same time, the large near-wall temperature gradients lead to very high wall heat fluxes. These fluxes are maintained for short durations and their characterization is also a difficult task in experiments.

When the flow within the chamber is turbulent, the interaction between the wall and the flame is even more complex. In addition to the interaction between the flame and the wall, the coupling phenomena between the wall and the turbulence on one hand, and between the turbulence and the flame on the other hand, must be considered. As a result, the overall picture of flame/wall interaction in turbulent flows is quite complex and modeling still in an early stage:

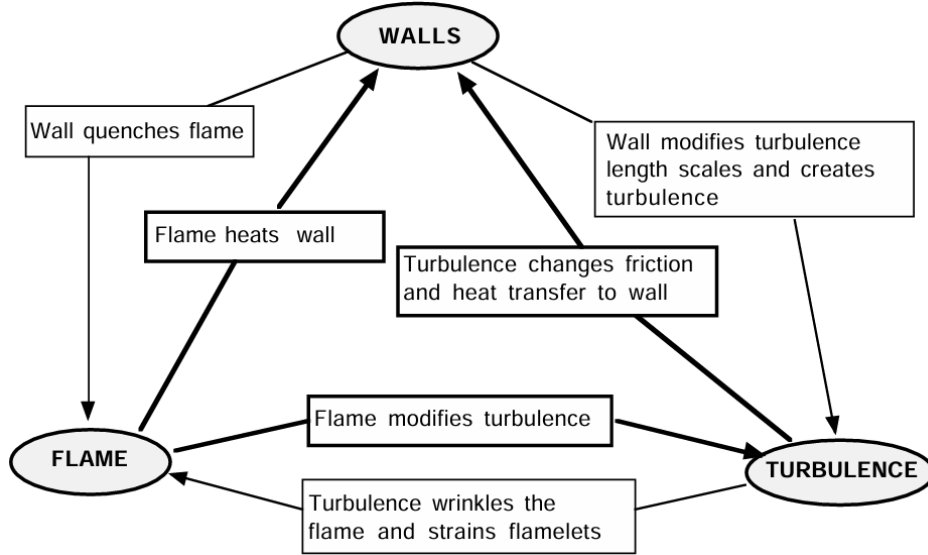


Figure 2.4: Interactions between walls, flame and turbulence.

### 2.5.1. Laminar Flame/Wall Interaction

The interaction between laminar flames and walls has been extensively studied, particularly focusing on wall quenching effects. These studies have investigated various scenarios characterized by parameters such as the distance between the flame and the wall (denoted as  $y$ ) and the heat flux through the wall (denoted as  $q$ ). The distance  $y$  is often normalized by the characteristic flame thickness  $\delta$ . This normalization allows for the definition of a local Peclet number:

$$Pe = \frac{y}{\delta} \quad (2.39)$$

providing insight into the flame/wall interaction.

The heat flux through the wall  $q$  is a critical parameter, typically defined as the negative of the gas thermal conductivity times the temperature gradient at the wall. This heat flux is then scaled by the laminar reference flame power, yielding:

$$F = \frac{q}{\rho_1 Y_{F,1} s_L^0 Q} \quad (2.40)$$

Where  $\rho_1$  and  $Y_{F,1}$  designate the fresh-gas density and fuel mass fraction,  $s_L^0$  is the unstretched laminar flame speed, and  $Q$  is the heat of reaction (defined by  $Y_{F,1} Q = c_p(T_2 - T_1)$  if  $T_1$  is the temperature of the fresh gases and  $T_2$  is the adiabatic flame temperature).

The flame/wall distance  $y$  and the wall heat flux  $q$  change with time. Consider the simplest case of Figure 2.5 where a one-dimensional laminar flame propagates into fresh reactants towards a cold wall. Far from the wall ( $t = t_1$ ), the flame propagates without modification. When the flame is close enough to the wall, it starts sensing its presence ( $t = t_2$ ). The wall extracts energy from the flame (through heat diffusion), playing a role similar to a heat loss term: the flame is weakened by this loss and slows down. A critical instant in flame/wall interaction corresponds to the flame quenching: at a certain distance  $y_Q$ , the flame stops and quenches ( $t = t_3$  on Figure 2.5). Generally, the wall heat flux  $q_Q$  peaks at the same instant. After quenching, the burnt gases are cooled down by the cold wall following a simple heat diffusion process.

The quenching distance  $y_Q$  is expressed by the quenching Peclet number  $Pe_Q$ :  $Pe_Q = y_Q/\delta$ .

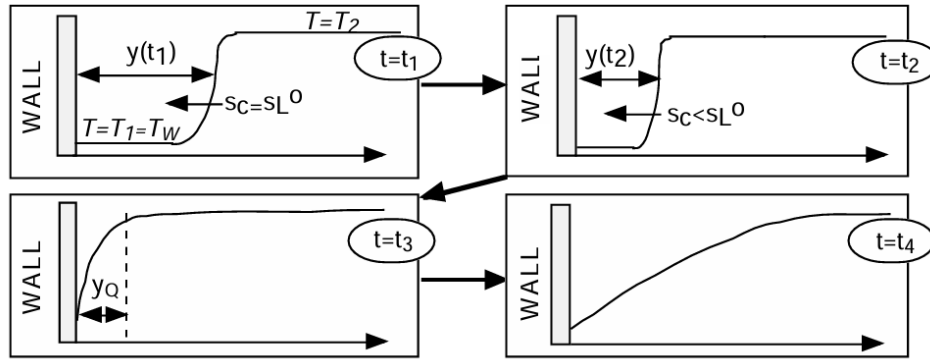


**Figure 2.5:** Laminar flame interacting with a cold wall. Temperature profiles at four consecutive instants  $t_1$  to  $t_4$ . The fresh gases temperature  $T_1$  is equal to the wall temperature  $T_W$ . Quenching occurs at  $t = t_3$ .

Flame/wall interaction can occur in different configurations, including head-on quenching (HOQ), side-wall quenching (SWQ), and tube quenching, as shown in Figure 2.6. In HOQ, the flame front directly encounters a cold wall, resulting in localized quenching. SWQ involves the propagation of a flame parallel to a wall, leading to localized quenching of the flame edge. Tube quenching occurs when a flame is completely quenched in a narrow tube due to heat loss to the walls.

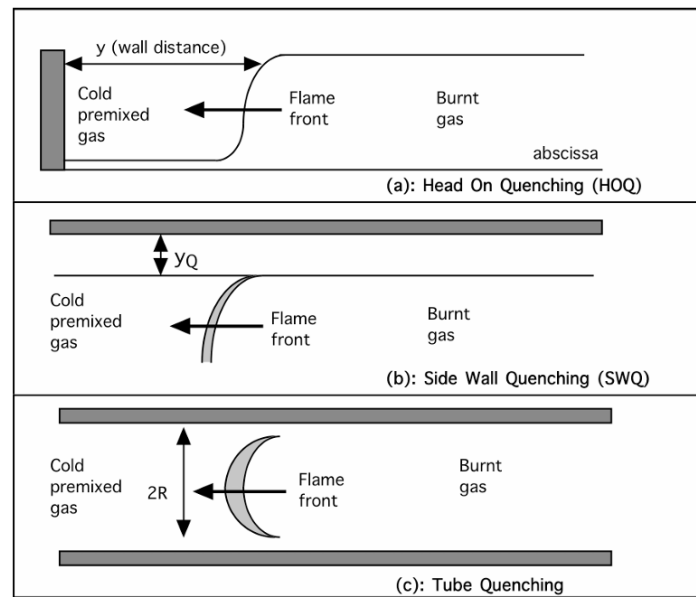


**Figure 2.6:** The three configurations for flame/wall interaction in laminar flows.

Analyzing flame/wall interaction involves considering both simple and complex chemical mechanisms.

Simple chemistry models provide valuable insights into the thermal effects of interaction, while complex chemistry models are necessary to capture the full range of chemical processes involved. Computational efforts must address challenges such as the high resolution required for accurate simulations, the influence of catalysis at the wall, and the inclusion of Soret and Dufour effects.

Experimental and computational studies have provided valuable insights into laminar flame/wall interaction, with results showing good agreement between different methods despite variations in assumptions and methodologies. The scaling of reduced heat flux  $F$  has proven to be effective in capturing the essential features of flame/wall interaction across various scenarios.

### 2.5.2. Turbulent Flame/Wall Interactions

While studies on laminar flame/wall interaction offer valuable insights into flame behaviour during interaction and wall heat fluxes, the influence of turbulence on this interaction remains unclear. Turbulent premixed flame-wall interaction encompasses all mechanisms described before for the laminar flame case.

In a turbulent flame, heat fluxes are influenced by the intermittency between fresh and burnt gases contacting the wall. When fresh reactants are in contact with the wall, heat fluxes remain low. Conversely, higher heat flux levels are observed when burnt gases are in contact with the wall. The passage of a flame in front of the detector marks the interaction of the wall with an active flame front, often resulting in intense heat flux at the wall.

This complex interaction poses several challenges for modeling:

- Predicting the maximum heat flux  $q_{max}$  resulting from the interaction between an active flame front and the wall is a significant challenge. RANS models are unable to predict this maximum flux level accurately. However, DNS studies suggest that  $q_{max}$  scales with the maximum heat flux observed at quenching for laminar flames  $q_Q$ , indicating the control of turbulent combustor maximum heat fluxes by flame/wall quenching.
- While RANS models may predict the mean heat flux at the wall, the intermittent nature of the interaction complicates averaging. When burnt gases are at the wall, the gas temperature-to-wall temperature ratio  $T/T_w$  can be substantial, making classical logarithmic laws inadequate.

Additional issues arise in turbulent interactions compared to laminar cases:

- Turbulence may affect maximum wall fluxes during quenching.
- Flame elements near the wall have a higher chance of quenching, necessitating their consideration in models.
- Wall constraints limit flame movement and reduce turbulent flame brush size.
- Wall influence alters turbulence structure, leading to laminarization near the wall and decreased turbulent stretch, thereby reducing flame area.
- Models for mean friction and wall heat fluxes need reevaluation.

#### Flame/Wall Interactions: Turbulence Models

The interaction between turbulent flames and walls poses a challenge for incorporating into CFD codes. Existing models typically involve an indirect coupling where walls influence turbulence time scales, affecting mean reaction rates.

However, this approach often yields non-physical results due to incompatibilities between near-wall and turbulent combustion models. Recent efforts aim to address this by modifying models near walls using physical insights, such as incorporating sink terms derived from DNS results [43]. These modified models offer more accurate predictions, as demonstrated in piston engine computations [44].

#### Flame/Wall Interactions: Heat Transfer

Maximum heat fluxes discussed in the previous sections are one important aspect of flame/wall interaction because they control the maximum local load imposed on materials. But to design cooling systems, mean heat fluxes are of greater importance than maximum fluxes. For these mean quantities, the interaction between active flames and wall is not the dominant factor. However, the presence of burnt gases must definitely be accounted for. This is not often the case: the traditional law-of-the-wall approach

used in many codes is valid only for flows in which temperature variations remain small (typically, the ratio of gas temperature to wall temperature  $T/T_w$  must be of order unity).

In combustion applications, this is rarely the case. This can induce very large errors on wall friction and wall heat fluxes. In [35], the principles of 'law of the wall' approaches are first described and their implementation is presented for the classical isothermal situation where  $T/T_w$  is of order unity. Then, possible extensions to cases where  $T/T_w$  is large are discussed.

## 2.6. Emissions

This section explores the parameters that affect the main emission species, and how the model can predict and analyze their formation in combustion simulations, such as empirical correlations, detailed and reduced chemical kinetics. Each emission species carries distinct environmental and health implications: understanding the mechanisms behind emission generation is essential for developing strategies to mitigate them.

### 2.6.1. NOx

NOx are emissions comprised of nitrogen oxide (NO) with smaller amounts of nitrogen dioxide (NO<sub>2</sub>) and nitrous oxide (N<sub>2</sub>O). Their Radiative Forcing effect (particularly that of NO<sub>2</sub>) is about 136 times more powerful than CO<sub>2</sub>, even though their lifetime is only a few weeks in the atmosphere [45].

In the stratosphere, they lead to the formation of ozone (O<sub>3</sub>), which is very dangerous and at the same time, they reduce the amount of ozone itself in the troposphere, where it is needed to protect the earth from ultraviolet rays.

Furthermore, NOx are harmful to humans, as they damage the respiratory system. Consequently, it is essential to reduce their emissions. The formation depends on numerous factors, such as the temperature, the residence time, and the equivalence ratio. Each path first involves the formation of NO which reacts with oxygen to form NO<sub>2</sub>.

The main NO formation pathways are thermal, prompt, NNH, N<sub>2</sub>O, and Fuel NO:

1. **Thermal NO or Zeldovich mechanism** [46]. The reactions of this mechanism require a high activation energy, thus high temperatures, to activate them.

- **R1:**  $N_2 + O \rightleftharpoons NO + N$
- **R2:**  $N + O_2 \rightleftharpoons NO + O$
- **R3:**  $N + OH \rightleftharpoons NO + H$

The rate of NO formation strongly depends on temperature, pressure, and residence time; decreasing any of these three reduces NO, but the exponential dependence on temperature makes the reduction of the combustion temperature the key strategy for low NOx combustion. Fortunately, thermal NOx formation rates are relatively slow, and therefore, equilibrium concentrations are never reached in the combustion devices. It is also dependent on the square root of the pressure. NOx emissions can be reduced by lowering the flame temperature or by reducing the time that the mixture spends in the combustor. With H<sub>2</sub>-blended fuel, it is possible to simultaneously reduce the length of the combustor and work with a leaner mixture due to the higher flame speed and the lower flammability limit compared to natural gas.

2. **Prompt NO or Fenimore mechanism** [47]. The mechanism initiated by attack of  $CH_n$  radicals on N<sub>2</sub> is termed prompt NO.

- **R4:**  $CH + N_2 \rightleftharpoons NCN + H$
- **R5:**  $NCN + O \rightleftharpoons NO + CN$
- **R6:**  $CN + O_2 \rightleftharpoons NO + CO$



- **R7:**  $\text{NCO} + \text{O} \rightleftharpoons \text{NO} + \text{CO}$
3. **NNH pathway** [48]. This mechanism is important at higher temperature conditions in the fuel-rich side of the flame zone as well as in the reaction zone.
- **R8:**  $\text{N}_2 + \text{H}(+\text{M}) \rightleftharpoons \text{NNH}(+\text{M})$
  - **R9:**  $\text{NNH} + \text{O} \rightleftharpoons \text{NO} + \text{NH}$
  - **R10:**  $\text{NNH} + \text{OH} \rightleftharpoons \text{NO} + \text{NH}_2$
4. **N2O pathway** [49]. The N2O pathway seems to be significant at high pressures and moderate temperatures in the fuel-lean flame conditions.
- **R11:**  $\text{N}_2 + \text{O}(+\text{M}) \rightleftharpoons \text{N}_2\text{O}(+\text{M})$
  - **R12:**  $\text{N}_2\text{O} + \text{H} \rightleftharpoons \text{NO} + \text{NH}$
  - **R13:**  $\text{N}_2\text{O} + \text{O} \rightleftharpoons 2\text{NO}$
5. **Fuel NO** [50]. When nitrogen is chemically bound to fuel (e.g.,  $\text{NH}_3$ ), it converts almost completely to  $\text{NO}_x$  in the exhaust gases. From the thermal decomposition of fuel bound compounds in the reaction zone, radicals such as  $\text{HCN}$ ,  $\text{NH}_3$ ,  $\text{N}$ ,  $\text{CN}$  and  $\text{NH}$  can be formed and converted to  $\text{NO}_x$ . While most gaseous fuels, such as natural gas, do not contain fuel-bound nitrogen, nitrogen is frequently present in liquid and solid fuels. Unprocessed fuel oil, for instance, can contain more than 1000 parts per million (ppm) of bound nitrogen, resulting in over 40 ppm of  $\text{NO}_x$  in the exhaust gases solely due to this mechanism. Fortunately, refining processes designed to remove sulfur also eliminate nitrogen from the fuel.

### 2.6.2. CO

When a combustion zone is operating fuel-rich, large amounts of CO are formed owing to the lack of sufficient oxygen to complete the reaction to  $\text{CO}_2$ .

If, however, the combustion zone mixture strength is stoichiometric or moderately fuel-lean, significant amounts of CO will also be present due to the dissociation of  $\text{CO}_2$ . In practice, CO emissions are found to be much higher than predicted from equilibrium calculations and to be highest at low-power conditions, where burning rates and peak temperatures are relatively low. This is in conflict with the predictions of equilibrium theory, and it suggests that much of the CO arises from incomplete combustion of the fuel, caused by one or more of the following:

- Inadequate burning rates in the primary zone, due to a fuel/air ratio that is too low and/or insufficient residence time
- Inadequate mixing of fuel and air, which produces some regions in which the mixture strength is too weak to support combustion, and others in which over-rich combustion yields high local concentrations of CO
- Quenching of the postflame products by entrainment into the liner wall-cooling air, especially in the primary zone

### 2.6.3. UHC

UHC include fuel that emerges from the combustor in the form of drops or vapor, as well as the products of the thermal degradation of the parent fuel into species of lower molecular weight. They are normally associated with poor atomization, inadequate burning rates, the chilling effects of film cooling air, or any combination of these.

The reaction kinetics of UHC formation are more complex than for CO formation, but it is generally found that those factors that influence CO emissions also influence UHC emissions and in much the same manner

### 2.6.4. Soot

Exhaust smoke is caused by the production of finely divided soot particles in fuel-rich regions of the flame that, in conventional combustors, are always close to the fuel spray. These are the regions in which recirculating burned products move upstream toward the fuel injector, and local pockets of fuel vapor become enveloped in oxygen-deficient gases at high temperature. In these fuel-rich zones, soot may be produced in considerable quantities.

Most of the soot produced in the primary zone is consumed in the high temperature regions downstream. Thus, from a smoke viewpoint, a combustor may be considered to comprise two separate zones—the primary zone, which governs the rate of soot formation, and the intermediate zone (and, on modern high-temperature engines, the dilution zone also), which determines the rate of soot consumption. Analysis of the soot found in exhaust gases shows that it consists mostly of carbon (96%) and a mixture of hydrogen, oxygen, and other elements. Soot is not an equilibrium product of combustion except at mixture strengths far richer than those employed in the primary zones of gas turbines. Thus, it is impossible to predict its rate of formation and final concentration from kinetic or thermodynamic data. In practice, the rate of soot formation tends to be governed more by the physical processes of atomization and fuel–air mixing than by kinetics.

## 2.7. Swirling Flows

Swirl has been commonly used for the stabilization of high-intensity combustion. The main effects of swirl are as follows:

- To reduce combustion lengths by producing higher rates of entrainment of the ambient fluid and fast mixing close to the exit nozzle and on the boundaries of recirculation zones
- To improve flame stability as a result of the formation of toroidal recirculation zones in strongly swirling zones
- As the blockage is aerodynamic, flame impingement on the burner may be minimized, thus ensuring minimum maintenance and extended life for the unit

These toroidal recirculation zones, which recirculate heat and active chemical species to the root of the flame, thus reducing velocity requirements for flame stabilization, are only formed beyond a critical swirl number  $SN \geq SN_{crit} \approx 0.6$ . The process for the formation of these inner/central recirculation zones arises as follows:

- Swirling flow generates a natural radial pressure gradient due to the centrifugal term  $\frac{v_\theta^2}{r}$
- Exiting through a nozzle causes axial decay of tangential velocity and hence radial pressure gradient.
- This in turn causes a negative axial pressure gradient to be set up in the vicinity of the axis, which in turn induces reverse flow and the formation of a Central Recirculation Zone (CRZ - sometimes also defined as Inner Recirculation Zone, IRZ).
- Where the tangential velocity distribution is of Rankine form (i.e. free/forced vortex combination), the central vortex core can become unstable, giving rise to the PVC phenomena.
- The formation of the CRZ is thus dependent on the decay of swirl velocity as swirling flow develops.

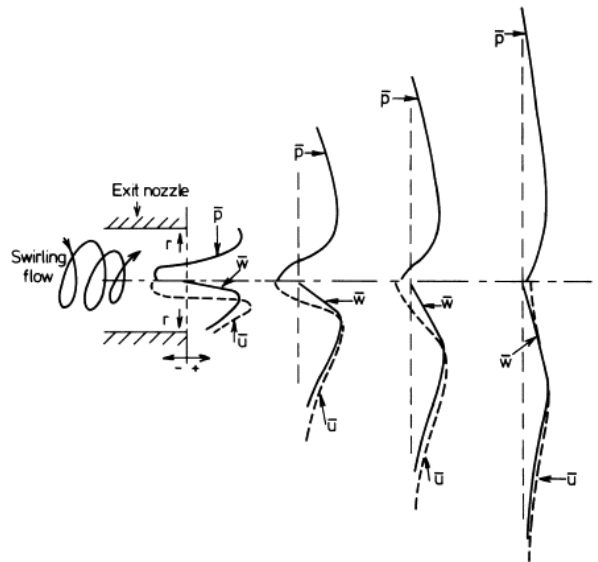


**Figure 2.7:** Schematic diagram of processing leading to CRZ formation: (1) tangential velocity profile creates a centrifugal pressure gradient and sub-atmospheric pressure near the central axis; (2) axial decay of tangential velocity causes decay of radial distribution of centrifugal pressure gradient in axial direction; (3) thus, an axial pressure gradient is set up in the central region towards the swirl burner, causing reverse flow.

With confinement, meaning the difference in cross-section area before and after the nozzle, this process is modified, the rate of decay of swirl velocity is considerably reduced, hence the size and

strength of the CRZ (and ORZ - Outer Recirculation Zone) formed.

The above-mentioned **swirl number** is a significant similarity criterion for swirling flows. It essentially quantifies the ratio of the axial component of the flow rate of angular momentum to the flow rate of axial momentum:

$$SN(x) = \frac{G_\theta(x)}{R(x) \cdot G_x(x)} \quad (2.41)$$

where  $G_\theta(x)$  is the time average of the axial component of the flow rate of angular momentum integrated over the cross-section (plane  $yz$ ) at a certain axial coordinate  $x$ ,  $R(x)$  is a characteristic radius of the swirling flow and  $G_x(x)$  is the time average of the flow rate of axial momentum across the axial cross-section.

A suitable definition of the swirl number factors is not a straightforward task, as  $G_\theta$  and  $G_x$  are conserved in free jets and in confined flows only if the duct has a constant cross-section and viscous losses at the wall are negligible.

An overview of the hierarchy of simplified definitions derived in the literature to determine the swirl number in practical flows is given in [51], assessing the shortcomings of the various formulations and giving advice on which definitions to use in practice.

Based on the findings of Beér and Chigier [52], it has been shown that flows characterized by a low swirl number ( $SN = 0.6$ ) do not exhibit any recirculation of the flow:

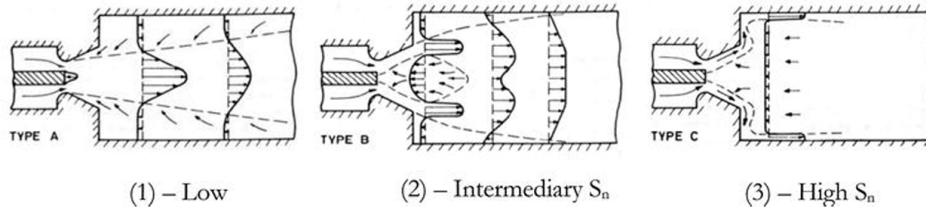


**Figure 2.8:** Swirl effect on flames. (1) Low  $SN$ , (2) Intermediate  $SN$ , (3) High  $SN$ .

The swirl increases ambient fluid entrainment and decreases flow axial velocity. Axial velocity radial profiles remain Gaussian when  $SN$  is below 0.5 (case 1 in Figure 2.8), lifting the flame. When approaching  $SN = 0.6$  (case 2 in Figure 2.8), where the flame is stabilized closer to the burner in the recirculation zone rich in fresh gases, velocity maximum deviates from the axis and turbulence increases. With increasing swirl number (case 3 in Figure 2.8), jet opening and entrained mass flow rise continually.

A recirculation zone appears in the main flow at 0.6 swirl intensity. The swirl intensity affects the size and location of the recirculation zone.

Fresh and flue gases mix in the recirculation zone. In addition, swirl enhances gas entrainment and raises flame blow-off limit. The interaction of hot products and active chemical species with entering fresh gases (air and fuel) in this zone helps sustaining the flame. Fresh gases in the center recirculation zone stabilize the flame next to the burner outlet due to their low speed. A corner external recirculation zone may be created downstream of the backward-facing step.

Moreover, extensive research efforts have been focused on the swirling flows characterization in a dynamic framework, particularly in the description of the instabilities of swirling flows [53], [54], [55], [56], [57], [58].

The existence of swirling in a fluid flow gives rise to instability and mechanisms of disturbance propagation that are different from those caused by shear forces. Swirling flows display a diverse range of behaviors that are dependent upon factors such as geometry, swirl number, Reynolds number, and

several other characteristics.

It is important to acknowledge that combustion triggers the vortex breakdown: Combustion induced vortex breakdown (CIVB) refers to a particular vortex breakdown that arises as a consequence of the thermal energy release resulting from combustion. The heat release may induce the expansion and acceleration of the fluid, resulting in the development of a low-pressure zone in the core of the vortex. Subsequently, the presence of this zone of reduced pressure has the potential to initiate the phenomenon known as vortex breakdown.

Next, we proceed to examine the dynamic nature of the area where the flow recirculates, referred to as central recirculation zone (CRZ). As previously mentioned, a prominent characteristic of vortex breakdown is the existence of a flow stagnation point located at the beginning of the bubble. The stagnation point has the potential to remain at the flow centerline, which is known as axisymmetric breakdown. Alternatively, it may deviate from the centerline and undergo rotational movement around it, which is referred to as spiral breakdown. Within the CRZ, the fluid motion exhibits characteristics of both unsteadiness and non-axisymmetry. The fluid that is entrained into the bubble undergoes an emptying and filling process of the bubble, that takes place in its downstream region. Furthermore, it should be noted that the rotational motion does not occur instantly around the geometrical centerline. In contrast, the location with zero azimuthal velocity is situated away from the center, and this particular point undergoes rotational motion around the geometric center, as seen in Figure 2.9.

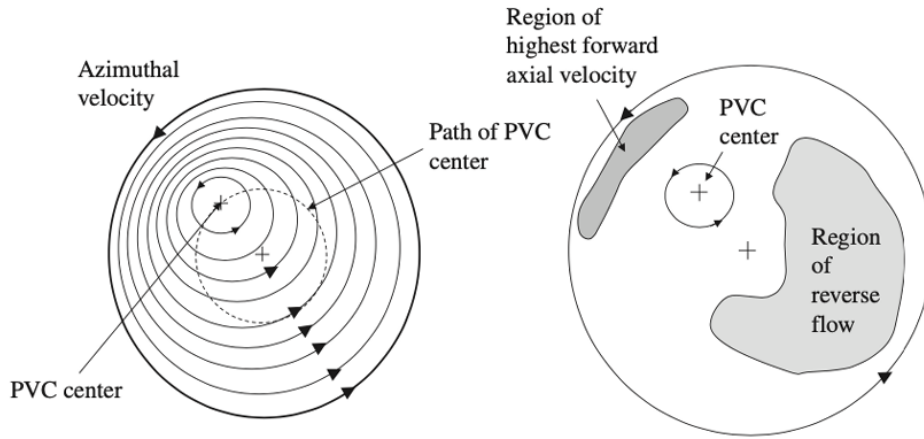


**Figure 2.9:** Sketch of instantaneous (a) azimuthal and (b) axial velocity inside the vortex breakdown bubble showing precessing vortex core (PVC) [59]

The location at which the azimuthal velocity is zero is often known as the precessing vortex core (PVC).

The rotational frequency of the PVC scales with a Strouhal number, which is calculated based on the axial flow velocity and the diameter of the pipe:

$$St = \frac{fD}{u_b} \quad (2.42)$$

where  $f$  is the frequency of the PVC,  $D$  is the diameter of the pipe and  $u_b$  is the axial flow bulk velocity. The alignment of the positive and negative axial flow velocity areas in the center of the PVC, as shown in Figure 2.9, may not always be opposed to each other. Additionally, the degree of offset between these regions changes along the axial direction. As a consequence, a helical pattern emerges in the instantaneous axial flow velocity.

In conclusion, it is crucial to distinguish the PVC from other helical shear flow patterns that may coexist,

such as those arising from shear layer instabilities.

A significant modification of these flow characteristics may be seen in swirling flows with combustion. The zone of vortex breakdown undergoes changes in its shape and size, resulting in substantial effects on the spreading angle and velocity of the outer flow circumnavigating the bubble.

The observed discrepancies are frequently credited to the influence of gas expansion on the inner vortical structures. Due to the expansion of gas inside the flame, the flowfield situated downstream of the flame exhibits elevated axial velocities, while experiencing little changes in azimuthal velocity. This translates into a significant decrease in the swirl number.

The presence of a central recirculation zone may provide significant advantages in terms of enhancing the mixing and preheating of fuel and air. However, it is important to note that this phenomenon can also lead to equipment damage due to the resonances generated by the interplay between the coherent structures formed and natural system resonances and combustion induced oscillations. These instabilities include PVC.

### 2.7.1. Swirling Flows and Emissions

As previously stated, the use of swirlers in the combustion chamber serves to augment turbulence and promote the thorough mixing of fuel and air. This, in turn, results in improved combustion efficiency and a subsequent decrease in emissions. Consequently, this phenomenon may have an impact on the temperature of the flame and result in a decrease in the release of harmful substances, particularly in scenarios that need minimal levels of nitrogen oxide (NO<sub>x</sub>) emissions.

Schmitt et al. [60] demonstrated that the use of swirl in non-premixed combustion has the potential to effectively mitigate the release of pollutant emissions, namely nitrogen oxides. The introduction of a swirling motion and subsequent enhancement of reactant mixing results in a reduction in flame temperature, thus leading to a decrease in the generation of NO<sub>x</sub> through the Zeldovich mechanism. Furthermore, when the strength of the swirling is significant, augmenting the *SN* leads to a decrease in the amount of time spent in high-temperature regions, which has the consequence of restricting the generation of NO<sub>x</sub>. Nevertheless, it is vital to identify an optimal swirling intensity that strikes a balance between mitigating pollutant emissions and maintaining a safe distance between the flame burner in order to prevent the occurrence of flashback.

The research conducted by Coghe et al. [61] examined the performance of a lean natural gas burner with a fuel-air equivalence ratio of 0.69. The findings revealed that the reduction of NO<sub>x</sub> may reach up to 30% within a range of swirl numbers between 0.7 and 0.82.

The impact of the swirl number on the emissions of NO<sub>x</sub> and CO was investigated by Boushaki et al. [62] and Nazim et al. [63] as documented in their respective studies.

It was discovered that when the swirl number is 1.4, the *EI<sub>CO</sub>* rate (i.e. CO emission index, indicating the ratio of CO mass exiting the engine to the mass of fuel intake) is marginally lower compared to a swirl number of 0.8. The researchers observed that the intensity of the swirl may tend to augment the mixing process and prolong the duration of stay inside the reaction zone. This, in turn, facilitates the conversion of CO to CO<sub>2</sub>. With regards to the emissions of nitrogen oxides, the researchers observed that an increase in the swirl number has a tendency to decrease the creation of *EI<sub>NO<sub>x</sub></sub>*, especially when the oxygen rate is below 27.

In their study, Burguette and Costa [64] conducted an assessment of the impact of swirl intensity on NO<sub>x</sub> emissions by examining the angle of the blades that make up the swirler. The researchers discovered that the NO<sub>x</sub> rate is the highest at an angle of 45°, whereas NO<sub>x</sub> emissions fall when the angle deviates from 45°, either lower or higher. The authors provide an explanation for these findings based on the observation that a recirculation zone starts at a 45° angle. This leads to an increase in residence time in proximity to the burner, where the temperature is higher, with a subsequently higher generation of NO<sub>x</sub>.

Cozzi and Coghe [65] conducted a study on the emissions of NO<sub>x</sub> in a coaxial swirling flame fueled

by natural gas. According to their findings, the intensity of swirl significantly impacts non-premixed flames, resulting in greater amounts of NO<sub>x</sub> reduction at increased swirl levels. Swirlers have the potential to enhance the overall efficiency of a combustion system. Enhancing flame stability and combustion quality may result in increased thermal efficiency and reduced operational expenses.

### 2.7.2. An Operating Limit of Swirl-Stabilized Combustors: Flashback

The use of premixed combustion has the benefit of attaining much reduced levels of NO<sub>x</sub> compared to non-premixed flames. This is mostly due to the considerably lower flame temperature resulting from a significantly reduced local equivalency ratio. Nevertheless, premixed flames are prone to a phenomenon known as flashback, when the fresh mixture velocity has a component normal to the flame front which is below the turbulent flame speed, resulting in the propagation of the flame in the upstream direction. This phenomenon may lead to the deterioration and subsequent shutdown of the burner.

Hydrogen exhibits a flame speed that is approximately five times greater than that of methane. While this mitigates the likelihood of flame blowoff, it concurrently elevates the potential for flashback. Four different types of flashback are possible:

1. **Flashback in the turbulent core.** As the turbulent flame velocity  $s_T$  surpasses the component of the flow velocity normal to the flame front, an upstream movement of the flame front occurs. As turbulence ( $u'$ , rms of velocity fluctuations), pressure and temperature rise, the value of  $s_T/s_L^0$  rises.

On the one hand, it is therefore preferable to conduct operations at low pressures, on the other hand, higher pressure allows for smaller combustors. When utilizing highly reactive fuels, such as hydrogen, a low-swirl burner operating at low pressures is preferred in order to decrease the turbulent flame speed. Conversely, this contradicts the criteria for sequential combustors, which habitually function under elevated pressures accompanied by substantial turbulence.

One potential resolution entails diminishing the pressure and swirl in order to significantly increase the axial velocity above the turbulent flame speed. Nonetheless, such an outcome would result in diminished operational efficiency, compromised mixing, and a heightened propensity for autoignition and instability. As illustrated in Figure 2.10, Eichler [66] explains that this particular form of flashback can be disregarded during typical gas turbine operations due to the fact that the free stream velocity is typically greater than the flame speed.

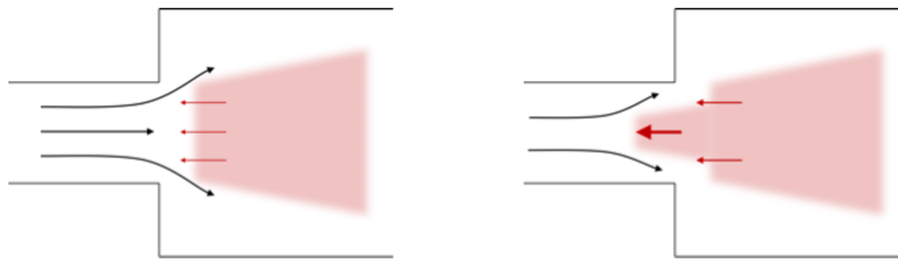


**Figure 2.10:** Flashback in the core flow. The red shaded area indicates the region of burned gases, red arrows correspond to flame propagation and black arrows to the flow. The size of the arrow is drawn relative to the speed (flow or flame). [67]

2. **Boundary Layer Flashback (BLF).** The boundary layer is characterized by a no-slip condition: velocity in the burner decreases to zero close to the wall. The formation of a boundary layer flashback occurs when local flow velocities fall below the  $s_T$  turbulent flame speed. This results in the initiation of upstream flame propagation, as shown in Figure 2.11. Nevertheless, this issue is mitigated by the heat discharge from the flame towards the wall, which effectively suppresses it (i.e., the heat discharge locally reduces the flame temperature, thereby diminishing its reaction

rate to the point where it ceases to exist; in other words, the combustion reactions decelerate to the extent that they cease to exist and the flame quenches). This type of flashback is more prevalent in hydrogen owing to its elevated flame velocity and reactivity, which leads to an exceptionally small quenching distance (i.e. flame sustains without quenching even in pipes with small diameters, where heat dissipation becomes more important with respect to heat release). This is the primary flashback mechanism for low-turbulence and low-swirl flows, described in more details in [68].

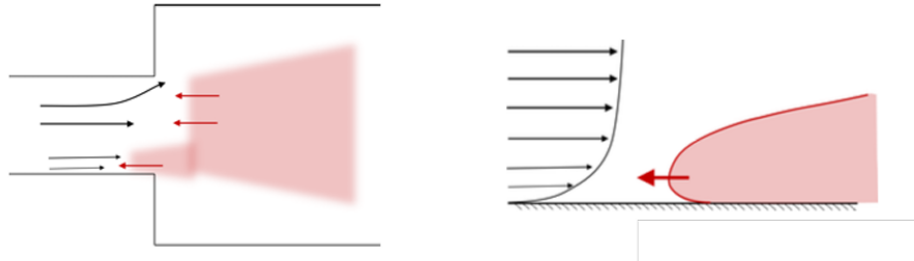


**Figure 2.11:** boundary-layer flashback. The shading and arrows are the same as in Figure 2.10

3. **Flashback due to combustion instabilities.** This flashback mechanism causes both boundary layer and core layer flashbacks, as illustrated in Figure 2.12. These flashbacks are caused by fluctuating pressure pulsations resulting from unsteady heat release rates of the mixture, which lead to periodic occurrences of the flashback itself [69].

Typically, they result from two mechanisms: fluctuations in the local equivalence ratio and vortex shedding.

Acoustic oscillations in the mixing tube are the source of local equivalence ratio fluctuations.

Vortex shedding occurs when rotating flows generate large coherent vortical structures through vortex breakdown. Alterations in heat release result from both mechanisms, which subsequently generate oscillations in flow velocity and culminate in the formation of flashbacks at low frequencies. In order to mitigate this form of flashback, the elimination of low-frequency pressure fluctuations is imperative, through active or passive control [70].

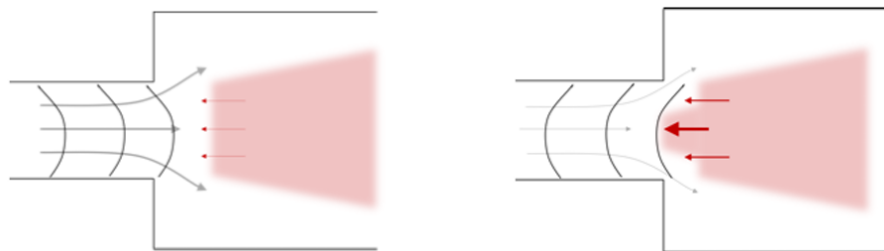


**Figure 2.12:** Flashback - combustion instability-induced. The shading and arrows are the same as in Figure 2.10.

4. **Flashback due to Combustion Induced Vortex Breakdown (CIVB).** Flashback may occur along the centerline of a swirl-stabilized burner, which is typical of gas turbines burners. This can be attributed to the upstream propagation of the recirculation zone, as illustrated in Figure 2.13. This flashback mechanism is more hazardous in the case of hydrogen as a result of the increased flame speed and chemical kinetics, which increase the likelihood of this type of flashback. Locally quenching the flame prevents it from propagating upstream, despite the movement of the recirculation zone, which proves to be a crucial aspect of this mechanism. Hydrogen's elevated resistance to quenching, because of its small quenching distance, indicates an increased likelihood



of experiencing this form of flashback. Also influencing this is the swirl number, as a lower swirl number is more effective at preventing this instability. CIVB flashback can be avoided through a proper aerodynamic burner design [71].

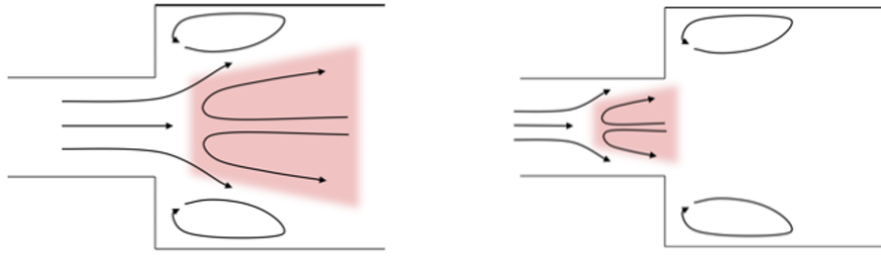


**Figure 2.13:** Flashback- combustion-induced vortex breakdown (CIVB). The flow enters from the mixing tube on the left into the combustion chamber. The shading and arrows are the same as in Figure 2.10.

In summary, a number of factors contribute to the facilitation of flashback, which includes elevated swirl number, high fuel reactivity, high equivalence ratio, and low axial velocity. Air injection provides great margins of operation stability due to the fact that the diameter of the air nozzles can be altered while the combustor is in operation in order to satisfy flame stabilization [69]. Specifically, the LLF (Lower Limit of Flashback, as shown in Figure 2.14) is impacted by axial air injection, which modifies the flashback mechanism generated by induced vortex breakdown flashback (CIVB). The central air injection specifically enhances flame stability through its influence on the aerodynamic of the flow field located downstream of the burner mouth. It decreases the axial velocity defect at the recirculation zone's apex, which is one of the primary causes of CIVB flashback

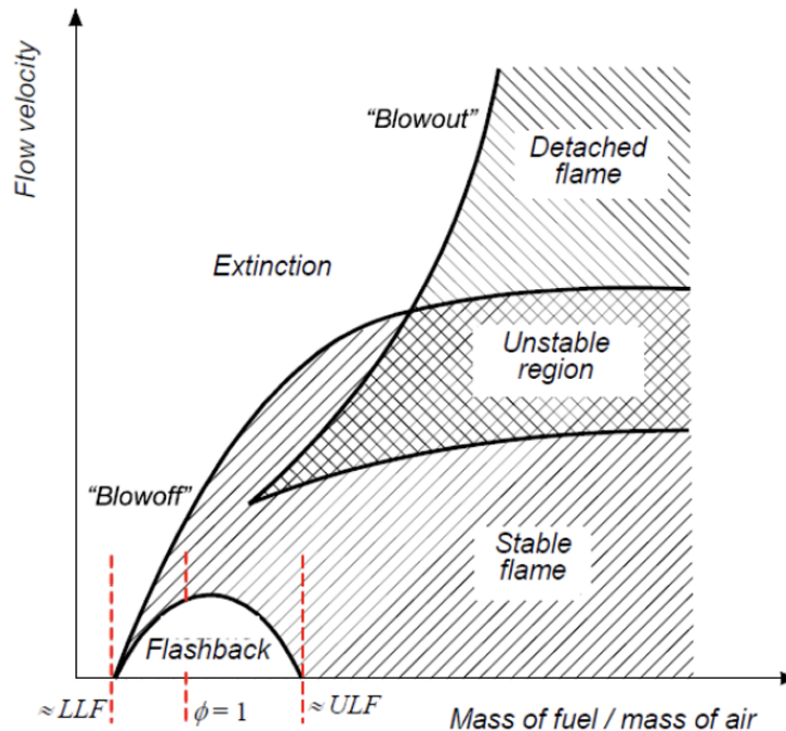


**Figure 2.14:** Flame stability diagram for different equivalence ratios, with the Lower and Upper limit Flashback (LLF and ULF) indicated.

# Literature Review

Dicebat Bernardus Carnotensis nos esse quasi nanos gigantium humeris insidentes, ut possim plura eis et remotiora videre, non utique proprii visus acumine aut eminentia corporis, sed quia in altum subvehimur et extollimur magnitudine gigantea

---

*John of Salisbury*

In this chapter, a thorough literature review is presented, focusing on the combustion systems utilizing blends of H<sub>2</sub> and hydrocarbons. Initially, an exploration of various architectural examples currently available in the market for land-based gas turbines is provided.

Then, the most pertinent experimental and numerical discoveries related to test rig combustors are examined. The relevance of these findings lies in the operating setups involving blends of H<sub>2</sub> and CH<sub>4</sub>, the focus on analyzing heat loss effects, and the exploration of combustor geometries such as swirl-stabilized combustors with axial air injection, similar to the TU Delft APPU combustor which will be analyzed in this thesis.

## 3.1. State of the Art in Land-Based Gas Turbines

Given that the main emission produced by H<sub>2</sub> combustion is NO<sub>x</sub>, it is necessary to describe the NO<sub>x</sub> reduction strategies currently employed by state-of-the-art land-based gas turbines: they are divided into primary and secondary measures.

- The **primary** measures involve the modification of the combustion process, such as peak temperatures or residence times reduction
- The **secondary** measures consist of the treatment of the exhausted gases downstream of the combustion chamber, with the aim of converting the NO<sub>x</sub> into less harmful gases, such as H<sub>2</sub>O and N<sub>2</sub>.

In most cases, the primary measures require geometric modifications and are, therefore, more suitable for new combustor designs but more difficult to apply in combustors already in operation. The reduction of the reaction temperature can be obtained using lean mixtures or by the injection of water and/or steam inside the combustion chamber.

NO<sub>x</sub> reduction technologies that do not consider water or steam injection are called “Dry Low NO<sub>x</sub>” (DLN) or “Dry Low Emission” (DLE) technologies. Since the injection of water or steam into the combustion chamber leads to a reduction of the combustion efficiency and of the entire thermodynamic cycle of the plant, the attention is mainly directed to DLE technologies.

The DLN or DLE combustion technologies are all lean premixed or partially premixed since this allows for greater temperature and NO<sub>x</sub> control. A good mixing is required for the abatement process to be effective.

However, residence times and sufficient volumes may be necessary, such that it is difficult to avoid self-ignition or flash-back. As noted in [72] and [73], these combustion strategies tend to show dangerous thermo-acoustic instabilities (especially close to lean blow out conditions), which can reduce the machine availability for unplanned maintenance or even damage it seriously. Figure 3.1 qualitatively highlights the ability of lean premixed technologies to control pollutant emissions, thanks to the adoption of a low equivalence ratio, and at the same time, it shows the narrow operating range due to the onset of thermo-acoustic instabilities.

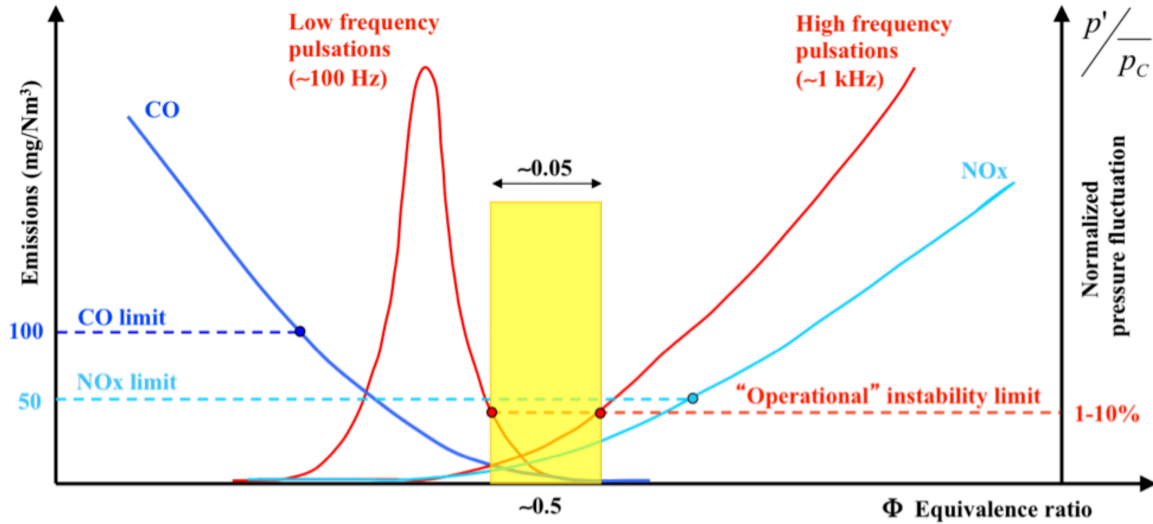


**Figure 3.1:** Qualitative representation of NO<sub>x</sub> and CO emissions and normalized pressure fluctuation, as a function of the equivalence ratio. The nominal equivalence ratio and its stable range are purely qualitative. The pollutant emission limits refer to the Industrial Emissions Directives (IED) on natural gas combustion of November 2010. It should be noted that the limits may be lower than those shown here, depending on what is agreed in the relevant Best Available Technologies (BAT) reference document (BREF). Permission levels for individual sites can also be lower. From [27].

The following sections report the combustion technologies implemented to reduce NO<sub>x</sub> formation, with a particular emphasis on those technologies aimed at increasing the fuel flexibility in gas turbines, i.e., increasing the range of H<sub>2</sub> content in natural gas hydrogen mixtures [30]. These systems can be classified into four groups, depending on the strategy adopted for stabilizing combustion:

1. Combustion aerodynamically stabilized by propagation
2. Combustion stabilized by self-ignition
3. Staged combustion, stabilized with different methodologies (by propagation and/or self-ignition)
4. Micro-mixing combustion, with many small premixed, partially premixed or diffusive flames

These strategies can be hybridized with the recirculation of burnt gases at the compressor intake, a technology known as Exhaust Gas Recirculation (EGR). To ensure the relevance of the discussed topics, only the first, second and third strategies will be described.

### 3.1.1. Aerodynamically Stabilized Combustion

These combustors are based on the generation of suitable recirculation zones which stabilize the combustion, generally by propagation. An aerodynamic stabilization strategy of widely used premixed flames consists of the use of swirled jets, from which the denomination **swirl-stabilized flames**. These burners

generate a flow with a strong rotational component by means of vanes or tangential jets that stabilizes the flames in several ways, improving combustion quality and shortening the reaction zone, as already discussed in section 2.7. Figure 3.2 shows an advanced burner of the DLN type with the vortex breakdown stabilization mechanism: the ALSTOM/ANSALDO EV burner. A more efficient version of EV is developed by means of sequential combustion [74]

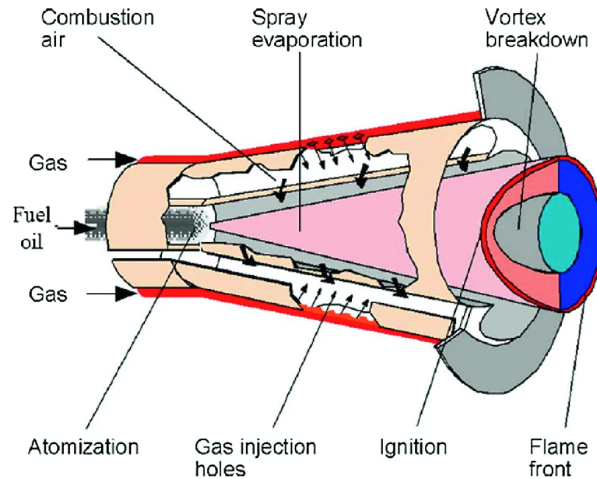


**Figure 3.2:** A schematic diagram showing an EV burner [33]

Another aerodynamic stabilization technique of premixed flames is that of SOLAR Turbines, which in 1992, developed the **SoLoNOx™** (Solar Low NOx) combustion technology, which is used to control NOx and CO emissions. The concept exploits a premixed system (lean premixed combustion) with a pilot. It is based on the following insight provided by [45]: CO is mainly formed below 1400 °C while NOx is basically formed at a temperature above 1500 °C. By keeping the temperature within this range, the emission levels of the two pollutants remain within acceptable levels. In 2021, the technology operated up to 20% hydrogen by volume.

A strategy in which a macro-recirculation used for combustion stabilization is produced by geometric effect is instead the **Trapped Vortex Combustor (TVC)** [34]. Combustion stability is obtained by geometric cavities, where recirculation zones of hot products are generated by the direct injection of fuel and air, and which act as a continuous source of ignition for the incoming fuel-air main flow. The Trapped Vortex Combustor is an efficient and compact combustor, with a stable performance over a wide range of fuel flow rates and with low pressure losses. Different strategies can be implemented in order to reduce NOx: the rapid mixing of fuel and oxidant, staged combustion with a lean or premixed mixture, high inlet velocities with reduced residence time, and in the rich-burn quick-quench lean-burn (RQL) mode.

A recent premixed combustion technology, which belongs to the aerodynamically stabilized burner category, is the **FlameSheet™** by THOMASSEN Energy [75] [76]. It has considerable similarities with the TVC, but in this case, the vortex which guarantees flame anchoring and stability is “trapped” aerodynamically and not geometrically.

The strong recirculation zone, which constitutes the aerodynamically trapped vortex, stabilizes the flame (similar mechanism to a backward facing step, but more effective), while the considerable aerodynamic stretching prevents the pre-ignition of the reactants.

It is shown from the results from the test rig at General Electric Fclass conditions that up to 65% of blended hydrogen by volume with natural gas can be consumed safely without the risk of flashback and

with a NO<sub>x</sub> emission performance below 7 ppm. The FlameSheet™ technology has been demonstrated up to 80% of hydrogen by volume on a single full-scale, full power can in a test facility, with low NO<sub>x</sub> emissions and without the need for a diluent such as nitrogen and without a performance impact. The combustor offers superior turn-down. If, at full load, both stages are used, at low loads only the main stage operates, in a stable and low CO emissions condition. This technology is suitable for retrofitting gas turbines, since it has been designed with a view to replace the combustors of various gas turbines already existing on the market (GE (6F, 7E, 7F, 9E, 9F), Siemens/Mitsubishi (501F, 501G, 701F, 701G), and Siemens (501B/D)).

### 3.1.2. Stabilized Combustion for Self-Ignition

Self-ignition combustion occurs when the reactants are injected into a region with a higher temperature than the ignition temperature. An example can be found in the second combustor of the constant pressure sequential combustion developed by ALSTOM/ANSALDO, in which the fuel is injected into the exhaust gas stream coming from the first combustor (of the EV type, cited above), to which fresh air has been added.

**Flameless Oxidation** (FLOX™) is another example of self-ignition combustion technology. In FLOX or MILD combustion, flue gas (N<sub>2</sub>, CO<sub>2</sub>, H<sub>2</sub>O) is recirculated within the combustor back to the flame front to reduce the O<sub>2</sub> concentration in the oxidant and to heat the reactants above the auto-ignition temperature. This strategy generates uniform temperature distribution, with reduced peaks, and a consequent reduction of NO<sub>x</sub> formation; moreover, the flame is not visible (low OH concentrations). Basically, this approach is based on the creation of a volumetric reaction zone, where the fuel and oxidizer, separated or partially premixed, are injected into the combustion chamber at high speed. The momentum of the jets and a suitable combustion chamber geometry promote the internal recirculation of the hot flue gases which preheat and dilute the reactants, stabilizing the combustion. Although the residence time increases in this way, NO<sub>x</sub> production is limited due to the low temperatures. Figure 3.3 schematically shows the operating principle of a flameless combustor.

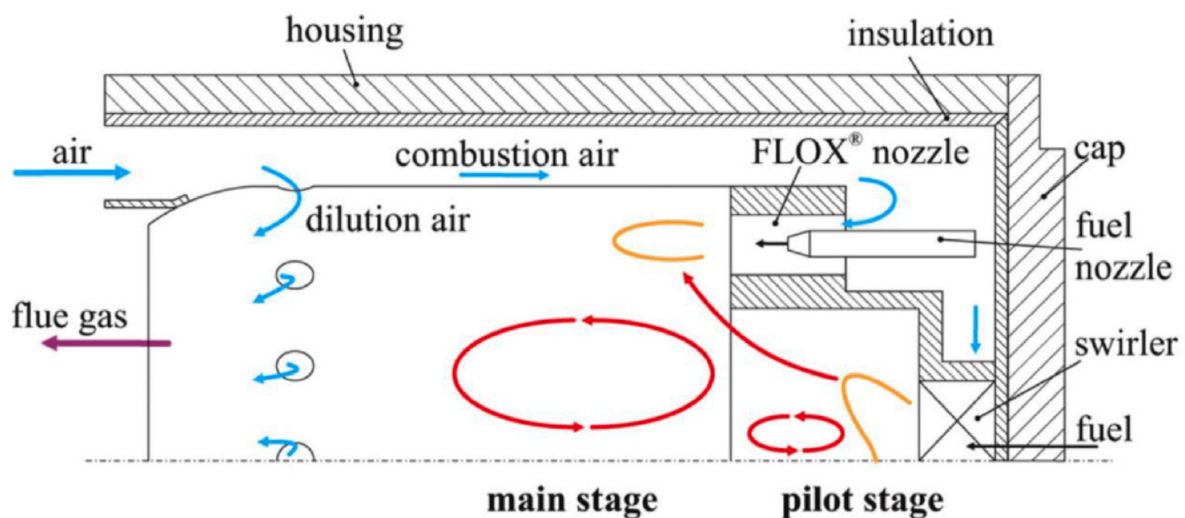


Figure 3.3: Schematic of the FLOX® combustion principle implemented in [77]

Its principle was originally discovered by Wunning for atmospheric industrial furnaces used in the steel industry. The flameless combustion technology is commercially available for reheating furnaces in the steel sector, with devices already able to operate with natural gas and hydrogen mixtures up to 100% H<sub>2</sub>. The uniform distribution of temperatures offers the potential for attaining elevated combustion

chamber temperatures, thereby enhancing overall efficiency. In the gas turbine sector, there are only some numerical and experimental examples [78]. Banihabib et al. [77] conducted modifications on a 100 KWAE-T100 PH micro-gas turbine swirl-type combustor, originally designed for natural gas usage. They implemented the FLOX™ stabilization principle (specifically, the F400s.3 combustion system developed by DLR) to enable the use of hydrogen-enriched fuel and eventually, pure hydrogen. The hydrogen content in the fuel was volume-based and ranged from 40% to 100%. Their findings demonstrated the sustained operation of the micro-gas turbine with NO<sub>x</sub> emissions consistently below the regulated limits. For pure hydrogen at full-load operation, the highest recorded NO<sub>x</sub> emissions were 22 ppm, which corresponds to 62 ppm when corrected based on a reference of 15% oxygen in the exhaust gas.

### 3.1.3. Staged Combustion

In staged combustion, the reaction zone can be divided in two parts: a zone with a high equivalence ratio (first stage) and a zone where the equivalence ratio is lower (second stage). As an example, we can report the **RQL concept** (Rich-Burn, Quench (or Quick-mix), Lean-Burn) introduced in 1980 by Mosier and Pierce [79]. It is essentially a staging technique still used successfully today.

In the first stage, the reacting mixture is characterized by an average equivalence ratio of about 1.4. In this area, the low temperatures and low oxygen concentration do not allow the formation of NO<sub>x</sub>. In the second stage, dilution air is added, thus producing a lean mixture zone. In this area, the formation of nitrogen oxides is limited by the temperature reduction caused by the addition of dilution air. The main problem is the transition between the rich and the lean zone, which necessarily implies the passage through stoichiometric conditions, causing a high production of thermal NO<sub>x</sub> due to high temperatures. To limit the formation of NO<sub>x</sub> in this phase, the mixing with the secondary air must be very rapid and uniform to reduce the residence times at high temperatures and, consequently, the formation of thermal NO<sub>x</sub>.

Today, there are advanced forms of combustion in longitudinal/axial stages on the market: the constant pressure sequential combustion (CPSC) by ANSALDO Energia, the distributed combustion system (DCS) by SIEMENS, and GE's Axial Fuel Staging (AFS).

Sequential combustion was initially developed by ABB/ALSTOM to increase load (operational) flexibility and to increase efficiency at partial loads. A first application of sequential combustion is found in the GT24 and GT26 turbines [80] developed by ABB and ALSTOM. In these machines, there is, in cascade, a high-pressure combustor (EV, first stage), a high-pressure turbine, an afterburner operating at approximately 20 bar and 1300 K (SEV, second stage), and a low-pressure turbine.



## 3.2. State of the Art in Test Rigs

As previously mentioned, this section will explore a more specific application: the use of hydrogen-enriched methane flames on swirl-stabilized test rigs, as observed in research studies.

The burners are categorized into different sections, considering that each burner exhibits variations in geometry, operating point, and type of fuel or simply because of the focus that each study reserved for a particular branch of combustion research. A concluding remark after each combustor encapsulates all the relevant findings related to the thesis topic, foreshadowing the definition of the research gap and the corresponding research questions.

### 3.2.1. TD Combustor

Experiments on the swirl-stabilized TD burner show flame stabilization only at the inner shear layer, as reported in [81], whereas turbulent combustion models predict stabilization at both the inner and the outer shear layers.

In Figure 3.4, experimental results from [82] for a very similar combustion chamber are shown: they depict the OH\* chemiluminescence emissions with contours as measure of the heat release, and the velocity obtained by particle image velocimetry is represented by vectors.

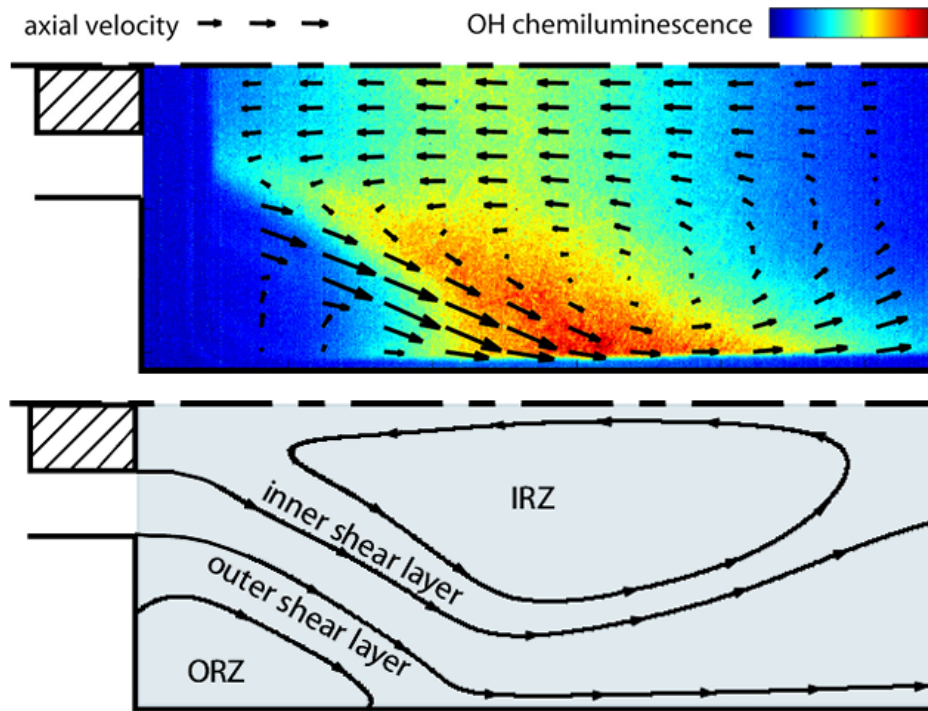


**Figure 3.4:** Top: OH\* chemiluminescence measurement using a swirl burner in a square section non-adiabatic combustor [82].

Bottom: Scheme for the shear layers and recirculation zones.

The distribution of the OH\* emissions corresponds to a line-of-sight integration over the depth of the combustion chamber. It can be seen that the flame stabilizes only at the inner shear layer. The stabilization behaviour of the flame at the outer shear layer is supposed to be strongly affected by the presence of both flame stretch and heat losses, with the latter appearing since the products transported in the ORZ are cooled by the combustor wall cooling.

In their study, Tay Wo Chong et al. [83] try to:

- Quantitatively investigate the impact of strain and heat loss on laminar flames through numerical simulations with detailed chemistry.
- Derive correlations, based on Markstein number, Karlovitz number, and non-dimensional heat loss parameter, for the consumption speed of strained laminar flames from the collected data.
- Develop a turbulent combustion model integrating these effects to accurately predict stabilization behaviour.
- Validate the results obtained from Reynolds-averaged Navier-Stokes (RANS) Computational Fluid Dynamics (CFD) simulations by comparing them with experimental data.

Flame stretch is created by the combined effects of strain and curvature. Nevertheless, in highly turbulent flows with a Karlovitz number higher than 0.1, the influence of curvature is very small [84]. Thus, the curvature is neglected for this study and only effects of strain are taken into account.

The geometry of the burner and the experimental setup are described in [83] and [81], and a view of the CFD geometry is shown in Figure 3.5.

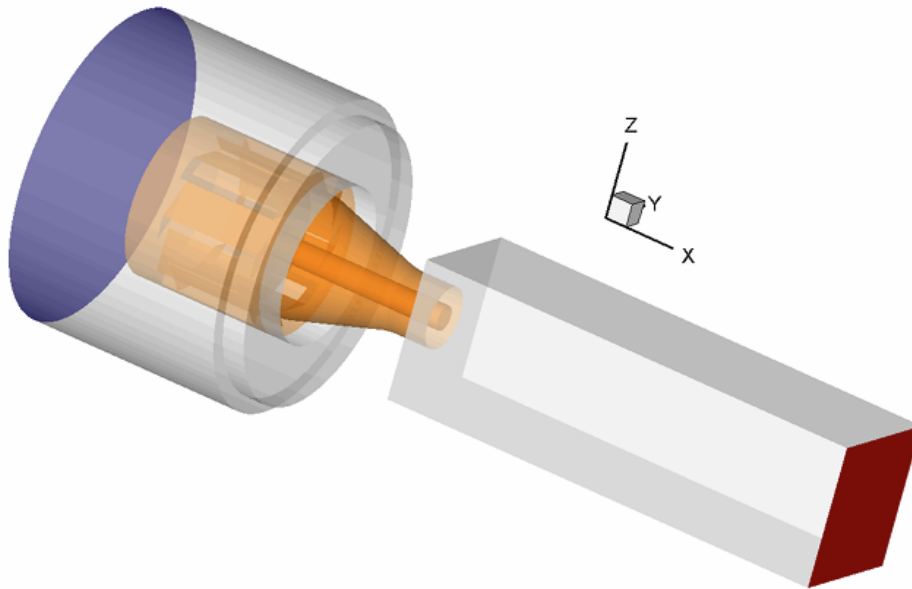


**Figure 3.5:** CFD geometry with the TD burner. From [83]

A mixture of methane-air with  $\phi = 0.71$ , 1 atm and 293 K was introduced at the inlet. The combustor walls were set to a constant wall temperature of 600 K.

Two configurations are employed, one with a thermal power  $P_{th} = 80kW$  and one, not shown in the results, with  $P_{th} = 60kW$ . The Turbulent Flame speed Closure (TFC) combustion model was included in the commercial solver Ansys CFX by the Burning Velocity Model (BVM). In the BVM model, the transport equations of the weighted progress variable and the total enthalpy (sensible plus chemical enthalpy) are solved [85].

Figure 3.6 show results from URANS simulations for the original TFC combustion model with a critical strain rate of 8000 1/s (figure a), for the extended TFC model considering only the influence of strain on the laminar flame speed (figure b) and for the extended TFC model considering the influence of strain and heat losses on the laminar flame speed (figure c).

The original TFC combustion model predicts a flame stabilized in both shear layers and not accorded to experiments. If only the effects of strain are included in the extended TFC model (the heat loss



parameter is equal to zero), the flame also presents stabilization in the outer shear layer. When the extended TFC includes both effects of strain and heat losses, it was possible to get a flame that exhibits the correct stabilization behaviour only at the inner shear layer.

This happens because the sensitivity to strain from the flame is increased drastically in the presence of heat losses, as shown in a simple 1D counterflow premixed configuration with varying temperatures of the products, present in [83] and not reported in this review for sake of brevity.

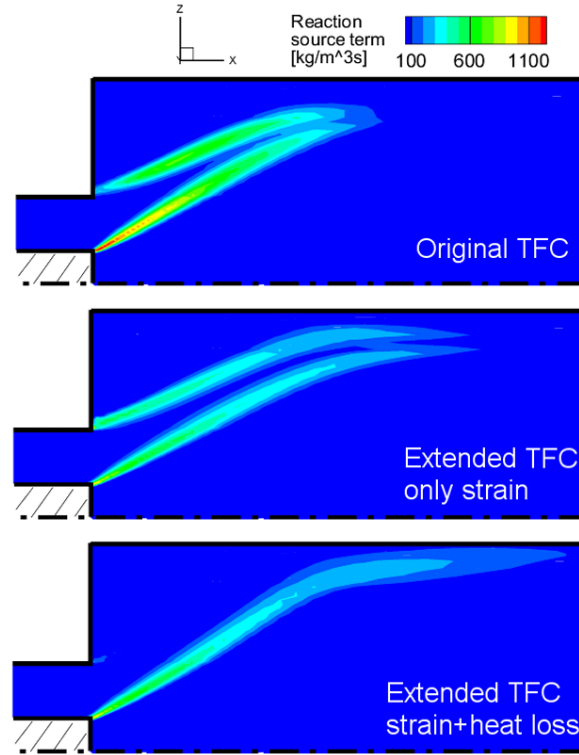


**Figure 3.6:** Reaction source term at cross plane from CFD simulations. (a) Original TFC model, (b) Extended TFC model with  $S_L$  without heat loss effects, (c) Extended TFC model with  $S_L$  with effects of strain and heat loss. From [83].

Given that accurate measurements of the thermal boundary conditions and flame shape were not available, the comparisons between simulations and experiments remained qualitative. However, thanks to the two extensions of the combustion model, the effects of these modifications can be ascribed separately to strain and heat losses: the main effect of strain is the reduction in reaction source term in highly strained zones, precisely the one at the burner lip. However, this is not enough to completely quench the flame on the OSL, which is ascribed totally to the heat loss effect.

The key takeaway from this paper is that for a swirl-stabilized methane flame, the effect of strain and heat loss cannot be neglected in simulations. Even a simple isothermal boundary condition can lead to an increased accuracy of the simulations.

From the same author, a similar research has been conducted on the BRS burner [86], also studied in [87], highlighting once again the importance of heat losses and strain on a CH<sub>4</sub>/air swirl-stabilized flame.

### 3.2.2. EM2C Combustor

Starting from the subject covered in the paper reviewed in the previous section, an additional layer of complexity is introduced with multifuel combustion, as the effect of strain on laminar flame speed (and generally on flame reactivity and resistance to heat losses) becomes dependent on the Lewis number of

the species involved.

In this regard, the research conducted by Mercier et al. [88] aims to experimentally and numerically assess the effect of thermal boundary conditions on  $\text{CH}_4/\text{H}_2/\text{air}$  premixed flames stabilized over a bluff-body swirling injector, namely the combustion chamber recently studied experimentally at the EM2C laboratory [89], with the geometry reported in Figure 3.7.

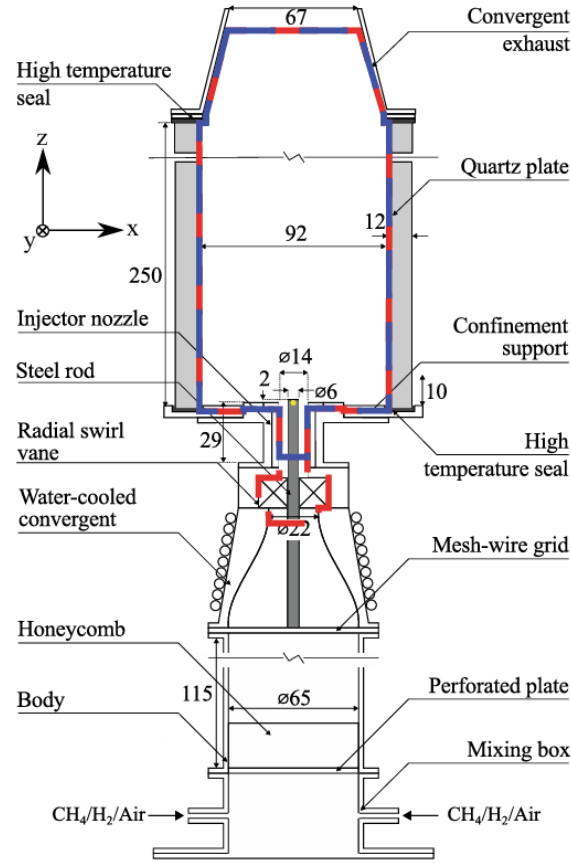


**Figure 3.7:** Schematic of the test-rig. Dimensions are in mm. The reference computational domain for both non-reacting and reacting cases is delimited by the blue dashed line. The red dashed line represents the preliminary computational domain used to extract the velocity boundary conditions for the reference domain. The yellow dot at the tip of the central rod indicates the origin of the numerical frames. From [88]

The simulations have been carried out through the use of the turbulent combustion model F-TACLES (Filtered TABulated Chemistry for LES) based on the tabulation of filtered 1-D premixed flames [90], extended to account for heat losses.

All temperatures of solid walls of the experimental setup, including the combustor dump plane, the injector central rod tip, the combustor sidewalls, and the quartz windows, were also characterized. Assuming a fully adiabatic combustion chamber, LES always predicts an M flame shape and does not capture the transition from V to M shape observed in experiments when the hydrogen concentration in the fuel blend is increased.

However, by considering non-adiabaticity using measured thermal boundary conditions, simulations predict the correct flame stabilization for both V and M flames and show good agreement with experiments in terms of flame shape, as shown in Figure 3.8.

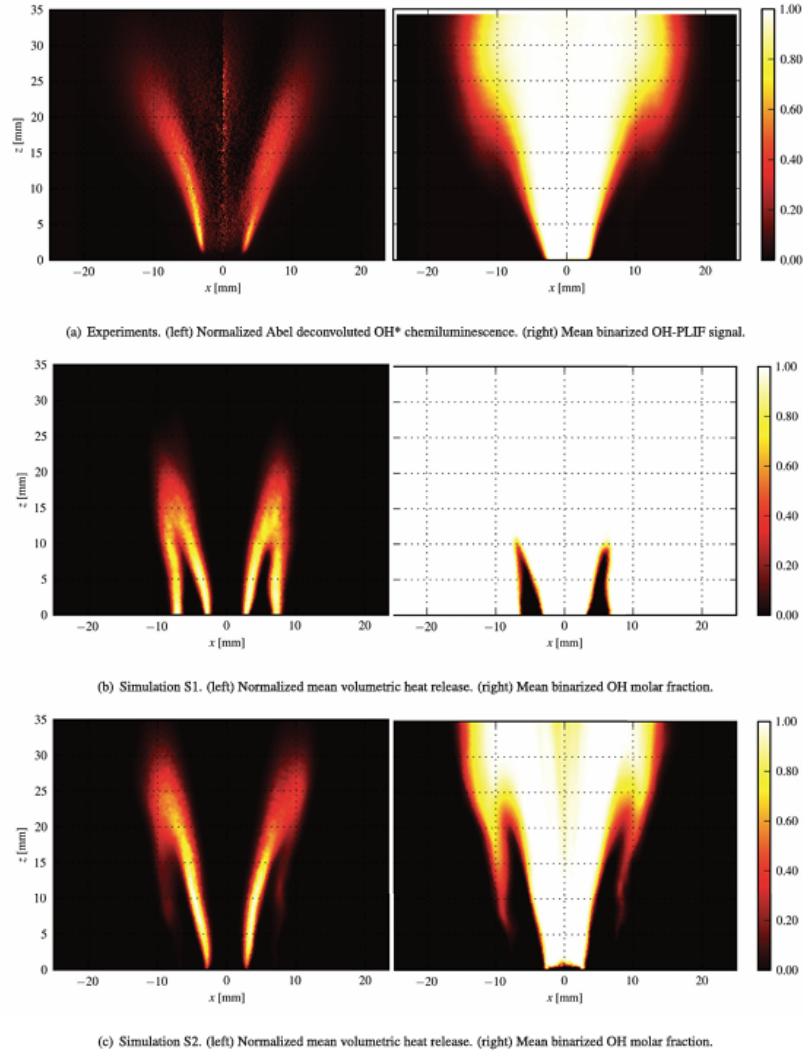


**Figure 3.8:** Comparisons of the mean flame position for the case  $X_{H_2} = 0.6$ . Experiments, adiabatic (S1) and non-adiabatic (S2) simulations results are shown. From [88].

Experiments in [89] show that flame stabilization is strongly influenced by heat losses at the combustor wall. In addition, transitions between V and M flame shapes are observed when increasing the  $H_2$  concentration in the  $CH_4/H_2$  fuel blend. Two fuel compositions are retained for this study:

- $X_{H_2} = 0.6$  and  $X_{CH_4} = 0.4$
- $X_{H_2} = 0.9$  and  $X_{CH_4} = 0.1$

Experiments show that a V flame shape is observed for the first case, whereas an M flame shape is detected for the second case.

For all cases, the flame power is  $P_{th} = 4kW$  and the equivalence ratio is set to  $\phi = 0.7$ .

Temperature measurements were conducted under reacting conditions once thermal steady-state was achieved ( $\approx 45$  mins):

- Thermocouples were placed on a vertical steel bar at the edge of the combustion chamber
- Laser Induced Phosphorescence (LIP) measurements were utilized for obtaining radial temperature profiles on the backplane and planar temperature distributions on the inside face of one of the quartz windows

Isothermal wall boundary conditions are imposed in the non-adiabatic simulations. As the wall temperature measurements only partially cover the combustor surface, linear interpolations and extrapolations are performed to provide complete temperature boundary conditions. Although the temperature of the bluff-body wall surface (rod tip) is imposed to 500 K (measured value), the wall surfaces within the injection tube are assumed adiabatic. Therefore, the preheating of the fresh gases within the injection tube is not considered in the present work. This assumption is reasonable since a simple convective heat transfer analysis estimates the elevation of the fresh gas temperature flowing near the heated tube to  $T = +4$  K. It means that a solid-gas temperature gap of 200 K is not sufficient to preheat significantly the injected fresh gases in the present flow conditions.

As the model accounts for the impact of heat losses on the chemical activity, the reactive layer intensity differs between the Inner Shear Layer (ISL) and Outer Shear Layer (OSL). Indeed, heat losses induced by the sidewalls of the combustion chamber cool the burnt gases in the ORZ, which are convected to the OSL, decreasing the mixture reactivity. Unlike the adiabatic simulation results, the outer flame front is not attached to the burner lips anymore when considering a non-adiabatic simulation. However, in contrast with experiments, a weak reactive layer still exists in the downstream OSL, near the flame tip. This reaction layer is an artifact, not observed in experiment, where the flame is quenched because of combined effect of strain and heat losses, as postulated in the research by Tay-Wo Chong et al. reviewed before [83]. To capture this phenomenon, the present model should account for the impact of local strain rate on the flame consumption speed, which is very challenging because it occurs at the sub-grid scale.

In order to assess the effect of a more intense hydrogen-enrichment, a simulation with  $X_{H_2} = 0.9$  has been conducted: by accounting for both the effect of heat losses and hydrogen enrichments, the LES recovers the correct M flame shape observed in the experiment, as reported in Figure 3.9.

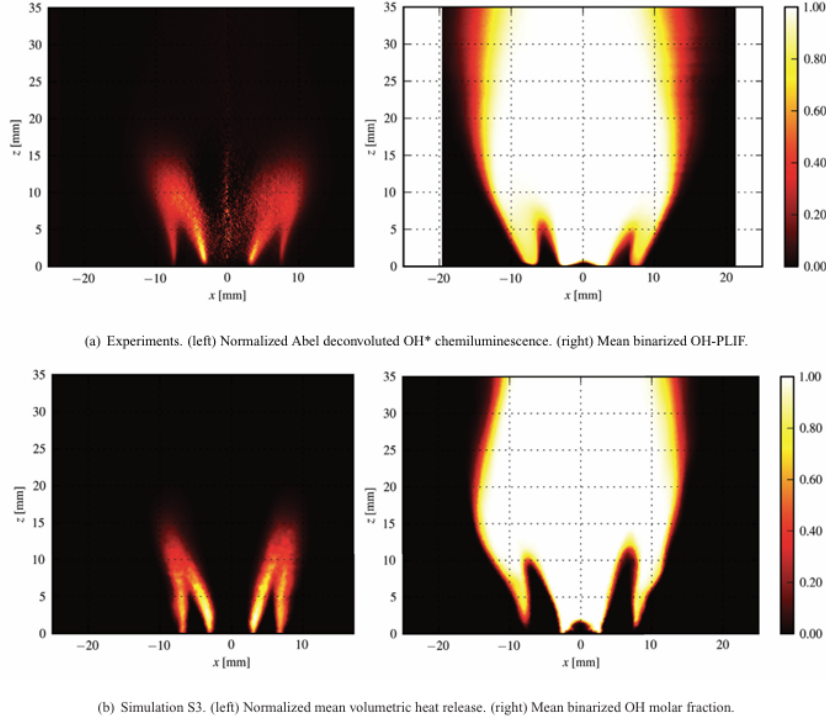


**Figure 3.9:** Comparisons of the mean flame position for the case  $X_{H_2} = 0.9$ . Experiments and non-adiabatic simulation results are shown. From [88].

There are however still differences between the experiment and the simulation. The flame length is slightly overpredicted in the simulation. In the experiment, the reactivity is elevated in the ISL and much lower in the OSL. The reactivity then progressively decreases towards the flame tip. In the simulation, the reactivity keeps high values in the ISL, but also in the OSL, except close to the flame tip where it drops rapidly. The turbulent flame brush in the experiment also spreads over a wider region than in the simulation.

These differences might be attributed to the sub-grid scale wrinkling model that does not fully capture the flame wrinkling near the flame tip. As both flame fronts are located at the ISL and OSL, flame strain effects, which are not accounted for by the F-TACLES model, may also explain the differences in reactivity. It is however worth recalling that the shape of the flame is well captured by the proposed methodology.

The paper by Mercier et al. [88] follows the same path as Tay-Wo Chong et al. [83], highlighting the importance of a well-defined thermal boundary condition and improving the previously reviewed paper by the introduction of more accurate and precise measurements of the temperature at the boundary of the burner.

Additionally, the paper examines the impact of hydrogen enrichment. It concludes that the discrepancies in the validation process could be attributed to strain, which is not accounted for in the F-TACLES model.

### 3.2.3. PRECCINSTA Combustor

Designed within the EU project PRECCINSTA, the combustor is derived from an industrial design by SAFRAN Helicopter Engines, representative of a real aeronautical gas turbine combustor. It was widely studied experimentally [91] and numerically [92], [93], [90], [94] and [95]. The geometry consists of three parts, shown in Figure 3.10: plenum, swirler and chamber. The premixed methane-air mixture is injected into the plenum and swirled through the injector by twelve radial veins before entering the chamber through a converging nozzle with a central conical bluff-body.

The chamber has a square cross-section of  $86 \times 86 \text{ mm}^2$  and a height of 110 mm. The burnt gases leave the burner by a cone-shaped exhaust pipe. 1.5 mm-thick quartz windows are placed on the combustor side walls to enable optical diagnostics.

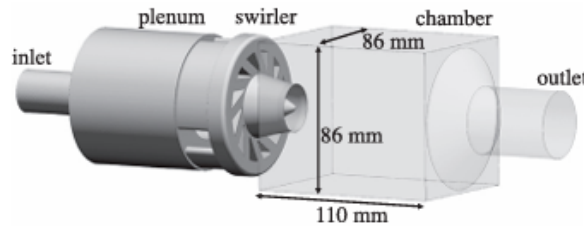


**Figure 3.10:** Computed geometry of the PRECCINSTA burner. From [96].

Although air and fuel are injected separately in the experiment, a perfectly premixed injection condition is assumed in the studies cited above. At the specific operating conditions they studied, Franzelli et al. [97] showed that this assumption has a negligible effect on the results. From Moureau et al. [98], the integral length scale is estimated as  $l_T \approx 7.0 \text{ mm}$  and the Kolmogorov length scale as  $\eta_K \approx 29 \mu\text{m}$ . The eddy turn-over time and the Precessing Vortex Core characteristic time scale have a similar value, around 2.0 ms, while the Flow Through Time is estimated around 30 ms.

One common aspect of the studies conducted on this burner is that most of them focus on LES with adiabatic wall conditions. These computations were not able to correctly capture the flame structure,

in fact in the research of Franzelli et al. [97] this discrepancy has been attributed to the adiabatic wall conditions, while focusing more on the influence of the chemistry description, and finally in the work of Moureau et al. [98] the strong influence of mesh resolution is pointed out.

In the study from Benard et al. [96], convective heat transfer through the injector system and quartz windows is modeled as a local temperature Dirichlet boundary condition (i.e. a profile of temperature over the boundary condition is specified). The wall temperature was not measured experimentally and was obtained through a trial and error procedure based on non-adiabatic LES computations. The boundary condition was calibrated for mesh 2 and validated for mesh 3, two of the computational grids used in this study, shown in Table 3.1, where also a comparison with characteristic length of the flow is included:

	<b>Mesh 1</b>	<b>Mesh 2</b>	<b>Mesh 3</b>	<b>Mesh 4</b>
#Nodes [Millions]	0.4	2.3	18.5	147
#Cells [Millions]	1.7	14	110	877
$\Delta$ [mm]	1.2	0.6	0.3	0.15
$l_T/\Delta$	5.8	11.7	23.3	46.5
$\Delta/\eta_K$	441.4	20.7	10.3	5.1
$\delta_L^0/\Delta$	0.35	0.71	1.41	2.83

**Table 3.1:** Resolution parameters for the LES computational grids. From [96].

A first guess of the temperature profile was designed from experimental data, knowing that there is water-cooling in the injector and natural convection for lateral walls. Then, seven temperature profiles were necessary to achieve the final results. The cost function of the optimization process was based on the temperature in the corner recirculation zones and the maximum CO mass fraction in the outer branch. It was found that almost no heat loss appear on the injector nozzle but mainly on the combustion chamber base, due to the swirler water cooling system, and quartz windows. Therefore, the nozzle is considered adiabatic, and heat transfer occurs at the external wall of the injector, the chamber base and the chamber lateral walls.

The results presented in this paragraph are shown in Figure 3.11. Several setups have been considered, using the meshes listed in Table 3.1 and adiabatic or non-adiabatic boundary conditions at the relevant walls. With the coarsest mesh and adiabatic condition, the flame surface does not exhibit resolved wrinkling. As the resolution increases, resolved wrinkling appears and pockets of reactants detach from the flame front. The flame presents an M-shape structure with an internal flame attached to the nozzle and an external front attached to the chamber base. When heat loss occurs, however, the temperature in the reaction zone of the outer flame front lies between 1300 and 1500 K, while 1550 K is found in the adiabatic cases: this changes the flame structure, showing a detached external flame front, while also the temperature and CO distributions are then highly affected. The non-adiabatic case with the most refined grid shows the best agreement to experimental results.

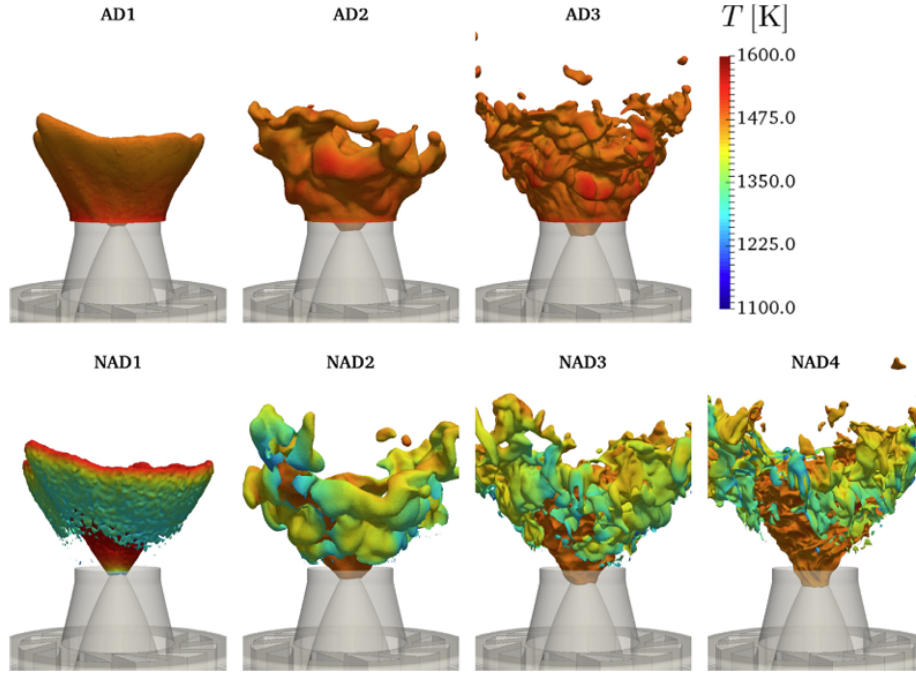


**Figure 3.11:** Normalized progress variable iso-contour  $c = 0.7$ , conditioned to heat release rate values exceeding 1% of its maximum value, colored by the temperature. From [96]

Also, an interesting insight is pointed out in the non-adiabatic, mesh 4 case: from the analysis of velocity gradient norm (estimation of the strain rate) and enthalpy loss it is possible to hinder that enthalpy defect alone may not be the sole factor influencing the flame quenching process: considering the strain rate it becomes possible to clearly distinguish between the reacting points with low strain rates and the quenched points with higher strain rates, as clustered in the scatter plot in Figure 3.12.

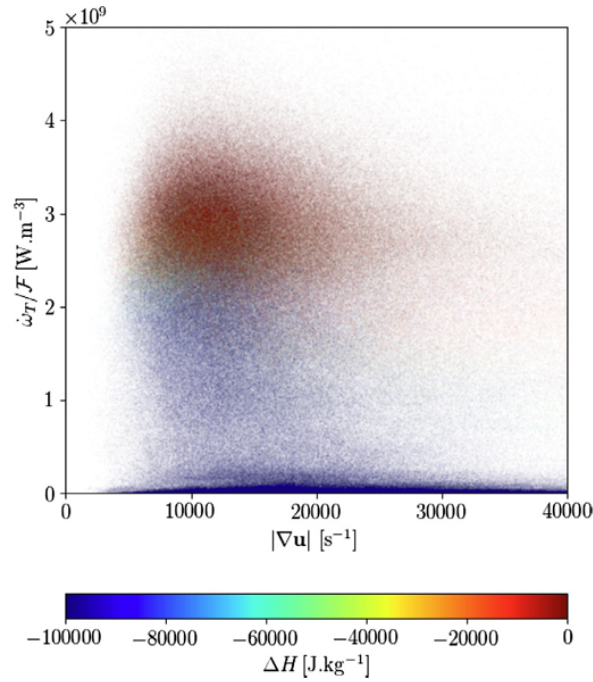


**Figure 3.12:** Scatter plot of the heat release rate against the velocity gradient norm, for points with  $0.75 \leq c \leq 0.8$ , colored by the enthalpy defect for NAD4 simulation. From [96].



The increased quenching of the non-adiabatic, mesh 4 case is therefore attributed to higher resolved strain rates on the refined grids, resulting in an expansion of the quenched flame surface. It is necessary to point out that this is a prerogative of the Thickened Flame Model: an increase in resolution, especially on the flame front, is always beneficial for the correct modelling of the flame surface. This finding aligns with previous research conducted on counterflow flame configurations [99], which demonstrated that the enthalpy defect in burnt gases reduces the resistance of premixed flame fronts to large strain rates.

In the study conducted by Agostinelli [100]<sup>1</sup>, the impact of hydrogen enrichment and heat losses on methane flame stabilization and dynamics was investigated using Large Eddy Simulations. The objective was to assess how H<sub>2</sub> enrichment and Conjugate Heat Transfer (CHT) influence flame behaviour, especially in the context of low-carbon combustion technologies.

To assess the impact of thermal wall boundary conditions for the PRECCINSTA test bench, two approaches are tested:

- **Heat Resistance Tuning (HRT):** A local resistance is tuned using experimental temperature data
- **Conjugate Heat Transfer (CHT):** The chamber wall temperature is solved and coupled to the flow computation

First of all, the thermal boundary conditions approaches listed here do not contain the ones used until now: isothermal boundary conditions. From the study of Agostinelli [100], this method is not considered as appropriate as the HRT and CHT approaches for the following reasons:

- Temperature is an output of the simulation and its profile on the wall should depend on the evolution of the flowfield and flame shape during the simulations. If a fixed temperature profile is rigidly imposed, the model will not be able to correctly capture temperature wall variations due to eventual interactions of the flame with the wall.
- Since the wall surface temperature is case dependent, the procedure proposed by Benard et al. [96] cannot be used for other operating conditions. The HRT strategy, relying on thermal resistances, is therefore more general and it is expected to be more accurate.

The results reveal that the HRT method captures the mean flame correctly but the predicted flame becomes unstable and responds to a thermoacoustic oscillation which is not observed experimentally. On the contrary, using CHT, the flame is correctly predicted and stable as in the experiments.

In this work, an experimentally stable condition is computed for a global equivalence ratio of  $\phi = 0.8$  ( $\dot{m}_{air} = 4.29g/s$  and  $\dot{m}_{CH_4} = 0.2g/s$ ) and a thermal power of  $P_{th} = 10kW$  at atmospheric conditions.

Both cases, employing HRT and CHT, are performed using the same computational grid of 20.3M tetrahedral elements which was optimized applying static mesh refinement criteria, as stated in [100].

Another heat loss mechanism, thermal radiation from the hot gases, has to be taken into account, as pointed out in the paper of Fredrich et al. [106]. The overall heat losses incurred through radiation and wall heat transfer respectively, amount to about 5% and less than 1% of the total integrated heat release rate. Radiative losses are implemented in the LES solver with the Optically Thin Assumption (OTA) [107] for the most radiating species CH<sub>4</sub>, CO, CO<sub>2</sub>, and H<sub>2</sub>O: gases are supposed to be optically thin and re-absorption is neglected while the Planck mean-absorption coefficients are provided for each

<sup>1</sup>From this research activity, more articles are present in literature, such as [101], [102], [103], [104] and [105]



species as polynomial functions of temperature[108].

In the following paragraphs, the two approaches used by Agostinelli in his PhD thesis [100] are described.

### HRT Approach

Using this framework, a heat flux has to be imposed at each point of the wall, defined as:

$$\Phi = \frac{T_f - T_{ref}}{R} \quad (3.1)$$

Where:

- $T_{ref}$  is a reference temperature: the air temperature in the room or the external wall-temperature
- $T_f$  is the temperature of the fluid at the wall
- $R$  is the thermal resistance

An example of thermal resistance could be the corresponding heat conduction resistance through the chamber walls. However, a more accurate approach consists of the inclusion of the natural (or forced, but not in this case) convection, accounting for the heat losses from the chamber walls to the laboratory environment.

These boundary conditions are only applied on walls where relevant heat transfer is expected: on other walls a simple adiabatic boundary condition is assumed. After tuning and application of the thermal resistance method on cases at  $P_{th} = 30kW$  and  $P_{th} = 20kW$ , for which experimental temperature profiles were available, it has been pointed out the poor accuracy of using isothermal boundary conditions for different power settings.

Then, the HRT approach has been employed to simulate the operating point which is the objective of this study,  $P_{th} = 10kW$ : as seen also in Figure 3.13, LES captures the mean flame angle while the flame length is slightly underestimated. A global satisfactory agreement is achieved in terms of flame shape with the HRT approach, the only main difference being the region of heat release rate in the OSL which is not observed in experiments.

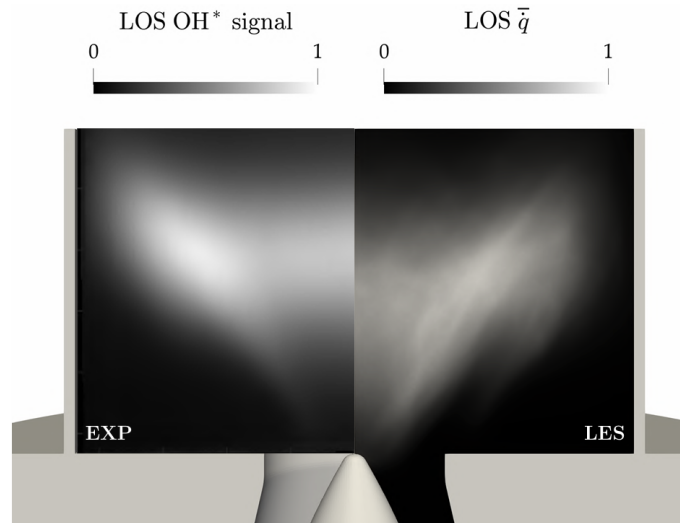


**Figure 3.13:** Validation of the LES simulations with HRT approach for case  $P_{th} = 10kW$ . Comparison of experimental normalized time-averaged LOS OH\* chemiluminescence image with LOS of predicted heat release rate  $\bar{q}$ . From [100].

As far as the steady quantities are considered, the flame is reasonably captured: the limits of this approach become visible when the flame dynamics are considered, with amplitude and phase differences with the experimental pressure oscillations.

### CHT Approach

To remove uncertainties on the heat transfer between the fluid and the solid, CHT simulations are performed by coupling the LES solver with the AVTP code which solves for heat conduction in the walls of the chamber using the energy conservation equation:

$$\rho_s C_s \frac{\partial T(x_i, t)}{\partial t} = - \frac{\partial \Phi_{q,i}}{\partial x_i} \quad (3.2)$$

Where  $\rho_s$  and  $C_s$  are the solid density and heat capacity respectively,  $T$  is the solid temperature and  $\Phi_{q,i}$  is the conduction heat flux described by Fourier's law:

$$\Phi_{q,i} = -\lambda_s \frac{\partial T}{\partial x_i} \quad (3.3)$$

Which is controlled by the heat conductivity of the solid  $\lambda_s$ . AVTP takes into account local changes of  $\lambda_s$  and  $C_s$  due to the different materials of the rig (e.g. inconel, quartz, etc) and to the local temperature.

While the heat fluxes at the solid boundaries in contact with the fluid are determined from the LES solutions, thermal boundary conditions must be fixed for the solid surfaces that are not in contact with the fluid domain (e.g. external chamber walls, external plenum walls). To do so, the required heat exchange coefficients at the boundaries have been determined through correlations for natural convection on the external side of the chamber and plenum walls.

From the unstable phase predicted with the HRT approach in which pressure and heat release rate oscillations were almost in phase satisfying the Rayleigh criterion, a stable condition is recovered when CHT simulations are started. The pressure fluctuations amplitude is of the order of 200 Pa and corresponds to the level observed experimentally.

Another important feature captured by the CHT approach is the preheating of gases, which, due to the heat conduction in the backplane, results in an inlet temperature of the reactants in the chamber of almost 400 K, rather than the temperature at the inlet, 293 K, as shown in Figure 3.14.

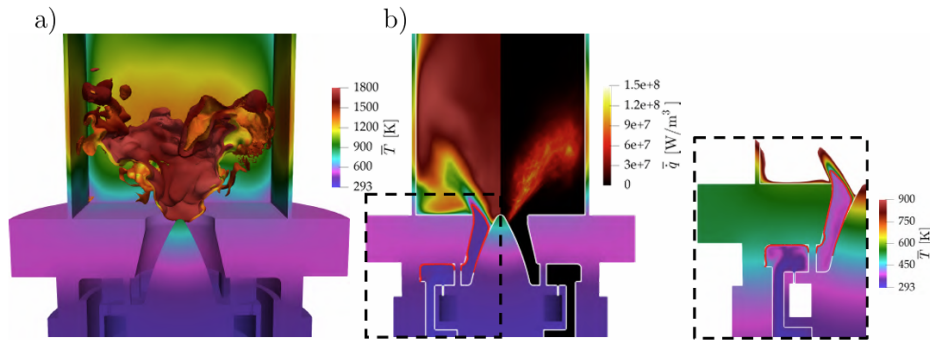


**Figure 3.14:** (a) Instantaneous field of solid temperature and iso-contour of heat-release rate  $\dot{q}$  at 10% of maximum value; (b) cut-plane showing the time-averaged temperature  $\bar{T}$  and heat release rate  $\dot{q}$  predicted by CHT simulations. The added red iso-contour line corresponds to a temperature of 450 K, showing the pre-heating of the fresh gases by the solid walls. A zoom showing the temperature field with a different colorbar helps visualize the pre-heating of the gases and the temperature gradient in the solid. The fluid domain is delimited by a white line to visualize the separation between solid and fluid parts.

From [100].

In general, the length and flame angle retrieved by the CHT simulations show better agreement with respect to the HRT approach. LES is also able to predict the high region of heat release rate in the top central part of the flame while low intensity is predicted in the CRZ, just downstream of the centerbody. The flame tip shape is correctly predicted together with the distance from the external chamber walls.

## H2 Enrichment

When hydrogen combustion is involved, the impact of the imposed thermal boundary conditions is expected to be even stronger, since H<sub>2</sub>-enriched flames are shorter and tend to stabilize closer to the chamber walls due to the increased laminar flame speed which inevitably increase the thermal load on the combustor components. For this particular analysis, three cases are considered:

Case	$X_{H_2} [\%]$	$\dot{m}_{air} [g/s]$	$\dot{m}_{CH_4} [g/s]$	$\dot{m}_{H_2} [g/s]$	$\phi$	$P_{th} [kW]$
A	0%	4.29	0.2	0.0	0.8	10
B	20%	4.23	0.186	0.006	0.8	10
C	50%	4.12	0.154	0.0019	0.8	10

**Table 3.2:** Hydrogen-enriched operating points

Case A was already discussed in Figure 3.2.3 and Figure 3.2.3.

For case B, shown in Figure 3.15, the flame presents a clear V-shape and appears to be sensibly shorter if compared to case A.

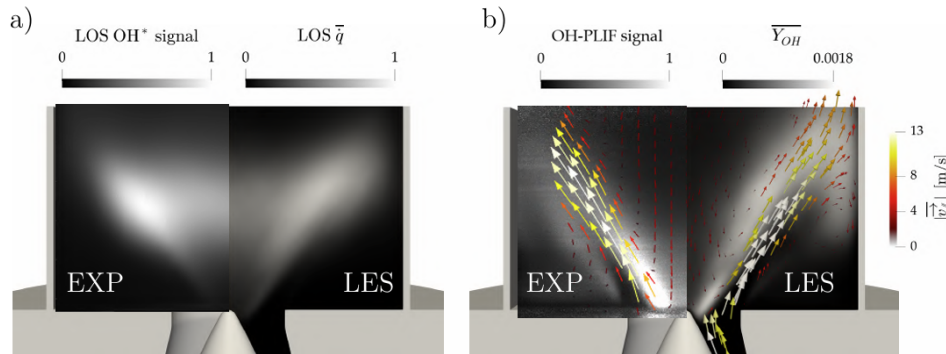


**Figure 3.15:** Validation of CHT simulations. (a) Comparison of experimental normalized time-averaged Line of Sight (LOS) OH\* chemiluminescence image with LOS predicted heat release rate  $\bar{q}$ . (b) Comparison of experimental normalized time-averaged OH-PLIF signal with predicted OH mass fraction. The arrows are tangential to the experimental and numerical time-averaged velocity field in the PIV plane. Their length and color indicate the velocity magnitude. Case B: 20% H<sub>2</sub>. From [100]

The flame is relatively more distant from the combustion chamber and presents a higher signal region in the central part while no flame is observed downstream the centerbody tip.

The temperature of the chamber walls on the internal side reaches a maximum value of around 1250K, which is slightly lower than case A, probably due to the larger distance between the flame tip and the chamber walls. The backplane instead presents a temperature close to 580 K, very similar to case A. On the contrary, the centerbody tip presents a much larger temperature, close to 1000 K, probably due to the different flame stabilization. Indeed, the iso-contour of heat-release rate  $\dot{q}$  shows that the flame is stabilized sensibly closer to the centerbody and slightly more upstream, probably due to the higher laminar flame speed and the larger resistance to strain of the 20% H<sub>2</sub>-enriched flame if compared to the pure CH<sub>4</sub> case.

The study found significant changes in flame dynamics for case C. However, focusing solely on flame shape and temperature effects, the flame was observed to become shorter and more compact with the increased H<sub>2</sub> enrichment, as shown in Figure 3.16, reaching temperatures as high as 1200 K, particularly at the centerbody tip. The flame also tended to stabilize further upstream, leading to pre-heating of fresh gases and increased temperatures in the outer recirculation zones.

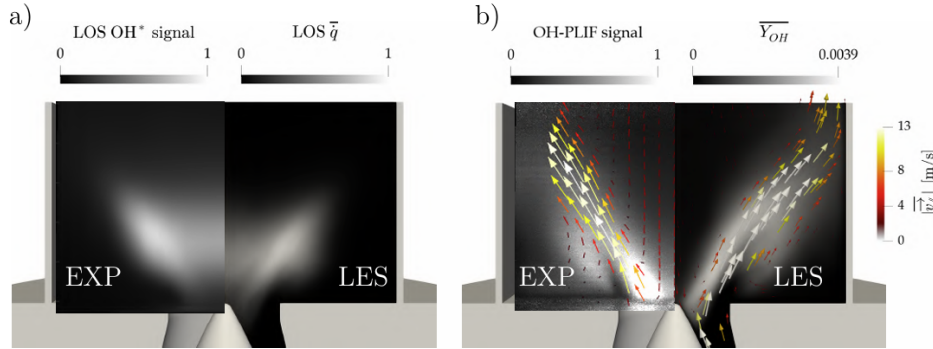


**Figure 3.16:** Validation of CHT simulations. (a) Comparison of experimental normalized time-averaged Line of Sight (LOS) OH\* chemiluminescence image with LOS predicted heat release rate  $\dot{q}$ . (b) Comparison of experimental normalized time-averaged OH-PLIF signal with predicted OH mass fraction. The arrows are tangential to the experimental and numerical time-averaged velocity field in the PIV plane. Their length and color indicate the velocity magnitude. Case C: 50% H<sub>2</sub>. From [100].

For all considered H<sub>2</sub>-enrichment cases, LES proved to be able to successfully predict the complex flame dynamics in the CHT context, providing interesting insights about the hydrogen addition impact on the test rig components temperature.

The key takeaways from the analysis of the papers that dealt with the PRECCINSTA combustor are multiple:

- Once again, the importance of heat losses is highlighted and two approaches, Heat Resistance Tuning and Conjugate Heat Transfer, are proposed to address possible inconsistencies in the flame validation process.
- HRT presents itself as a useful approach if the interest is mainly focused on the flame topology and steady conditions, but it mispredicts unsteady effects, which are correctly captured, with the downside of increased computational cost, by the CHT approach.
- The main effects of H<sub>2</sub> enrichment are highlighted: a shorter flame which tends to stabilize more upstream affects the reactants, resulting in the preheating of the gases. However, it is necessary to point out that this is also dependent on the particular case of the PRECCINSTA combustor: material, geometry of the combustor/flow path and thermal power lead to the presence of a uniformly hot backplane of the combustor which, in turn, increases the temperature of the reactants.

### 3.2.4. TU Berlin AHEAD Combustor

The swirl-stabilized combustor at TU Berlin, developed in the context of the AHEAD project, shows one more feature that makes it more similar to the TU Delft APPU combustor: the presence of axial air injection, visible in the geometry depicted in Figure 3.17.

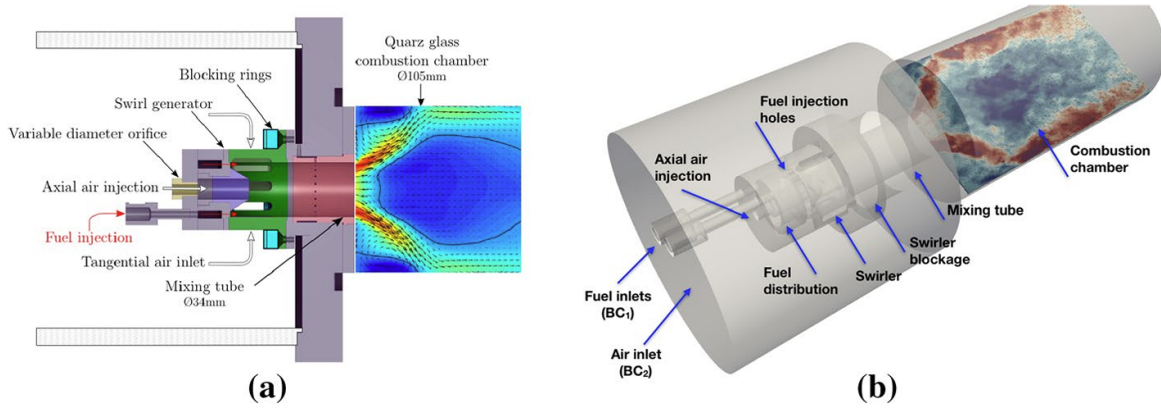


**Figure 3.17:** (a) Experimental configuration (Reichel and Paschereit [71]) and (b) Computational domain. From [109].

However, to the knowledge of the author, there have not been any simulations or experiments with blends of hydrogen with hydrocarbons in literature, only pure hydrogen/air premixed flames.

A numerical characterization of this premixed hydrogen flame is described in [109]. In this work the following point is investigated: from experiments, it is suggested that the axial momentum ratio  $J$  between fuel and air dominates the flame stabilization mechanism and flashback resistance over mixing and equivalence ratio fluctuations.  $J$  is defined as follows:

$$J = \frac{\rho_{fuel} u_{inj, fuel}^2}{\rho_{air} u_{inj, air}^2} \quad (3.4)$$

In order to enable premixed combustion, hydrogen is injected at the upstream end of the mixing tube. This is done by non-swirling jets at high speed. The air flow in the mixing tube has axial as well as tangential momentum due to the swirl generator. The additional axial momentum introduced by the 16 small jets at high-speed has an impact on the swirl number and hence, the formation of flow instabilities.

The swirl number is defined as the ratio of tangential to axial momentum and in this particular configuration it has been chosen to follow the definition of Terhaar et al. [110], which accounts for the reduction of the geometrical swirl number of the swirler  $SN_g$  due to the axial injection:

$$SN = \frac{2\pi\rho \int_0^R uwr^2 dr}{R2\pi\rho \int_0^R (u^2 - 0.5w^2) r dr} \quad (3.5)$$

Although, Terhaar made an interesting extension to this swirl number definition: with an increasing rate of AAI, the mass flow through the swirl generator is reduced, and this effect can be modeled as follows:

$$SN = \frac{(1 - AAI)^2 2\pi\rho \int_0^R uwr^2 dr}{R \left( (1 - AAI)^2 2\pi\rho \int_0^R (u^2 - 0.5w^2) r dr + \rho AAI^2 u_0^2 (A_{MT}^2 / C_d A_i) \right)} \quad (3.6)$$

With  $A_{MT}$  mixing tube cross section area,  $A_i$  axial injection cross section area,  $C_d = 0.6$  discharge coefficient to fit the measurement data, attributed to the supply port for the axial injection, which is of a smaller diameter than the axial injection.

The first insight of Mira et al. concerns the swirl number: the effect of an increased axial momentum is to decrease the swirl number by more than 10% compared to the non reactive, only-air case.

Moreover, the PVC is suppressed by the additional fuel momentum at high  $J$ .

The results of the reacting flow demonstrate generally good agreement with experimental data when considering the momentum ratio  $J$  in conjunction with a perfectly premixed assumption. Key findings include accurately predicted size and location of central and corner recirculations, along with matching spreading rates with experimental measurements. However, there are instances of underprediction, notably in the position of the stagnation point and central recirculation size. This underprediction is attributed to the impact of axial fuel momentum on velocity distribution, particularly near flashback conditions.

Despite these discrepancies, velocity distributions across the flame front align well with experimental data for both cases. While there are minor deviations in predicting reverse flow, overall correlation with experimental data is satisfactory. Differences between the two studied cases are observed, particularly in flame compactness and location of central recirculation, influenced by variations in equivalence ratio and axial momentum.

The study confirms the significance of axial momentum ratio in controlling flame dynamics and stabilization. The increase in axial momentum from the case at a lower equivalence ratio and low  $J$  to the case at a higher equivalence ratio and high  $J$  counteracts the gain in turbulent burning velocity, resulting in a downstream shift of the flame. This shift affects flashback resistance, consistent with experimental observations.

However, these findings did not consider heat loss effects, which were considered in subsequent research by Capurso et al. [111]: to account for the effect of heat transfer on flame stabilization and NOx formation, conjugate heat transfer (CHT) simulations are performed. Two operating conditions are investigated in this work: a non-reactive and a reactive stable point, the latter characterized by a global equivalence ratio of  $\phi_g = 0.6$ , which corresponds to a fuel/air momentum ratio  $J = 2.4$  and a thermal power output  $P_{th} = 105kW$ , while the non-reactive case has the same air mass flow rate  $\dot{m}_{air} = 50g/s$  but no fuel mass flow rate.

The results demonstrate good agreement between the numerical simulations and experimental data for the cold flow LES of a technically premixed burner: velocity profiles and RMS levels show consistency with experimental measurements, with slight discrepancies observed near the backplane, potentially attributed to experimental uncertainties.

The structure of recirculation zones and flow angle opening align well with experimental observations. The study highlights the importance of considering compressibility effects, particularly in the orifice region, where the flow is slightly below the transonic regime.

Mesh refinement is performed to accurately capture jet dynamics and pressure drop, with grid resolution impacting jet structure and equivalence ratio distribution. The LES predicts an air splitting rate through the orifice, consistent with previous calculations, suggesting a potential increase in flow rate due to fuel injection.

The study first evaluates the stable reactive case at a global equivalence ratio of 0.6, focusing on the mixing process and flame structure, particularly in relation to NOx formation. The mixing process analysis reveals the dynamics of fuel-air interaction, indicating radial stratification and the importance of grid refinement. The entrance of the combustion chamber shows some variability in equivalence ratio, underscoring the need for accurate modeling of air/fuel injection and mixing.

The study also investigates the impact of conjugate heat transfer (CHT) on flame stabilization and emissions. Comparison between adiabatic and LES-CHT simulations demonstrates significant heat losses



at the walls, influencing flame structure and pollutant formation. The LES-CHT approach improves agreement with experimental observations, showing reduced heat release rate near the backplane and lower NO<sub>x</sub> production, consistent with experimental measurements. Additionally, the study evaluates N<sub>2</sub>O formation, showing increased concentration near walls due to heat losses, with LES-CHT predicting a higher N<sub>2</sub>O emission index compared to adiabatic simulations.

Finally, it focuses on one of the main characteristics of hydrogen combustion: preferential diffusion. Due to hydrogen's lightweight nature, it diffuses faster than other species. Consequently, turbulent wrinkling can lead to fluctuations in the equivalence ratio on flame fronts, significantly affecting local flame temperature and, consequently, NO<sub>x</sub> production [112]. In lean hydrogen flames, such equivalence ratio fluctuations may eventually lead (or be supported) to intrinsic thermodiffusive instabilities.

Figure 3.18 illustrates instantaneous contours of the LES-CHT predicted Heat Release Rate (HRR) of the turbulent flame stabilized in the combustor.

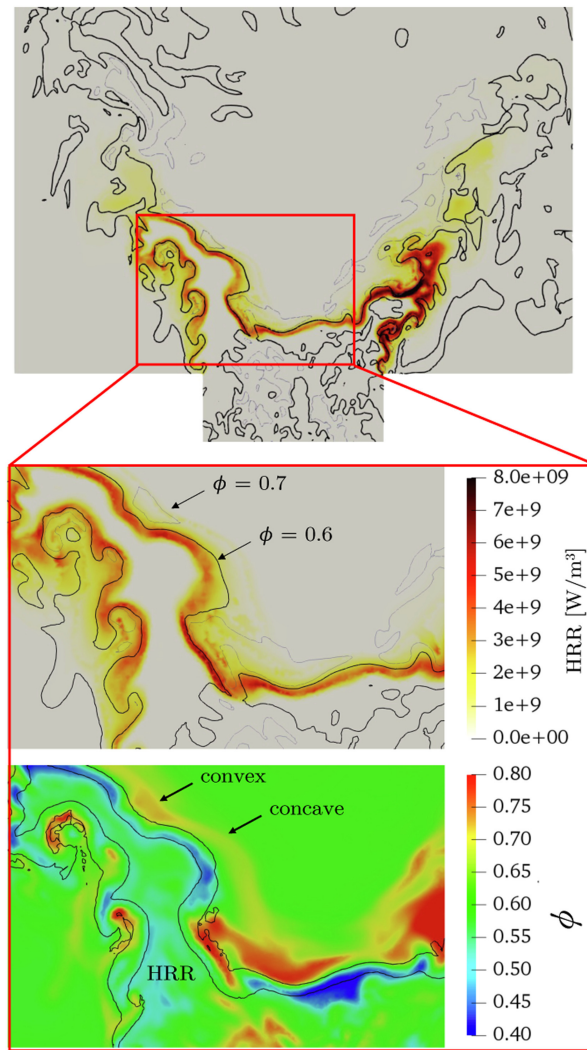


**Figure 3.18:** Instantaneous fields of HRR and equivalence ratio  $\phi$  in a vertical cut plane for the LES-CHT case, with an isocontour of HRR at  $2 \times 10^9 \text{ W/m}^3$ . Representation of the concave and convex parts around the flame front (defined with respect to the fresh gasses). From [111].

The black iso-contour at  $2 \times 10^9 \text{ W/m}^3$  is utilized to locate the flame front. Upon zooming into a portion of the flame front, it becomes apparent that, due to differential diffusion effects, light molecules

such as  $H_2$  and the radical  $H$  accumulate (or diffuse-out) in convex (or concave) curvatures, resulting in equivalence ratio variability, as depicted in Figure 3.18 (bottom).

The impact of these fluctuations on  $NO_x$  emissions is subsequently analyzed.  $NO$  production in hydrogen combustion involves three distinct pathways: thermal  $NO$ ,  $N_2O$ , and  $NNH$ . Instantaneous fields of radical  $O$ ,  $NO$ ,  $H$ , and temperature in a vertical cut plane close to the chamber inlet are shown in Figure 3.19.

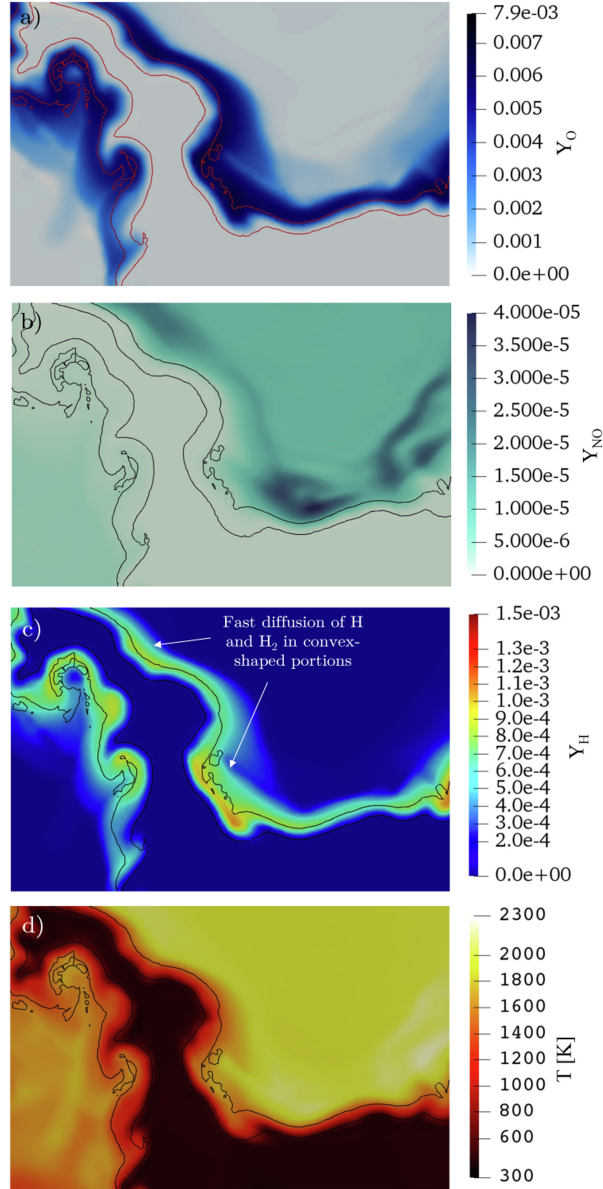


**Figure 3.19:** (a–d) Instantaneous fields of  $O$ ,  $NO$ ,  $H$  mass fractions and temperature in a vertical cut plane close to the chamber inlet for the LES-CHT case. Iso-contour of HRR at  $2 \times 10^9 W/m^3$  indicating the flame front (black/red lines). From [111].

Observing Figure 3.18 and Figure 3.19, several preliminary conclusions can be drawn. A higher concentration of  $H_2$  suggests a more intense release of energy and an increase in temperature, resulting in a larger thermal  $NO$  production compared to a flame front with uniform  $\phi$ . Moreover, the instantaneous distribution of radical  $O$  indicates peaks not only in the post-flame region but also near the flame front, contributing to both thermal  $NO$  and  $N_2O$  pathways.



Similarly, the analysis extends to the radical H, which is formed in the reacting zone. However, due to its lightweight, H accumulates in convex-shaped flame zones. H atoms contribute to the heat release rate through specific reactions, influencing NO production pathways.

From the study of this combustor, Mira et al. [109] warn about the correct identification of the actors behind the flame stabilization mechanism and flashback resistance, finding in the **Fuel/Air Axial Momentum Ratio** one of the most important features. This is a variable the authors chose as the combustor features an axial fuel injection. It will be interesting to transpose this concept in the TU Delft APPU combustor as in this last burner the fuel injection is perpendicular to the axial coordinate. The work of Capurso et al. [111], on the other hand, focuses more on the particular behaviours of H<sub>2</sub>, identifying thermodiffusive instabilities which lead to fluctuations of equivalence ratio  $\phi$  and subsequent larger NO<sub>x</sub> production.

### 3.2.5. TU Delft APPU Combustor

This combustor will be studied in this thesis: a description of the geometry, numerical and experimental methodologies will be provided in the next chapter.

One of the main numerical works conducted on this combustor is [113]: this study comprises non-reacting and reacting cases of a methane flame and a hydrogen-enriched methane flame, as in Table 3.3, using LES with thickened flame model and detailed chemistry.

Property	100% CH <sub>4</sub>	Blend CH <sub>4</sub> -H <sub>2</sub>
$\dot{m}_{air}$ [g/s]	5.061	5.061
$P$ [kW]	11	11
$AAI$ [%]	5	5
$T_{in}$ [K]	288	288
$p_{out}$ [Pa]	101325	101325
$Y_{CH_4}$ [–]	1.0	0.84
$Y_{H_2}$ [–]	0.0	0.16
$X_{CH_4}$ [–]	1.0	0.4
$X_{H_2}$ [–]	0.0	0.6
$\phi$ [–]	0.75	0.7
$\rho_{reac}$ [kg/m <sup>3</sup> ]	1.181	1.108
$\rho_{prod}$ [kg/m <sup>3</sup> ]	0.177	0.175
$T_{ad}$ [K]	1913	1892
$s_L^0$ [m/s]	0.21	0.34
$\delta_l^T$ [mm]	0.59	0.44

**Table 3.3:** Operating conditions and results from freely propagating flames computed from the solver CHEM1D [114] with the GRI3.0 chemical kinetics mechanism. From [113].

The methane-only case is simulated first and the results are compared with available PIV data. The predicted velocity field in the reacting case compares well with the experimental data in the region of the flame, while the results from the non-reacting case were found not to be directly comparable to those from the experiments due to some uncertainty in the boundary conditions.

The highest temperature is also lower in the hydrogen blend case, which is a consequence of the lower global equivalence ratio and this is consistent with a priori flamelet computations (see the resulting  $T_{ad}$  in Table 3.3). This is very beneficial in terms of emissions reduction, in particular NO<sub>x</sub> which is observed to decrease more than 70% in respect to the methane-only case, as shown in Table 3.4.

Species	100% CH4	Blend CH4-H2
$\langle \tilde{Y}_{CO_2} \rangle$	0.12	0.08
$\langle \tilde{Y}_{CO} \rangle$	2.21e-4	2.55e-5
$\langle \tilde{Y}_{NO} \rangle$	5.08e-5	1.41e-5
$\langle \tilde{Y}_{NO_2} \rangle$	7.62e-8	5.32e-8

**Table 3.4:** Section-averaged mean mass fractions of main emissions species and CO2 from LES at the combustor exit. From [113].

Nevertheless, the flame shifts significantly upstream in the case of the hydrogen blend and enters the mixing tube along with the recirculation bubble (most upstream part of the central recirculation zone).

The higher flame speed of the hydrogen blend (despite the lower equivalence ratio) and its higher resistance to lean extinction are found to only partly explain this upstream propagation. An analysis of equivalence ratio distribution in the mixing tube reveals in fact that mixing is mostly driven by turbulent and molecular diffusion and this leads to a richer mixture near the centreline in the region immediately upstream the combustor entrance in the case of the hydrogen blend, due to the stronger diffusivity of the latter. Although flashback was not observed in the present work, these variations of equivalence ratio could couple with heat release and the vorticity generated by the recirculation bubble to trigger combustion induced vortex breakdown, for which the use of axial air injection might become ineffective.

This work has been quite useful for the strategy planning employed to correctly capture the main features of these flames: one of the hint given in the paper was attributing the reason of the overestimation of axial velocity not only to the approaching flashback region in the experiment, but also to heat losses, as shown in [115], which were not taken into account in these simulations, which used a simple adiabatic wall assumption on the whole geometry.

A similar work has been conducted by Abbasciano in his MSc thesis at TU Delft: Large Eddy Simulations of a Lean Premixed Swirl-stabilized Combustor.

A peculiarity of this combustor is the difference in characteristic time between the swirler and the combustion chamber: to properly refine the mesh (using a static mesh refinement), smaller cell sizes are needed in the swirler. Consequently, in order to maintain the Courant-Friedrichs-Lewy (CFL) condition below the predetermined threshold, the time step must be limited.

Therefore, the approach followed in this simulation is the following: an initial simulation using only air has been performed, resolving the flow field in the swirler, and for the next simulations, involving changes in the fuel flow and in the simulation setup in general, an inflow turbulence generator is used in order to generate a flow field that has the same mean and variance as the extracted field.

First of all, the turbulence generator has been tuned, acting on the azimuthal velocity at the exit of the swirler, and the LES model with a 50% showed the highest level of agreement with the experimental PIV data, demonstrating a notable accuracy in its ability to forecast the flow field. Therefore, the adjustment of the azimuthal component of the velocity has been maintained in this study.

The following section investigates the influence of density fluctuations on swirling flow via non-reactive full methane LES. Initial analysis focuses on mass flow rate variations due to density changes. Comparative analysis with Particle Image Velocimetry (PIV) data shows discrepancies in axial velocity profiles, with LES indicating higher velocities, particularly in the core region. While LES accurately predicts the position of velocity peaks and central recirculation zone downstream, discrepancies arise in velocity magnitudes, especially at the chamber entrance.

The author lists possible causes for discrepancies:

- Inadequate representation of methane-air mixture, resulting in temperature oscillations, hence causing expansion and acceleration of the mixture
- Potential reduction in velocity peaks due to density augmentation - the density of air is specifically modified by a 4% increment using the inflow turbulence generator
- Discrepancies in mixture fraction gradient affecting mixing efficiency

The last section delves into the analysis of reactive full methane LES. Validation against PIV data involves comparing simulated flow fields. Preliminary NO emission analysis includes comparisons with experimental and tabulated data, and an alternative model incorporating additional transport equations for NO mass fraction and reaction rate.

Validation against PIV data reveals disparities in axial velocity profiles, with LES predicting higher velocities but failing to capture precise magnitudes inside the chamber. The observed residence time decreases compared to non-reactive simulations, favoring computational efficiency.

Despite accurately predicting peak axial velocity positions, LES fails to accurately estimate magnitudes inside the chamber.

Discrepancies between reactive and non-reactive simulations suggest complexities in chemistry-turbulence interactions. Thermal expansion, influenced by temperature field and mixture fraction distribution, affects combustion and flow field, potentially leading to relaminarization.

Neglecting heat losses in simulations may contribute to discrepancies such as higher predicted velocities and flame attachment to burner. Recommendations include implementing five-dimensional tabulations to account for heat losses, given that the combustion method consists in an adiabatic flamelet model with a presumed PDF.

Analysis of mixture fraction field could provide insights into mixing accuracy, which was thought to be a reason for the discrepancy in validation of the non-reactive methane case.

The reaction rate shows variations based on mixture concentration, leading to localized temperature elevations. No flashback occurrence is predicted, consistent with experimental observations under 0% axial air injection.

On the same combustor, experiments have been carried out in [116], focusing mainly on the effect of changes in geometry (the confinement ratio, the ratio between the cross-section area of the mixing tube - before the flame - and the cross-section area of the combustion chamber - after the flame) and Axial Air Injection (AAI) on the dynamics of the flow.

### 3.3. Knowledge Gap and Objectives of the Thesis

As the global push for cleaner and more efficient combustion technologies intensifies, researchers are increasingly focusing on hydrogen-enriched hydrocarbon fuels as promising alternatives. Within this context, the correct indication of thermal boundary conditions has emerged as a critical area of interest, particularly in swirl-stabilized combustion configurations with axial air injection.

Despite a growing body of literature on this topic, there remains a need for deeper exploration, especially concerning strain effects on hydrogen-enriched hydrocarbon flames, as reported in several research papers reviewed in this chapter, highlighting the significant influence of strain on the resistance to heat loss in combustion systems.

This influence, which can be either positive or negative depending on the Markstein number of the fuel, presents a complex yet pivotal aspect of combustion, both in its steady features and dynamics. However, there is still much to uncover regarding how strain interacts with thermal boundary conditions in hydrogen-enriched hydrocarbon flames, particularly within the particular configuration of swirl-stabilized combustors with axial air injection.

#### 3.3.1. Knowledge Gap

The knowledge gap can be condensed into four key questions, which, based on the comprehensive review of the current state of the art, remain still inadequately addressed by existing research:

**1. Are there low-cost, yet reasonably accurate methodologies for predicting wall temperature?**

This question underscores the multidisciplinary nature inherent to combustion studies, as it brings the solid domain into consideration. It also emphasizes the crucial need to develop solutions that reduce the computational burden associated with resolving the thermal boundary condition problem, increased when considering the difference in characteristic times of solid heating and flame quenching.

**2. How do thermal sinks impact a strained flame?**

This question can be already answered from 1D calculations, but given the complex interplay that thermal sinks, flames and wall-bounded turbulent flows have, it grows exponentially in complexity when applied to 3D simulations, which moreover could show transient behaviours, which are usually not taken into account in steady, more simple cases.

**3. What is the effect of hydrogen enrichment on these flames?**

The need to solve this gap introduces an additional layer of complexity to the study, building upon the previous two inquiries. It underscores the importance of understanding how changes in fuel composition, specifically through hydrogen enrichment, alter flame behaviour, mixing, temperature fields and emissions.

**4. Is Axial Air Injection a valid prevention method for flashback?**

This question addresses the evaluation of a specific flashback prevention strategy, particularly in a system, the TU Delft APPU combustor, where axial air injection is coupled with fuel injection in crossflow, unlike the TU Berlin AHEAD combustor. It raises the need to assess whether this method can effectively prevent flashback across varying operating conditions and with different fuel blends of hydrogen/methane. Understanding its efficacy is essential for developing a truly fuel-agnostic combustor, capable of maintaining stability and safety regardless of the fuel composition.

#### 3.3.2. Objectives of the Thesis

This thesis seeks to address these knowledge gaps by delving into the interplay between strain, thermal boundary conditions, and hydrogen-enriched hydrocarbon flames in the particular case of a swirl-stabilized combustor with axial air injection. Specifically, the study aims to leverage Large Eddy Sim-

ulations (LES) on the APPU combustor at TU Delft to explore these phenomena in detail. The objectives of the thesis are stated as follows:

**1. Evaluation of Heat Loss and Strain Effects on Flame Shape Prediction:**

In the context of ongoing simulations that have historically struggled to accurately predict flame shapes —such as the baseline operating condition described in the simulation matrix in subsection 4.5.2, where simulations have indicated an M-flame, while experiments have observed a V-flame— this study explores whether imposing non-adiabatic thermal boundary conditions could resolve these discrepancies, as it has in similar situations in the past.

In particular, this study employs and refines the use of Heat Resistance Tuning [100], incorporating additional features that aim to enhance its performance while maintaining low computational costs.

Additionally, this task involves a detailed examination of how the interaction between strain and heat dissipation influences flame stability, mixing efficiency, and overall combustion performance, considering both steady and unsteady scenarios.

**2. Investigation of the Advantages and Disadvantages of Axial Air Injection on Hydrogen-Enriched Methane Flames:**

One of the objectives of this thesis is to explore the advantages and limitations of using axial air injection in flames fueled by hydrogen-enriched methane. The study aims to evaluate how this technique influences flame stability, mixing, and emissions within this specific fuel mixture. Given that axial air injection is a crucial method for preventing flashback in highly hydrogen-enriched methane and hydrogen/air premixed flames, the research will also address the potential drawbacks of this approach. This assessment is particularly relevant in the context of the TU Delft APPU combustor, where fuel is injected in crossflow, adding an additional layer of complexity to the evaluation.

**3. Exploration of Hydrogen Addition Effects:** Investigate the influence of hydrogen addition on the combustion dynamics of methane flames within a swirl-stabilized combustor.

This involves scrutinizing alterations in flame morphology, temperature profiles, mixing performance, unsteady effects and emissions behaviour resulting from the introduction of hydrogen.

# Modeling and Methodology

Egli è scritto in lingua matematica, e i caratteri son triangoli, cerchi ed altre figure geometriche, senza i quali mezzi è impossibile a intenderne umanamente parola; senza questi è un aggirarsi vanamente per un oscuro labirinto.

---

Galileo Galilei

This chapter details the methods used to model the behaviours theorized in chapter 2, including descriptions of the turbulence, combustion, and heat transfer models applied in the simulations. The results of these simulations will be interpreted in chapter 5.

Additionally, the chapter outlines the geometry of the TU Delft APPU combustor and the simulation matrix explored in section 4.5. Then it lists preliminary 1D simulations designed to provide a clearer understanding of the interplay between heat losses, strain, and hydrogen enrichment in laminar methane flames. This approach is consistent with methods commonly found in the literature for non-adiabatic flamelets.

Special attention is given to the improvements made to the HRT approach for the temperature profile prediction, discussed in subsection 4.5.3. Finally, subsection 4.5.4 introduces Proper Orthogonal Decomposition (POD), a tool often used in similar transient simulations. In this context, POD is employed not only for its standard application in detecting the Precessing Vortex Core (PVC) through tangential velocity analysis but also to investigate the equivalence ratio and heat release rate (HRR), aiming to uncover any underlying correlations.

## 4.1. Discretization of the Transport Equations

The conservation equations for reacting flows, as discussed in section 2.1, cannot be solved analytically, requiring them to be discretized. The numerical methods used to solve fluid dynamics problems fall under the domain of Computational Fluid Dynamics (CFD). This thesis employs the commercial software CONVERGE CFD 3.1 [117], which utilizes a collocated finite volume approach to numerically solve these conservation equations. These equations, a set of nonlinear coupled second-order partial differential equations, are calculated and stored at the cell center. By applying the Gauss theorem, the software solves the integral form of the conservation equations rather than their differential form.

### 4.1.1. Iterative Algorithms

Understanding the sequence in which the transport equations are solved is crucial for correctly configuring simulation parameters. Figure 4.1 below provides a summary of the order in which CONVERGE solves these transport equations.

Iterative algorithms are used in CFD simulations because the equations governing fluid flow are nonlinear and coupled, making them challenging to solve directly. Iterative methods provide a way to approximate the solution by repeatedly refining estimates until they converge to an acceptable level of accuracy. This approach is particularly effective for large and complex problems, where direct solutions would be computationally infeasible or inefficient. By iteratively solving the equations, CFD simulations can handle the complexities of fluid dynamics, including turbulence, heat transfer, and chemical reactions, with greater flexibility and accuracy.

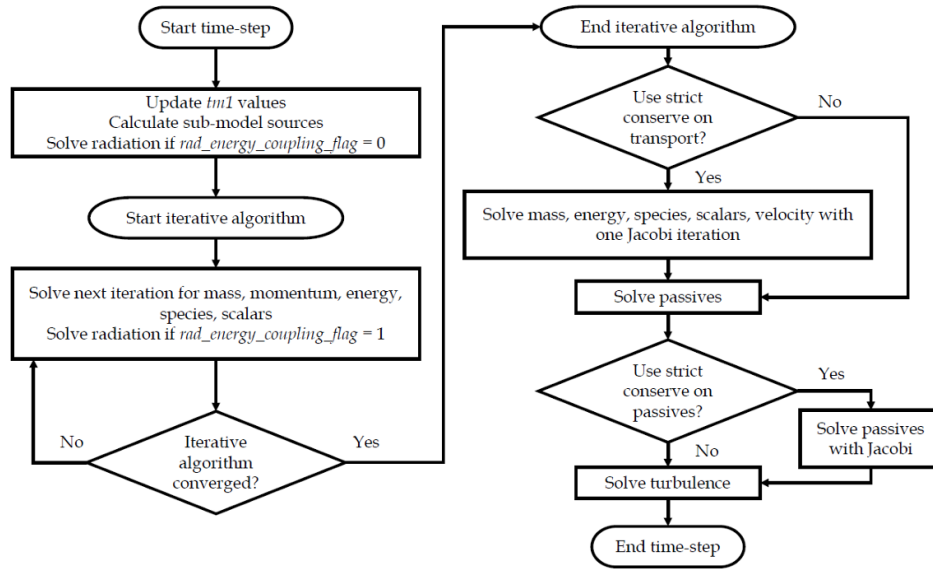


**Figure 4.1:** Solution order of the transport equations. In most cases, the turbulence equations are outside of the iterative algorithm loop for efficiency reasons.

At the start of each time-step, the previous values (the time-step minus 1 [ $tm1$  in Figure 4.1]) are stored for all transported quantities. Next, explicit sources are calculated for each submodel that is currently activated and radiation is solved if energy and radiation are decoupled. CONVERGE next enters an iterative algorithm to solve for mass, momentum, energy, species, and scalars. CONVERGE performs a tolerance check at the end of each iteration, and exits the iterative algorithm if the solution has converged to within tolerance, or if the maximum number of iterations is reached. After exiting the iterative algorithm, CONVERGE may perform an additional Jacobi iteration to enforce strict conservation. The Jacobi iteration guarantees that the quantity is conserved to machine zero, rather than to the tolerance set for the iterative algorithm. After the optional Jacobi iteration, CONVERGE solves the turbulence equations and ends the time-step.

CONVERGE offers two main iterative algorithms for the solution of mass, momentum, energy, species, and scalar transport: they are called PISO and SIMPLE. The algorithm that will be used in the simulations is the second one, which stands for modified Semi-Implicit Method for Pressure-Linked Equations (SIMPLE) method of Patankar [118]. The modified algorithm differs from the PISO algorithm (developed by Issa [119]) in that the momentum equation is solved within the iterative algorithm, rather than as a predictor step. At each iteration, SIMPLE solves the momentum equation, then a derived pressure equation. As with PISO, after the pressure solution is used to update the velocity, the other transport equations are solved in series.

The practical difference between SIMPLE and PISO is that SIMPLE more strongly couples the momentum equation with the rest of the transport equations. While this is more numerically expensive than the PISO approach, it is more robust in some flows, particularly those which may be locally dominated by

viscosity. The reason why SIMPLE was the algorithm of choice is the increased stability in transient in simulations with a large time-step, given the long characteristic times that the TU Delft APPU combustor requires.

Finally, the various models used to approximate physical behaviours are listed below:

- **Species diffusion:** A mixture-averaged diffusion coefficient is computed for each species (before the computation, storing them in a table for computational efficiency):

$$D_i = \frac{1 - X_i}{\sum_{j,j \neq i} \frac{X_j}{D_{ij}}} \quad (4.1)$$

With  $D_{ij}$  binary diffusion coefficient for species  $i$  and  $j$ , computed from the transport.dat file obtained from [120], using the method of Hirschfelder et al. [121]:

$$D_{ij} = \frac{3}{16} \frac{\sqrt{2\pi k_B^3 T^3 / m_{ij}}}{P\pi\sigma_{ij}^2\Omega^{(1,1*)}} \quad (4.2)$$

Where  $k_B$  is Boltzmann's constant,  $m_{ij}$  is the reduced molecular mass,  $\sigma_{ij}$  is the reduced collision diameter and  $\Omega^{(1,1*)}$  is the collision integral.

Apart from the molecular mass diffusion coefficient  $D_i$ , given that a turbulence model is present, there is the addition of the turbulent mass diffusion coefficient  $D_t = \frac{\nu_t}{Sc_t}$ , with  $Sc_t$  turbulent Schmidt number.

Finally, in order to ensure mass conservation, CONVERGE constrains the net diffusion flux to be 0 as described by Coffee and Heimerl<sup>1</sup> [122]

- **Turbulence:** subsection 4.2.1 is dedicated to describe turbulence modeling and the particular model used in this research.
- **Combustion:** section 4.3 reviews the basics of turbulent combustion modeling and subsection 4.3.1 describes the combustion model employed in this research.

## 4.2. Turbulence Modeling in Computational Fluid Dynamics

Turbulence in computational fluid dynamics can be modelled using three different approaches. Below is a brief summary of each one of them, with a more detailed discussion of the second method, Large Eddy Simulations (LES), which will be the focus used in this thesis:

1. **Reynolds Averaged Navier Stokes (RANS)** equations offer solutions for temporal means of all variables. These equations are derived by averaging the instantaneous balance equations, resulting in equations describing the temporal-averaged values based on Reynolds averaging. A thorough discussion on the principles of statistical averaging, and how temporal averaging can convert to statistical averaging through the ergodicity principle can be found in Appendix A of the book by Sagaut [123].  
To complete the RANS equations, closure rules are essential. These rules necessitate the use of a turbulence model to manage flow dynamics, closing the Reynolds stress tensor.
2. **Large Eddy Simulations (LES)** represent the intermediate level in simulating turbulent flows. In LES, the influence of the smallest turbulent scales is approximated through subgrid closure rules, while the larger turbulent scales are directly computed. The derivation of balance equations for LES involves filtering the instantaneous balance equations, akin to applying a low-pass filter, a process to be elaborated later in subsection 4.2.1.

<sup>1</sup>Precisely, this approach corresponds to Method III in [122]



3. **Direct Numerical Simulations (DNS)** constitute the highest tier of combustion simulations, representing the third level. DNS solves the complete instantaneous balance equations without employing any turbulence models, thus directly computing all turbulence scales and their influence on combustion. In DNS, temperature prediction mirrors experimental measurements obtained via high-resolution sensors.

As the cut-off length scale (the LES filter size) approaches zero, LES naturally converge towards DNS. In contrast, RANS simulations only model mean flow fields, without explicitly capturing turbulent motion.

#### 4.2.1. Large Eddy Simulations

In turbulent flows, big structures are typically governed by the system's geometry. Smaller scales, on the other hand, have more universal characteristics. In light of this, turbulence models might be more effective when they are only required to explain the smallest structures, while the large scale motions, much more energetic, are the most effective transporters of the conserved properties.

Therefore, it is necessary to separate scales by applying a scale high-pass (or frequency low-pass) filter to the exact solution, represented mathematically by a convolution product. The resolved part  $\tilde{\phi}(\vec{x}, t)$  of a space-time variable  $\phi(\vec{x}, t)$  is defined by the relation:

$$\tilde{\phi}(\vec{x}, t) = \int_{-\infty}^{+\infty} \int_{-\infty}^{+\infty} \phi(\vec{\xi}, t') G(\vec{x} - \vec{\xi}, t' - t) dt' d^3\xi \quad (4.3)$$

In which the convolution kernel  $G$  is characteristic of the filter used, which is associated with the cutoff scales in space and time,  $\bar{\Delta}$  and  $\bar{\tau}_c$ , respectively.

In order to be able to manipulate the Navier Stokes equations after applying a filter, it is required that the filter verify the three following properties:

1. **Conservation of constants**
2. **Linearity**: This property is automatically satisfied, as the product of convolution verifies it independently of the characteristics of the kernel  $G$
3. **Commutation with derivation**

The usual LES filters are, for a cutoff length  $\bar{\Delta}$ , in the monodimensional case:

- **Box or top-hat filter:**

$$G(x - \xi) = \begin{cases} \frac{1}{\bar{\Delta}} & \text{if } |x - \xi| \leq \frac{\bar{\Delta}}{2} \\ 0 & \text{otherwise.} \end{cases} \quad (4.4)$$

$$\hat{G}(k) = \frac{\sin(k\bar{\Delta}/2)}{k\bar{\Delta}/2} \quad (4.5)$$

- **Gaussian filter:**

$$G(x - \xi) = \left( \frac{\gamma}{\pi\bar{\Delta}^2} \right)^{1/2} e^{-\frac{\gamma|x-\xi|^2}{\bar{\Delta}^2}} \quad (4.6)$$

$$\hat{G}(k) = e^{\left( \frac{-\bar{\Delta}^2 k^2}{4\gamma} \right)} \quad (4.7)$$

In which  $\gamma$  is a constant generally taken to be equal to 6 [123].

- **Spectral or sharp cutoff filter:**

$$G(x - \xi) = \frac{\sin(\frac{\pi}{\bar{\Delta}}(x - \xi))}{\frac{\pi}{\bar{\Delta}}(x - \xi)} \quad (4.8)$$

$$\hat{G}(k) = \begin{cases} 1, & \text{if } |k| \leq \pi/\Delta \\ 0 & \text{otherwise.} \end{cases} \quad (4.9)$$

This filter preserves the length scales greater than the cut-off length scale  $2\Delta$  and suppresses all the length scales smaller than the cut-off length scale  $2\Delta$ .

**Favre Filtering** In reactive flows, because of the varying density due to the heat release, applying the filtering operator to the Navier-Stokes equations results in a further term to model,  $\overline{\rho' f'}$ . In order to avoid the modeling of this additional term, the mass-weighted Favre-filtering is used, resulting in:

$$\tilde{f}(\vec{x}) = \frac{\int \rho f(\vec{x}^*) F(\vec{x} - \vec{x}^*) d\vec{x}^*}{\bar{\rho}} \quad (4.10)$$

The balance equations for the filtered values can be derived from filtering the instantaneous balance equations. Any quantity may be decomposed into a filtered component  $\tilde{f}$ , which is resolved in the numerical simulation, and  $f' = f - \tilde{f}$ , corresponding to the unresolved part of the quantity  $f$  (i.e. the subgrid-scale part, due to the unresolved flow motions).

Finally, the derivation of balance equations for the filtered quantities  $\tilde{f}$  requires the exchange of filtering and differentiation operators. This exchange is theoretically valid only under restrictive assumptions and is wrong, for example, when the filter size varies.

Note that the mesh size is dependent on the spatial position, and the filter size is correlated to that size. In [124], this issue has been thoroughly examined. Nonetheless, in most simulations, the uncertainties brought on by this operator exchange are typically ignored and are presumed to be taken into account in subgrid-scale modeling.

**Filtered Equations** The Favre-filtered equations can be derived, as in [35], using the Favre-filter on Equation 2.2, Equation 2.3, Equation 2.4, Equation 2.5 and Equation 2.16:

**Mass**

$$\frac{\partial \bar{\rho}}{\partial t} + \vec{\nabla} \cdot (\bar{\rho} \vec{u}) = 0 \quad (4.11)$$

**Momentum**

$$\frac{\partial \bar{\rho} \vec{u}}{\partial t} + \vec{\nabla} \cdot (\bar{\rho} \vec{u} \vec{u}) + \vec{\nabla} \bar{p} - \vec{\nabla} \cdot (\bar{\tau} - \bar{\rho} (\vec{u} \vec{u} - \vec{u} \vec{u})) = 0 \quad (4.12)$$

**Species**

$$\frac{\partial \bar{\rho} \tilde{Y}_k}{\partial t} + \vec{\nabla} \cdot (\bar{\rho} \vec{u} \tilde{Y}_k) = \vec{\nabla} \cdot [\bar{\rho} \vec{V}_k Y_k - \bar{\rho} (\vec{u} \tilde{Y}_k - \tilde{u} Y_k)] + \bar{\omega}_k \quad (4.13)$$

**Sensible Enthalpy**

$$\frac{\partial \bar{\rho} \tilde{h}_s}{\partial t} + \vec{\nabla} \cdot (\bar{\rho} \vec{u} \tilde{h}_s) = - \sum_{k=1}^N h_{f,k}^0 \bar{\omega}_k + \vec{\nabla} \cdot [\bar{\lambda}_m \vec{\nabla} T - \bar{\rho} (\vec{u} \tilde{h}_s - \tilde{u} h_s)] - \vec{\nabla} \cdot \left( \bar{\rho} \sum_{k=1}^N \vec{V}_k Y_k h_k^s \right) \quad (4.14)$$

**Equation of State**

$$\bar{p} = \frac{\bar{\rho} R \tilde{T}}{\bar{W}} \quad (4.15)$$

In LES, operating the filtering leads to unclosed terms that need to be modeled. Closure models are proposed for the unknown quantities appearing in the filtered balance equations, such as:

- **Unresolved Reynolds stresses**  $\overline{u_i u_j - \tilde{u}_i \tilde{u}_j}$ .
- **Unresolved species fluxes**  $\overline{u_j Y_k - \tilde{u}_j \tilde{Y}_k}$
- **Enthalpy fluxes**  $\overline{u_j h_s - \tilde{u}_j \tilde{h}_s}$
- **Filtered species laminar diffusive fluxes**  $\overline{\rho \vec{V}_k Y_k}$
- **Enthalpy laminar diffusive fluxes**  $\overline{\rho \sum_{k=1}^N \vec{V}_k Y_k h_k^s}$
- **Laminar heat diffusion flux**  $\overline{\lambda_m \vec{\nabla} T}$
- **Filtered species chemical reaction rates**  $\overline{\dot{\omega}_k}$

### 4.2.2. Turbulence Modeling

The closure for the laminar diffusive fluxes in this work is done using the classical gradient assumption:

$$\overline{\rho \vec{V}_k Y_k} = -\bar{\rho} \bar{D}_k \vec{\nabla} \tilde{Y}_k \quad (4.16)$$

$$\overline{\lambda_m \vec{\nabla} T} = \bar{\lambda}_m \vec{\nabla} \tilde{T} \quad (4.17)$$

Hence the unresolved Reynolds stresses  $(\overline{u_i u_j - \tilde{u}_i \tilde{u}_j})$ , the unresolved species  $(\overline{u_j Y_k - \tilde{u}_j \tilde{Y}_k})$  and enthalpy fluxes  $(\overline{\rho \sum_{k=1}^N \vec{V}_k Y_k h_k^s})$ , and the filtered reaction rate  $\overline{\dot{\omega}_k}$  must now be modeled.

**Reynolds Stresses** The most popular models available on CONVERGE CFD for the Reynolds stresses are the following:

- The Smagorinsky model, which expresses unresolved momentum fluxes according to the Boussinesq assumption [125] - namely, momentum transfer caused by turbulent eddies can be modeled with an eddy viscosity, and therefore the Reynolds/sub-grid stress tensor,  $\tau_{ij}$ , is proportional to the trace-less mean strain rate tensor,  $S_{ij}^*$
- The Germano 'dynamic Smagorinsky' model, which estimates small-scale dissipation from the knowledge of the resolved eddies
- The one-equation model, where an additional transport equation is solved for sub-grid kinetic energy
- Two-equation models, where transport equations are solved for sub-grid kinetic energy and sub-grid dissipation

A detailed analysis of each one of the turbulence models can be found in [126], while in this chapter only the main elements of the turbulence model used for the simulations are described.

**Smagorinsky Model** The Smagorinsky model is a zero-equation LES turbulence model which relates the sub-grid viscosity to the magnitude of the strain rate tensor and cell size. The model for the sub-grid stress tensor is:

$$\tau_{ij} = -2\nu_t \bar{S}_{ij} \quad (4.18)$$

Where the subgrid viscosity,  $\nu_t$ , is defined as:

$$\nu_t = C_s^2 \Delta^2 \sqrt{S_{ij} S_{ij}} \quad (4.19)$$

Where  $C_s$  is an appropriately defined constant.

**Dynamic Smagorinsky Model** The problem with the Smagorinsky model, mentioned before, is that the appropriate value of the constant  $C_s$  is different in different flow regimes. The dynamic Smagorinsky model, which will be employed in the simulations shown in this thesis, provides a methodology for determining the local value of the Smagorinsky constant  $C_s$ , which now becomes time- and space-dependent:  $C_s(\vec{x}, t)$ .

The formulation of a dynamic model requires a second filtering operation designated as *test level filter*,  $\hat{\Delta}$ , which is usually twice the value of the grid filter  $\Delta$ .

The multiplicative Germano identity relates the grid level stress tensor and the test level stress tensor, which is defined as the Leonard stress term:

$$L_{ij} = T_{i,j} - \tau_{i,j} = \widehat{\widetilde{u_i u_j}} - \hat{u}_i \hat{u}_j - (\widetilde{\widehat{u_i u_j}} - \widetilde{\hat{u}_i \hat{u}_j}) \quad (4.20)$$

We then assume that the two subgrid tensors  $\tau$  and  $T$  can be modeled by the same constant  $C_s$  for both filtering levels. The use of the same subgrid model with the same constant is equivalent to a scale-invariance assumption on both the subgrid fluxes and the filter. This, mathematically, results in:

$$\tau_{ij} - \frac{1}{3} \tau_{kk} \delta_{ij} = C_s \beta_{ij} \quad (4.21)$$

$$T_{ij} - \frac{1}{3} T_{kk} \delta_{ij} = C_s \alpha_{ij} \quad (4.22)$$

Introducing these equations in the Germano identity, we obtain:

$$L_{ij} - \frac{1}{3} L_{kk} \delta_{ij} = C_s \alpha_{ij} - \widehat{C_s \beta_{ij}} \quad (4.23)$$

Considering that  $C_s$  is constant over an interval at least equal to the test filter cutoff length, it is possible to make the approximation:

$$\widehat{C_s \beta_{ij}} = C_s \widehat{\beta_{ij}} \quad (4.24)$$

And therefore  $C_s$  will be computed in such a way as to minimize the error committed, evaluated using the residual  $E_{ij}$ :

$$E_{ij} = L_{ij} - \frac{1}{3} L_{kk} \delta_{ij} - C_s \alpha_{ij} + C_s \widehat{\beta_{ij}} \quad (4.25)$$

Germano closes the problem by proposing to contract the last derived relation with the resolved strain rate tensor, meaning that the value sought for the constant is a solution of the problem:

$$\frac{\partial E_{ij} \widetilde{S_{ij}}}{\partial C_s} = 0 \quad (4.26)$$

And Lilly [127] further improves the problem well-posedness, remedying the problem of determination when  $\widetilde{S_{ij}}$  cancels out, proposing calculating the constant  $C_s$  by a least-squares method:

$$\frac{\partial E_{ij} E_{ij}}{\partial C_s} = 0 \quad (4.27)$$

**Unresolved Scalar Transport** LES unresolved scalar fluxes are often described using a gradient assumption:

$$\widetilde{u_j Y_k} - \widetilde{u_j} \widetilde{Y_k} = -\frac{\nu_t}{Sc_k} \frac{\partial \widetilde{Y_k}}{\partial x_i} \quad (4.28)$$

where  $Sc_k$  is a subgrid-scale Schmidt number. The subgrid-scale viscosity  $\nu_t$  is estimated from the unresolved Reynolds stresses models.

Since the majority of transport is addressed at large scales and only a portion needs to be represented, the gradient hypothesis in LES is effective in the majority of cases.

## 4.3. Turbulent Combustion Models

The main modeling challenges of turbulent reacting flows are:

- Turbulence itself is probably the most complex phenomenon in non-reacting fluid mechanics. Various time and length scales are involved and the structure and the description of turbulence remain open questions.
- Combustion, even without turbulence, is an intrinsically complex process involving a large range of chemical time and length scales. Some of the chemical phenomena controlling flames take place in short times over thin layers and are associated with very large mass fractions, temperature and density gradients. The full description of chemical mechanisms in laminar flames may require hundreds of species and thousands of reactions leading to considerable numerical difficulties.
- Turbulent combustion results from the two-way interaction of chemistry and turbulence. When a flame interacts with a turbulent flow, turbulence is modified by combustion because of the strong flow accelerations through the flame front induced by heat release, and because of the large changes in kinematic viscosity associated with temperature changes. This mechanism may generate turbulence, called “flame-generated turbulence” or damp it (relaminarization due to combustion). On the other hand, turbulence alters the flame structure, which may enhance the chemical reaction but also, in extreme cases, completely inhibit it, leading to flame quenching.

The only term that is left to close is the filtered species chemical reaction rates  $\overline{\dot{\omega}_k}$ . The most direct approach is to develop the chemical rate in Taylor series as a function of species mass fractions and temperature (which is actually a procedure of interest in supersonic reacting flows and atmospheric boundary layers where the temperature may be assumed to be constant). However, this analysis is limited by two main factors:

- The strong non-linearity of the Arrhenius form of the species chemical reaction rates makes it impossible to accurately reproduce the behaviour of the analytical form unless a computationally expensive number of terms is used in the Taylor expansion, making it necessary to introduce more closures for the new terms.
- This increased complexity has to be reproduced for each species, and the number of species in a detailed chemistry mechanism spans from 50 to 500.

So it is not possible to close the filtered species chemical reaction rates through analytical efforts. Therefore, modeling turbulent combustion interaction calls for the development of new tools that describe turbulent flames, providing an estimation of mean production rates of chemical species, based on known quantities or on quantities that may be easily modeled.

The basic ingredients to describe turbulent flames remain the quantities introduced for laminar flame analysis: the progress variable  $c$  for premixed combustion, introduced in section 2.2; the flame position would correspond to values of the progress variable  $c$  lying between 0 and 1.

There are three main approaches to the solution of this problem, which have been only cited here, but the reader can refer to the thorough review of Veynante and Vervisch in [36]:

1. **Turbulent mixing:** The burning rate may be quantified in terms of turbulent mixing. When the Damköhler number  $Da = \tau_t/\tau_c$  is large, the reaction rate is limited by turbulent mixing, described in terms of scalar dissipation rates.  
The small scale dissipation rate of species controls the mixing of the reactants and, accordingly, plays a dominant role in combustion modeling, even for finite rate chemistry
2. **Geometrical analysis:** The flame is described as a geometrical surface. This approach is usually linked to a flamelet assumption (the flame is thin compared to all flow scales).  
Following this view, two sub-approaches can be taken:

- (a) Scalar fields ( $c$ ) are studied in terms of dynamics and physical properties of **iso-value surfaces**, defined as flame surfaces.
  - (b) A **flame normal** analysis is derived by focusing the attention on the structure of the reacting flow along the normal to the above-mentioned flame surface
3. **Statistical analysis:** The statistical properties of scalar fields may be collected and analyzed for any location within the flow. Mean values and correlations are then extracted via the knowledge of a one-point probability density function (pdf), leading to the necessity of a submodel: **pdf modeling**

#### 4.3.1. TFM

The Thickened Flame Model has been selected for this thesis, and a brief description is detailed here. A challenging issue arises in large eddy simulations of premixed flames: the flame thickness ( $\delta_L^0$ ) is typically on the order of 0.1 mm, often smaller than the LES mesh size ( $\Delta_x$ ). The progress variable, denoted by  $c$ , representing the nondimensionalized fuel mass fraction or temperature, poses stiffness in computations as the flame front cannot be adequately resolved, leading to numerical instabilities. To address this challenge, three main approaches have been proposed:

- Simulation of an artificially thickened flame.
- Use of flame front tracking techniques (such as the G-equation).
- Deployment of a filter larger than the computational mesh size.

The concept behind the thickened flame (TF) approach involves considering a flame thicker than the actual one while maintaining the same laminar flame speeds, as shown by the pioneering work of O'Rourke and Bracco [128]. By simple theories of laminar premixed flames, the flame speed ( $s_L^0$ ) and thickness ( $\delta_L^0$ ) can be expressed as:

$$s_L^0 \propto \sqrt{D\bar{\omega}_c} \quad (4.29)$$

$$\delta_L^0 \propto \frac{D}{s_L^0} \quad (4.30)$$

Where  $D$  is the molecular diffusivity and  $\bar{\omega}_c$  is the mean reaction rate. Increasing the flame thickness by a factor  $F$  with a constant flame speed can be achieved by adjusting thermal and molecular diffusivities ( $a$  and  $D$ ) by  $Fa$  and  $FD$ , and the reaction rate ( $\bar{\omega}_c$ ) by  $\bar{\omega}_c/F$ . Typically, when  $F$  is sufficiently large (typically 5 to 30), the thickened flame front can be resolved on the LES computational mesh.

This approach offers several advantages:

1. Numerically, chemical reactions are described directly on the LES computational grid, with the actual flame replaced by a thicker laminar flame, eliminating the need for a subgrid scale model.
2. Utilizing an Arrhenius law accounts for various phenomena directly without relying on ad-hoc submodels.
3. Theoretically extendable to complex chemistry, although resolving all chemical species on the numerical grid may pose challenges.
4. However, comparisons between equations for steady-state laminar flames reveal modifications in response to unsteady phenomena and strain rates induced by velocity fields, which may be less significant for laminar flame elements but crucial for complex chemistry and high turbulence levels.

However, thickening the flame alters the interaction between turbulence and chemistry, decreasing the Damkohler number ( $Da$ ) to  $Da/F$ , which compares turbulent and chemical timescales. This alteration may necessitate adjustments, such as introducing a subgrid scale mixing and reaction model or

incorporating flame surface wrinkling descriptions to estimate subgrid scale turbulent flame speed.

Based on the previous work by Meneveau and Poinso [129], Colin et al. [130] derive an efficiency function to counteract the decrease in flame surface wrinkling observed with increasing  $F$ . This efficiency function, which depends on the characteristics of the laminar flame (such as speed and thickness) and the subgrid scale turbulence, as well as the flame thickening factor  $F$ , serves as a subgrid scale model. The efficiency function is developed from DNS of flame-vortex interactions and then it is implemented and validated on a LES of a Lateral Injection Combustor (LIC), for which experimental data are available and show noticeable agreement.

Another expression for the efficiency function can be found in the work of Charlette et al. [131] [132].

The model just described, developed by Colin et al. [130], presents a downside: it considers a constant thickening factor, which outside of the flame zones could result in a wrong overprediction of the diffusivity. This point is particularly important for gas turbine applications, for example, where pure mixing (without chemical reaction), premixed and non-premixed zones can coexist.

To overcome this difficulty, a local thickening factor  $F$  is active only in the vicinity of the flame front ( $F > 1$ ) and relaxes to  $F = 1$  (no effect) far away from the flame.

The decision on whether to thicken the flame or not is determined by a sensor, which can be of various forms (an example can be found in [133]). The one retrieved in [134] is based on an "Arrhenius-like" expression:

$$\Omega = Y_F^{\nu_F} Y_O^{\nu_O} \exp \left( -\Gamma \frac{T_a}{T} \right) \quad (4.31)$$

This sensor detects the presence of the reaction zone within a broader region due to the  $\Gamma$  parameter, which effectively lowers the activation temperature ( $\Gamma < 1$ ). Controlling the thickening coefficient  $F$  is achieved through:

$$F = 1 + (F_{max} - 1) \tanh \left( \beta \frac{\Omega}{\Omega_{max}} \right) \quad (4.32)$$

Here,  $\Omega_{max}$  represents the maximum value of  $\Omega$  (which can be analytically determined for a stoichiometric premixed flame) and is a parameter that governs the thickness of the transition layer between thickened and non-thickened zones.

Finally, CONVERGE enables the Thickened Flame (TF) model to be integrated with the Adaptive Mesh Refinement (AMR) strategy. This integration reduces the cell size where the flame sensor is active, thereby lowering the thickening factor. As a result, the need for an efficiency function is nearly eliminated, since the flame thickening is minimized, reducing its impact on the underestimation of flame surface wrinkling.

## 4.4. 1D Simulations: A framework for 3D interpretation

The cases outlined in Table 4.1 were analyzed using the 1D solver CHEM1D [114]. These 1D simulations spanned through relevant operating conditions for the application to the subsequent 3D simulations.

The CHEM1D solver is incorporated in a MATLAB script which first obtains the solution of a freely propagating flame for a given equivalence ratio and hydrogen volume fraction, then introduces strain through the use of a counterflow premixed flame (Reactant to Products - R2P, as described in Figure 4.2) and it further expands the study through the introduction of heat losses, reducing the temperature of the products from the adiabatic freely propagating flame temperature to a reduced temperature, following

the Heat Loss Parameter (HL) definition, adapted from [135]:

$$HL = \frac{T_p - T_u}{T_{ad} - T_u} \quad (4.33)$$

With:

- $T_p$ : Non adiabatic product temperature, employed in the counterflow R2P configuration
- $T_{ad}$ : Adiabatic product temperature, extracted from the freely propagating flame and employed in the counterflow R2P configuration
- $T_u$ : Unburnt reactants temperature, fixed at 300 K

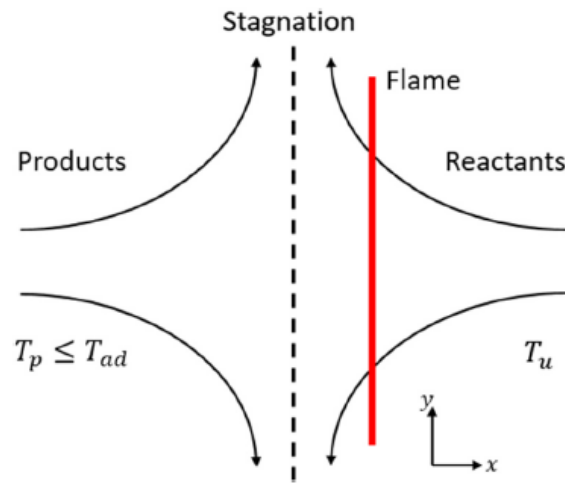


**Figure 4.2:** Reactants-to-products counterflow flame configuration, with temperature symbols annotation. Adapted from [135]

Quantity	Symbol	Range Explored
Equivalence Ratio	$\phi$	[0.4 0.6 0.8]
Hydrogen Volume Fraction	$H_2\%_{vol}$	[0.25 0.6]
Strain	$a$	[100, 200, 500, 1000, 2000, 5000, 10000, 20000, 50000, 100000]
Heat Loss Parameter	$HL$	[1.0, 0.9, 0.8, 0.7, 0.6]

**Table 4.1:** Range of operating conditions explored in CHEM1D simulations

These 1D simulations aim to describe the main characteristics of hydrogen/methane blends under strain/heat loss effects, providing in this way a framework for the analysis of the subsequent 3D simulations.

The quantities on which this study focuses are the heat release rate and the NO volumetric source, as well as the characteristic components of flame structure, such as speed and thickness.



## 4.5. 3D Simulations

The 3D simulations are conducted on the TU Delft APPU combustor, a swirl stabilized combustor that employs axial air injection to prevent flashback.

The geometry of the APPU combustor is detailed in subsection 4.5.1, providing the foundation for the analysis. This section also outlines the simulation matrix used to explore various operational scenarios, introduces the Heat Resistance Tuning approach to optimize thermal boundary condition prediction and describes the Proper Orthogonal Decomposition (POD) method to identify key flow structures and correlations within the combustion process.

### 4.5.1. Computational Domain

The fluid domain extracted from the combustor is displayed in Figure 4.3 and Figure 4.4. It presents a 90° periodic design, so only a profile view and a section are shown. There are three inlets: four ports for the fuel, four ports for the swirling air and a port for the axial air.

The swirler is designed to have a geometrical swirl number of 1.1 [116], and the fuel is then injected in crossflow. Special care has been introduced in handling the correct geometrical definition of the fuel ports, which present a quasi-elliptical geometry at the inlet, with short and long axis of 2.42mm and 3.18mm respectively, connected to a 2mm long cylinder with a diameter of 3.5mm.

The swirling and axial air flows enter the mixing tube of diameter  $D_{MT} = 0.024m$  and length  $L_{MT} = 0.060m$ , and the crossflow fuel injection is placed at 7.5mm from the mixing tube inlet. Then, after the mixing process takes place, the mixture enters the combustion chamber, which has a diameter of  $D_{chamber} = 0.148m$  and length  $L_{chamber} = 0.380m$ .

Finally, the flow exits the combustor where a constant pressure of  $p = 101325Pa$  is imposed.

The solid domain considered for the HRT procedure consists of three parts: the mixing tube and the plate, made in stainless steel AISI 316, and the quartz chamber glass. Relevant dimensions are shown in Figure 4.5.

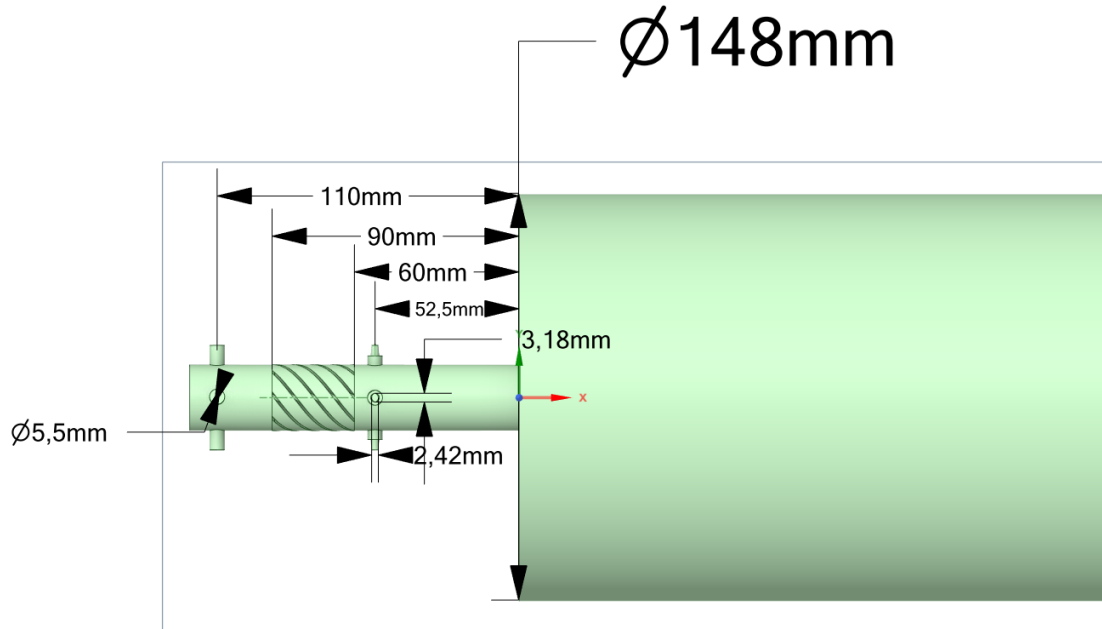


**Figure 4.3:** Fluid computational domain of the APPU combustor, with annotations on main dimensions. Given the long chamber, compared to the length of the prechamber (inlets, swirler and mixing tube), only the first 200 mm of chamber are shown.

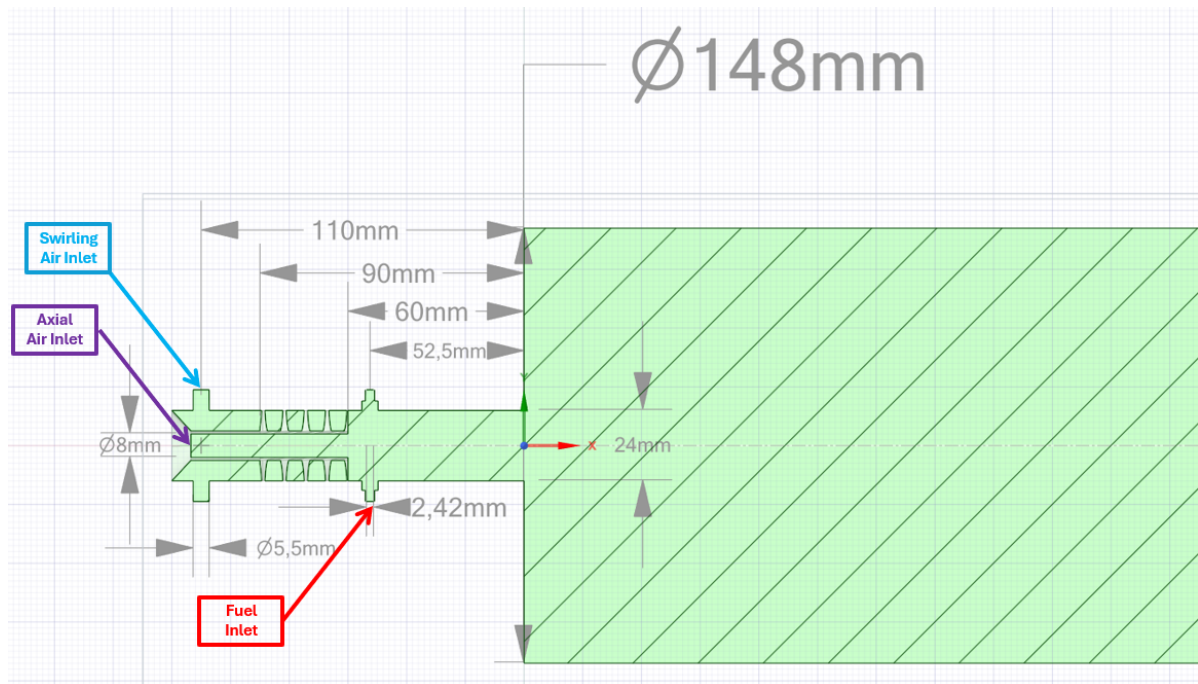


**Figure 4.4:** Section of the fluid computational domain of the APPU combustor. Inlets are highlighted, main dimensions are annotated.

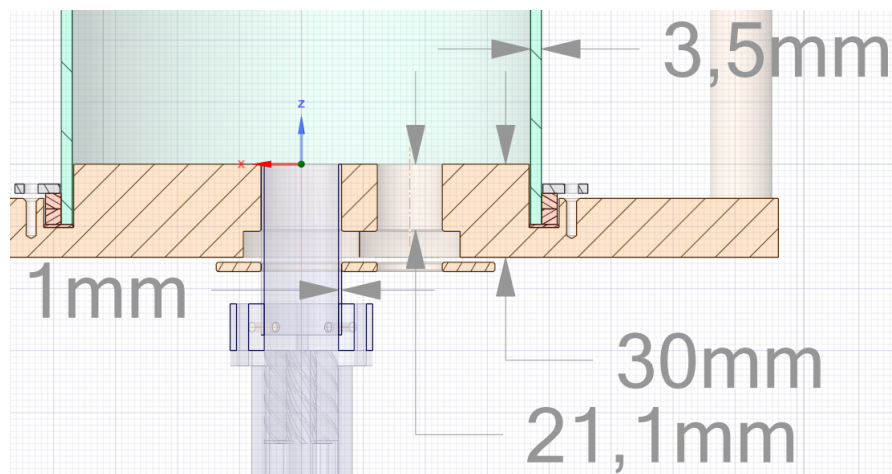


**Figure 4.5:** Detail of relevant solid domain of the APPU combustor, with annotations on main dimensions

#### 4.5.1.1. Mesh Characterization

The simulations for the TU Delft APPU combustor are performed with a mesh consisting of approximately 4 million cells. Due to the high computational cost associated with each simulation, a grid convergence study was only feasible between 2 million and 4 million cells. Further refinement was limited by the prohibitive simulation time required for larger meshes.

In the adaptive mesh refinement (AMR) strategy, the mesh is dynamically adjusted based on sub-grid scale values to ensure adequate resolution where needed. When a sub-grid scale value, such as velocity or temperature, exceeds a predefined threshold, the affected cell undergoes a process known as *embedding*. This process involves subdividing the cell into 8 smaller cells, each with half the side

length of the original. This refinement effectively reduces the subgrid scale values within the newly created smaller cells. The robustness of this strategy lies in its self-regulating nature; as the mesh is refined and cell sizes decrease, the subgrid scale values are inherently reduced, creating a negative feedback loop that prevents the mesh from continuously increasing in size. This ensures that the refinement process stabilizes and does not result in an unmanageable number of cells, maintaining computational efficiency while capturing critical details of the flow and combustion processes.

However, one disadvantage of this approach is that it is not coupled with the timestep that is currently being used, so it could result in the local increase in CFL number, affecting the stability of the solution.

The key details of this mesh are as follows: the maximum element size is  $\Delta x = 10$  mm, and the highest level of mesh refinement achievable is level 6, resulting in a minimum element size of  $dx = \frac{\Delta x}{2^6} = 0.15625$  mm. To put this in context, the laminar flame thickness used in the coupled TFM-AMR strategy is  $\delta_L^0 = 0.095187$  mm, which corresponds to a freely propagating laminar flame at the nominal equivalence ratio and fuel mixture.

Given that the minimum cell size is on the same order of magnitude as the predicted flame thickness, the mesh thickening will correspond to the intended number of grid points across the flame front—specifically, five points. This should result in an average thickening factor within this range, except for flame fronts with higher equivalence ratios, where the flame thickness is reduced and greater thickening may be required.

To assess the performance of the adaptive mesh refinement (AMR) strategy and the quality of the resulting mesh, several key metrics are presented:

#### Velocity Subgrid Scale:

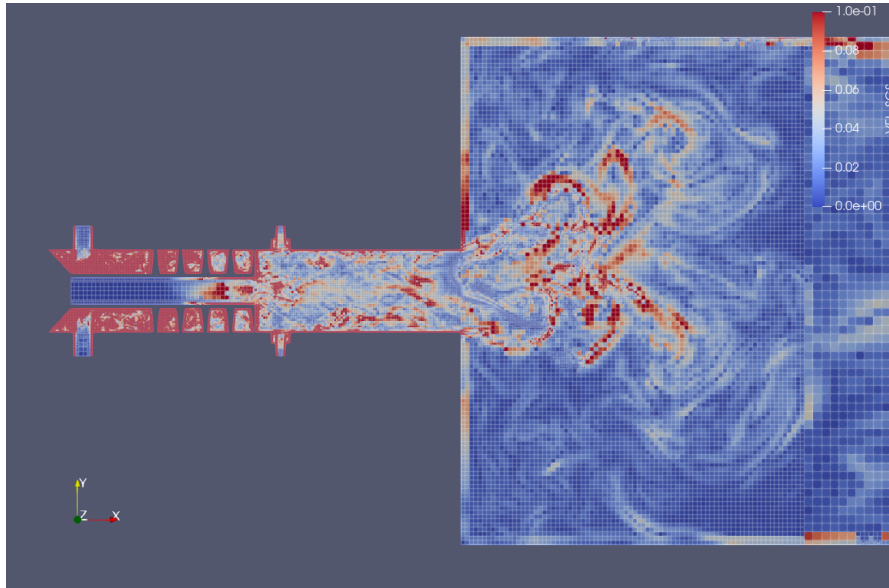


**Figure 4.6:** Visualization of the velocity subgrid scale across the computational domain. The upper limit of the contour values has been clipped to the threshold embedding value.

#### Normalized Subgrid Scale Velocity:

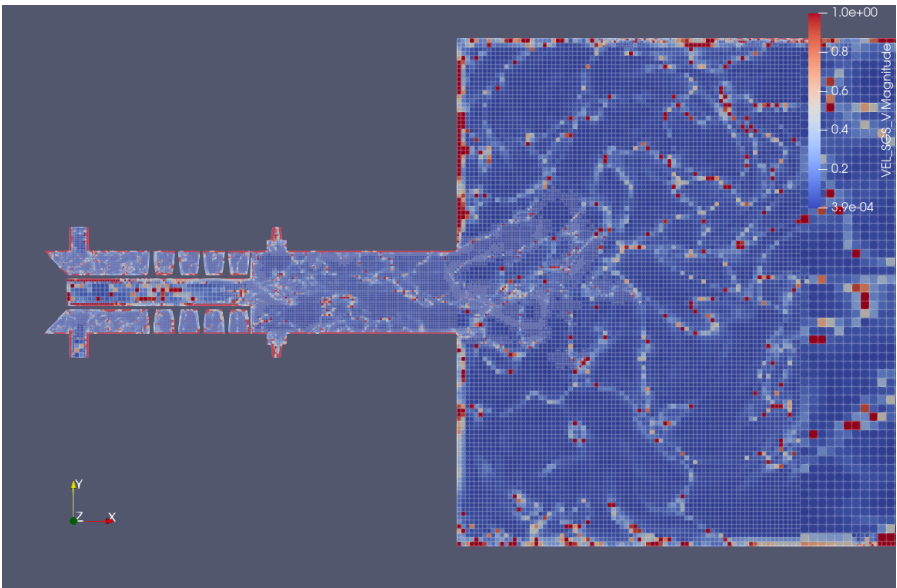


**Figure 4.7:** Ratio of the velocity subgrid scale to the velocity magnitude, providing a normalized view of the subgrid scale velocity across the domain.

**TFM Efficiency:**

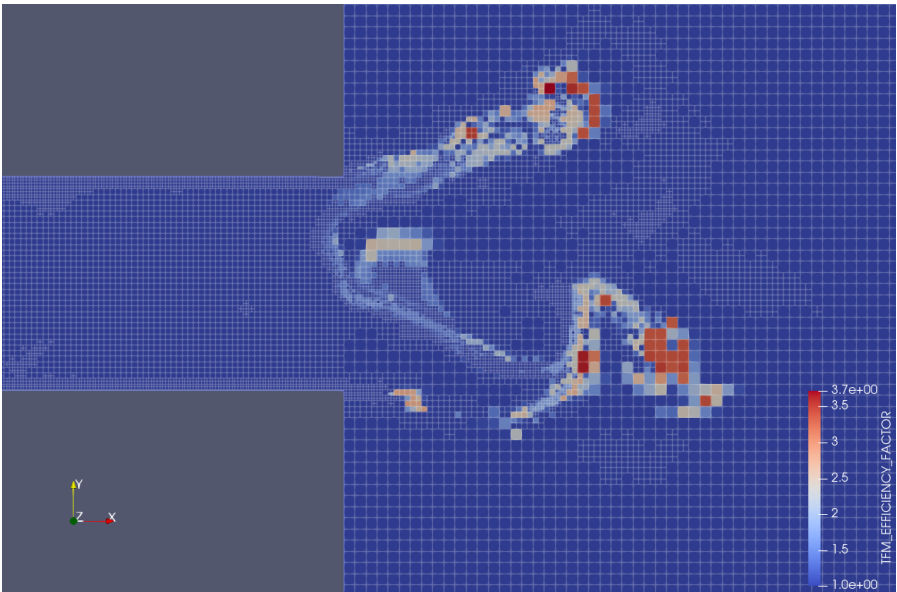


**Figure 4.8:** Illustration of the Thickened Flame Model (TFM) efficiency across the mesh.

**Thickening Factor:**

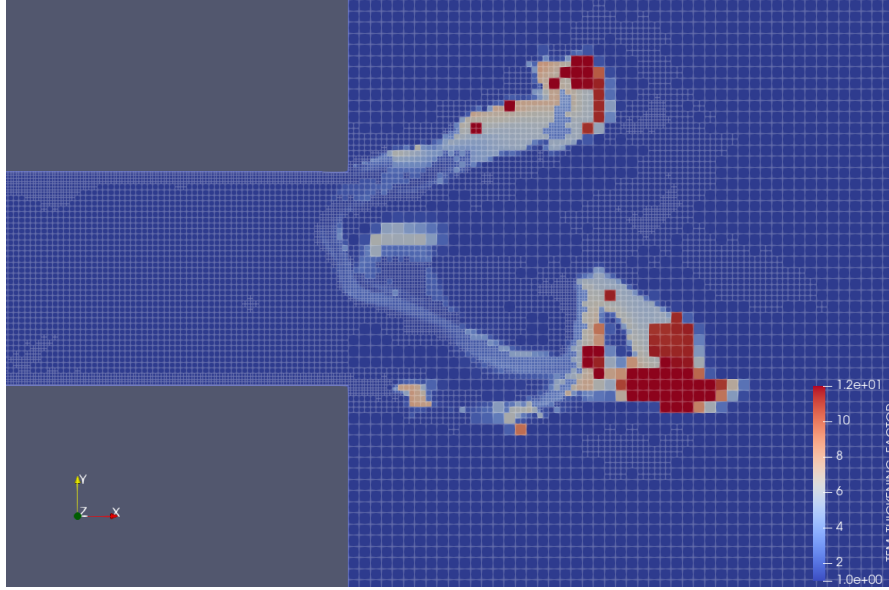


**Figure 4.9:** Depiction of the thickening factor throughout the computational domain.

The figures collectively illustrate the effectiveness of the adaptive mesh refinement strategy. Figure 4.6 shows how the mesh resolution is adjusted based on the velocity subgrid scale, highlighting areas where finer resolution is required. Figure 4.7 normalizes the subgrid scale velocity by the velocity magnitude, showing that, apart from a few outliers at zero velocity magnitude, the normalized subgrid scale values do not reach concerning levels.

Unfortunately, the significant differences in characteristic velocity, time scales, and dimensions between the swirler/mixing tube region and the combustion chamber necessitate finding a balance between these zones. It is essential to adaptively choose mesh size and timestep to manage the Courant-Friedrichs-Lewy (CFL) number and prevent excessively high values.

Figure 4.8 demonstrates the efficiency of the Thickened Flame Model (TFM) across the mesh, indicating how well the mesh captures the flame structure. Finally, Figure 4.9 depicts the thickening factor throughout the domain, revealing adjustments made to flame thickness and identifying areas requiring increased refinement. Together, these figures confirm that the AMR strategy effectively captures critical features of the combustion process while maintaining computational efficiency.

#### 4.5.2. Simulation Matrix

The baseline simulation contains 25% of H<sub>2</sub> and 75% of CH<sub>4</sub> in the fuel mixture, and it can be stabilized without the need for AAI at a thermal power of  $P = 11\text{ kW}$ . This operating point is called **S1**.

There are PIV and OH\* chemiluminescence images and thermocouple measurements for 4 points on the outside of the chamber and the plate, which will be presented in chapter 5, with a comparison with the results obtained with the simulations.

The same fuel mixture can also be studied with an AAI of 20 %, presenting the same diagnostic techniques, to explore the effect of AAI on a swirl-stabilized flame. This operating point is called **S2**.

Last but not least, the effect of hydrogen enrichment is studied progressing to the case with 60% of H<sub>2</sub> and 40% of CH<sub>4</sub> in the fuel mixture, which present a stable configuration only when an AAI of 20% is applied, maintaining the same thermal power and air mass flow rate. This operating point is called **S3**.

A summary of the different simulation setups is provided below in three tables. Each table presents specific aspects of the simulations for the TU Delft APPU combustor.

##### 1. Operating Conditions:



Table 4.2 summarizes the operating conditions and key parameters for the different simulation setups. It includes air and fuel mass flow rates, reactants temperature, operating pressure, and thermal power, among other parameters.

Quantity	Symbol	S1	S2	S3
AAI air mass flow rate	$\dot{m}_{air,AAI}$	0.0 kg/s		1.076e-03 kg/s
Swirling air mass flow rate	$\dot{m}_{air,sw}$	5.380e-03 kg/s		4.304e-03 kg/s
Reactants Temperature	$T_{air}, T_{fuel}$	283 K		
Operating Pressure	$p$	101325 Pa		
Air Density	$\rho_{air}$	1.248 kg/m <sup>3</sup>		
Thermal Power	$P$	11 kW		
Fuel mass flow rate	$\dot{m}_{fuel}$	2.082e-04 kg/s		1.797e-04 kg/s
Fuel Density	$\rho_{fuel}$	0.538 kg/m <sup>3</sup>		0.327 kg/s
H2 Volume Fraction	H2% <sub>vol</sub>	0.25		0.6
CH4 Volume Fraction	CH4% <sub>vol</sub>	0.75		0.4
H2 Power Fraction	H2% <sub>power</sub>	0.09		0.31
CH4 Power Fraction	CH4% <sub>power</sub>	0.91		0.69
H2 Mass Fraction	H2% <sub>mass</sub>	0.04		0.16
CH4 Mass Fraction	CH4% <sub>mass</sub>	0.96		0.84
Equivalence Ratio	$\phi$	0.694		0.667

**Table 4.2:** Operating conditions and key parameters for the simulation setups.

## 2. Bulk Velocities and Port Areas:

Table 4.3 provides estimates of bulk velocities at characteristic points within the APPU combustor, as well as the areas of various inlet ports. It includes fuel inlet velocities, swirling air velocities, and two different fuel/air momentum ratio definitions: the Momentum Flux Ratio defined by Reichel et al. in [136] follows the formula:

$$J = J_{MT} = \frac{\rho_{fuel} u_{inj,fuel}^2}{\rho_{air} u_{air,bulk}^2} \quad (4.34)$$

In this specific case, however, the fuel is injected into a crossflow and becomes entrained solely within the swirling flow, without interacting directly with the axial airflow. Additionally, the fuel injection ports are located just 5 mm from the swirler exit, meaning that the swirling airflow has not yet fully mixed.

Due to these factors, the Momentum Flux Ratio is redefined to account for the swirling air bulk velocity:

$$J_{sw} = \frac{\rho_{fuel} u_{inj,fuel}^2}{\rho_{air} u_{air,sw,bulk}^2} \quad (4.35)$$

For clarity, the Momentum Flux Ratio as computed in [136], is named  $J_{MT}$ , while the modified definition is named  $J_{sw}$ .

Quantity	Symbol	S1	S2	S3
Fuel Inlet Ports Area	$A_{fuel}$	1.963e-05 m <sup>2</sup>		
Fuel Inlet Velocity	$u_{fuel}$	19.696 m/s		27.964 m/s
Swirling Air Inlet Ports Area	$A_{air,sw}$	9.503e-05 m <sup>2</sup>		
Swirling Air Inlet Velocity	$u_{air,sw}$	45.377 m/s	36.301 m/s	
Axial Air Inlet Port Area	$A_{air,AAI}$	5.026e-05 m <sup>2</sup>		
Axial Air Inlet Velocity	$u_{air,AAI}$	0.0 m/s	17.158 m/s	
Mixing Tube Area	$A_{MT}$	4.524e-04 m <sup>2</sup>		
Swirling Air Bulk Velocity - Mixing Tube	$u_{air,MT,bulk}$	9.532 m/s		
Swirling Air Vanes Area	$A_{air,sw,vanes}$	4.021e-04 m <sup>2</sup>		
Swirling Air Bulk Velocity - Swirler Vanes	$u_{air,sw,bulk}$	10.724 m/s	8.579 m/s	
Momentum Ratio - Mixing Tube	$J_{MT}$	1.842		2.257
Momentum Ratio - Swirler	$J_{sw}$	1.455	2.274	2.787
Reactants Mixture Density	$\rho_{reac}$	1.185 kg/m <sup>3</sup>		1.139 kg/m <sup>3</sup>
Reactants Bulk velocity - Mixing Tube	$u_{reac,MT}$	10.428 m/s		10.788 m/s
Chamber cross section	$A_{chamber}$	1.720e-02 m <sup>2</sup>		
Reactants Bulk velocity - Chamber	$u_{reac,chamber}$	0.274 m/s		0.284 m/s

**Table 4.3:** Estimation of bulk velocity at characteristic points of the APPU combustor.

### 3. Flame Properties:

Table 4.4 lists computed properties from preliminary 1D freely propagating flames. This includes laminar flame speed, laminar flame thickness, and adiabatic flame temperature for different simulation setups.

Quantity	Symbol	S1	S2	S3
Laminar Flame Speed	$s_L^0$	0.226 m/s	0.277 m/s	
Laminar Flame Thickness	$\delta_T$	6.83e-04 m	5.91e-04 m	
Adiabatic Flame Temperature	$T_{ad}$	1813.37 K	1771.67 K	

**Table 4.4:** Computed properties from preliminary 1D freely propagating flames.

#### 4.5.3. Heat Resistance Tuning

In this study a different approach to Heat Resistance Tuning is proposed, starting from the concept developed by Agostinelli in [100]: in the cited PhD thesis, in fact, experimental measures were already present, so the Heat Resistances, conceived as global variables, were tuned iteratively to match the experimental temperatures.

This study tries to improve the HRT approach through these two additions:

1. **Local expression of the thermal resistances:** The PRECCINSTA combustor presented a quite compact design, with the size of the flame spanning from the centerbody until the chamber walls, meaning that it is reasonable to assume constant thermal resistance throughout the plate and the quartz, as the thermal load was distributed more homogeneously compared to the TU Delft combustor, where the confinement ratio (the ratio between chamber and mixing tube) is particularly big ( $CR = \frac{A_{chamber}}{A_{MT}} = \frac{0.0172m^2}{0.000452m^2} = 38.05$ ) and the chamber is particularly long ( $L = 0.38m$ ), with a flame that is close to the plate and it does not reach the chamber walls, except for the stagnation point of hot products, requiring a more *local* definition of the thermal resistances.

2. **Avoided reliance on experimental measurements:** Instead of relying on experimental measurements, as sometimes they are difficult to retrieve, through the iterative change of thermal resistance boundary condition profiles, it is theorized that the solid thermal boundary condition could converge to a profile that respects the energy equation in the interfaces fluid-wall and wall-laboratory.

Subsequently, these results have been checked with the use of thermocouple measurements.

The HRT approach primarily relies on simplifying the multidimensional solid heat transfer problem into a 1D model, with the upside of easy implementation of more heat transfer models, such as natural/-forced convection and radiation.

The 1D heat transfer assumption is valid for materials with a dominant direction of heat transfer, such as quartz, which has low thermal conductivity and therefore minimal multidimensional conductive heat transfer, but a - relatively - strong convective/radiative heat transfer in the outward direction.

However, this assumption does not hold for the metal plate and mixing tube, as the high conductivity of steel results in significant perpendicular heat transfer, invalidating the 1D model. Nonetheless, the typical behavior of plates with high Biot numbers offers an advantage: the high conductivity makes the isothermal boundary condition a reasonable approximation when thermal steady state has been reached.

#### 4.5.3.1.HRT: Workflow

First of all, it is necessary to point out that some heat transfer resistances are neglected, as they are considered to be poorly contributing to the heat transfer balance:

- The radiative heat transfer (RHT) from the gases is neglected for two reasons: from first principles, following the work of Liu et al. [137], these operating conditions and the main species involved do not require a thorough evaluation of the RHT effects. Secondly, in studies that present a similar operating condition [100], the scarce presence of soot and radiative heat transfer was poorly contributing to the overall energy balance.
- The convective heat transfer from the fluid to the wall is not considered, as it is resolved in the computational fluid domain.
- The radiative heat transfer from the quartz inside wall is not considered, as it would require a computationally expensive coupling with the fluid solver, deemed not worth for the task.

The Heat Resistances are therefore placed on the quartz glass as depicted in Figure 4.10:

- **Conductive Heat Transfer Resistance ( $R_{cond}$ ):** This resistance connects the inner wall temperature  $T_{i,w}$  to the outer wall temperature  $T_{o,w}$ .

As the work by Sergeev et al. [138] shows, the thermal conductivity of quartz glass spans from a value of  $\lambda_{quartz} = 1.30W/(m \cdot K)$  at  $T = 300K$  to a value of  $\lambda_{quartz} = 1.80W/(m \cdot K)$  at  $T = 800K$ .

Using the average between the inner wall temperature and the outer wall temperature as reference temperature, it is possible to consider the quartz glass as a cylindrical shell, with a thermal resistance given by:

$$R_{cond} = \frac{\ln\left(\frac{r_{o,w}}{r_{i,w}}\right)}{2\pi\lambda_{quartz}(T)dx} \quad (4.36)$$

With  $r_{o,w}$  and  $r_{i,w}$  the outer and inner wall radius, respectively, and  $dx$  as the axial length of the section of quartz glass considered.

- **Convective Heat Transfer Resistance ( $R_{conv}$ ):** This resistance connects the outer wall temperature  $T_{o,w}$  with the ambient temperature of the lab  $T_{amb}$ .



The convective heat transfer type is natural, and it has been chosen to use a correlation retrieved in [139]:

$$\text{Nu} = \begin{cases} 0.68 + 0.67 \cdot (\text{Ra} \cdot \psi)^{\frac{1}{4}}, & \text{if } \text{Ra} \leq 10^9 \\ 0.68 + 0.67 \cdot (\text{Ra} \cdot \psi)^{\frac{1}{4}} \cdot (1 + 1.6 \times 10^{-8} \cdot \text{Ra} \cdot \psi)^{\frac{1}{12}}, & \text{if } \text{Ra} > 10^9 \end{cases}$$

From which the convective heat resistance is derived:

$$h = \frac{k_{\text{air}}(T_{\text{film}}) \cdot \text{Nu}}{x} \quad (4.37)$$

$$R_{\text{conv}} = \frac{1}{h} \cdot A_{\text{QW}} \quad (4.38)$$

With:

- $\text{Ra} = \frac{T_{o,w} - T_{\text{amb}}}{T_{\text{film}}} \cdot 9.81 \cdot \text{Pr} \cdot x^3 / \nu^2(T_{\text{film}})$
  - $\psi = \left(1 + \left(\frac{0.492}{\text{Pr}}\right)^{\frac{9}{16}}\right)^{-\frac{16}{9}}$
  - $T_{\text{film}} = \frac{T_{o,w} + T_{i,w}}{2}$
  - $\text{Pr} = 0.71$ : Prandtl number of air, considered constant
  - $\nu(T)$ : Kinematic viscosity of air, computed through a look-up table as described in [140]
  - $x$ : Axial position of the section of quartz glass considered
- **Radiative Heat Transfer Resistance ( $R_{\text{rad}}$ ):** This resistance connects the outer wall temperature  $T_{o,w}$  with the ambient temperature of the lab  $T_{\text{amb}}$ , following a grey body approach and using a view factor of 1 between the quartz glass and the surrounding environment at  $T_{\text{amb}}$ :

$$R_{\text{rad}} = \frac{T_{o,w} - T_{\text{amb}}}{A_{\text{QW}} \cdot \epsilon_{\text{QW}} \cdot \sigma \cdot (T_{o,w}^4 - T_{\text{amb}}^4)} \quad (4.39)$$

With  $\epsilon_{\text{QW}} = 0.8$  and the Stefan-Boltzmann constant  $\sigma = 5.67e - 8 \text{ W}/(\text{m}^2 \text{K}^4)$

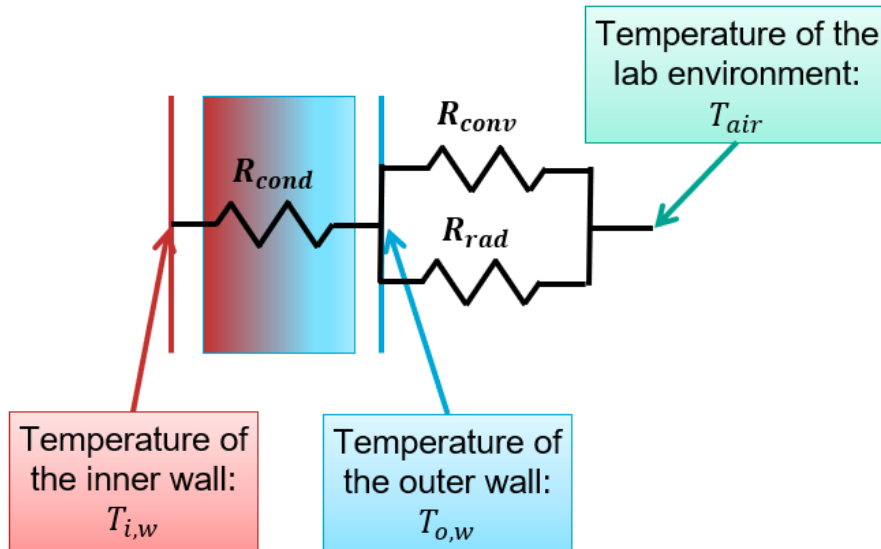


Figure 4.10: Heat Resistance Circuit

This means that the resulting thermal circuit consists of an equivalent thermal resistance, given by:

$$R_{eq} = R_{cond} + \frac{1}{\frac{1}{R_{conv}} + \frac{1}{R_{rad}}} \quad (4.40)$$

However, the computation of the values of the single thermal resistances is not so straightforward, as they depend on the wall temperatures.

Therefore, the workflow of the newly developed HRT routine is described as follows:

1. Initially, the simulation starts from a developed RANS non-reactive solution, with adiabatic thermal boundary conditions.
2. Then, the following step consists of imposing an isothermal boundary condition of  $T = 500K$  on the relevant walls, and igniting the mixture.
3. Once the pseudotransient is absent, the converged inner wall temperatures are used for the computation of the heat resistance profiles
4. Then the computed heat resistance profiles are imposed to the simulation, with a damping coefficient to avoid strong oscillations and speed up the convergence
5. In the following step, after waiting for the stabilization of the temperature field, we go back to step 3. and when a sufficiently reasonable convergence is reached on the maximum error of inner wall temperature, the loop is exited.

The described workflow iterates on profiles of  $T_{i,w}$ , but there is also a hidden inner loop that is entered in step 3: while  $T_{i,w}$  is known,  $T_{o,w}$  is not. However, through a simple fixed point iteration, it is possible to retrieve the value of  $T_{o,w}$  that satisfies the energy balance within the solid-lab control volume.

#### 4.5.4. POD

One aspect of swirl-stabilized flows is its presence of coherent structures, such as the PVC, as explored in section 2.7.

In order to explore this feature of the flame, it is possible to describe with a limited number of deterministic functions - the POD modes - the elusive coherent structures that populate turbulent flows but yet are surprisingly difficult to define and observe.

POD stands for **Proper Orthogonal Decomposition**, and it aims to decompose a random vector field  $\vec{u}'(\vec{x}, t)$  into a set of deterministic spatial functions  $\vec{\Phi}_k(\vec{x})$  modulated by corresponding time coefficients  $a_k(t)$ :

$$\vec{u}'(\vec{x}, t) = \sum_k^{+\infty} a_k(t) \vec{\Phi}_k(\vec{x}) \quad (4.41)$$

The decomposition is **Proper** in the sense that it allows to minimize the number of the first  $n$  spatial modes, maximizing the kinetic energy that can be captured by these spatial modes.

Finally, it is **Orthogonal** because the modes are orthonormal, implying that the  $k - th$  time coefficient only affects and depends on the corresponding  $k - th$  mode.

While regions of high correlation can indeed indicate the presence of coherent structures—especially when the associated energy is significantly greater than that of other modes—many POD modes are required to fully reconstruct the flow when multiplied by their respective time coefficients. The turbulent nature of most practical flows means that these zones of correlation often appear randomly, indicating that some modes are simply manifestations of turbulence's inherent randomness.

Despite these limitations, POD is a valuable tool for reconstructing flow fields using only a few of the

most energetic modes, enabling the identification of patterns that might be obscured in the raw data. This observation is significant for two reasons: first, because this motion is not easily discernible in the original data, due to the superimposed turbulence at various scales; and second, because this mode is associated with a substantial portion of the TKE (Turbulent Kinetic Energy), indicating its practical importance in the flow's dynamics.

The relevance in diagnostics of vortical structures is displayed in an example found in [141], where a Von Karman Vortex Street is extracted from raw data, using the first two modes of the POD: mode 2 closely resembles mode 1, differing primarily by a spatial translation of about a quarter wavelength. These coefficients are nearly sinusoidal (showing a clear peak in their FFT) and offset by a quarter period. Consequently, when the first two spatial modes are combined with their respective time coefficients, they replicate the alternating and translating nature of the wake vortices.

In this cylinder case, the first two modes, which account for over 90% of the TKE, suffice to accurately reconstruct the original flow. Here, a low-order model comprising just these two modes is a good approximation of the flow. However, this case might be considered overly simple, as the coherent vortices are readily apparent in the original snapshots, hence the sufficiency of only two modes to capture the flow's essential features. In more complex turbulent flows, like the ones that will be analyzed in this thesis, many modes are typically needed to account for 90% of the TKE, making their interpretation less straightforward. Nevertheless, the logic applied to the cylinder case can be extended, as the higher energetic modes correspond often to coherent structures that need to be unravelled from raw data.

In general, interpreting POD modes is easier when a few modes account for a large portion of the TKE. This is analogous to identifying peaks in a Fourier power spectrum, though with the distinction that the POD spectrum is inherently decreasing, and the dominant modes are the first ones by design. Nonetheless, one should approach the physical interpretation of these modes with caution, recognizing that they are mathematical constructs representing spatial zones of correlation, so coherent turbulent structures indeed show corresponding higher energetic modes, but it is not possible to always affirm the opposite.

Moreover, the location where the POD is also deemed of importance, as the storage of data is quite computationally intense and it is necessary to predict where the main coherent structures will be beforehand.

For this case, it has been chosen to use two slices of the mixing tube, one at  $x = -0.03m$  and one at  $x = 0.0m$ , normal to the  $x$  axis, and two slices at  $z = 0m$ , normal to the  $z$  axis, one in the mixing tube and one in the chamber, all of them with a grid size of  $dx = 0.5$  mm.

Finally, it is important to note that POD is not limited to velocity fields. In some cases, other variables, such as the vorticity field or the grayscale level of Schlieren images, might better represent the data or be easier to acquire. The algorithms discussed above can be directly applied once a suitable snapshot matrix is constructed. In fact, in this thesis, POD will be applied also to equivalence ratio and heat release rate, in order to check for the existence of correlations between velocity field, coherent structures, mixing and flame.

# 5

## Results

It does not make any difference how beautiful your guess is, how smart you are, who made the guess, or what his name is – if it disagrees with experiments it is wrong. That's all there's to it.

---

*Richard Feynman*

In this chapter, the 1D simulations are discussed, as they will be the basic knowledge on which the 3D simulation results will be interpreted. Next, the HRT results will be compared with the thermocouple measurements to verify the accuracy and validity of the HRT approach.

Finally, the results of the three 3D simulations will be analyzed and compared with the corresponding experimental results. Comparison will be carried out also among the simulations, to investigate on AAI and H<sub>2</sub> enrichment effects.

### 5.1. 1D Simulations

Simulating the range of variables described in Table 4.1, the figures of merit analyzed are:

- **Heat Release Rate:** This variable displays the activity of the flame, and it goes to 0 when the flame is extinguished, due to aerodynamic/thermal quenching.
- **NO Source Term:** This variable shows the NO production, which is the main remaining emission when switching to increasing H<sub>2</sub> content in the fuel mixture.

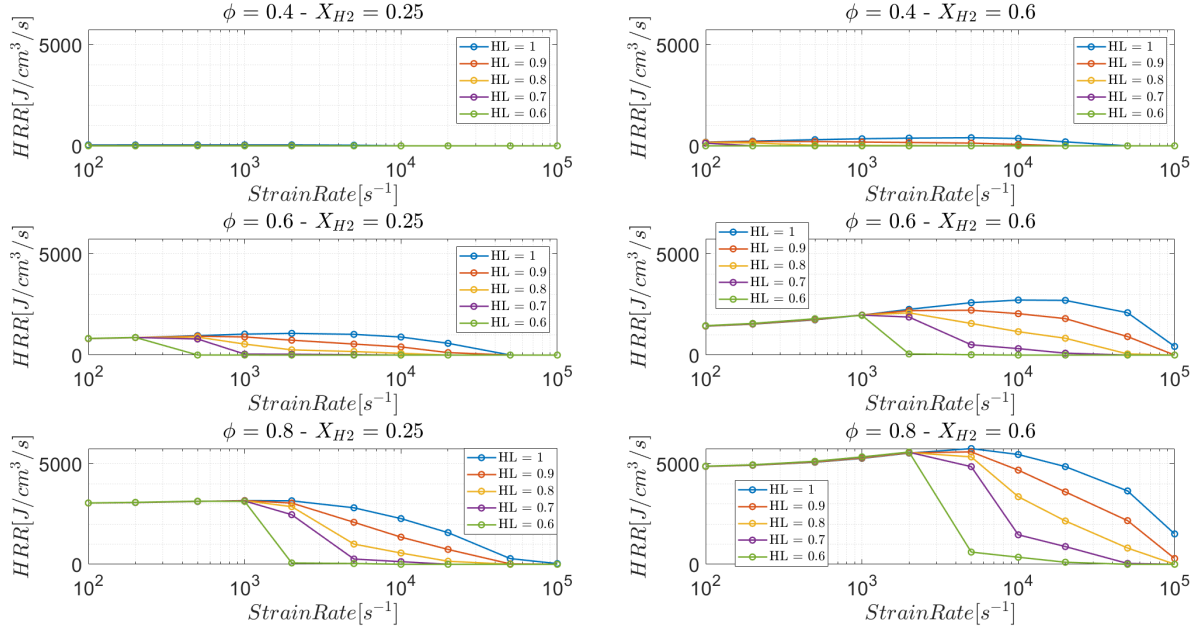


**Figure 5.1:** Peak Heat Release Rate in counterflow premixed R2P CHEM1D simulations across various levels of Heat Loss parameters (HL = 1 corresponds to the adiabatic case). The rows represent increasing equivalence ratios, while the columns show increasing hydrogen enrichment.

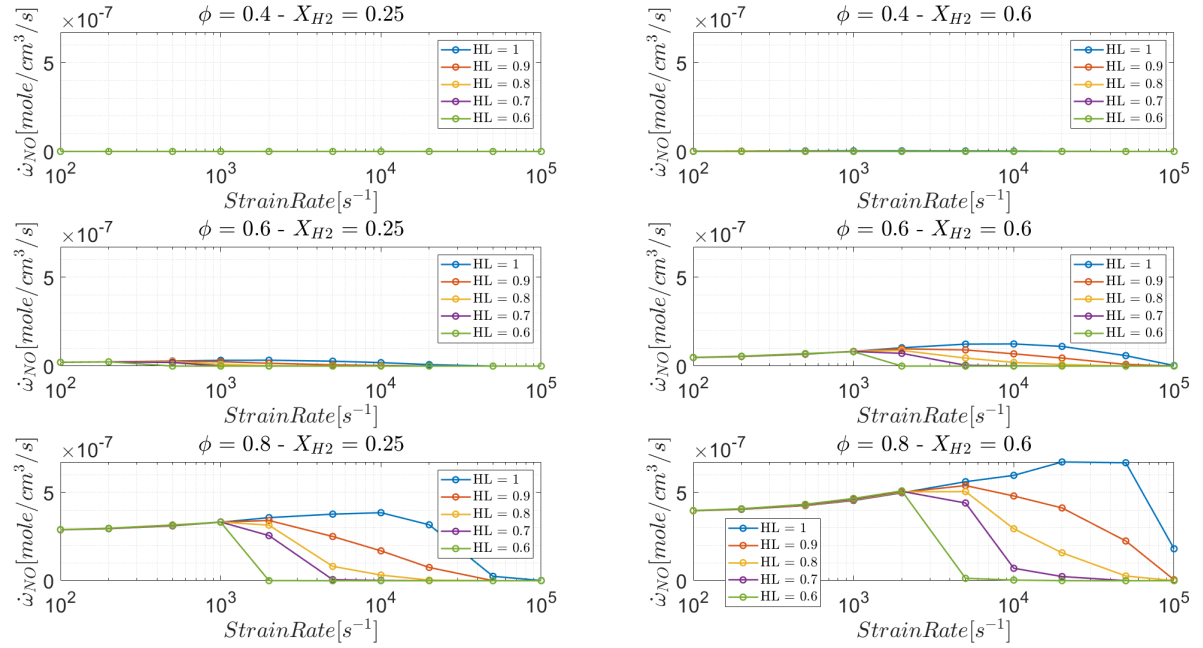


**Figure 5.2:** Peak NO Source term in counterflow premixed R2P CHEM1D simulations across various levels of Heat Loss parameters (HL = 1 corresponds to the adiabatic case). The rows represent increasing equivalence ratios, while the columns show increasing hydrogen enrichment.

What this preliminary study wants to prove is the existence of **resistance to heat losses** and to quantify how certain factors can affect it:

- **Hydrogen Enrichment:** Adding H<sub>2</sub> to the fuel mixture increases resistance to heat losses, with this effect becoming more pronounced under high strain conditions.

Additionally, the LBO equivalence ratio of the hydrogen-enriched fuel mixture is higher, therefore at the same equivalence ratio of  $\phi = 0.4$ , the hydrogen-enriched mixture can sustain a flame, above all when the strain level is increased.

The HL parameter at which the quenching takes place is quite high when low percentages of H<sub>2</sub> are in the fuel, meaning that a flame with high percentages of H<sub>2</sub> can sustain itself in highly-strained, cold environments.

- **Equivalence Ratio:** Higher equivalence ratios are able to sustain greater heat losses. However, resistance to highly strained, high heat loss conditions, leading to flames with increased Heat Release Rates (HRR), in turn, can result in higher NO emissions, primarily due to the thermal NO mechanism.

This finding highlights the importance of thorough mixing and avoiding high equivalence ratio reactant pockets to minimize NO emissions. For instance, a flame operating at a lower equivalence ratio with a high hydrogen content ( $\phi = 0.6$ , H<sub>2</sub> = 0.6) produces significantly lower NO emissions compared to a richer, low-hydrogen case ( $\phi = 0.8$ , H<sub>2</sub> = 0.25), even though the HRR is in the same order of magnitude. This further emphasizes that one of the key advantages of hydrogen combustion lies in its effectiveness in lean and ultra-lean configurations, above all when employed in highly strained configurations.

## 5.2. HRT Results

This section validates the results of the newly improved HRT approach for determining the temperature profile under thermal boundary conditions for low Biot number bodies, specifically quartz glass. The outcomes of the iterative process described in subsubsection 4.5.3.1 are presented in Figure 5.3 and Figure 5.4 for simulation **S1**, with a similar behaviour observed in simulation **S2**:

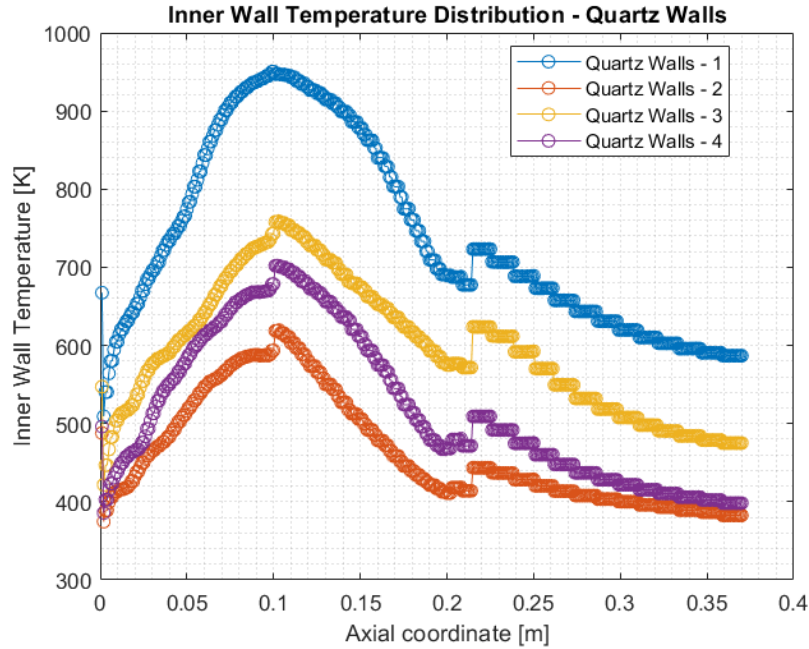


Figure 5.3: Inner Wall Temperature profile convergence

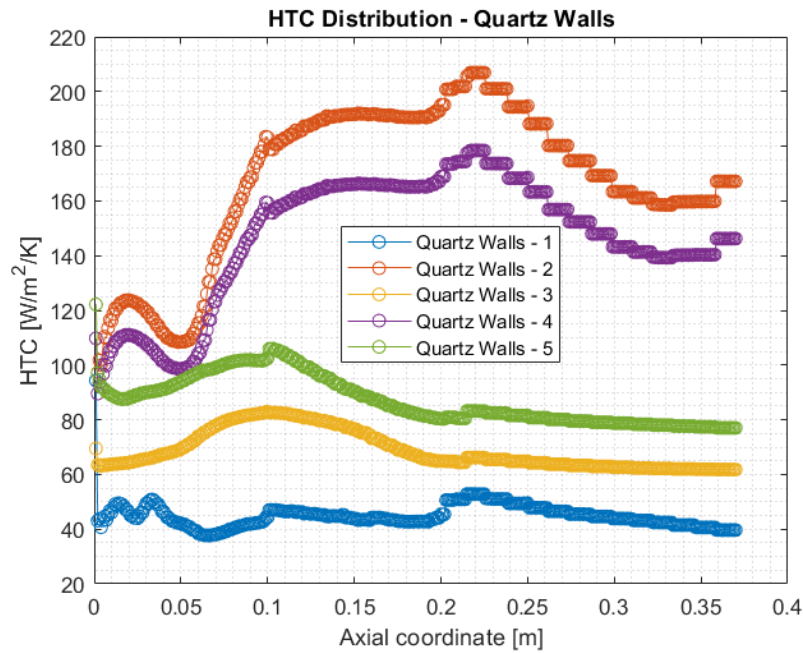
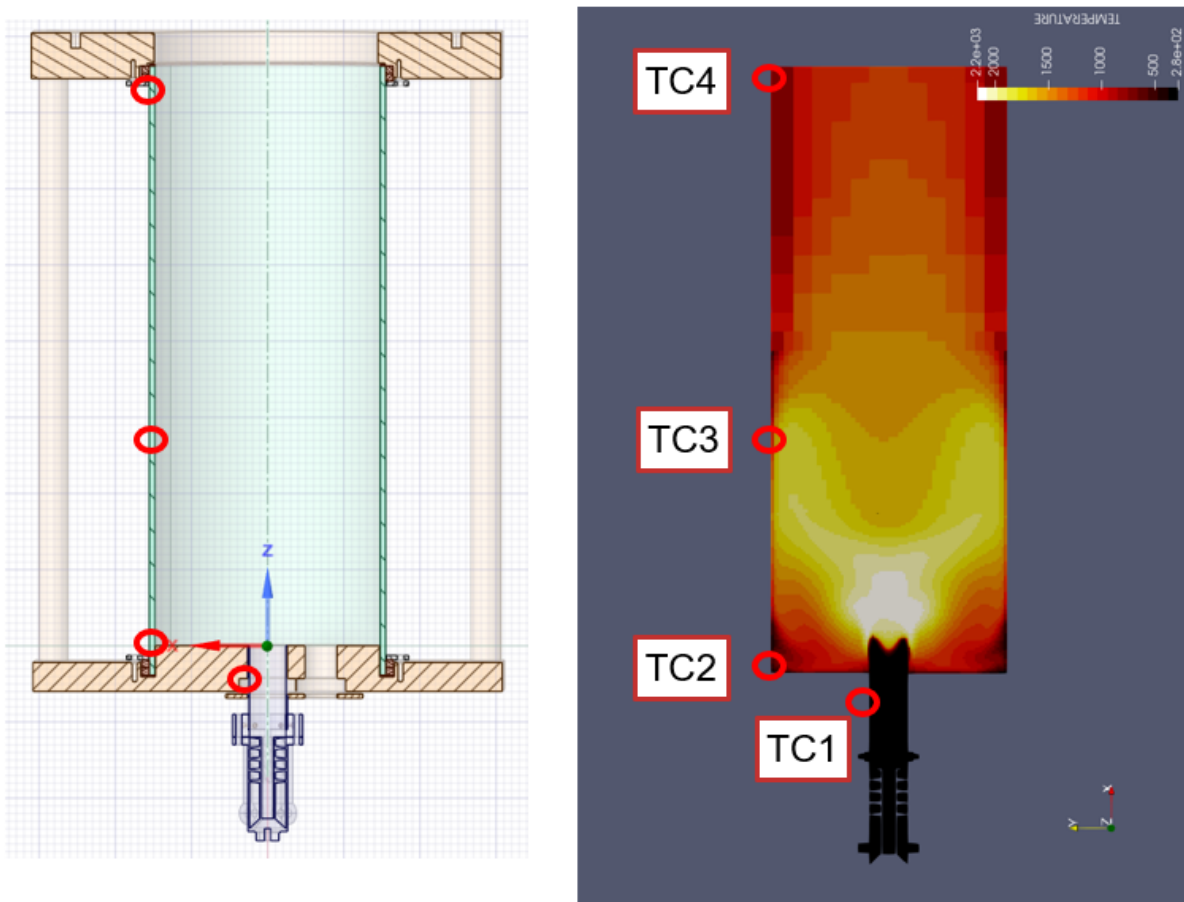


Figure 5.4: Heat Transfer Coefficient (HTC) profile convergence

During initial studies, it was observed that the convergence process was not entirely smooth, with thermal resistances oscillating between two solutions. One solution involved an attached flame, which elevated the quartz temperature and led to a very low thermal resistance (due to its dependence on the outer wall temperature, and consequently the inner wall temperature). This scenario is illustrated by the first iteration in both Figure 5.3 and Figure 5.4.

The low thermal resistance resulted in significant heat losses from the flame, extinguishing the highly strained OSL branches and forming a V-shaped flame with a lower quartz temperature and higher thermal resistance, as shown by the second iteration in the same figures. This oscillating behaviour was mitigated by applying a damping coefficient to the thermal resistance, allowing for a smoother convergence of both the thermal resistance and quartz temperature profiles.

To validate this approach, thermocouple measurements were compared with the thermal profiles derived from the HRT method for both cases, S1 and S2. The results for case S1 are presented here.



**Figure 5.5:** Thermocouple placement. TC1 was introduced to estimate the plate temperature, while TC2, TC3 and TC4 tried to report the main points of the quartz, respectively the ORZ, the stagnation point of the swirled hot products and the outlet temperature.



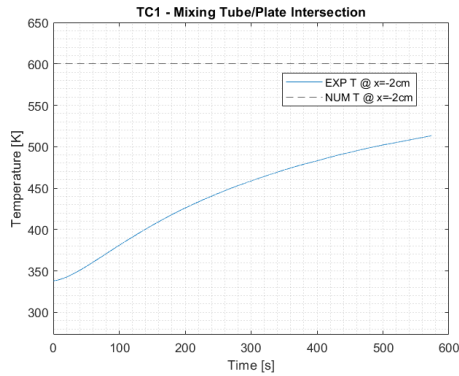


**Figure 5.6:** This comparison between numerical expected value and thermocouple measured value shows the difficulty in retrieving the temperature of the metal plate, which has a high thermal inertia.

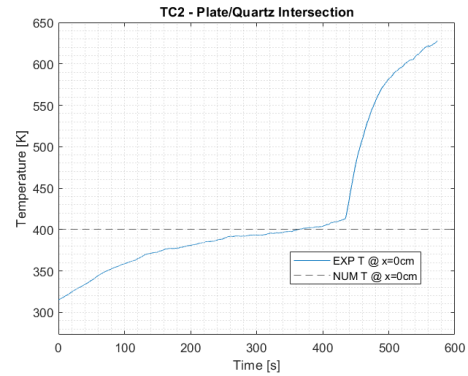


**Figure 5.7:** The figure shows a reasonable agreement of the numerically expected value compared to the thermocouple diagnosed value. The last abrupt increase in temperature is due to the detachment of the sensor, which came into contact with the hotter plate.

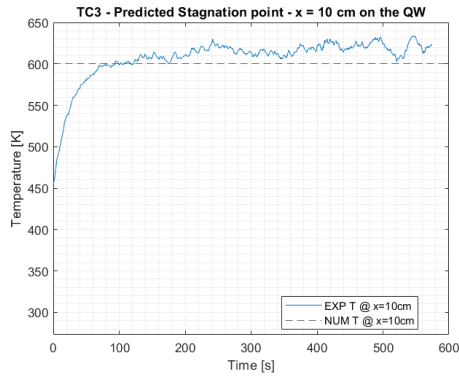


**Figure 5.8:** In this figure the accuracy of the prediction shows its best performance, as the predicted stagnation point of the swirling hot products is maintained at almost a constant temperature of 600 K.

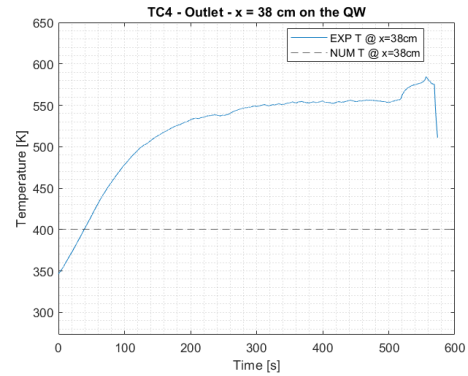


**Figure 5.9:** The poor agreement on the outlet temperature prediction is to be attributed to a main reason, and it is a too coarse mesh on the outlet region, which unfortunately could not be resolved more due to compromises in the computational expense and relevance of the zone.

It is important to note that these experimental measurements are time-dependent, as the temperature has not yet reached a steady state. This indicates that the solids are still undergoing thermal transients, particularly the metal plate, which has a higher thermal inertia compared to the quartz glass. In contrast, the quartz glass shows minimal changes and stabilizes in an earlier stage at a consistent temperature measurement, so it is possible to conduct comparisons on this particular temperature profile.

Since the most relevant measurement locations for the flow were those closest to the flame—specifically TC2 and TC3—and a reasonable agreement has been observed, this approach is deemed appropriate. Since CONVERGE does not allow for a time-variant thermal boundary condition expressed through thermal resistances, the decision was made to use these temperature profiles as boundary conditions for the quartz. An isothermal boundary condition of 500 K, based on the average measurement from TC1, was applied to the plate.

### 5.3. Baseline Simulation: H2-25% with 0% AAI

The baseline simulation results are here presented and discussed, comparing them with the corresponding experimental results. However, the comparison of averages that are usually seen in the literature is not completely appropriate for this case, as there are long transient effects which completely change the flame shape, for example.

Moreover, there are some further investigations conducted on the mixing/flame interaction which are currently conducted on this combustor that could further prove the validity of this study, or shed light on the reason for some of the disagreements.

#### 5.3.1. Averaged fields

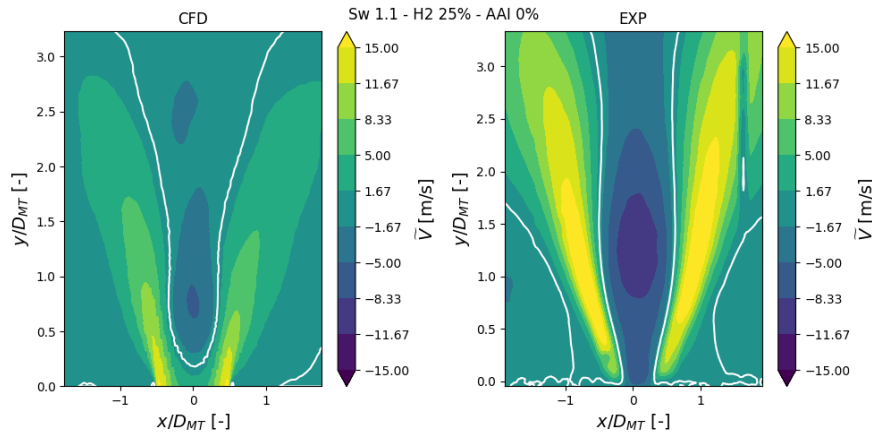


**Figure 5.10:** Averaged axial velocity field. An isoline is showed at  $V = 0\text{ m/s}$  to distinguish the recirculation zones.

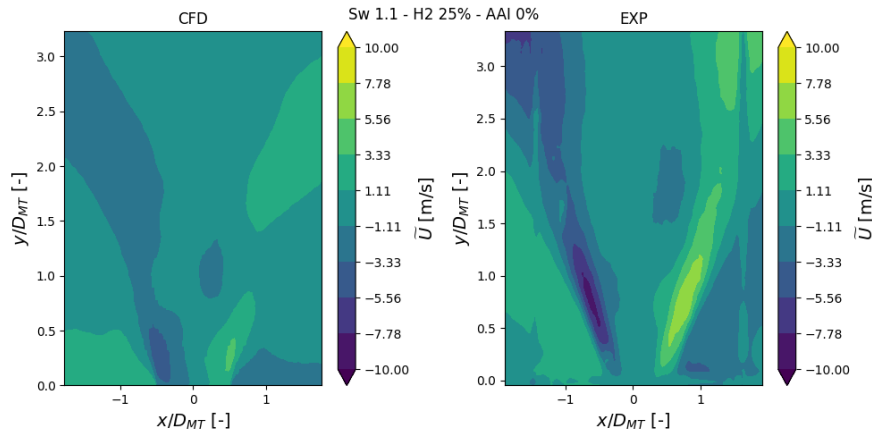


**Figure 5.11:** Averaged radial velocity field.

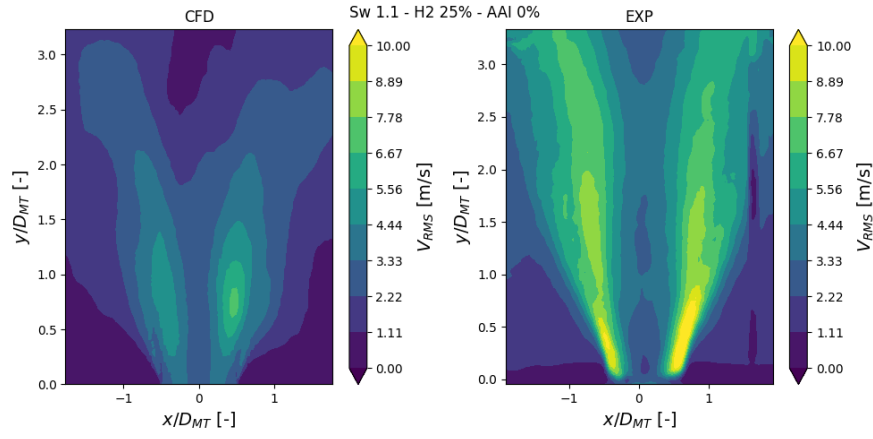


Figure 5.12: Axial velocity RMS field.

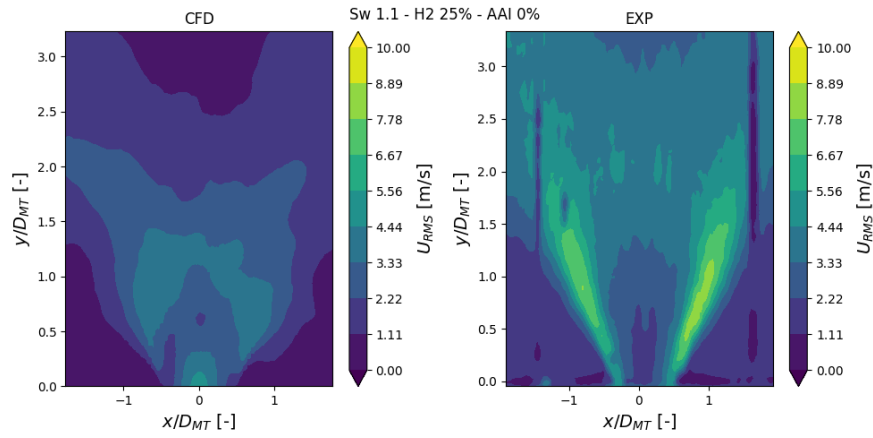


Figure 5.13: Radial velocity RMS field.

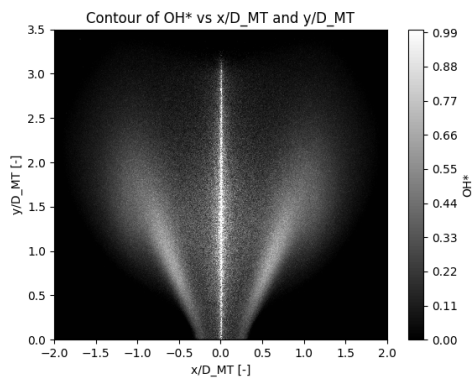


Figure 5.14: OH\* chemiluminescence image from experimental campaign.

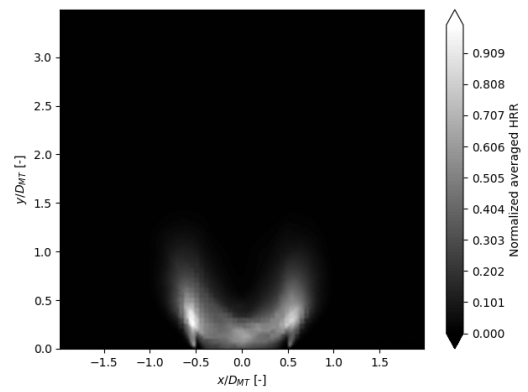
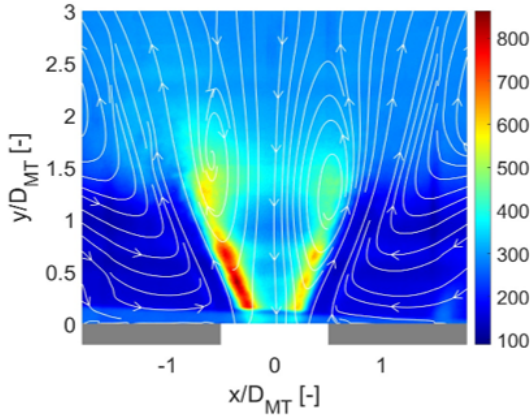
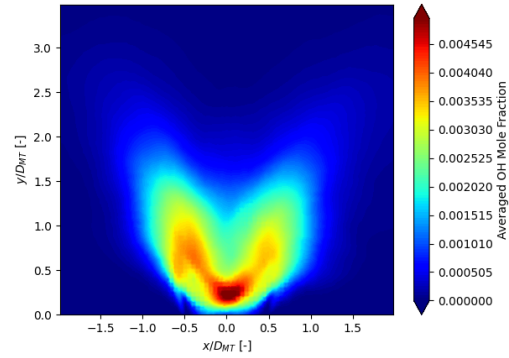


Figure 5.15: HRR averaged value.



**Figure 5.16:** OH PLIF image from experimental campaign.



**Figure 5.17:** OH mole fraction averaged value.

The comparison between the simulation and experimental results reveals some differences, particularly in the averaged fields.

Both axial and radial components of velocity show an underpredicted strength of the Inner Recirculation Zone (IRZ) and Outer Recirculation Zone (ORZ), as well as the intensity of the swirling flow's axial velocity.

The reasons for this underprediction are multiple:

- The upstream point of the flame is predicted further downstream in the simulation compared to the OH\* chemiluminescence and OH-PLIF images. Also, given that the flame upstream point is outside the mixing tube, the flame angle retrieved by the simulation is bigger than the experimental one.
- Unresolved plenum flow: sometimes, in literature [142], it has been seen that the boundary conditions of fuel and air inlets are too complex to be only described as mass flow rate inlets. Therefore, it becomes necessary to include in the computational domain a point that is within the tube that then inject -in this case- fuel and swirling and axial air.
- Underpredicted mixing: As seen in Figure 5.33 and Figure 5.34, the LES model predicts a lean core and a richer swirling flow. If, however, in experimental results (which are not yet available), a more homogeneous mixture is seen in the mixing tube, differences in density could lead to difference in axial velocity prediction.

However, at an earlier snapshot taken at 269 ms, the accuracy of the simulation shows significant improvement.

This better agreement at the earlier timestep can be attributed to the low temperature in the ORZ and the presence of a V-shaped flame structure. Before the transition to an M-flame configuration, the simulated and experimental fields align reasonably well. However, after the transition, the averaged simulation results begin to deviate more noticeably from the experimental observations.

It's important to note that pinpointing the exact timestep when the V-to-M flame shape transition occurs is challenging. The outer shear layer branch of the flame initially fails to ignite, then goes through cycles of ignition and quenching until the frequency of these cycles increases to the point where the M-flame configuration becomes more stable.

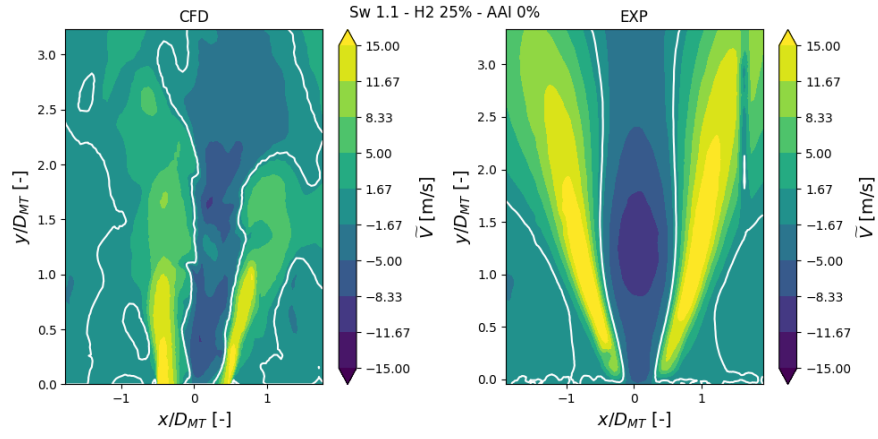


**Figure 5.18:** Axial velocity field at  $t = 269$  ms.

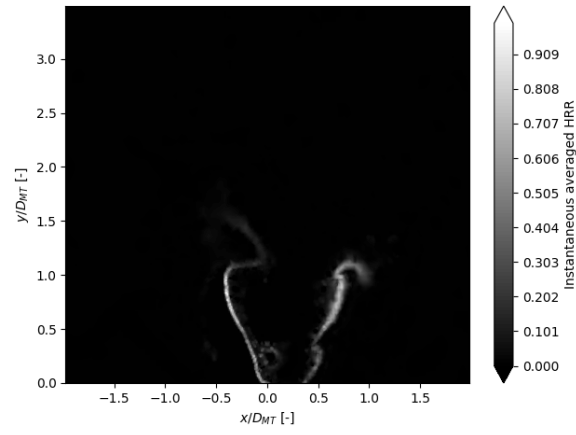


**Figure 5.19:** HRR instantaneous value at  $t = 269$  ms.

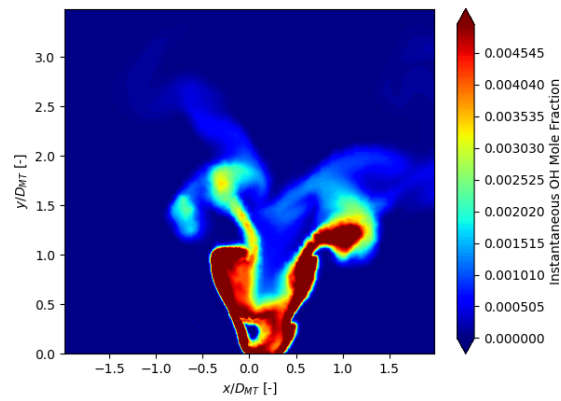


**Figure 5.20:** OH mole fraction instantaneous value at  $t = 269$  ms.

### 5.3.2. V-to-M Flame Shape Transition

As highlighted in numerous studies reviewed in the literature, a critical challenge in current research on CH<sub>4</sub>/H<sub>2</sub> flames, and hydrogen blends in general, is the accurate prediction of flame position and shape. This issue becomes particularly evident when examining the heat release rate fields, where a transition in flame shape is observed.

In earlier simulations using adiabatic boundary conditions, an M-flame was predicted, whereas experimental OH\* chemiluminescence images displayed a V-flame. However, by applying the new HRT-derived thermal boundary conditions, the simulation more accurately captures the V-flame structure, as illustrated by the instantaneous temperature field slice in Figure 5.21:

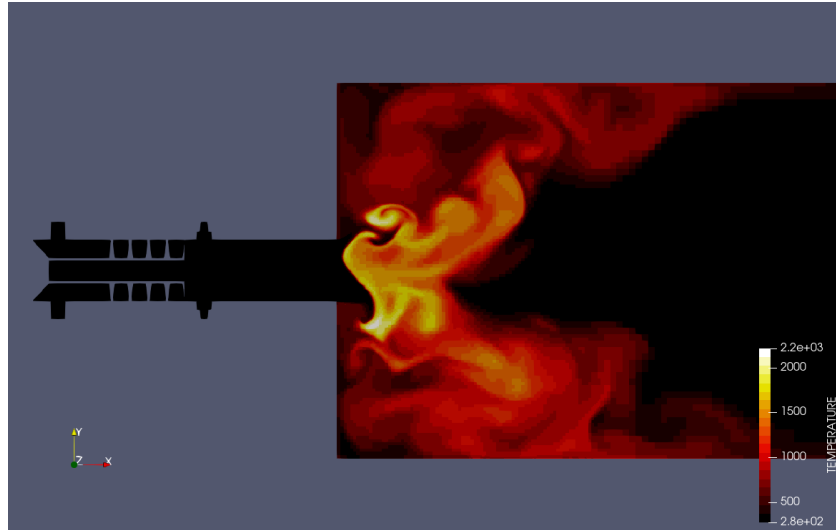


**Figure 5.21:** Instantaneous temperature field extracted at 150 ms after ignition - 1/2 Flow Through Time (FTT). *Note:* only the first 200 mm of the chamber are shown.

However, this seems to be only a transient solution, as the OSL starts igniting more frequently with time, as the temperature in the ORZ increases, resulting in an M-flame when the quantities are postprocessed at a further timestep ( $t = 600\text{ms}$  - 2 FTT), as shown in Figure 5.22:

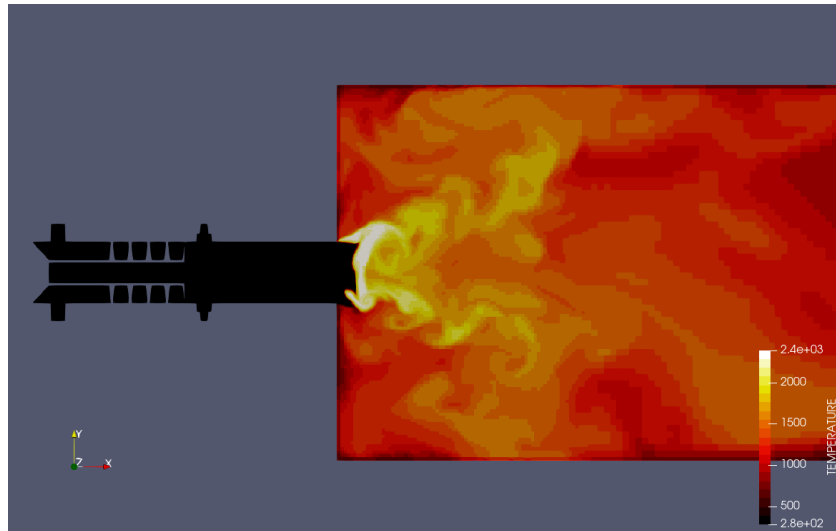


**Figure 5.22:** Instantaneous temperature field extracted at 600 ms after ignition - 2 Flow Through Time (FTT). *Note:* only the first 200 mm of the chamber are shown.

Another evidence of this transient behaviour is the flame Lift-Off Height (LOH) temporal evolution, displayed in Figure 5.23: this quantity corresponds to the average of the axial coordinate of the flame region, which is the set of points  $\vec{x}$  that satisfy the inequality  $\text{HRR}(\vec{x}) \geq 0.9 \text{HRR}_{max}$ , weighted with the HRR value.

Sometimes the LOH is defined in the literature as the minimum axial coordinate of the flame isovolume, but the strong dependency on the flame isovolume definition deemed this definition as arbitrary, so it was chosen to use a more general definition such as the centroid of the flame isovolume.

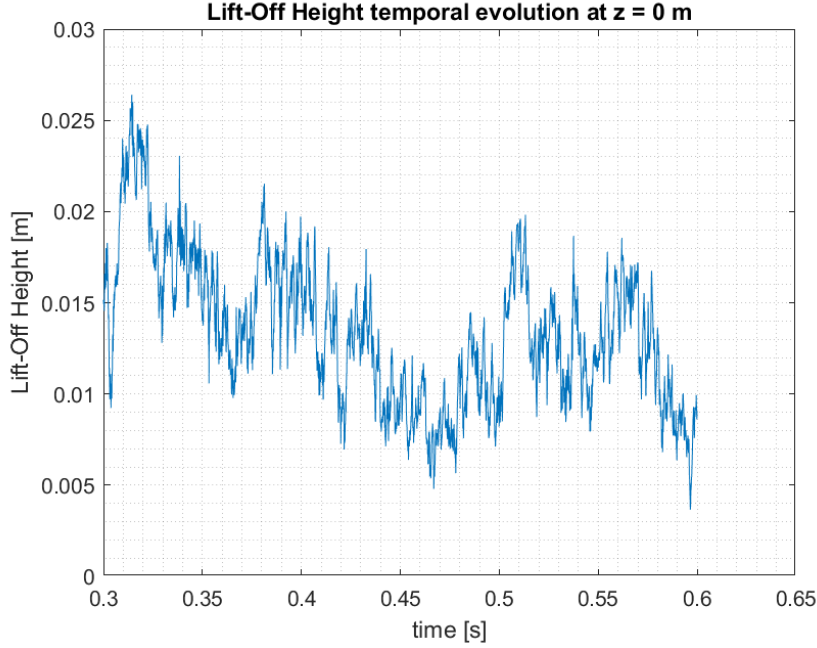


**Figure 5.23:** Temporal evolution of the flame Lift-Off Height (LOH). The data acquisition started from  $0.3 \text{ s} = 1 \text{ FTT}$  and finished at  $0.6 \text{ s} = 2 \text{ FTT}$ .

The most plausible reason is the temperature increase in the chamber, above all in the ORZ, which eases the ignition of the highly strained mixture in this location. Once the OSL is ignited, as discussed by Terhaar in the PhD thesis [143], a feedback loop is initiated, where the hotter ORZ maintains a more stable environment for the OSL mixture to keep igniting, despite the presence of heat losses to the surrounding environment.

To prove the existence of this feedback mechanism for OSL flame stabilization, two additional simulations have been conducted, even though they have not been simulated until averaging because the focus is on the ignition process:

- **Wider Spark Case:** The actual experiment is conducted igniting from a central pilot flame, so for the simulation mentioned before the virtual spherical spark is inserted at the axis of the combustor, at a distance of  $1 D_{MT}$  from the origin of the axis, with a diameter of  $1 D_{MT}$ . This shape does not ignite the OSL mixture, so in order to check if it is a matter of initial condition, a cylinder with a diameter of  $2 D_{MT}$  and  $1 D_{MT}$  height is placed on the origin of the axis, covering the OSL. The result is the ignition of the OSL and the faster rate of ORZ temperature increase, which, in turn, reignites and stabilizes the OSL, starting and keeping in place the M-flame.
- **Adiabatic Boundary Condition Case:** This case checks for the utility of imposing a different thermal boundary condition. The small spark does not ignite the OSL right away, so there is, for a small amount of time, a V-flame stabilized, but then the adiabatic thermal boundaries affect

the rate of temperature increase, moving the V-to-M flame shape transition at an earlier timestep -namely, from 450 ms to 150 ms after ignition.

One last insight that can be extracted from these simulations, in line with the findings of a study presented in the thesis above [143], is the hysteresis effect that is seen in flame shape transitions. This effect comes directly from the feedback loop in which the flame is currently in, as a V-flame tends to stay a V-flame and an M-flame tends to stay an M-flame, unless high temperature changes are detected in the recirculation zones. This happens because, as shown in Figure 5.33 and Figure 5.34, the OSL mixture usually has a higher equivalence ratio mixture, which, once the ORZ products become hotter, eventually ignites, following the same insights extracted from the CHEM1D simulations in section 5.1.

In conclusion, the HRT approach has proven to be a valid method for obtaining thermal boundary conditions. However, its true potential lies in its dynamic formulation. If the alternating flame/temperature behaviour observed in the iterative RANS simulations were to occur in an LES, it is reasonable to assume that the temperature increase seen in Figure 5.22 could have been followed by a decrease in thermal resistance and an increase in heat flux, ultimately returning the flame to its V-shape configuration.

### 5.3.3. PVC, Mixing and Flame Interaction

From the POD analysis of the PIV results, it appears that the Precessing Vortex Core (PVC) is suppressed. This observation aligns with findings from a similar swirl-stabilized combustor, which, unlike the current setup, included a centerbody where the flame was able to attach [144]. In the non-reactive flow, a global instability mode was observed; however, upon ignition, the PVC was suppressed due to density stratification on the Inner Shear Layer (ISL).

When performing the POD analysis on the  $z = 0m$  plane used for the PIV measurements, the characteristic pair of modes, typically shifted by a quarter wavelength and indicative of a vortical structure, are present in the non reactive case, as shown in Figure 5.24, but they disappear in the reactive case, shown in Figure 5.26. Below are the POD modes and the FFT conducted on the time coefficients, showing a clear peak on  $f = 287Hz$ , similar to the  $f = 300Hz$  frequency retrieved during the experimental campaign.

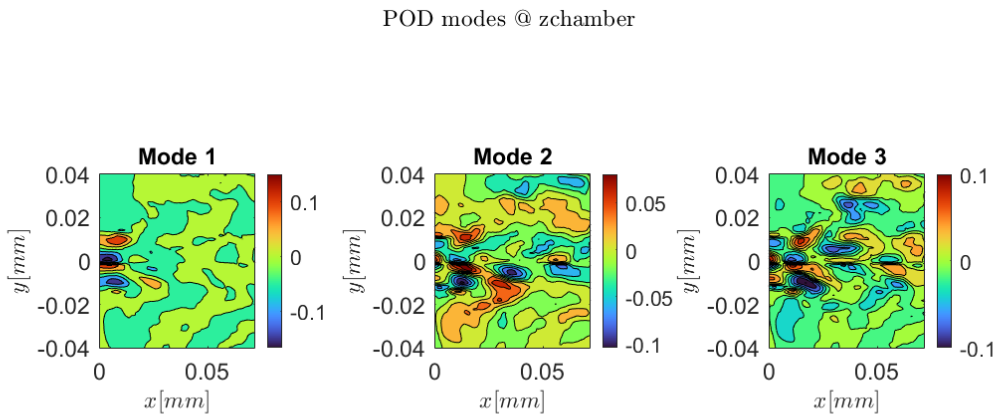


**Figure 5.24:** Non Reactive S1 case - Spatial POD modes on  $z = 0m$  slice. POD is conducted on the azimuthal component of the velocity using as sampling period  $t = 1e - 4s$  and as overall sampling time  $T = 100ms$



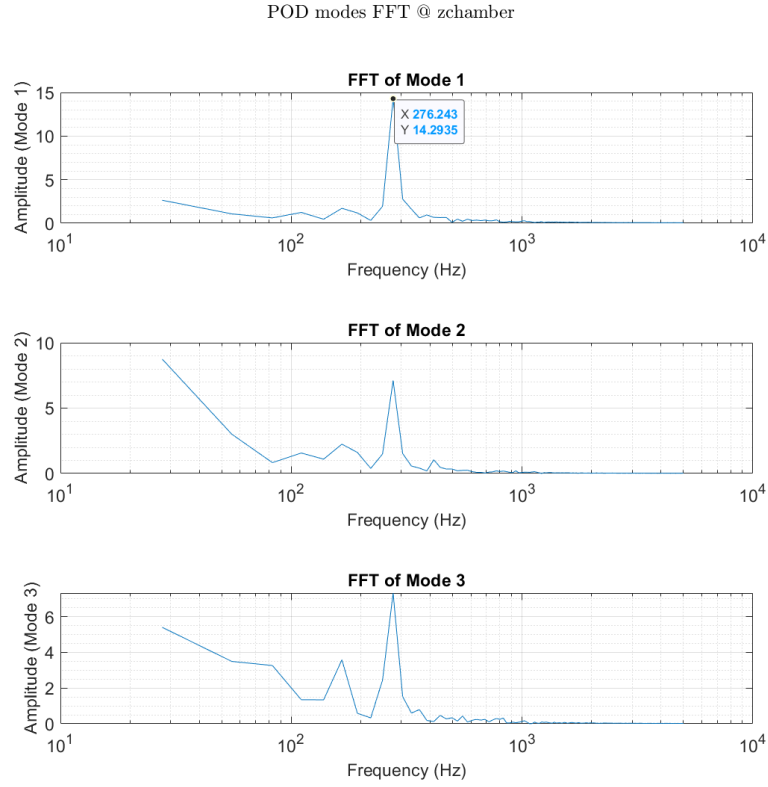


**Figure 5.25:** Non Reactive S1 case - FFT applied to the POD modes time coefficients on  $z = 0m$  slice. POD is conducted on the azimuthal component of the velocity using as sampling period  $t = 1e - 4s$  and as overall sampling time  $T = 100ms$

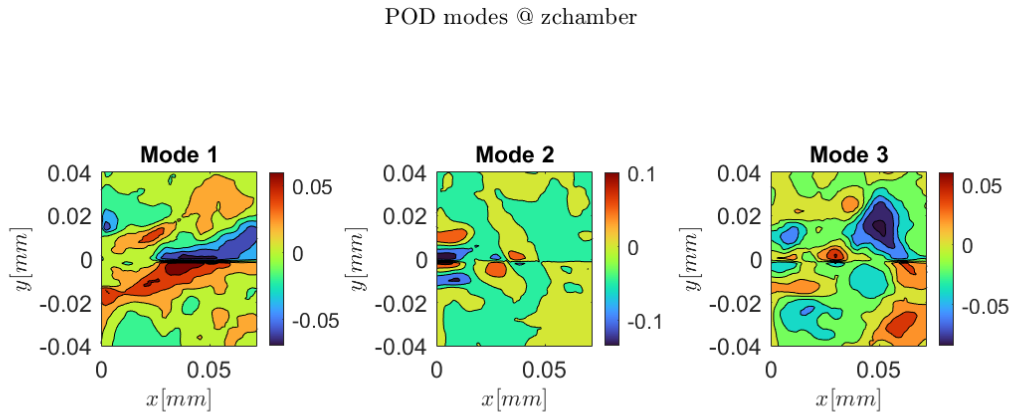


**Figure 5.26:** Reactive S1 case - Spatial POD modes on  $z = 0m$  slice. POD is conducted on the azimuthal component of the velocity using as sampling period  $t = 1e - 4s$  and as overall sampling time  $T = 100ms$

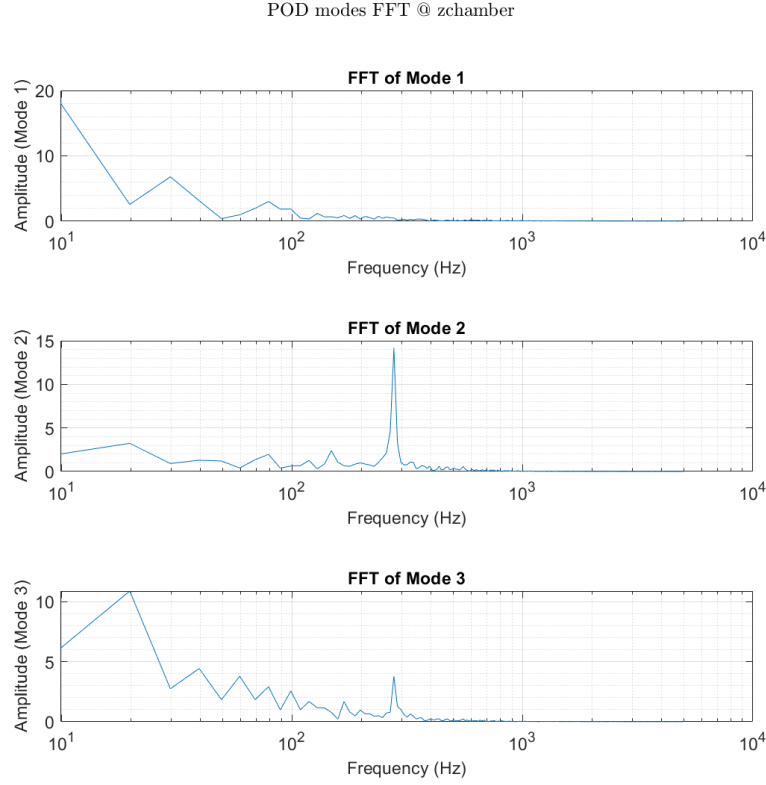


**Figure 5.27:** Reactive S1 case - FFT applied to the POD modes time coefficients on  $z = 0m$  slice. POD is conducted on the azimuthal component of the velocity using as sampling period  $t = 1e - 4s$  and as overall sampling time  $T = 100ms$

In Figure 5.26, mode 2 is similar to mode 1 in Figure 5.24, and it shows the same peak in frequency. However, it is not followed by a coupled mode, therefore the PVC cannot be diagnosed. However, even though the mixing tube was not accessible during experiments, it is possible to access simulation field points that are not visible during experiments. So it has been chosen to check for the existence of a PVC in two slices of the mixing tube, precisely at  $x = -0.03m$  and  $x = 0.0m$ , normal to the  $x$  axis, respectively half of the mixing tube and the inlet in the chamber. The results make it clear that a PVC is indeed present, it is the dominant turbulent structure accounting for almost 80% of the TKE, and the 90 degree phase shift is evident in both Figure 5.29 and Figure 5.30 with the same frequency as detected in the non reactive case. This finding does not clash with the experimental results, as the density stratification suppresses indeed the PVC in the chamber: it does not mean, however, that the PVC is not present in the mixing tube, where the flame and the subsequent density gradient are absent.

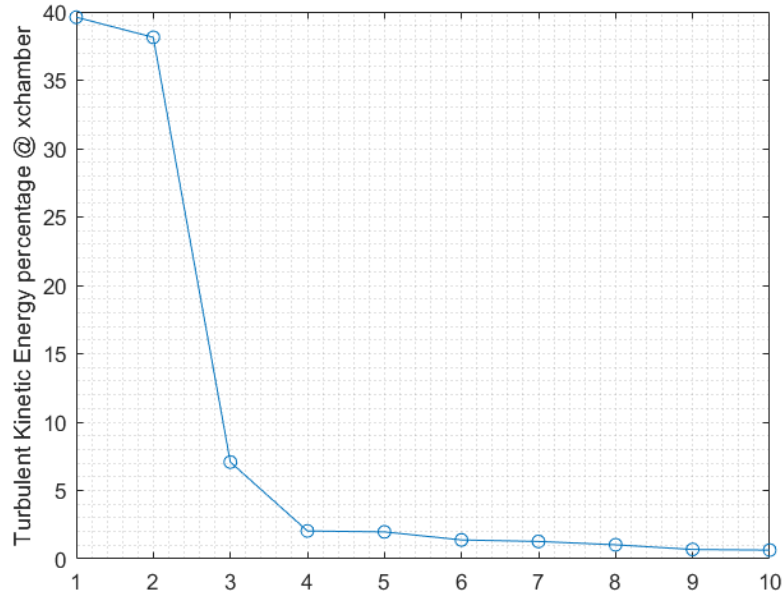


**Figure 5.28:** Reactive S1 case - TKE of the first 10 POD modes on  $x = 0m$  slice. POD is conducted on the azimuthal component of the velocity using as sampling period  $t = 1e - 4s$  and as overall sampling time  $T = 100ms$

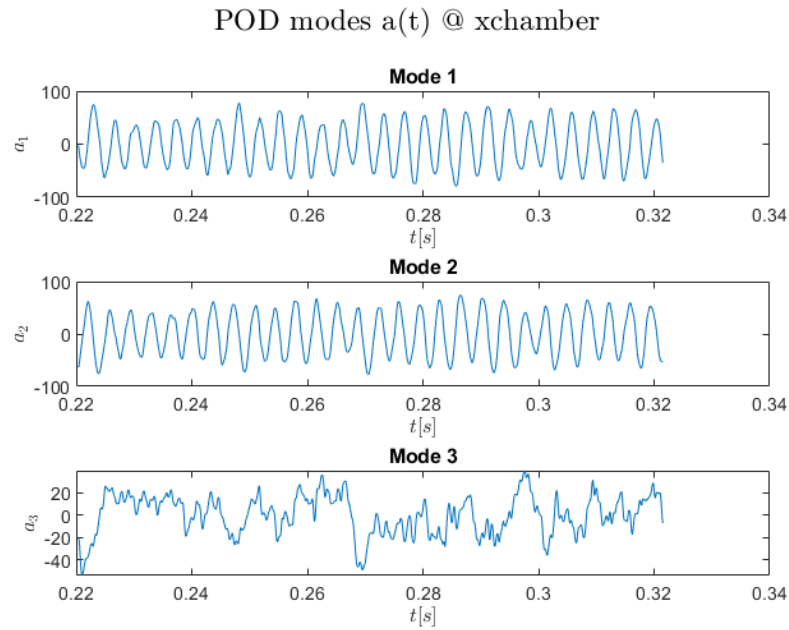


**Figure 5.29:** Reactive S1 case - First three POD modes time coefficients on  $x = 0m$  slice. POD is conducted on the azimuthal component of the velocity using as sampling period  $t = 1e - 4s$  and as overall sampling time  $T = 100ms$

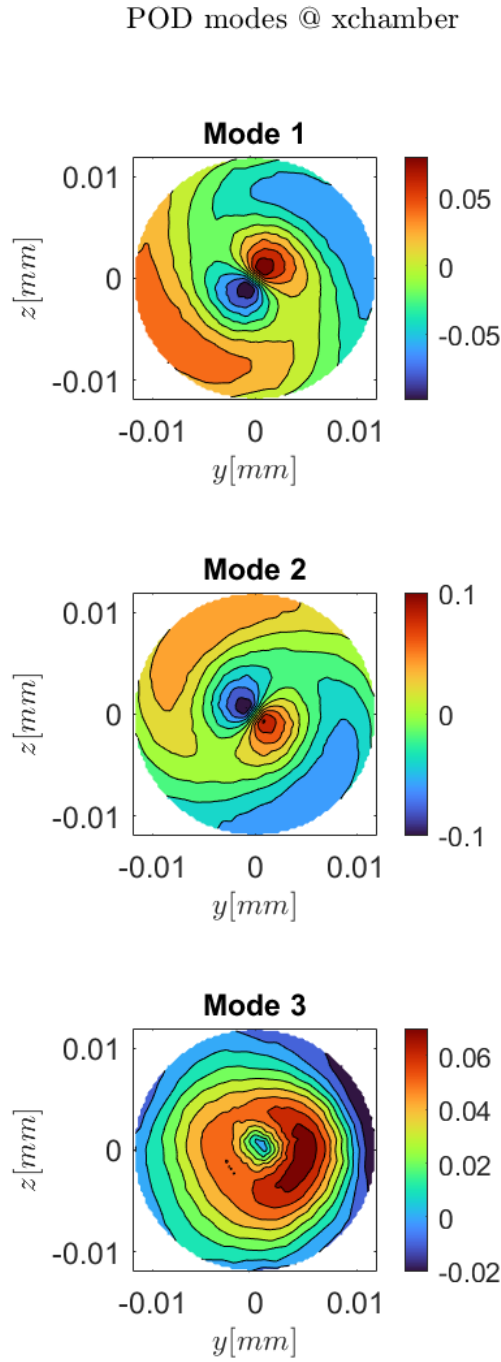


**Figure 5.30:** Reactive S1 case - Spatial POD modes on  $x = 0m$  slice. POD is conducted on the azimuthal component of the velocity using as sampling period  $t = 1e - 4s$  and as overall sampling time  $T = 100ms$

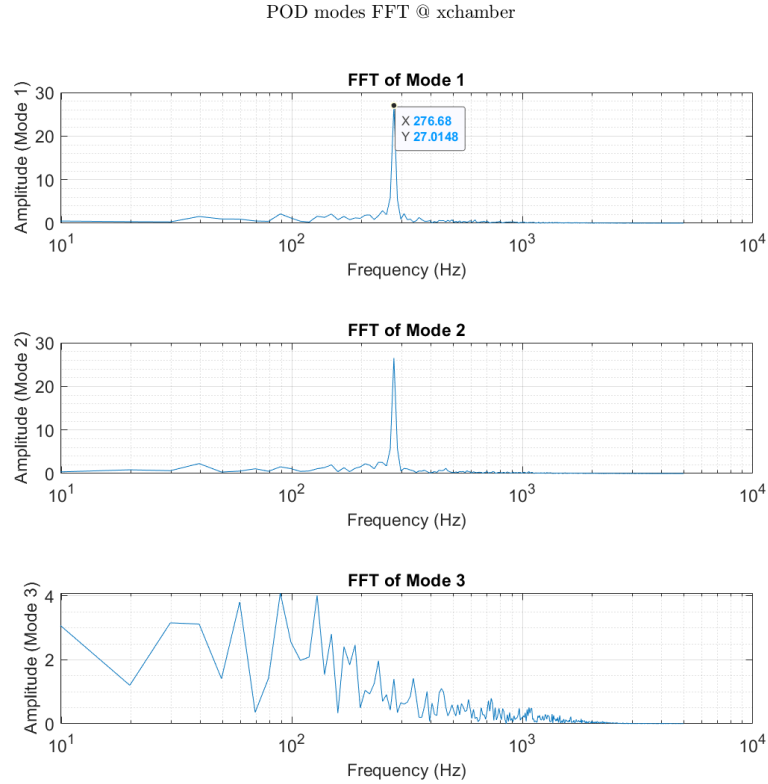


**Figure 5.31:** Reactive S1 case - FFT applied to the POD modes time coefficients on  $x = 0m$  slice. POD is conducted on the azimuthal component of the velocity using as sampling period  $t = 1e - 4s$  and as overall sampling time  $T = 100ms$

The presence of the PVC brings with it as main effect the formation of pockets of reactants with a high equivalence ratio on one side, while the opposite side has a lower equivalence ratio. This affects the ISL branches, as the one with a higher equivalence ratio moves upstream and the one with a lower equivalence ratio moves downstream, sometimes even extinguishing when the equivalence ratio becomes smaller than the Lean Blow-Out limit. Evidence can be found in a histogram of the equivalence ratio of the flame region, which shows that some zones of the swirling mixture are reacting at a mixture which does not correspond to the nominal equivalence ratio:

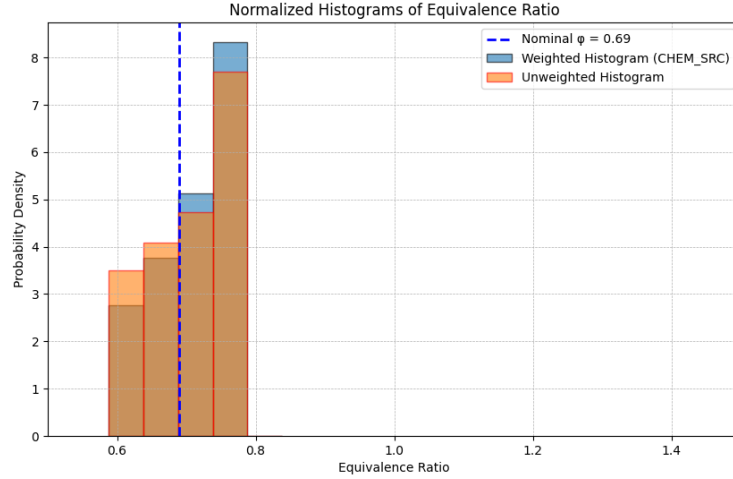


**Figure 5.32:** Equivalence Ratio Histogram. In order to acquire relevant data for the description of the flame, the datapoints  $\vec{x}$  are conditioned to satisfy  $\text{HRR}(\vec{x}) \geq 0.9\text{HRR}_{max}$

Moreover, analyzing the single timestep results, it is possible to see traces of local extinctions and pockets of high equivalence ratio reactants that reignite the flame. The following figure is taken at half a PVC period of distance, and it is possible to see how the upstream point of the flame is at a 180 degree phase difference with respect to the PVC:

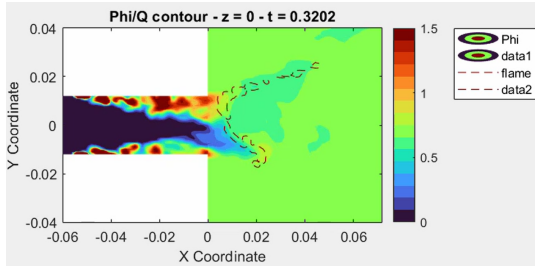


**Figure 5.33:** Equivalence ratio contour with HRR isosurface at time  $t = 0.3202s$

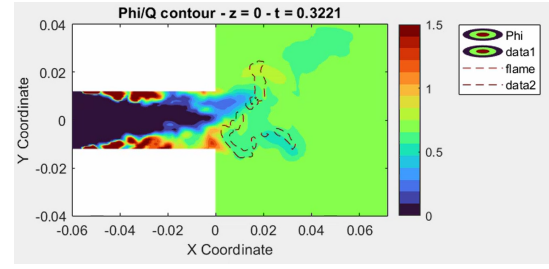


**Figure 5.34:** Equivalence ratio contour with HRR isosurface at time  $t = 0.3221s$

Here is a planar view of the  $x = 0.0m$  slice, displaying a vector field composed of radial and azimuthal velocities, referred to as the planar velocity  $V_{planar}$ , overlaid on the contour of its magnitude. A white cross marks the point where  $V_{planar} = 0m/s$ , clearly indicating the typical off-axis center of the Precessing Vortex Core (PVC). It's interesting to observe that, when examining the same timesteps and slice location, the equivalence ratio field closely follows the structure of the velocity field, revealing how interconnected the two fields are.

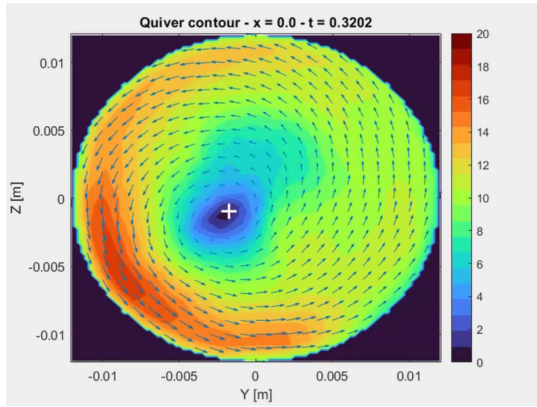


**Figure 5.35:** Planar view at  $x = 0.0m$  of planar velocity vector field at time  $t = 0.3202s$

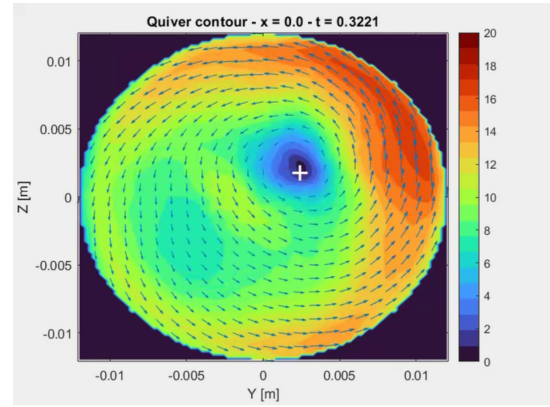


**Figure 5.36:** Planar view at  $x = 0.0m$  of planar velocity vector field at time  $t = 0.3221s$

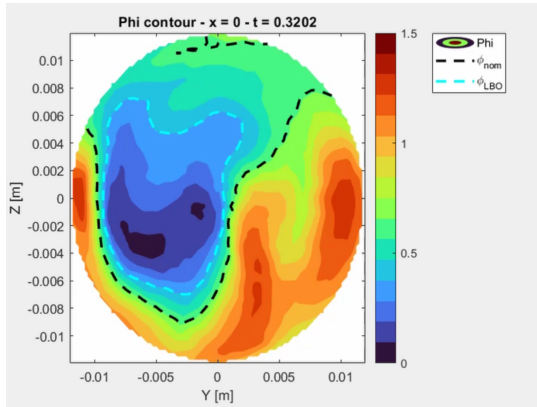


**Figure 5.37:** Planar view at  $x = 0.0m$  of equivalence ratio field at time  $t = 0.3202s$ . Isosurfaces of nominal and LBO equivalence ratio are shown.

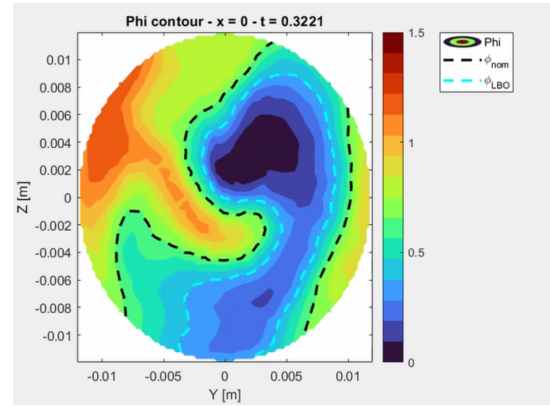


**Figure 5.38:** Planar view at  $x = 0.0m$  of equivalence ratio field at time  $t = 0.3221s$ . Isosurfaces of nominal and LBO equivalence ratio are shown.

Finally, additional evidence of this strong connection is demonstrated by the application of Proper Orthogonal Decomposition (POD) on both the equivalence ratio and the heat release rate, revealing the same coherent vortex structure, with a distinct peak observed at a frequency of 287 Hz. This is proof that the PVC affects mixing and therefore the flame position.

## Phi POD modes @ xchamber

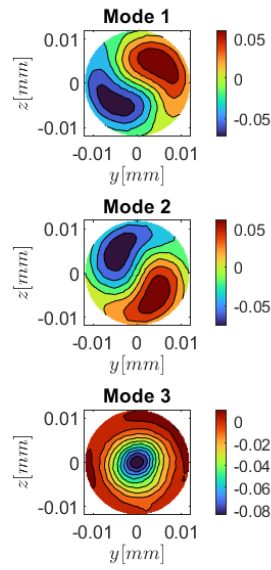


**Figure 5.39:** Reactive S1 case - Spatial POD modes on  $x = 0m$  slice. POD is conducted on the equivalence ratio using as sampling period  $t = 1e - 4s$  and as overall sampling time  $T = 100ms$

## Phi POD modes FFT @ xchamber

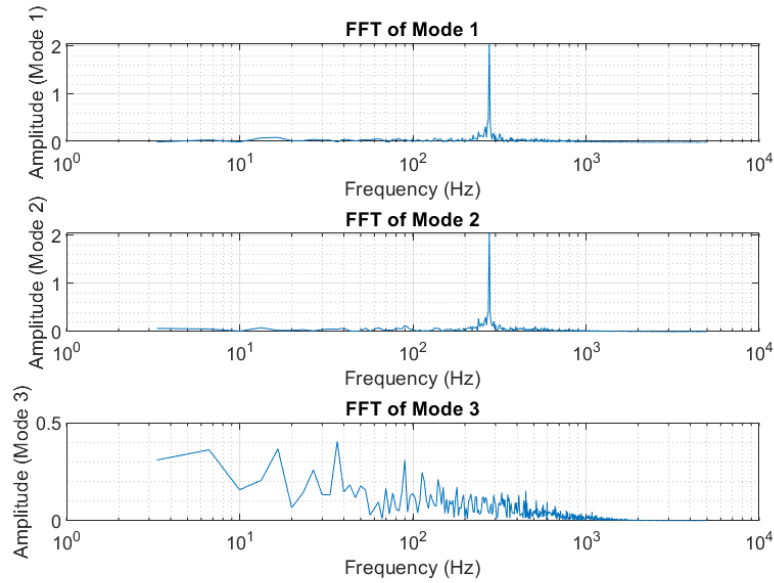


**Figure 5.40:** Reactive S1 case - FFT applied to the POD modes time coefficients on  $x = 0m$  slice. POD is conducted on the equivalence ratio using as sampling period  $t = 1e - 4s$  and as overall sampling time  $T = 100ms$



## Q POD modes @ xchamber

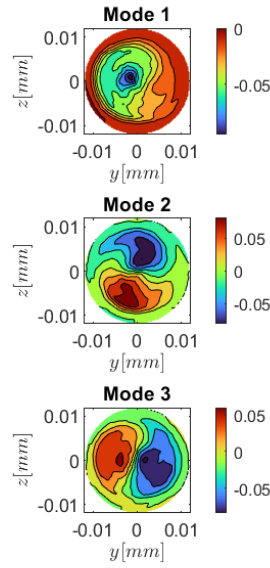


**Figure 5.41:** Reactive S1 case - Spatial POD modes on  $x = 0m$  slice. POD is conducted on the heat release rate using as sampling period  $t = 1e - 4s$  and as overall sampling time  $T = 100ms$

## Q POD modes FFT @ xchamber

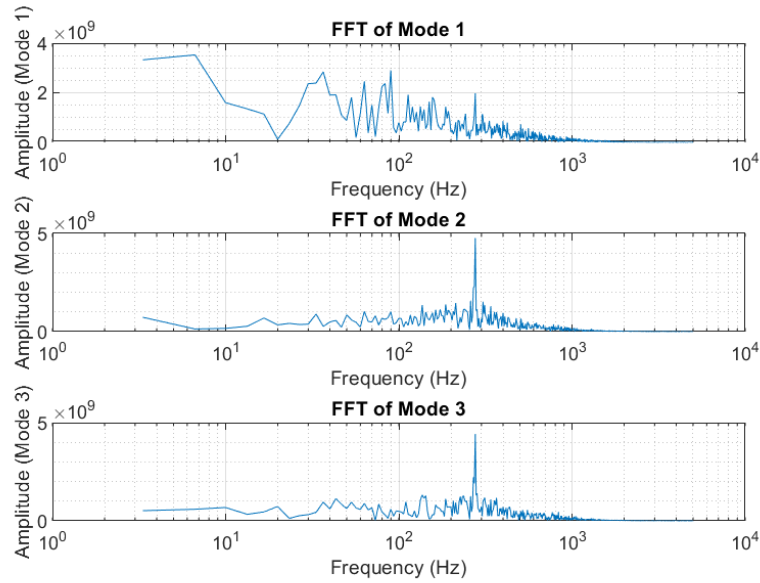


**Figure 5.42:** Reactive S1 case - FFT applied to the POD modes time coefficients on  $x = 0m$  slice. POD is conducted on the heat release rate using as sampling period  $t = 1e - 4s$  and as overall sampling time  $T = 100ms$

## 5.4. The Effect of AAI: H2-25% with 20% AAI

For case S2, the comparison between the simulation and experimental results reveals significant discrepancies in the velocity fields. Notably, the simulation fails to capture the Inner Recirculation Zone (IRZ) observed in the PIV experimental data. This discrepancy could be partially attributed to an under-

prediction of flow reversal at the outlet boundary—suggesting that extending the computational domain into the fume hood might help.

However, the more likely cause is the underestimation of mixing between the axial air injection (AAI) flow and the swirling flow. In the simulation, these flows remain largely separated, whereas the PIV results show that the AAI has lower intensity and integrates more effectively with the swirling flow.

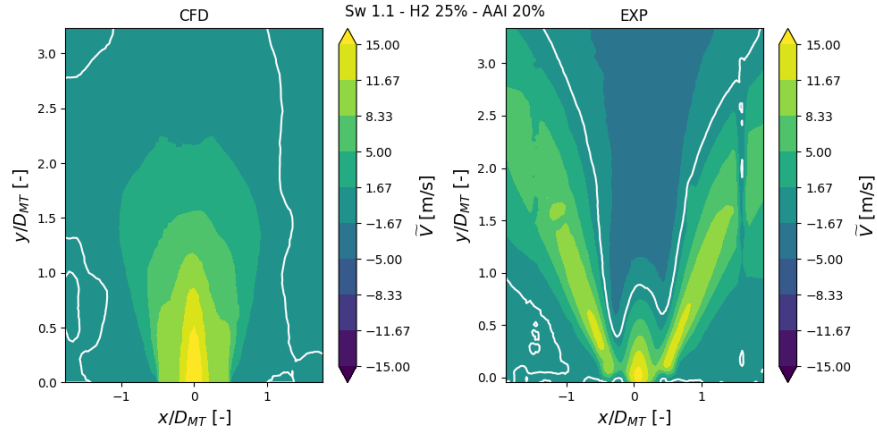


**Figure 5.43:** Averaged axial velocity field. An isoline is showed at  $V = 0\text{ m/s}$  to distinguish the recirculation zones.

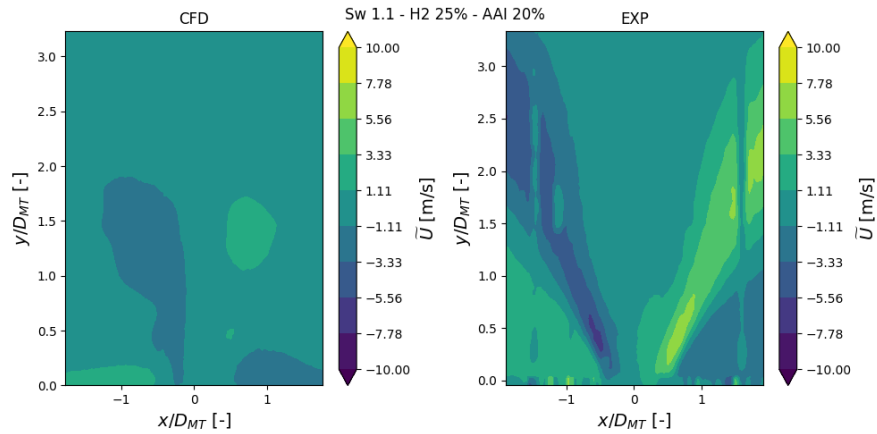


**Figure 5.44:** Averaged radial velocity field.

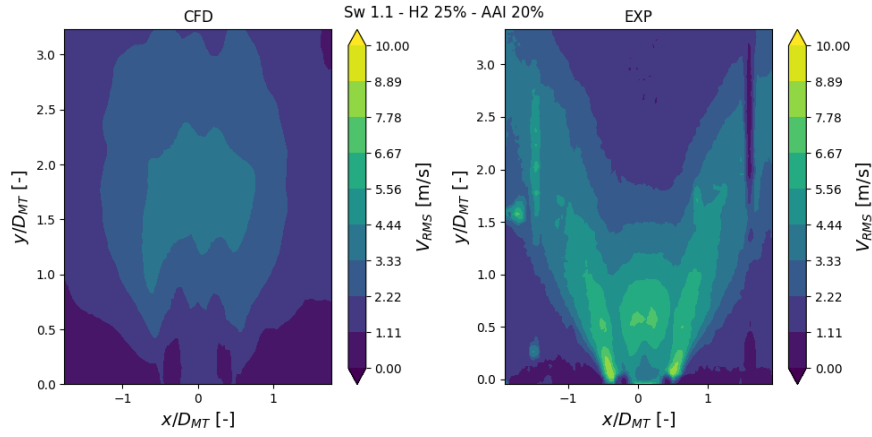


Figure 5.45: Axial velocity RMS field.

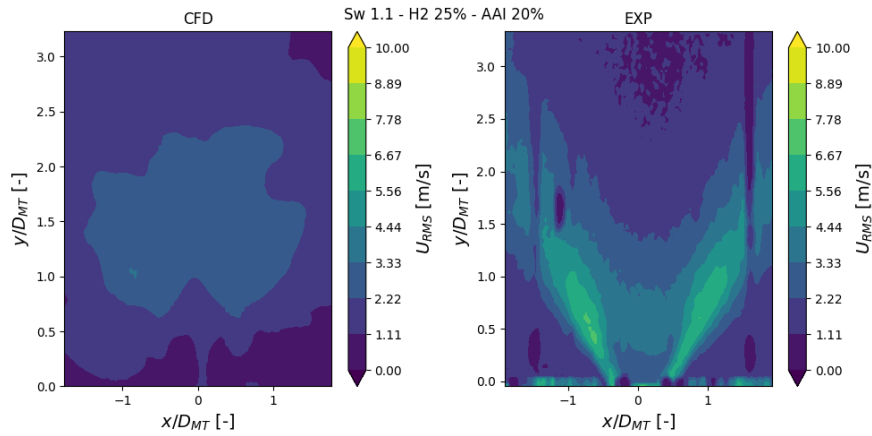
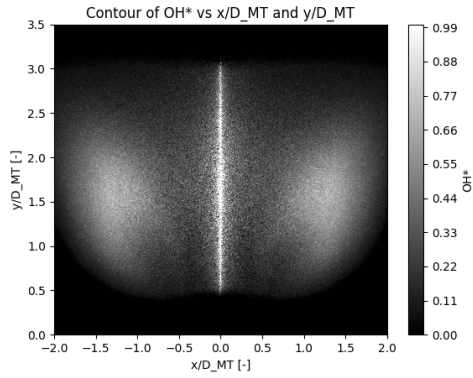
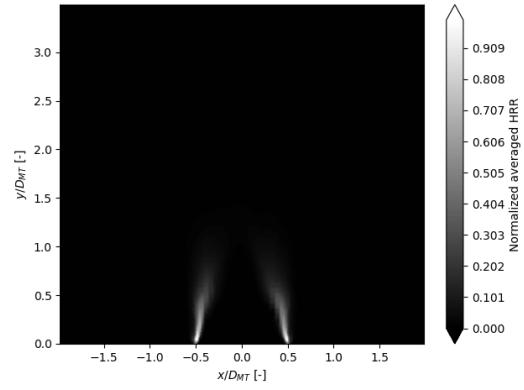


Figure 5.46: Radial velocity RMS field.

This velocity field misprediction impacts flame positioning, with the flame in the experiments being lifted, while in the simulation it remains attached to the burner lip. One reason could be found in the underprediction of the strain level in the outer shear layer in the simulation, resulting in a much more closed exit angle of the swirling flow compared to the experiments. This explains why the flame in the simulation attaches to the lip, whereas if we were to apply the same velocity gradients present in the simulation, the flame would likely quench and reposition further downstream where the lower heat loss and strain conditions are more favourable, as seen in the experimental OH\* chemiluminescence image.



**Figure 5.47:** OH\* chemiluminescence image from experimental campaign.



**Figure 5.48:** HRR averaged value.

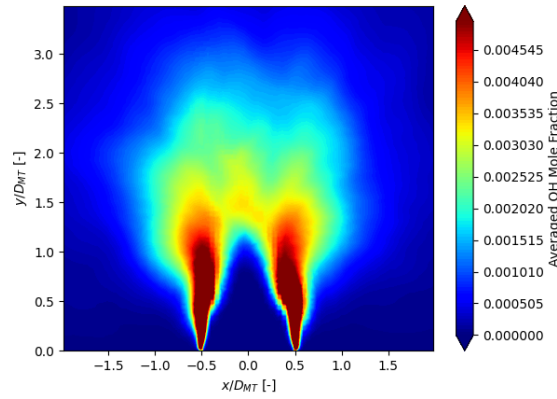


**Figure 5.49:** Averaged OH molar fraction

#### 5.4.1. Observations on PVC

As documented in similar swirl-stabilized combustors with axial air injection, the increase of Axial Air Injection over a certain threshold disrupts the flowfield, with the vortex breakdown type shifting from a bubble type to a cone type and finally to no vortex breakdown [145].

Therefore, the POD applied to the fields of the cases with AAI = 20 % showed no particular features.

#### 5.4.2. Observations on Mixing

The Axial Air Injection affects the mixing as there is quite an abrupt division between the central non-swirling air and the swirling mixture.

The axial air injection mass flow rate decreases the swirling flow mass flow rate of the same quantity, maintaining the same total air mass flow rate in the combustor, so that the global equivalence ratio stays the same as the configuration without axial air injection. Still, unfortunately, given that there is no mixing between the central jet and the swirling jet, the equivalence ratio at which the flame will ignite will be inevitably higher.

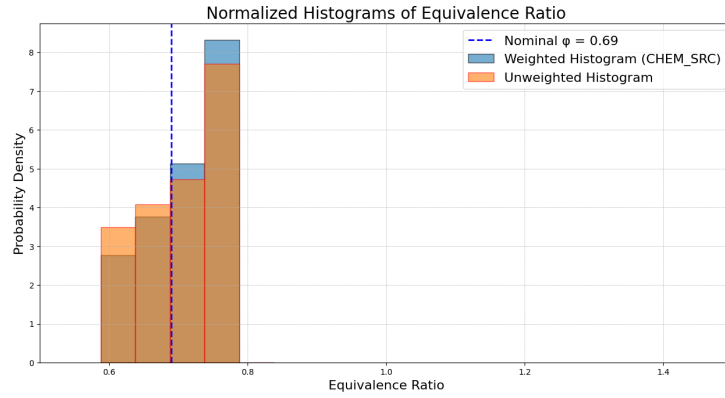


**Figure 5.50:** Equivalence Ratio Histogram for simulation S1. In order to acquire relevant data for the description of the flame, the datapoints  $\vec{x}$  are conditioned to satisfy  $HRR(\vec{x}) \geq 0.9HRR_{max}$

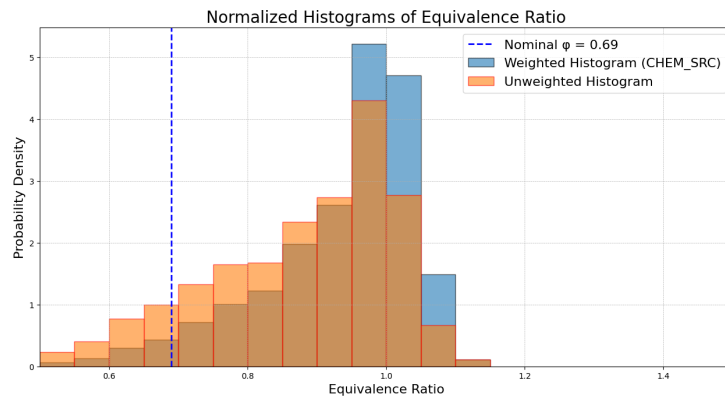


**Figure 5.51:** Equivalence Ratio Histogram for simulation S2. In order to acquire relevant data for the description of the flame, the datapoints  $\vec{x}$  are conditioned to satisfy  $HRR(\vec{x}) \geq 0.9HRR_{max}$

A comparison between the case without AAI and with AAI, including the resulting position of the flame, is shown below:

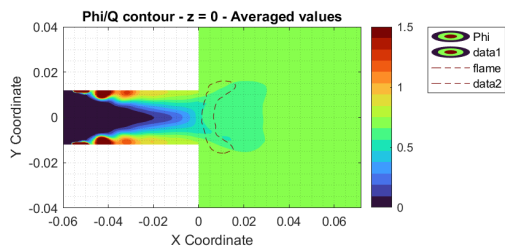


**Figure 5.52:** Averaged equivalence ratio contour with HRR isosurface for case S1

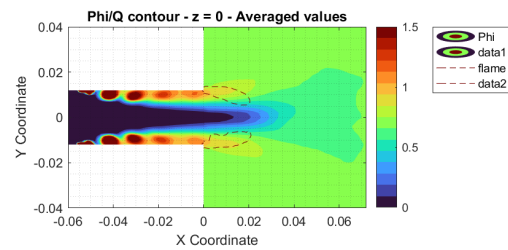


**Figure 5.53:** Averaged equivalence ratio contour with HRR isosurface for case S2

The comparison between the equivalence ratio and flame position increased the number of reasons for the misplacement of the flame position: the poor mixing in the S2 case also contributed to the upward shift in flame position, as the higher equivalence ratio mixture now present near the burner lip is more resistant to the combined effects of heat loss and strain.

### 5.4.3. Observations on NO Emissions

The observed variations in NO emissions are closely related to the mixing patterns and local equivalence ratios within the combustor. In particular, the poor mixing observed in case S2 results in higher NO emissions compared to case S1.

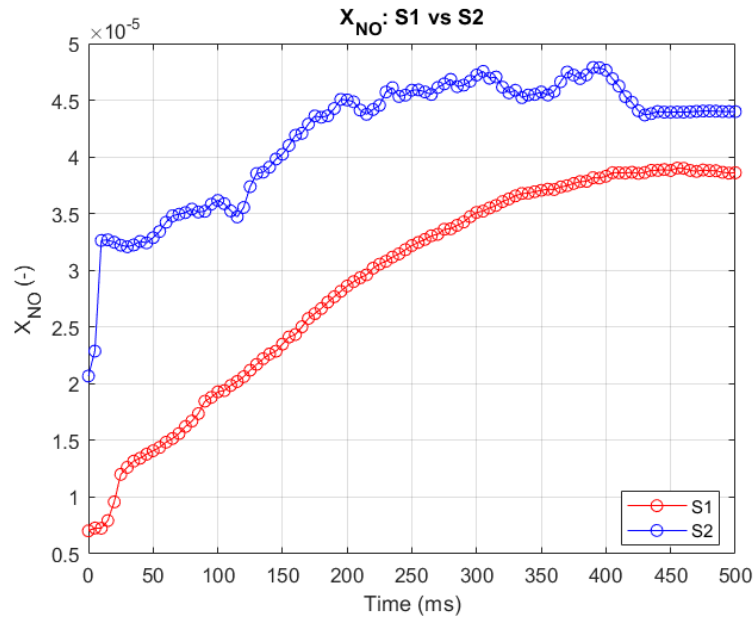


**Figure 5.54:** Volume-averaged NO molar fraction in the first 10 cm of the combustion chamber. Sampling starts 100 ms after the ignition.

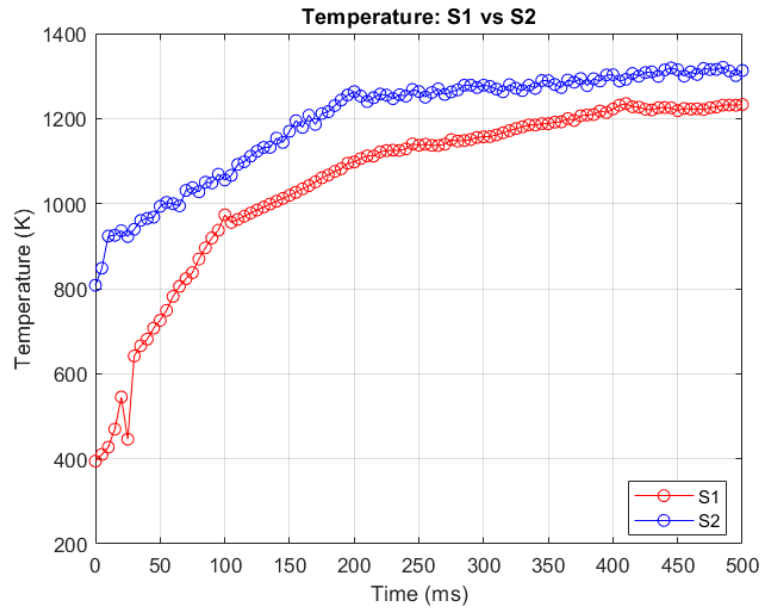


**Figure 5.55:** Volume-averaged Temperature in the first 10 cm of the combustion chamber. Sampling starts 100 ms after the ignition.

Analyzing the results from case S1, the extended residence times in the Outer Recirculation Zone (ORZ) underscore the importance of preventing ignition on the Outer Shear Layer (OSL). This is crucial to avoid the accumulation of hot, slow-moving combustion products within the chamber. The transition from a V-flame to an M-flame is further evidenced by a rapid change in temperature increase rate observed in the combustion chamber. Initially, 100 ms after ignition, the environment remains relatively low in NO emissions. However, around 200 ms post-ignition, the high temperatures in the ORZ facilitate the transition to an M-flame, which eventually results in NO levels comparable to those observed in case S2.

The following figures illustrate the local relationship between equivalence ratio and NO emissions for case 1, after the flame shape transition:

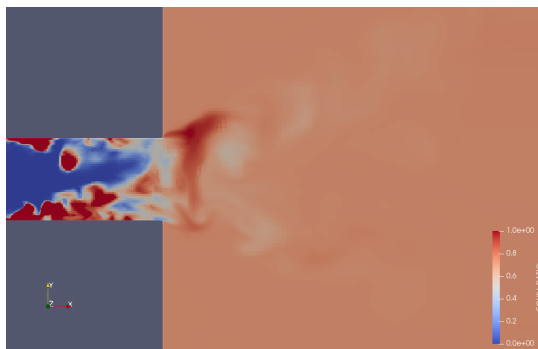


**Figure 5.56:** Equivalence ratio field in the flame region. The current flame shape is an M, with suppressed PVC in the chamber, but not in the mixing tube, resulting in richer reactant pockets.

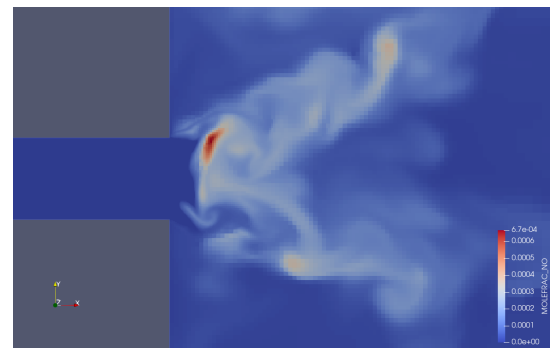


**Figure 5.57:** NO molar fraction field in the flame region. The richer reactant pockets result in higher flame temperatures, and on the same location higher levels of NO molar fraction are present.

The overall higher NO levels in case S2 can be attributed to the elevated local equivalence ratios in the flame region. A higher equivalence ratio in the flame region typically corresponds to a higher temperature, as the richer mixture leads to more intense combustion.

The elevated temperatures result in increased production rates of NO through the thermal NO<sub>x</sub> mechanism, which is sensitive to temperature changes. The thermal NO<sub>x</sub> formation is significantly influenced by the flame temperature, making the higher temperatures in case S2 a major factor in the observed increase in NO emissions. The higher NO presence does not necessarily overlap with a zone of high NO production, as the species can be produced elsewhere and convected in a different location.

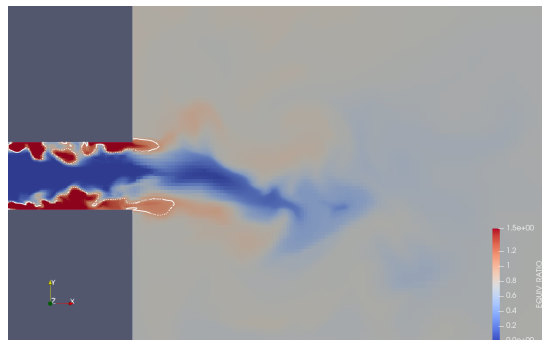


**Figure 5.58:** Equivalence ratio field in the flame region. A white isoline highlights the points at the stoichiometric equivalence ratio.

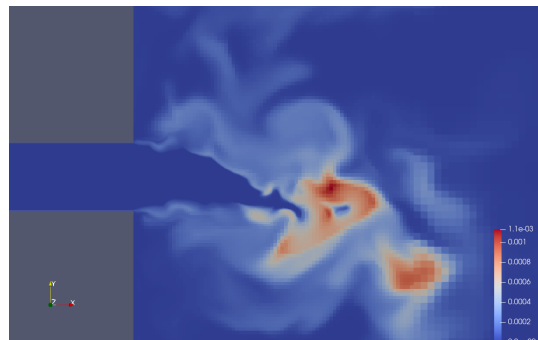


**Figure 5.59:** NO molar fraction field in the flame region. The higher concentration is present at the tip of the axial air flow, where high temperatures, N<sub>2</sub> and O<sub>2</sub> are both present in high quantity.

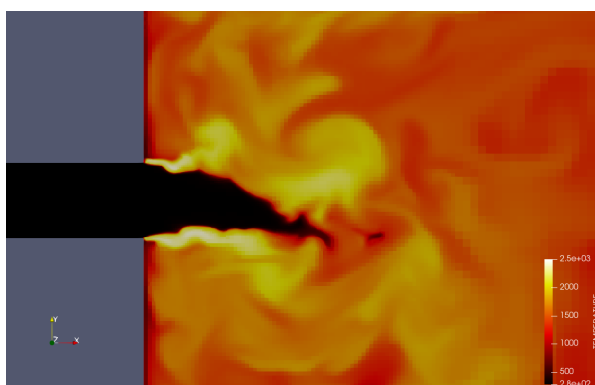


**Figure 5.60:** Temperature field in the flame region. High temperature combustion can be seen at the lip of the burner, where the flame is stabilized, but the hot products are convected to the center of the chamber, resulting in a higher average temperature of the flame region.

In this case, analyzing the flame front and its characteristics, it is possible to state that the higher NO production zone lies probably on the flame front, as shown by the scatterplots in Figure 5.61 and Figure 5.62, which try to recreate the framework study employed in a much simpler environment, 1D premixed flames, showed in Figure 5.1 and Figure 5.2. Analyzing the figures, the same HRR-NO correlation is identified, highlighting once again the responsibility of mixing in high NO production.



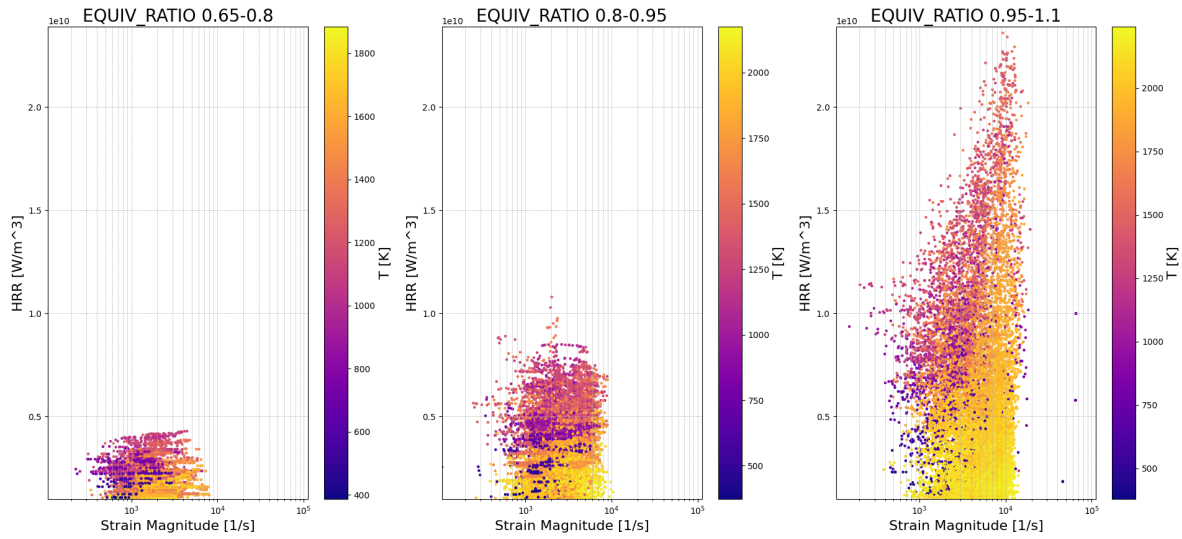


**Figure 5.61:** Simulation S2 - Heat Release Rate vs Strain scatterplot, coloured with temperature, to resemble the levels of Heat Loss parameters employed in CHEM1D. The strain magnitude is estimated following an approximation common in literature, retrieved in the Ansys theory manual [146].

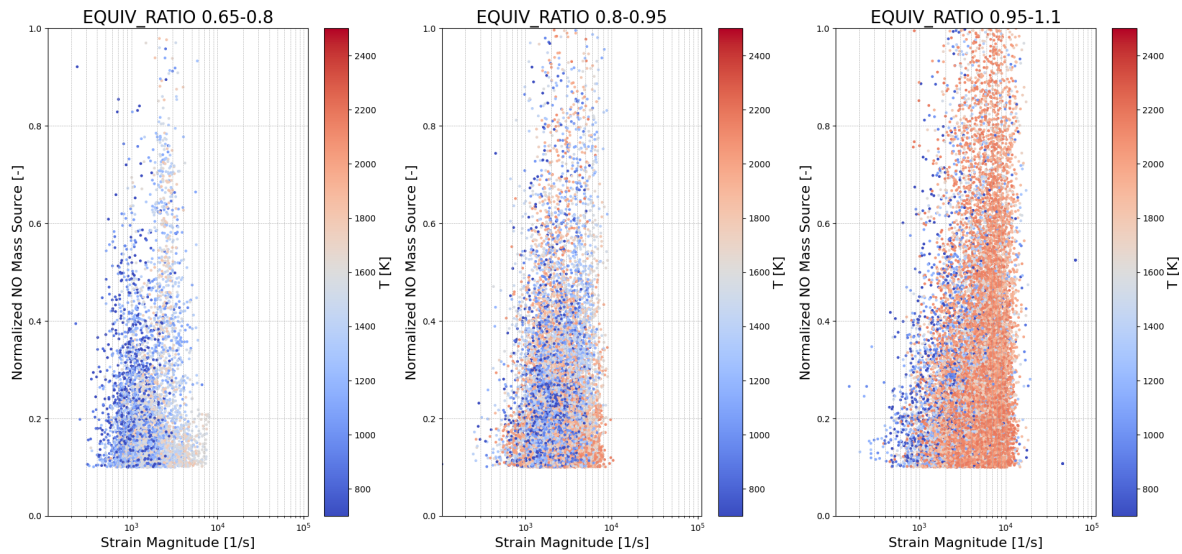


**Figure 5.62:** Simulation S2 - NO Mass Source vs Strain scatterplot, coloured with temperature, to resemble the levels of Heat Loss parameters employed in CHEM1D. *Note: only positive contribution are considered for this study.*

The comparison between cases S1 and S2 reveals that the inadequate mixing in case S2 indirectly results in higher NO emissions. This is primarily because the elevated local equivalence ratio and increased flame temperatures create a hotter environment. In this setting, the axial air injection, which does not participate to combustion, becomes a significant source of NO production. Of course, given that the level of NO in the combustion chamber accumulates in time, what should be extracted from this analysis is the rate of NO increase, as the characteristic time of the combustor would need an excessive amount of computational power to retrieve stable enough averages.

## 5.5. The Effect of H2 Enrichment: H2-60% with 20% AAI

Similar disagreements are found on the S3 case. However, given the high resistance to strain/heat-losses that are featured by highly hydrogen-enriched methane flames, the flame positions itself closer to the burner lip.

However, there is an inner shear layer flame region detected by the OH\* chemiluminescence images that the simulation does not predict, due again to the underestimation of axial-swirling flow interaction.

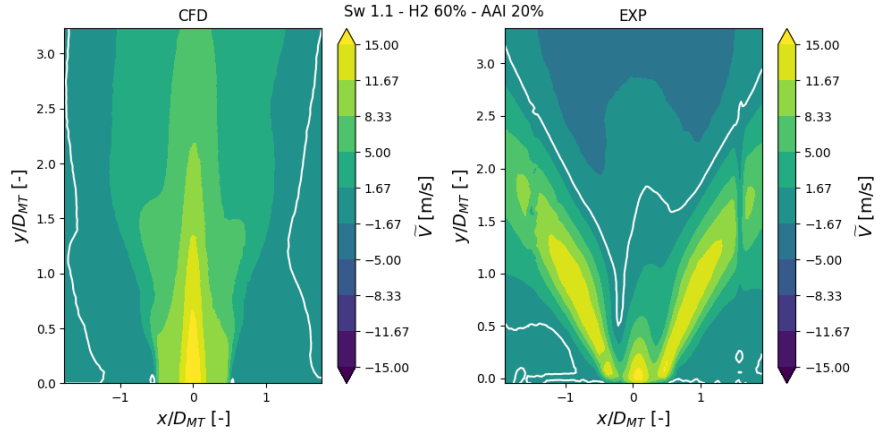


**Figure 5.63:** Averaged axial velocity field. An isoline is showed at  $V = 0\text{ m/s}$  to distinguish the recirculation zones.

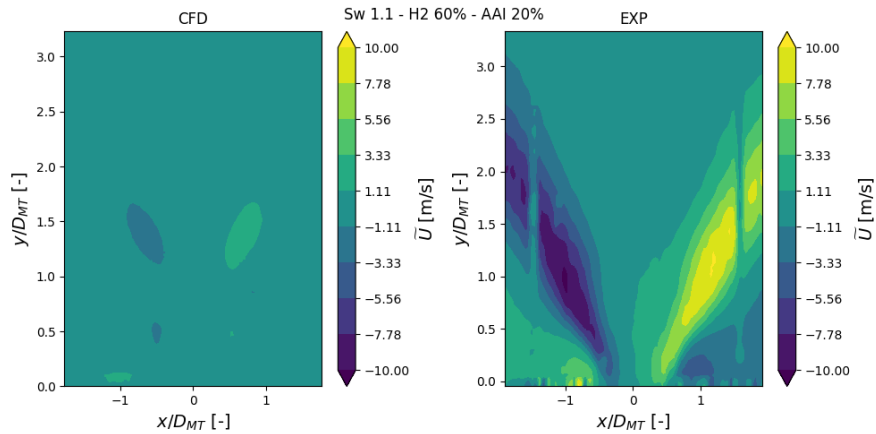


**Figure 5.64:** Averaged radial velocity field.

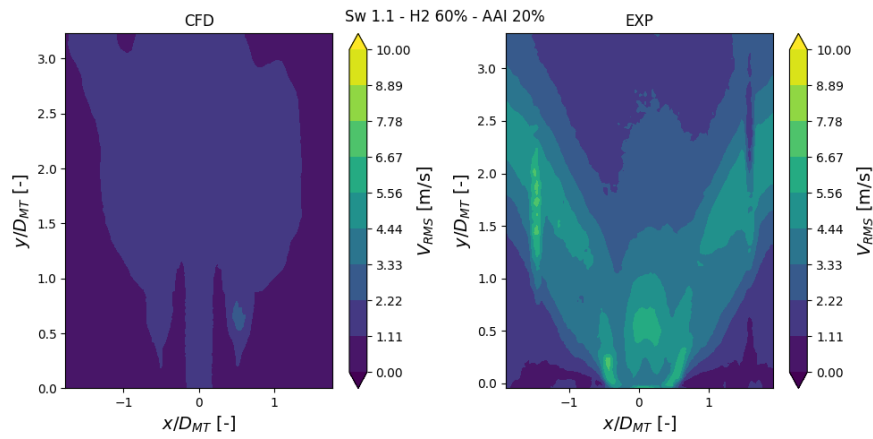


Figure 5.65: Axial velocity RMS field.

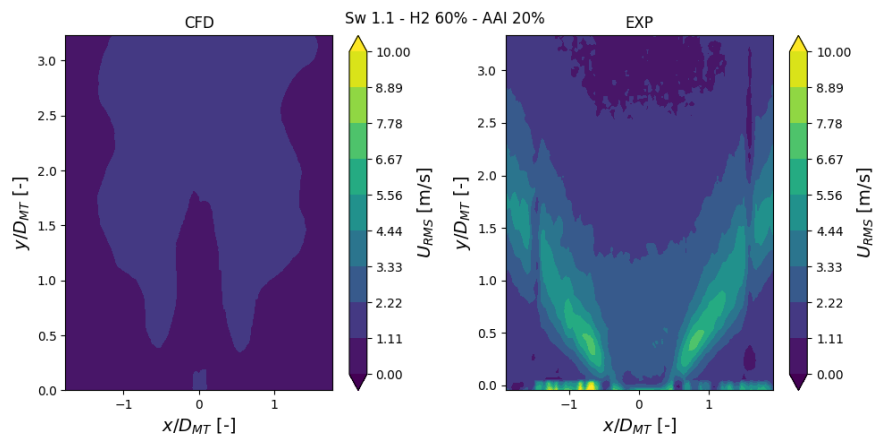


Figure 5.66: Radial velocity RMS field.

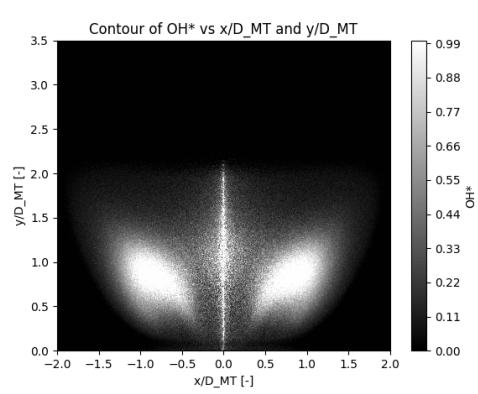


Figure 5.67: OH\* chemiluminescence image from experimental campaign.

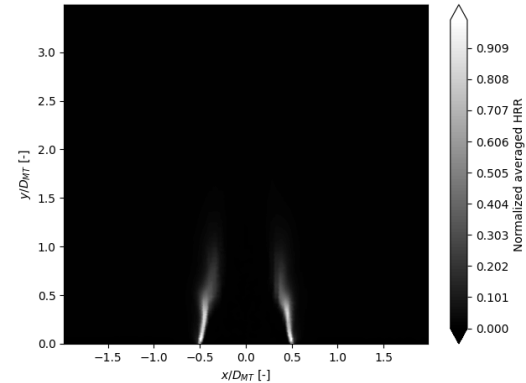
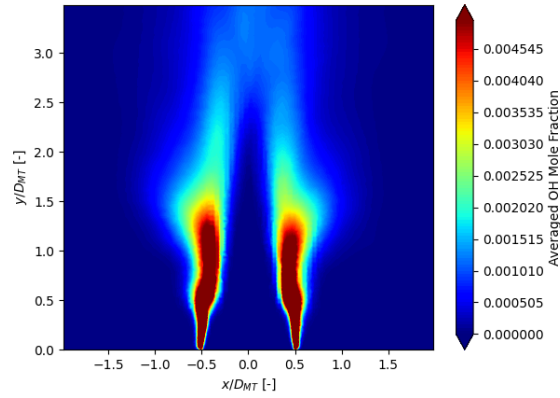


Figure 5.68: HRR averaged value.



**Figure 5.69:** Averaged OH molar fraction

### 5.5.1. Observations on Mixing - Effect of Fuel Momentum

Comparing the equivalence ratio conditioned at high values of HRR, it seems that switching to a higher percentage of hydrogen in the fuel mixture when injected in crossflow can be detrimental to mixing.

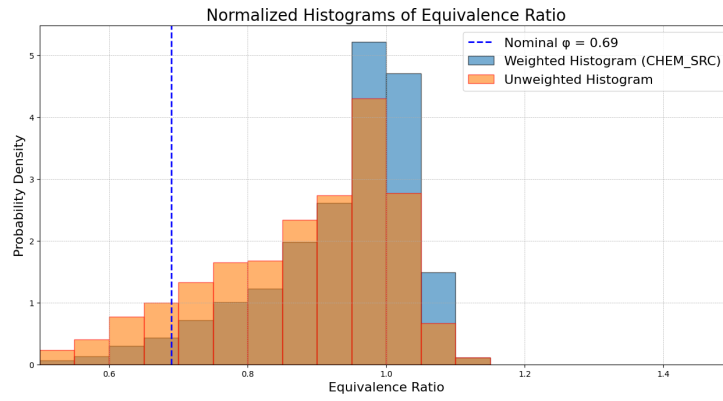


**Figure 5.70:** Equivalence Ratio Histogram for simulation S2. In order to acquire relevant data for the description of the flame, the datapoints  $\vec{x}$  are conditioned to satisfy  $\text{HRR}(\vec{x}) \geq 0.9\text{HRR}_{max}$

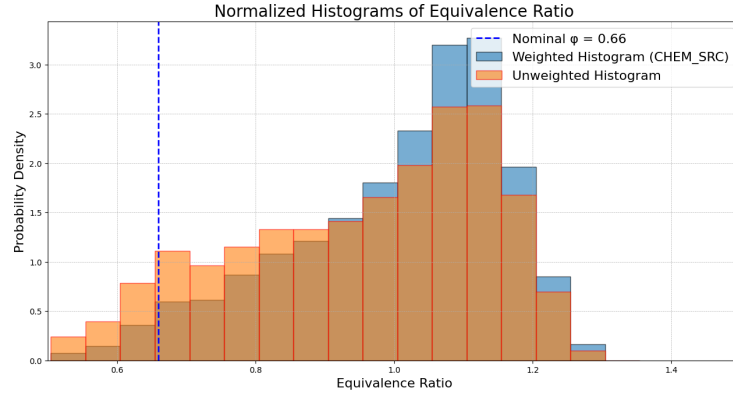


**Figure 5.71:** Equivalence Ratio Histogram for simulation S3. In order to acquire relevant data for the description of the flame, the datapoints  $\vec{x}$  are conditioned to satisfy  $\text{HRR}(\vec{x}) \geq 0.9\text{HRR}_{max}$

One reason for the reduced mixing could lie in the fuel to air momentum ratio increase: as mentioned before in some preliminary characteristic length and speed estimation listed in Table 4.3, the fuel momentum ratio increases from 2.274 to 2.787, with the fuel inlet velocity increasing from 19.696  $m/s$  to 27.964  $m/s$ , while the swirling air stays at 8.579  $m/s$ .

However, this increase seems to be poorly contributing to the reduced mixing, as, locally, close to the injection point ( $x = -0.055m$ ), there is no significant difference in the depth reached by the equivalence ratio peak.

This is probably due to the high pressure gradient due to the swirling motion, preventing the crossflow injection to pierce through the swirling flow:

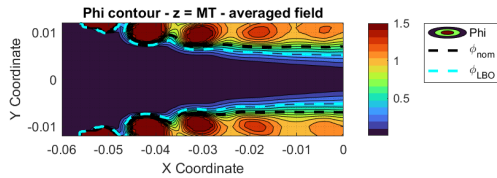


**Figure 5.72:** Averaged equivalence ratio contour with Lean Blow Off Limit and nominal equivalence ratio isosurface for case S2

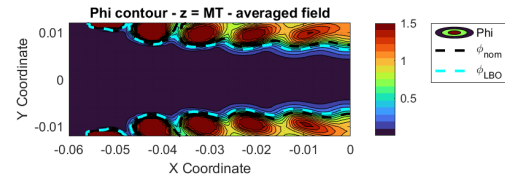


**Figure 5.73:** Averaged equivalence ratio contour with Lean Blow Off Limit and nominal equivalence ratio isosurface for case S3

Even though, as just mentioned, the local injection velocity does not result in relevant jet penetration, from Figure 5.74 and Figure 5.75 it is possible to see, through contours of equivalence ratio at a x-normal slice at  $x = -0.03m$  in the mixing tube, how the case S3 is already less mixed at this stage.

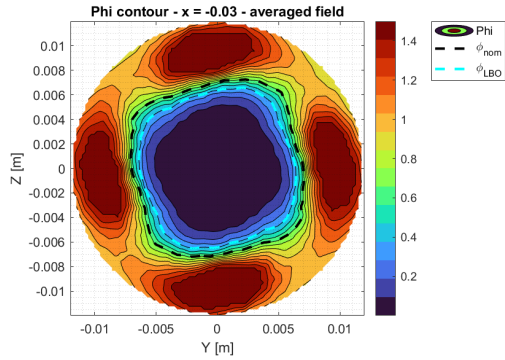


**Figure 5.74:** Averaged equivalence ratio contour with Lean Blow Off Limit and nominal equivalence ratio isosurface for case S2

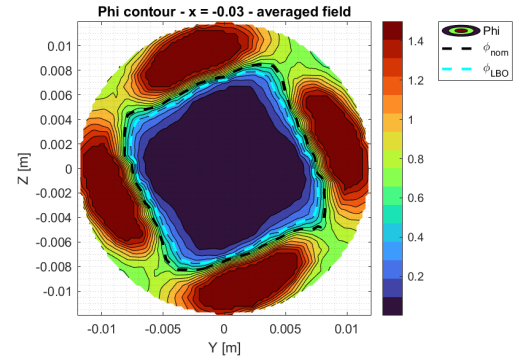


**Figure 5.75:** Averaged equivalence ratio contour with Lean Blow Off Limit and nominal equivalence ratio isosurface for case S3

The S3 case presents lower equivalence ratio zones between the fuel streaks. Assuming that the losses in fuel momentum, when entrained in the swirling flow, are low, this loss in mixing efficiency could be attributed to the higher velocity difference between the fuel and swirling air, reducing the time spent in the mixing tube, resulting in a lower exchange of mass/species.

Following the swirling motion up to the x-normal slice at  $x = 0.0m$ , at the mixing tube exit, it is possible to see that the hydrogen-rich fuel tends to stay closer to the wall of the mixing tube, further reducing its interaction with the core air.

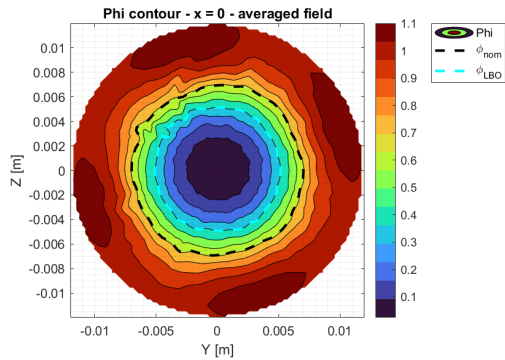


**Figure 5.76:** Averaged equivalence ratio contour with Lean Blow Off Limit and nominal equivalence ratio isosurface for case S2

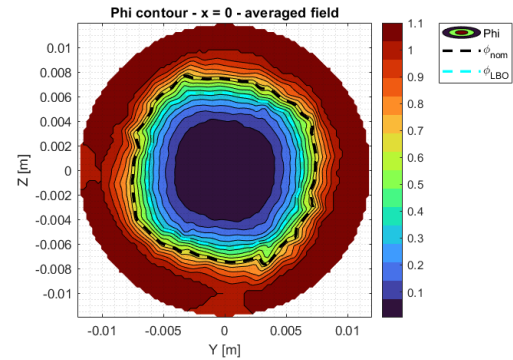


**Figure 5.77:** Averaged equivalence ratio contour with Lean Blow Off Limit and nominal equivalence ratio isosurface for case S3

This leads to poor mixing, incomplete combustion, and potentially higher emissions, as the fuel and air do not mix uniformly, compromising the overall performance of the combustion process.

### 5.5.2. Observations on NO Emissions

The insights gained from comparing NO levels between cases S1 and S2 are also applicable here, providing valuable information on the mixing performance of a hydrogen-enriched mixture.

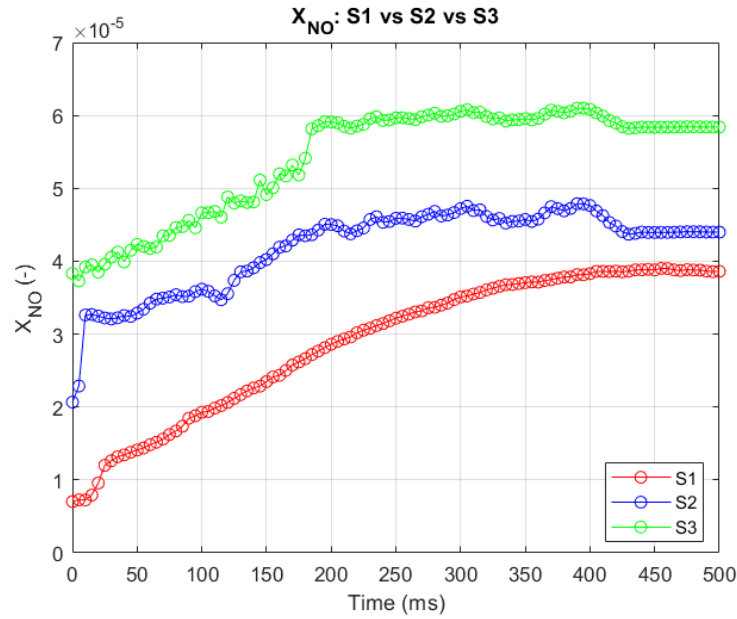


**Figure 5.78:** Volume-averaged NO molar fraction in the first 10 cm of the combustion chamber. Sampling starts 100 ms after the ignition.

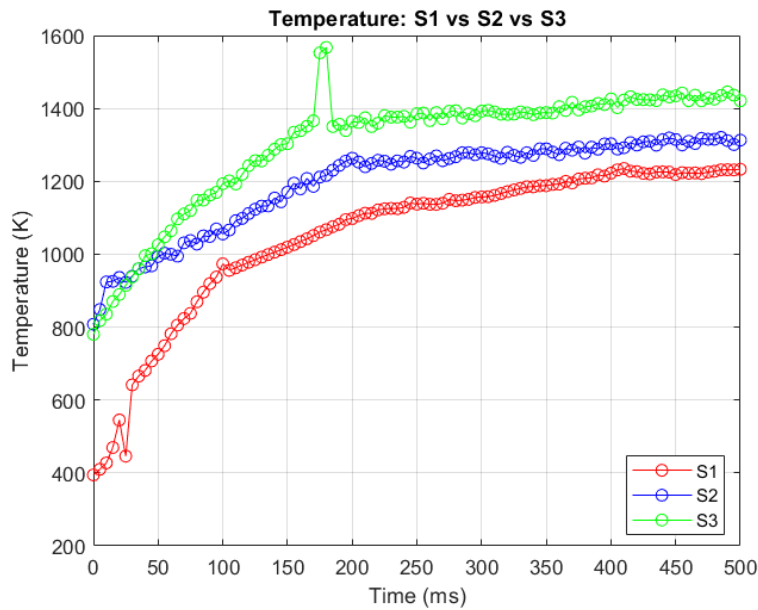


**Figure 5.79:** Volume-averaged Temperature in the first 10 cm of the combustion chamber. Sampling starts 100 ms after the ignition.

Compared to case S2, case S3 shows a further increase in NO production. The zone of high NO emission near the tip of the axial air injection jet mirrors the pattern observed in case S2. However, a stronger NO emission signal emerges in case S3: the flame itself. This is illustrated in the following figures:

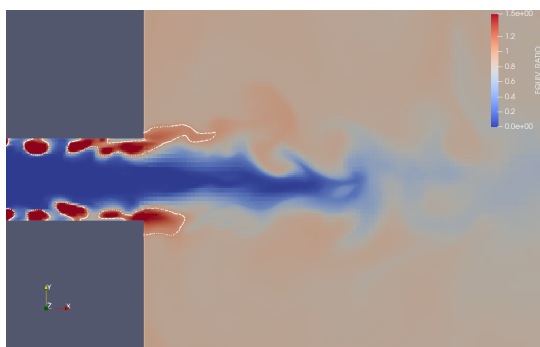


**Figure 5.80:** Equivalence ratio field in the flame region. A white isoline highlights the points at the stoichiometric equivalence ratio.

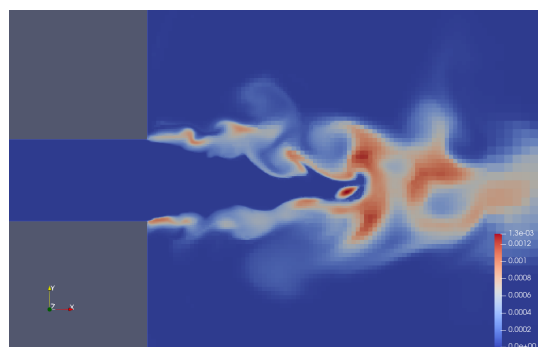


**Figure 5.81:** NO molar fraction field in the flame region. The higher concentration is present at the tip of the axial air flow, where high temperatures, N<sub>2</sub> and O<sub>2</sub> are both present in high quantity. Comparing it with Figure 5.59, however, a higher NO concentration can be seen also close to the flame.

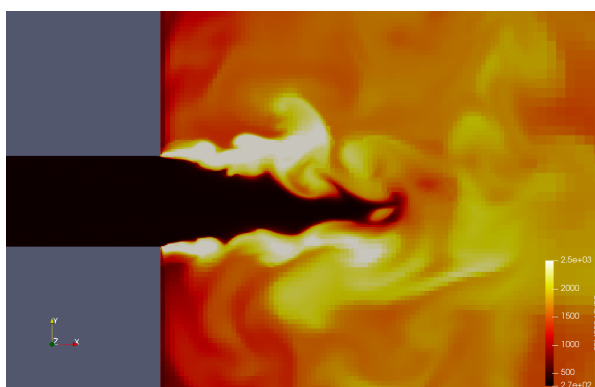


**Figure 5.82:** Temperature field in the flame region. High temperature combustion can be seen at the lip of the burner, where the flame is stabilized, but the hot products are convected to the center of the chamber, resulting in a higher average temperature of the flame region.

Consistent with the findings of Capurso et al. [111], the increased hydrogen fraction in the mixture may enhance other NO formation mechanisms, such as those involving N<sub>2</sub>O and NNH. This could lead to increased NO production with different rates, enhanced by the presence of O and H atoms, at the flame front:



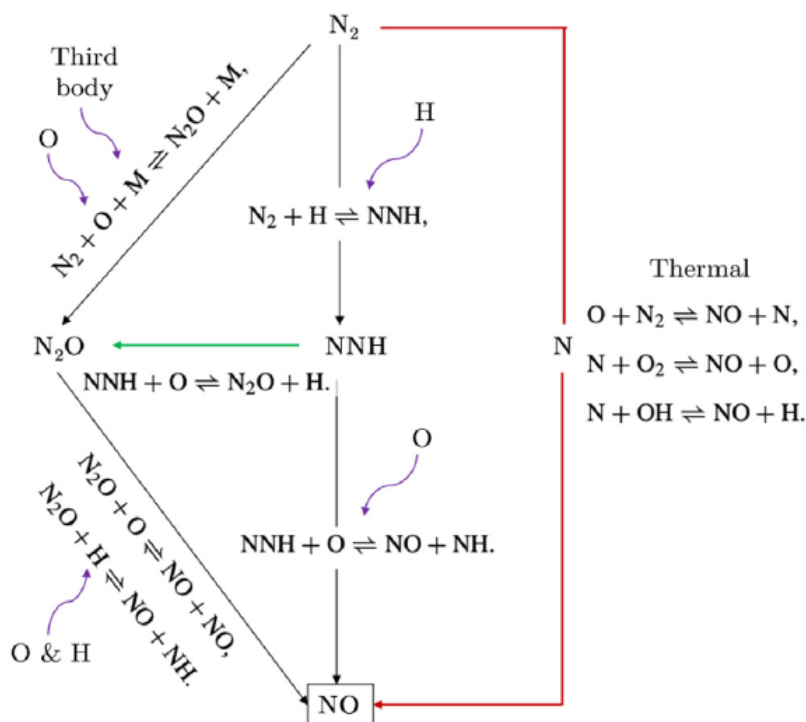


**Figure 5.83:** Schematic representation of the pathways, reactions and molecules involved in the NO formation for H<sub>2</sub>/air combustion. Adapted from [111].

Before concluding with certainty that the *secondary* NO production mechanisms are responsible for this increase in NO emissions, it is important to state that this could be just an effect of an excessively thickened flame front: when introducing more H<sub>2</sub> in the fuel mixture, the flame thickness tends to get shorter, making it necessary to thicken the flame region with high thickening factor, resulting in high pseudochemical times of brief-lived intermediate species, such as H and O, which are not encountered in the actual flame. Therefore, given this uncertainty and the impossibility to further refine the flame front because of exponentially growing computational costs, the NNH and N<sub>2</sub>O mechanisms remain a hypothesis. However, the quantification of their effects with respect to the simple higher temperature remains unsolved.

The analysis of NO emissions across different cases demonstrates significant insights into the effects of mixing performance and fuel composition on emission levels. The comparisons reveal that poor mixing, as observed in cases with axial air injection (S2), leads to elevated NO emissions due to the increased local equivalence ratio and higher flame temperatures. This trend is further amplified in the hydrogen-enriched case (S3), where the introduction of hydrogen enhances even other NO production mechanisms, such as N<sub>2</sub>O and NNH.

## Conclusions and Next Steps

This thesis has explored several key challenges and strategies related to the discovery of steady and unsteady characteristics of hydrogen-enriched swirl-stabilized flames with axial air injection. A method, Heat Resistance Tuning (HRT), has been modified, avoiding the reliance on thermal measurements when applied to low-Bi bodies, without incurring in high computational costs. It is necessary to say that unfortunately a promising feature of this approach has not been exploited: its dynamic formulation, recalculating Heat Resistance Tuning (HRT) at each iteration of the fluid solver, rather than waiting for a steady-state solution. This approach could reduce the risk of flame shape transition and the corresponding hysteresis.

In this set of simulations, a V-M flame shape transition was uncovered, providing insights into the stabilization mechanisms that characterize each flame shape. These experiments and simulations demonstrated the strong dependence of swirl-stabilized, hydrogen-enriched methane flames on initial and boundary conditions, such as ignition type and thermal boundary conditions, and they revealed how the resulting combustion characteristics, e.g. emissions, can be affected.

The Proper Orthogonal Decomposition (POD) method has proven invaluable in this research, particularly given the intrinsic unsteadiness of swirl-stabilized flows. Traditional averaging techniques are insufficient for capturing the complex dynamics at play. The strategic placement of diagnostic clouds of points revealed the presence of a Precessing Vortex Core (PVC) exclusively placed in the mixing tube, which was not detected in the experimental campaign. This detection revealed to be of the utmost importance, given the role of the PVC in the interaction between the PVC, mixing processes, and the flame, ultimately explaining the upstream positioning of the flame front, also thanks to the application of POD to other unusual quantities, such as the equivalence ratio and the heat release rate.

From a turbulent combustion modeling perspective, the Thickened Flame Model (TFM), combined with the Adaptive Mesh Refinement (AMR) strategy in CONVERGE, has shown promising results with relatively low computational effort. However, further care is needed in wall treatment. Currently, the TFM is deactivated when the distance from the wall is less than the flame thickness, but the influence of the wall on the flame can extend beyond this distance, both through direct and indirect mechanisms. This issue, discussed in the theoretical review of flame-wall interaction modeling, suggests that the current approach may underestimate the wall's impact.

Furthermore, the assessment of the Axial Air Injection (AAI) revealed a significant flaw of the flashback prevention method: a reduction in mixing efficiency when the combustor configuration involves fuel injection in crossflow, with further detrimental effects when higher fuel momentum ratio injections are performed. This decline in mixing efficiency seems to be the primary reason for the increase in NO emissions, despite the theoretically lower temperatures due to the reduced global equivalence ratio. In fact, from detailed examination of NO molar fractions, temperature fields, and equivalence ratios it

is highlighted that while the axial air injection prevents flashback, extending the flashback limits of a combustion setup, it inadvertently creates zones of high equivalence ratio and temperature that promote NO formation. The addition of hydrogen exacerbates this effect by accelerating the NO production processes within the flame region.

## 6.1. Next Steps

Looking ahead, several key areas warrant further investigation:

- **Thermal Boundary Condition Prediction:** Continued exploration of methods to improve thermal boundary condition predictions is crucial. *Implementing thermal capacitors [147] and dynamically recalculating HRT* during fluid solver iterations could significantly enhance the accuracy of these predictions without increasing computational demands. Additionally, incorporating Conjugate Heat Transfer (CHT) simulations will be essential for validating and refining these low-order heat transfer methods.
- **Experimental Validation:** To complement the computational findings, additional experimental studies are recommended, particularly those that can *validate the presence and impact of the PVC in the mixing tube*. Moreover, experiments employing high temperature bodies close to the flame should be performed in order to prove the high-Temperature-high-NO correlation displayed in 1D and 3D simulations presented in this thesis. This would provide a more comprehensive understanding of the flow and flame dynamics and further inform model development.
- **H<sub>2</sub>-Enriched Swirl-Stabilized Flame Dynamics:** Investigating the *influence of initial conditions*, such as pilot flame type, *dynamic fuel composition experiments and thermal boundary conditions* on flame shape dynamics could enhance our understanding and control of hydrogen-enriched methane flames. This includes examining the effects of varying the hydrogen volume fraction during experiments to observe flame shape transitions, hysteresis effects, and their impact on temperature and emissions.
- **Wall/Flame Interaction Modeling:** Further *refinement of wall treatment within the TFM* is needed to better capture the wall's influence on flame behaviour. This could involve developing new models or adjusting existing ones to account for wall effects over greater distances.
- **Mixing Efficiency and NO Emissions:** The observed reduction in mixing efficiency with AAI in crossflow fuel injection configurations highlights the need to *explore alternative injection strategies* that enhance mixing. Addressing this issue is critical for mitigating NO emissions, above all in cases where a lower global equivalence ratio is used.

By addressing these areas, future research can expand upon the groundwork established in this thesis, furthering our understanding of thermal load management, turbulent combustion, and flame dynamics, ultimately moving closer to achieving a truly fuel-agnostic combustion system.

# A

## Appendix A: Mechanism Reduction

The computational cost of simulating detailed chemical kinetics can be prohibitively high, especially when dealing with complex mechanisms like GRI 3.0 [148], which is widely used for modeling combustion of natural gas and other hydrocarbons. The GRI 3.0 mechanism consists of 53 species and 325 reactions, making it computationally intensive for high-fidelity simulations. To address this challenge, mechanism reduction techniques can be applied to create simplified versions of the mechanism that retain the essential chemical characteristics while significantly reducing computational demands.

### A.1. Mechanism reduction methodology

This chapter presents the results of the mechanism reduction process conducted on the GRI 3.0 mechanism using ANSYS-CHEMKIN Workbench [149]. The reduction aimed to minimize the number of species while maintaining critical combustion properties, such as the emission index of nitrogen oxides (EI\_NOx), ignition delay time, and flame speed, within a 5% tolerance of the original mechanism. The reduction was achieved using Direct Relation Graph (DRG), Directed Relation Graph with Error Propagation (DRGEP), and Directed Relation Graph with Sensitivity Analysis (DRGSA) [150] [151] [152].

- **Direct Relation Graph (DRG):**

DRG is a graph-based method where species and reactions are represented as nodes and edges. The method eliminates species with weak influence on the target species or reactions, determined by a user-defined threshold. DRG was applied as the initial step in the reduction process, providing a preliminary reduced mechanism by pruning less significant species and reactions.

- **Directed Relation Graph with Error Propagation (DRGEP):**

DRGEP improves upon DRG by considering the error propagation through the reaction network. This method ensures that the influence of removed species on the target species is minimal. DRGEP was used to refine the reduction obtained from DRG, further eliminating species while controlling the error in the predicted combustion properties.

- **Directed Relation Graph with Sensitivity Analysis (DRGSA):**

DRGSA combines the DRG approach with sensitivity analysis to assess the importance of species. Sensitivity analysis evaluates how variations in species concentration affect key combustion properties.

### A.2. Validation Across Operating Conditions

The original GRI 3.0 mechanism consists of 53 species and 325 reactions. Through the application of the DRG, DRGEP, and DRGSA techniques in sequence, the mechanism was successfully reduced to 23 species and 199 reactions.

	GRI 3.0	Reduced GRI 3.0
Number of Species	53	23
Number of Reactions	325	199
% Reduction in Species	0%	57%
% Reduction in Reactions	0%	39%

**Table A.1:** Summary of the reduction in species and reactions achieved in the GRI 3.0 mechanism through the application of DRG, DRGEP, and DRGSA techniques.

During the reduction process, the tolerances were imposed on the figures of merit cited before (EI\_NOx, IDT, LFS), but to ensure the robustness and applicability of the reduced mechanism, its performance was validated across a broader range of operating conditions. The operating conditions tested include a range of equivalence ratios: [0.5, 0.7, 0.9, 1.1, 1.3, 1.5], and hydrogen volume fractions: [0.0, 0.2, 0.4, 0.6, 0.8, 1.0]. Here it is reported the validation on a smaller set of variables:

- **Laminar Flame Speed:**

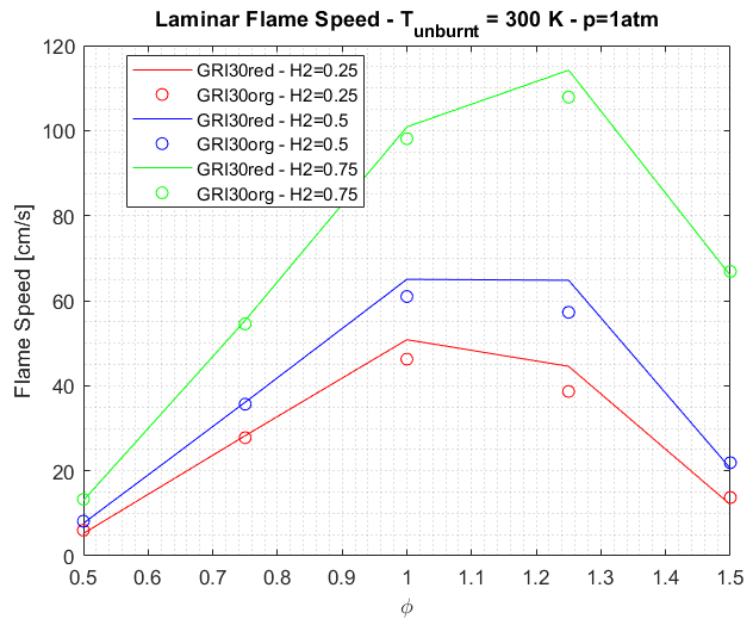


**Figure A.1:** Comparison of the laminar flame speed for the original GRI 3.0 and reduced GRI 3.0 mechanisms at varying equivalence ratios. The results are shown for different hydrogen fractions in the fuel mixture. The reduced mechanism closely matches the original mechanism across the range of equivalence ratios, indicating good performance in predicting flame speeds.

- **Ignition Delay Time:**

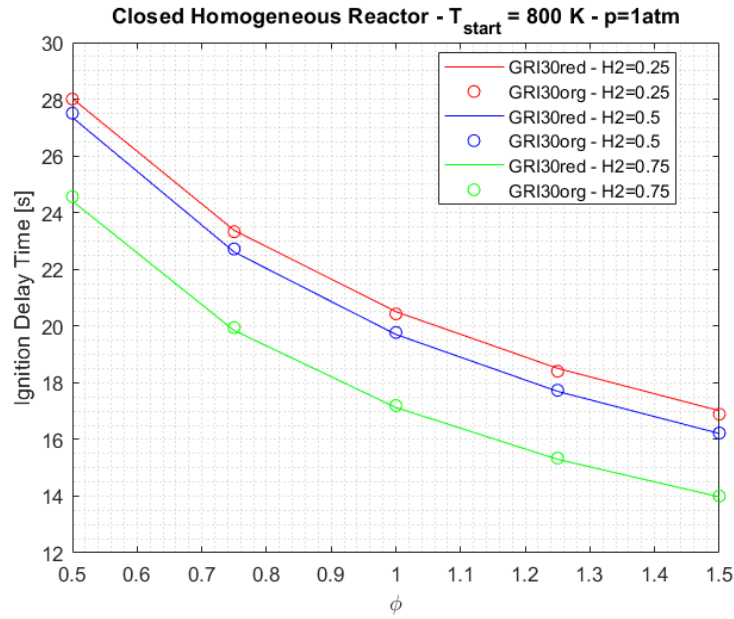


**Figure A.2:** Comparison of ignition delay times for the original GRI 3.0 and reduced GRI 3.0 mechanisms across various equivalence ratios and hydrogen fractions. The reduced mechanism demonstrates similar predictive capability to the original mechanism, maintaining accuracy in ignition delay times.

- **NO Emission Index:**

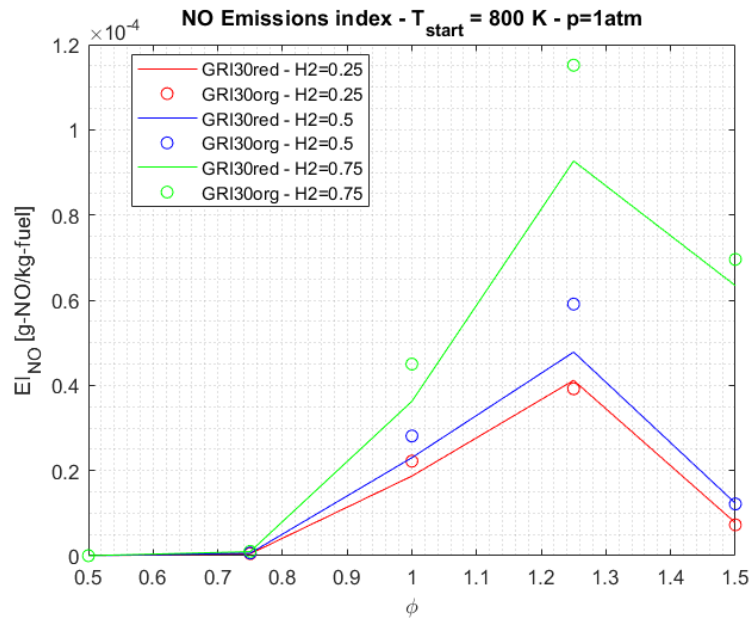


**Figure A.3:** Comparison of NO emission indices between the original GRI 3.0 and reduced GRI 3.0 mechanisms for different equivalence ratios and hydrogen fractions. The reduced mechanism provides a reliable estimation of NO emissions, closely following the trends observed in the original mechanism, validating its effectiveness for emissions prediction.

The results demonstrated that the reduced mechanism performs well across these varied conditions, retaining the essential characteristics needed for accurate simulations. This validation confirms the reduced mechanism's utility in computationally intensive simulations, where maintaining high fidelity with reduced computational expense is critical.

# References

- [1] *Sixth Assessment Report — IPCC*. URL: <https://www.ipcc.ch/assessment-report/ar6/> (visited on 02/28/2024).
- [2] *IPCC — Intergovernmental Panel on Climate Change*. URL: <https://www.ipcc.ch/> (visited on 02/28/2024).
- [3] Paola Arias et al. “Climate Change 2021: The Physical Science Basis. Contribution of Working Group I to the Sixth Assessment Report of the Intergovernmental Panel on Climate Change; Technical Summary”. In: ed. by Valérie Masson-Delmotte et al. Remote, 2021. URL: <https://www.ipcc.ch/report/ar6/wg1/> (visited on 02/28/2024).
- [4] Camille Parmesan, Mike D. Morecroft, and Yongyut Trisurat. *Climate Change 2022: Impacts, Adaptation and Vulnerability*. Research Report. GIEC, Feb. 2022. URL: <https://hal.science/hal-03774939> (visited on 02/28/2024).
- [5] Priyadarshi R. Shukla et al., eds. *Climate Change 2022: Impacts, Adaptation and Vulnerability. Contribution of Working Group III to the Sixth Assessment Report of the Intergovernmental Panel on Climate Change*. 2022. ISBN: 978-92-9169-160-9. DOI: 10.1017/9781009157926.
- [6] G.P. Brasseur et al. “European scientific assessment of the atmospheric effects of aircraft emissions”. en. In: *Atmospheric Environment* 32.13 (July 1998), pp. 2329–2418. ISSN: 13522310. DOI: 10.1016/S1352-2310(97)00486-X. URL: <https://linkinghub.elsevier.com/retrieve/pii/S135223109700486X> (visited on 02/28/2024).
- [7] *Aviation and the Global Atmosphere — IPCC*. URL: <https://www.ipcc.ch/report/aviation-and-the-global-atmosphere-2/> (visited on 02/28/2024).
- [8] David S. Lee et al. “Aviation and global climate change in the 21st century”. In: *Atmospheric Environment* 43.22 (July 2009), pp. 3520–3537. ISSN: 1352-2310. DOI: 10.1016/j.atmosenv.2009.04.024. URL: <https://www.sciencedirect.com/science/article/pii/S1352231009003574> (visited on 02/28/2024).
- [9] M. Prather et al. *Potential Climate Change from Aviation*. Contribution to a Collection. ISBN: 9780521663007 Publisher: Cambridge University Press Volume: p. 185-215. 1999. URL: <https://elib.dlr.de/9104/> (visited on 02/28/2024).
- [10] Don Wuebbles, Mohan Gupta, and Malcolm Ko. “Evaluating the impacts of aviation on climate change”. en. In: *Eos, Transactions American Geophysical Union* 88.14 (2007). \_eprint: <https://onlinelibrary.wiley.com/doi/pdf/10.1029/2007EO140001>, pp. 157–160. ISSN: 2324-9250. DOI: 10.1029/2007EO140001. URL: <https://onlinelibrary.wiley.com/doi/abs/10.1029/2007EO140001> (visited on 02/28/2024).
- [11] D. S. Lee et al. “The contribution of global aviation to anthropogenic climate forcing for 2000 to 2018”. In: *Atmospheric Environment* 244 (Jan. 2021), p. 117834. ISSN: 1352-2310. DOI: 10.1016/j.atmosenv.2020.117834. URL: <https://www.sciencedirect.com/science/article/pii/S1352231020305689> (visited on 02/28/2024).
- [12] *Commercial Market Outlook*. en-US. URL: <https://www.boeing.com/content/theboeingcompany/us/en/commercial/market/commercial-market-outlook> (visited on 02/28/2024).

- [13] *Airbus: Global Market Forecast 2019-2038 - Google Scholar*. URL: [https://scholar.google.com/scholar\\_lookup?title=Global%20Market%20Forecast%202017%E2%80%93932036&author=Airbus&publication\\_year=2017#d=gs\\_cit&t=1709131095549&u=%2Fscholar%3Fq%3Dinfo%3AwAYzCQ7RgPMJ%3Ascholar.google.com%2F%26output%3Dcite%26scirp%3D0%26hl%3Dit](https://scholar.google.com/scholar_lookup?title=Global%20Market%20Forecast%202017%E2%80%93932036&author=Airbus&publication_year=2017#d=gs_cit&t=1709131095549&u=%2Fscholar%3Fq%3Dinfo%3AwAYzCQ7RgPMJ%3Ascholar.google.com%2F%26output%3Dcite%26scirp%3D0%26hl%3Dit) (visited on 02/28/2024).
- [14] International Energy Agency (IEA). *Oil Information (2022 Edition)*. en. 2022. DOI: 10.5257/IEA/OIL/2022. URL: <https://beta.ukdataservice.ac.uk/datacatalogue/doi/?id=5187> (visited on 02/28/2024).
- [15] R. Sausen and U. Schumann. “Estimates of the climate response to aircraft CO<sub>2</sub> and NO(x) emissions scenarios”. English. In: *Climatic Change* 44.1-2 (2000), pp. 27–58. ISSN: 0165-0009. DOI: 10.1023/a:1005579306109.
- [16] *World Airlines Traffic and Capacity*. en-US. URL: <https://www.airlines.org/dataset/world-airlines-traffic-and-capacity/> (visited on 02/28/2024).
- [17] Corinne Le Quéré et al. “Global Carbon Budget 2018”. English. In: *Earth System Science Data* 10.4 (Dec. 2018). Publisher: Copernicus GmbH, pp. 2141–2194. ISSN: 1866-3508. DOI: 10.5194/essd-10-2141-2018. URL: <https://essd.copernicus.org/articles/10/2141/2018/> (visited on 02/28/2024).
- [18] *List of OECD Member countries - Ratification of the Convention on the OECD*. URL: <https://www.oecd.org/about/document/ratification-oecd-convention.htm> (visited on 02/28/2024).
- [19] Fuel Cells and Hydrogen 2 Joint Undertaking (EU body or agency) Now known as. *Hydrogen-powered aviation: a fact based study of hydrogen technology, economics, and climate impact by 2050*. eng. LU: Publications Office of the European Union, 2020. ISBN: 978-92-9246-342-7. URL: <https://data.europa.eu/doi/10.2843/471510> (visited on 02/28/2024).
- [20] Somtochukwu Godfrey Nnabuife et al. “Present and Projected Developments in Hydrogen Production: A Technological Review□”. In: *Carbon Capture Science & Technology* 3 (June 2022), p. 100042. ISSN: 2772-6568. DOI: 10.1016/j.ccst.2022.100042. URL: <https://www.sciencedirect.com/science/article/pii/S2772656822000136> (visited on 02/28/2024).
- [21] Yukitaka Murakami. “21 - Hydrogen embrittlement”. In: *Metal Fatigue (Second Edition)*. Ed. by Yukitaka Murakami. Academic Press, Jan. 2019, pp. 567–607. ISBN: 978-0-12-813876-2. DOI: 10.1016/B978-0-12-813876-2.00021-2. URL: <https://www.sciencedirect.com/science/article/pii/B9780128138762000212> (visited on 03/02/2024).
- [22] *The European Hydrogen Backbone (EHB) initiative | EHB European Hydrogen Backbone*. en. URL: <https://ehb.eu/> (visited on 02/28/2024).
- [23] S. Gersen et al. “Ignition properties of methane/hydrogen mixtures in a rapid compression machine”. In: *International Journal of Hydrogen Energy* 33.7 (Apr. 2008), pp. 1957–1964. ISSN: 0360-3199. DOI: 10.1016/j.ijhydene.2008.01.017. URL: <https://www.sciencedirect.com/science/article/pii/S036031990800089X> (visited on 03/01/2024).
- [24] RAMANAN SANKARAN and HONG G. IM. “Effects of Hydrogen Addition on the Markstein Length and Flammability Limit of Stretched Methane/Air Premixed Flames”. In: *Combustion Science and Technology* 178.9 (Sept. 2006). Publisher: Taylor & Francis \_eprint: <https://doi.org/10.1080/00102200500536217> pp. 1585–1611. ISSN: 0010-2202. DOI: 10.1080/00102200500536217. URL: <https://doi.org/10.1080/00102200500536217> (visited on 03/01/2024).



- [25] S. Taamallah et al. "Fuel flexibility, stability and emissions in premixed hydrogen-rich gas turbine combustion: Technology, fundamentals, and numerical simulations". In: *Applied Energy* 154 (Sept. 2015), pp. 1020–1047. ISSN: 0306-2619. DOI: 10.1016/j.apenergy.2015.04.044. URL: <https://www.sciencedirect.com/science/article/pii/S0306261915004997> (visited on 03/01/2024).
- [26] H. S. Zhen et al. "Characterization of biogas-hydrogen premixed flames using Bunsen burner". In: *International Journal of Hydrogen Energy* 39.25 (Aug. 2014), pp. 13292–13299. ISSN: 0360-3199. DOI: 10.1016/j.ijhydene.2014.06.126. URL: <https://www.sciencedirect.com/science/article/pii/S0360319914018667> (visited on 03/01/2024).
- [27] Donato Cecere et al. "Gas Turbine Combustion Technologies for Hydrogen Blends". en. In: *Energies* 16.19 (Jan. 2023). Number: 19 Publisher: Multidisciplinary Digital Publishing Institute, p. 6829. ISSN: 1996-1073. DOI: 10.3390/en16196829. URL: <https://www.mdpi.com/1996-1073/16/19/6829> (visited on 03/01/2024).
- [28] Maria H. du Toit, Alexander V. Avdeenkov, and Dmitri Bessarabov. "Reviewing H<sub>2</sub> Combustion: A Case Study for Non-Fuel-Cell Power Systems and Safety in Passive Autocatalytic Recombiners". In: *Energy & Fuels* 32.6 (June 2018). Publisher: American Chemical Society, pp. 6401–6422. ISSN: 0887-0624. DOI: 10.1021/acs.energyfuels.8b00724. URL: <https://doi.org/10.1021/acs.energyfuels.8b00724> (visited on 03/01/2024).
- [29] Chenglong Tang, Yingjia Zhang, and Zuohua Huang. "Progress in combustion investigations of hydrogen enriched hydrocarbons". In: *Renewable and Sustainable Energy Reviews* 30 (Feb. 2014), pp. 195–216. ISSN: 1364-0321. DOI: 10.1016/j.rser.2013.10.005. URL: <https://www.sciencedirect.com/science/article/pii/S1364032113007041> (visited on 03/01/2024).
- [30] David Noble et al. "Assessment of Current Capabilities and Near-Term Availability of Hydrogen-Fired Gas Turbines Considering a Low-Carbon Future". In: *Journal of Engineering for Gas Turbines and Power* 143.041002 (Feb. 2021). ISSN: 0742-4795. DOI: 10.1115/1.4049346. URL: <https://doi.org/10.1115/1.4049346> (visited on 03/01/2024).
- [31] H. H. -W. Funke, N. Beckmann, and S. Abanteriba. "An overview on dry low NO<sub>x</sub> micromix combustor development for hydrogen-rich gas turbine applications". In: *International Journal of Hydrogen Energy* 44.13 (Mar. 2019), pp. 6978–6990. ISSN: 0360-3199. DOI: 10.1016/j.ijhydene.2019.01.161. URL: <https://www.sciencedirect.com/science/article/pii/S0360319919303192> (visited on 03/01/2024).
- [32] Daesik Kim. "Review on the Development Trend of Hydrogen Gas Turbine Combustion Technology". en. In: *Journal of The Korean Society of Combustion*. Vol. 24. ISSN: 1226-0959, 2466-2089 Issue: 4 Journal Abbreviation: jksc. Dec. 2019, pp. 1–10. DOI: 10.15231/jksc.2019.24.4.001. URL: <http://www.dbpia.co.kr/Journal/ArticleDetail/NODE09283211> (visited on 03/01/2024).
- [33] T. Sattelmayer et al. "NO<sub>x</sub>-Abatement Potential of Lean-Premixed GT Combustors". In: *Journal of Engineering for Gas Turbines and Power* 120.1 (Jan. 1998), pp. 48–59. ISSN: 0742-4795. DOI: 10.1115/1.2818087. URL: <https://doi.org/10.1115/1.2818087> (visited on 03/05/2024).
- [34] Dan Zhao, Ephraim Gutmark, and Philip de Goey. "A review of cavity-based trapped vortex, ultra-compact, high-g, inter-turbine combustors". In: *Progress in Energy and Combustion Science* 66 (May 2018), pp. 42–82. ISSN: 0360-1285. DOI: 10.1016/j.pecs.2017.12.001. URL: <https://www.sciencedirect.com/science/article/pii/S0360128517300898> (visited on 03/01/2024).

- [35] Thierry Poinso and Denis Veynante. “Theoretical and Numerical Combustion”. In: *Prog. Energy Combust. Sci.* 28 (Jan. 2005).
- [36] Denis Veynante and Luc Vervisch. “Turbulent combustion modeling”. In: *Progress in Energy and Combustion Science* 28.3 (Mar. 2002), pp. 193–266. ISSN: 0360-1285. DOI: 10.1016/S0360-1285(01)00017-X. URL: <https://www.sciencedirect.com/science/article/pii/S036012850100017X> (visited on 03/10/2024).
- [37] Stewart Cant. “S. B. Pope, Turbulent Flows, Cambridge University Press, Cambridge, U.K., 2000, 771 pp.” In: *Combustion and Flame* 125 (Jan. 2001). ADS Bibcode: 2001CoFl..125.1361C, pp. 1361–1362. ISSN: 0010-2180. DOI: 10.1016/S0010-2180(01)00244-9. URL: <https://ui.adsabs.harvard.edu/abs/2001CoFl..125.1361C> (visited on 03/02/2024).
- [38] Andrei Nikolaevich Kolmogorov et al. “The local structure of turbulence in incompressible viscous fluid for very large Reynolds numbers”. In: *Proceedings of the Royal Society of London. Series A: Mathematical and Physical Sciences* 434.1890 (Jan. 1997). Publisher: Royal Society, pp. 9–13. DOI: 10.1098/rspa.1991.0075. URL: <https://royalsocietypublishing.org/doi/abs/10.1098/rspa.1991.0075> (visited on 03/02/2024).
- [39] Paul Laffitte, Pierre Jouguet, and Paul Pascal. “La propagation des flammes dans les mélanges gazeux”. In: (*No Title*) (1939). URL: <https://cir.nii.ac.jp/crid/1130282269229154048> (visited on 03/04/2024).
- [40] R. G. Abdel-Gayed et al. “Lewis number effects on turbulent burning velocity”. In: *Symposium (International) on Combustion*. Twentieth Symposium (International) on Combustion 20.1 (Jan. 1985), pp. 505–512. ISSN: 0082-0784. DOI: 10.1016/S0082-0784(85)80539-7. URL: <https://www.sciencedirect.com/science/article/pii/S0082078485805397> (visited on 03/04/2024).
- [41] James F. Driscoll et al. “Premixed flames subjected to extreme turbulence: Some questions and recent answers”. In: *Progress in Energy and Combustion Science* 76 (Jan. 2020), p. 100802. ISSN: 0360-1285. DOI: 10.1016/j.pecs.2019.100802. URL: <https://www.sciencedirect.com/science/article/pii/S036012851930036X> (visited on 03/10/2024).
- [42] R. Borghi and M. Destriau. “Combustion and flames: chemical and physical principles; La combustion et les flammes”. French. In: (Dec. 1998). URL: <https://www.osti.gov/etdweb/biblio/323360> (visited on 03/10/2024).
- [43] T. J. Poinso, D. C. Haworth, and G. Bruneaux. “Direct simulation and modeling of flame-wall interaction for premixed turbulent combustion”. In: *Combustion and Flame* 95.1 (Oct. 1993), pp. 118–132. ISSN: 0010-2180. DOI: 10.1016/0010-2180(93)90056-9. URL: <https://www.sciencedirect.com/science/article/pii/0010218093900569> (visited on 03/04/2024).
- [44] J. M. Duclos, G. Bruneaux, and T. A. Baritaud. “3D Modelling of Combustion and Pollutants in a 4-Valve SI Engine; Effect of Fuel and Residuals Distribution and Spark Location”. In: *SAE Transactions* 105 (1996). Publisher: SAE International, pp. 2048–2062. ISSN: 0096-736X. URL: <https://www.jstor.org/stable/44736419> (visited on 03/04/2024).
- [45] Peter Glarborg et al. “Modeling nitrogen chemistry in combustion”. In: *Progress in Energy and Combustion Science* 67 (July 2018), pp. 31–68. ISSN: 0360-1285. DOI: 10.1016/j.pecs.2018.01.002. URL: <https://www.sciencedirect.com/science/article/pii/S0360128517301600> (visited on 03/05/2024).

- [46] Yakov BorisovichHG Zeldovich. “25. The Oxidation of Nitrogen in Combustion and Explosions”. In: ed. by Rashid Alievich Sunyaev. Book Title: Selected Works of Yakov Borisovich Zeldovich, Volume I. Princeton University Press, Dec. 1992, pp. 364–403. ISBN: 978-1-4008-6297-9. DOI: 10.1515/9781400862979.364. URL: <https://www.degruyter.com/document/doi/10.1515/9781400862979.364/html> (visited on 03/01/2024).
- [47] C. P. Fenimore. “Formation of nitric oxide in premixed hydrocarbon flames”. In: *Symposium (International) on Combustion*. Thirteenth symposium (International) on Combustion 13.1 (Jan. 1971), pp. 373–380. ISSN: 0082-0784. DOI: 10.1016/S0082-0784(71)80040-1. URL: <https://www.sciencedirect.com/science/article/pii/S0082078471800401> (visited on 03/04/2024).
- [48] Joseph W. Bozzelli and Anthony M. Dean. “O + NNH: A possible new route for NOX formation in flames”. en. In: *International Journal of Chemical Kinetics* 27.11 (1995). \_eprint: <https://onlinelibrary.wiley.com/doi/pdf/10.1002/kin.550271107>, pp. 1097–1109. ISSN: 1097-4601. DOI: 10.1002/kin.550271107. URL: <https://onlinelibrary.wiley.com/doi/abs/10.1002/kin.550271107> (visited on 03/04/2024).
- [49] D. G. Nicol et al. “The Importance of the Nitrous Oxide Pathway to NOx in Lean-Premixed Combustion”. In: *Journal of Engineering for Gas Turbines and Power* 117.1 (Jan. 1995), pp. 100–111. ISSN: 0742-4795. DOI: 10.1115/1.2812756. URL: <https://doi.org/10.1115/1.2812756> (visited on 03/04/2024).
- [50] James A. Miller and Craig T. Bowman. “Mechanism and modeling of nitrogen chemistry in combustion”. In: *Progress in Energy and Combustion Science* 15.4 (Jan. 1989), pp. 287–338. ISSN: 0360-1285. DOI: 10.1016/0360-1285(89)90017-8. URL: <https://www.sciencedirect.com/science/article/pii/0360128589900178> (visited on 03/04/2024).
- [51] Guillaume Vignat, Daniel Durox, and Sébastien Candel. “The suitability of different swirl number definitions for describing swirl flows: Accurate, common and (over-) simplified formulations”. In: *Progress in Energy and Combustion Science* 89 (Mar. 2022), p. 100969. ISSN: 0360-1285. DOI: 10.1016/j.pecs.2021.100969. URL: <https://www.sciencedirect.com/science/article/pii/S0360128521000678> (visited on 02/21/2024).
- [52] János Miklós Beér. *Combustion Aerodynamics [by] J.M. Beér and N.A. Chigier*. en. Google-Books-ID: LQ3JtAEACAAJ. Applied Science Publishers Limited, 1972.
- [53] N. Syred and J. M. Beér. “Combustion in swirling flows: A review”. In: *Combustion and Flame* 23.2 (Oct. 1974), pp. 143–201. ISSN: 0010-2180. DOI: 10.1016/0010-2180(74)90057-1. URL: <https://www.sciencedirect.com/science/article/pii/0010218074900571> (visited on 03/04/2024).
- [54] Nicholas Syred. “A review of oscillation mechanisms and the role of the precessing vortex core (PVC) in swirl combustion systems”. In: *Progress in Energy and Combustion Science* 32.2 (Jan. 2006), pp. 93–161. ISSN: 0360-1285. DOI: 10.1016/j.pecs.2005.10.002. URL: <https://www.sciencedirect.com/science/article/pii/S0360128505000353> (visited on 03/04/2024).
- [55] P. Palies et al. “The combined dynamics of swirler and turbulent premixed swirling flames”. In: *Combustion and Flame* 157.9 (Sept. 2010), pp. 1698–1717. ISSN: 0010-2180. DOI: 10.1016/j.combustflame.2010.02.011. URL: <https://www.sciencedirect.com/science/article/pii/S001021801000057X> (visited on 03/04/2024).
- [56] *Full article: Experimental Study on the Effect of Swirler Geometry and Swirl Number on Flame Describing Functions*. URL: <https://www.tandfonline.com/doi/full/10.1080/00102202.2010.538103> (visited on 03/04/2024).

- [57] Sébastien Candel et al. “Dynamics of Swirling Flames”. In: *Annual Review of Fluid Mechanics* 46.1 (2014). \_eprint: <https://doi.org/10.1146/annurev-fluid-010313-141300>, pp. 147–173. DOI: 10.1146/annurev-fluid-010313-141300. URL: <https://doi.org/10.1146/annurev-fluid-010313-141300> (visited on 03/04/2024).
- [58] A. N. BELOUSOV and A. K. GUPTA. “Pvc and Instability in Swirl Combustors”. In: *Chemical Engineering Communications* 47.4-6 (Oct. 1986). Publisher: Taylor & Francis \_eprint: <https://doi.org/10.1080/00986448608911773>, pp. 363–380. ISSN: 0098-6445. DOI: 10.1080/00986448608911773. URL: <https://doi.org/10.1080/00986448608911773> (visited on 03/04/2024).
- [59] Tim C. Lieuwen. *Unsteady Combustor Physics*. en. Google-Books-ID: ZYJKEAAAQBAJ. Cambridge University Press, Oct. 2021. ISBN: 978-1-108-89685-6.
- [60] P. Schmittel et al. “Turbulent swirling flames: Experimental investigation of the flow field and formation of nitrogen oxide”. In: *Proceedings of the Combustion Institute* 28.1 (Jan. 2000), pp. 303–309. ISSN: 1540-7489. DOI: 10.1016/S0082-0784(00)80224-6. URL: <https://www.sciencedirect.com/science/article/pii/S0082078400802246> (visited on 03/04/2024).
- [61] Aldo Coghe, Giulio Solero, and Gianfranco Scribano. “Recirculation phenomena in a natural gas swirl combustor”. In: *Experimental Thermal and Fluid Science*. Third Mediterranean Combustion Symposium 28.7 (Sept. 2004), pp. 709–714. ISSN: 0894-1777. DOI: 10.1016/j.expthermflusci.2003.12.007. URL: <https://www.sciencedirect.com/science/article/pii/S0894177703001821> (visited on 03/04/2024).
- [62] Toufik Boushaki et al. “Study of pollutant emissions and dynamics of non-premixed turbulent oxygen enriched flames from a swirl burner”. In: *Proceedings of the Combustion Institute* 36.3 (Jan. 2017), pp. 3959–3968. ISSN: 1540-7489. DOI: 10.1016/j.proci.2016.06.046. URL: <https://www.sciencedirect.com/science/article/pii/S1540748916301043> (visited on 03/04/2024).
- [63] Nazim Merlo et al. “Experimental Study of Oxygen Enrichment Effects on Turbulent Non-premixed Swirling Flames”. In: *Energy & Fuels* 27.10 (Oct. 2013). Publisher: American Chemical Society, pp. 6191–6197. ISSN: 0887-0624. DOI: 10.1021/ef400843c. URL: <https://doi.org/10.1021/ef400843c> (visited on 03/04/2024).
- [64] Toufik Boushaki. *Swirling Flows and Flames*. en. Google-Books-ID: ozj8DwAAQBAJ. BoD – Books on Demand, June 2019. ISBN: 978-1-83880-743-6.
- [65] F. Cozzi and A. Coghe. “Effect of air staging on a coaxial swirled natural gas flame”. In: *Experimental Thermal and Fluid Science*. Seventh Mediterranean Combustion Symposium 43 (Nov. 2012), pp. 32–39. ISSN: 0894-1777. DOI: 10.1016/j.expthermflusci.2012.04.002. URL: <https://www.sciencedirect.com/science/article/pii/S0894177712000982> (visited on 03/04/2024).
- [66] Christian Thomas Eichler. *Flame flashback in wall boundary layers of premixed combustion systems*. Verlag Dr. Hut München, Germany, 2011. URL: <https://www.epc.ed.tum.de/fileadmin/w00cgc/td/Forschung/Dissertationen/Eichler.pdf> (visited on 03/04/2024).
- [67] James Bailey. “Analysis and modelling of boundary-layer flashback processes for hydrogen-rich gas-turbine combustion”. en. phd. University of Southampton, July 2021. URL: <https://eprints.soton.ac.uk/455946/> (visited on 03/04/2024).
- [68] J. Fritz, M. Krõner, and T. Sattelmayer. “Flashback in a Swirl Burner With Cylindrical Premixing Zone”. In: *Journal of Engineering for Gas Turbines and Power* 126.2 (June 2004), pp. 276–283. ISSN: 0742-4795. DOI: 10.1115/1.1473155. URL: <https://doi.org/10.1115/1.1473155> (visited on 03/04/2024).

- [69] Fares Hatem. “Flashback analysis and avoidance in swirl burners”. en. phd. Cardiff University, 2017. URL: <https://orca.cardiff.ac.uk/id/eprint/103700/> (visited on 03/04/2024).
- [70] Onur Tuncer, Sumanta Acharya, and Jong Ho Uhm. “Dynamics, NO<sub>x</sub> and Flashback Characteristics of Confined Pre-Mixed Hydrogen Enriched Methane Flames”. en. In: American Society of Mechanical Engineers Digital Collection, Mar. 2009, pp. 857–868. DOI: 10.1115/GT2007-28158. URL: <https://dx.doi.org/10.1115/GT2007-28158> (visited on 03/04/2024).
- [71] Thoralf G. Reichel, Katharina Goeckeler, and Oliver Paschereit. “Investigation of Lean Premixed Swirl-Stabilized Hydrogen Burner With Axial Air Injection Using OH-PLIF Imaging”. In: *Journal of Engineering for Gas Turbines and Power* 137.111513 (Sept. 2015). ISSN: 0742-4795. DOI: 10.1115/1.4031181. URL: <https://doi.org/10.1115/1.4031181> (visited on 03/04/2024).
- [72] H. Murat Altay et al. “Mitigation of thermoacoustic instability utilizing steady air injection near the flame anchoring zone”. In: *Combustion and Flame* 157.4 (Apr. 2010), pp. 686–700. ISSN: 0010-2180. DOI: 10.1016/j.combustflame.2010.01.012. URL: <https://www.sciencedirect.com/science/article/pii/S0010218010000234> (visited on 03/01/2024).
- [73] Ahmed F. Ghoniem et al. “Mechanism of combustion dynamics in a backward-facing step stabilized premixed flame”. In: *Proceedings of the Combustion Institute* 30.2 (Jan. 2005), pp. 1783–1790. ISSN: 1540-7489. DOI: 10.1016/j.proci.2004.08.201. URL: <https://www.sciencedirect.com/science/article/pii/S008207840400253X> (visited on 03/01/2024).
- [74] Franz Joos et al. “Field Experience of the Sequential Combustion System for the GT24/GT26 Gas Turbine Family”. en. In: *Volume 4: Heat Transfer; Electric Power; Industrial and Cogeneration*. Stockholm, Sweden: American Society of Mechanical Engineers, June 1998, V004T10A009. ISBN: 978-0-7918-7865-1. DOI: 10.1115/98-GT-220. URL: <https://asmedigitalcollection.asme.org/GT/proceedings/GT1998/78651/Stockholm,%20Sweden/248877> (visited on 03/01/2024).
- [75] Peter Stuttaford et al. “FlameSheet™ Combustor Engine and Rig Validation for Operational and Fuel Flexibility With Low Emissions”. en. In: American Society of Mechanical Engineers Digital Collection, Sept. 2016. DOI: 10.1115/GT2016-56696. URL: <https://dx.doi.org/10.1115/GT2016-56696> (visited on 03/01/2024).
- [76] Lars-Uno Axelsson et al. *High Hydrogen Gas Turbine Retrofit Solution to Eliminate Carbon Emissions*. Oct. 2021.
- [77] Reyhaneh Banihabib et al. “Development and testing of a 100 kW fuel-flexible micro gas turbine running on 100% hydrogen”. In: *International Journal of Hydrogen Energy* 49 (July 2023). DOI: 10.1016/j.ijhydene.2023.06.317.
- [78] André A. V. Perpignan, Arvind Gangoli Rao, and Dirk J. E. M. Roekaerts. “Flameless combustion and its potential towards gas turbines”. In: *Progress in Energy and Combustion Science* 69 (Nov. 2018), pp. 28–62. ISSN: 0360-1285. DOI: 10.1016/j.pecs.2018.06.002. URL: <https://www.sciencedirect.com/science/article/pii/S0360128517301296> (visited on 03/01/2024).
- [79] S. A. Mosier and R. M. Pierce. *Advanced combustion systems for stationary gas turbine engines*. 1980. URL: <https://www.osti.gov/servlets/purl/6640503#page=138> (visited on 03/01/2024).
- [80] Mark Stevens et al. “Increased operational flexibility from the latest GT26 (2011) upgrade”. In: *PowerGen Europe, Cologne, Germany* (2012).

- [81] A. Fischer, C. Hirsch, and T. Sattelmayer. “Comparison of multi-microphone transfer matrix measurements with acoustic network models of swirl burners”. In: *Journal of Sound and Vibration* 298.1 (Nov. 2006), pp. 73–83. ISSN: 0022-460X. DOI: 10.1016/j.jsv.2006.04.040. URL: <https://www.sciencedirect.com/science/article/pii/S0022460X06004160> (visited on 03/06/2024).
- [82] Thomas Komarek et al. *MODELING THE EFFECT OF HEAT LOSS ON FLAME STABILIZATION IN SHEAR LAYERS*. Sept. 2008.
- [83] L. Tay Wo Chong et al. “Influence of strain and heat loss on flame stabilization in a non-adiabatic combustor”. In: *Proc. Of European Comb. Meeting*. Citeseer, 2009. URL: <https://citeseerx.ist.psu.edu/document?repid=rep1&type=pdf&doi=7ebd2d678c1f1deb9b3249d2a73ba377b0692df4> (visited on 03/06/2024).
- [84] D. Bradley et al. “Generation of PDFs for flame curvature and for flame stretch rate in premixed turbulent combustion”. In: *Combustion and flame* 135.4 (2003). Publisher: Elsevier, pp. 503–523. URL: <https://www.sciencedirect.com/science/article/pii/S0010218003001810> (visited on 03/06/2024).
- [85] C. F. X. Ansys. “ANSYS CFX-solver theory guide”. In: *Ansys CFX Release* 15317 (2009), pp. 724–746.
- [86] Luis Tay-Wo-Chong et al. “Combined Influence of Strain and Heat Loss on Turbulent Premixed Flame Stabilization”. en. In: *Flow, Turbulence and Combustion* 97.1 (July 2016), pp. 263–294. ISSN: 1573-1987. DOI: 10.1007/s10494-015-9679-0. URL: <https://doi.org/10.1007/s10494-015-9679-0> (visited on 03/13/2024).
- [87] Thomas Komarek and Wolfgang Polifke. “Impact of Swirl Fluctuations on the Flame Response of a Perfectly Premixed Swirl Burner”. In: *Journal of Engineering for Gas Turbines and Power* 132.061503 (Mar. 2010). ISSN: 0742-4795. DOI: 10.1115/1.4000127. URL: <https://doi.org/10.1115/1.4000127> (visited on 03/13/2024).
- [88] R. Mercier et al. “Experimental and numerical investigation of the influence of thermal boundary conditions on premixed swirling flame stabilization”. In: *Combustion and Flame* 171 (Sept. 2016), pp. 42–58. ISSN: 0010-2180. DOI: 10.1016/j.combustflame.2016.05.006. URL: <https://www.sciencedirect.com/science/article/pii/S0010218016300815> (visited on 03/06/2024).
- [89] T. F. Guiberti et al. “Impact of heat loss and hydrogen enrichment on the shape of confined swirling flames”. In: *Proceedings of the Combustion Institute* 35.2 (Jan. 2015), pp. 1385–1392. ISSN: 1540-7489. DOI: 10.1016/j.proci.2014.06.016. URL: <https://www.sciencedirect.com/science/article/pii/S1540748914001746> (visited on 03/06/2024).
- [90] Benoît Fiorina et al. “A filtered tabulated chemistry model for LES of premixed combustion”. In: *Combustion and Flame* 157.3 (2010). Publisher: Elsevier, pp. 465–475. URL: <https://www.sciencedirect.com/science/article/pii/S0010218009002739> (visited on 03/11/2024).
- [91] W. Meier, X. R. Duan, and P. Weigand. “Reaction zone structures and mixing characteristics of partially premixed swirling CH<sub>4</sub>/air flames in a gas turbine model combustor”. In: *Proceedings of the Combustion Institute* 30.1 (Jan. 2005), pp. 835–842. ISSN: 1540-7489. DOI: 10.1016/j.proci.2004.08.065. URL: <https://www.sciencedirect.com/science/article/pii/S0082078404001249> (visited on 03/05/2024).

- [92] S. Roux et al. “Studies of mean and unsteady flow in a swirled combustor using experiments, acoustic analysis, and large eddy simulations”. In: *Combustion and Flame* 141.1 (Apr. 2005), pp. 40–54. ISSN: 0010-2180. DOI: 10.1016/j.combustflame.2004.12.007. URL: <https://www.sciencedirect.com/science/article/pii/S0010218005000039> (visited on 03/05/2024).
- [93] V. Moureau et al. “A ghost-fluid method for large-eddy simulations of premixed combustion in complex geometries”. In: *Journal of Computational Physics* 221.2 (Feb. 2007), pp. 600–614. ISSN: 0021-9991. DOI: 10.1016/j.jcp.2006.06.031. URL: <https://www.sciencedirect.com/science/article/pii/S0021999106003068> (visited on 03/05/2024).
- [94] Ping Wang et al. “A detailed comparison of two sub-grid scale combustion models via large eddy simulation of the PRECCINSTA gas turbine model combustor”. In: *Combustion and Flame* 164 (Feb. 2016), pp. 329–345. ISSN: 0010-2180. DOI: 10.1016/j.combustflame.2015.11.031. URL: <https://www.sciencedirect.com/science/article/pii/S0010218015004290> (visited on 03/05/2024).
- [95] J. -M. Lourier et al. “Scale Adaptive Simulation of a thermoacoustic instability in a partially premixed lean swirl combustor”. In: *Combustion and Flame* 183 (Sept. 2017), pp. 343–357. ISSN: 0010-2180. DOI: 10.1016/j.combustflame.2017.02.024. URL: <https://www.sciencedirect.com/science/article/pii/S0010218017300718> (visited on 03/05/2024).
- [96] P. Benard et al. “Large-Eddy Simulation of the lean-premixed PRECCINSTA burner with wall heat loss”. In: *Proceedings of the Combustion Institute* 37.4 (Jan. 2019), pp. 5233–5243. ISSN: 1540-7489. DOI: 10.1016/j.proci.2018.07.026. URL: <https://www.sciencedirect.com/science/article/pii/S1540748918304449> (visited on 02/21/2024).
- [97] Benedetta Franzelli, Eleonore Riber, and Bénédicte Cuenot. “Impact of the chemical description on a Large Eddy Simulation of a lean partially premixed swirled flame”. In: *Comptes Rendus Mécanique. Combustion, spray and flow dynamics for aerospace propulsion* 341.1 (Jan. 2013), pp. 247–256. ISSN: 1631-0721. DOI: 10.1016/j.crme.2012.11.007. URL: <https://www.sciencedirect.com/science/article/pii/S163107211200215X> (visited on 03/05/2024).
- [98] V. Moureau, P. Domingo, and L. Vervisch. “From Large-Eddy Simulation to Direct Numerical Simulation of a lean premixed swirl flame: Filtered laminar flame-PDF modeling”. In: *Combustion and Flame* 158.7 (July 2011), pp. 1340–1357. ISSN: 0010-2180. DOI: 10.1016/j.combustflame.2010.12.004. URL: <https://www.sciencedirect.com/science/article/pii/S0010218010003585> (visited on 03/05/2024).
- [99] Bruno Coriton, Mitchell D. Smooke, and Alessandro Gomez. “Effect of the composition of the hot product stream in the quasi-steady extinction of strained premixed flames”. In: *Combustion and Flame* 157.11 (Nov. 2010), pp. 2155–2164. ISSN: 0010-2180. DOI: 10.1016/j.combustflame.2010.05.002. URL: <https://www.sciencedirect.com/science/article/pii/S0010218010001264> (visited on 03/05/2024).
- [100] Pasquale Walter Agostinelli. “Assessment of Large Eddy Simulation in the Conjugate Heat Transfer context for engine operability : application to Hydrogen enrichment and Spinning Combustion Technology”. en. phd. Apr. 2022. URL: <https://oatao.univ-toulouse.fr/29027/> (visited on 03/05/2024).
- [101] P. W. Agostinelli et al. “Impact of wall heat transfer in Large Eddy Simulation of flame dynamics in a swirled combustion chamber”. In: *Combustion and Flame* 234 (Dec. 2021), p. 111728. ISSN: 0010-2180. DOI: 10.1016/j.combustflame.2021.111728. URL: <https://www.sciencedirect.com/science/article/pii/S0010218021004715> (visited on 03/05/2024).

- [102] P. W. Agostinelli et al. “Static mesh adaptation for reliable large eddy simulation of turbulent reacting flows”. In: *Physics of Fluids* 33.3 (Mar. 2021), p. 035141. ISSN: 1070-6631. DOI: 10.1063/5.0040719. URL: <https://doi.org/10.1063/5.0040719> (visited on 03/05/2024).
- [103] D. Laera et al. “Stabilization mechanisms of CH<sub>4</sub> premixed swirled flame enriched with a non-premixed hydrogen injection”. In: *Proceedings of the Combustion Institute* 38.4 (Jan. 2021), pp. 6355–6363. ISSN: 1540-7489. DOI: 10.1016/j.proci.2020.06.378. URL: <https://www.sciencedirect.com/science/article/pii/S1540748920305058> (visited on 03/05/2024).
- [104] P. W. Agostinelli et al. “On the impact of H<sub>2</sub>-enrichment on flame structure and combustion dynamics of a lean partially-premixed turbulent swirling flame”. In: *Combustion and Flame* 241 (July 2022), p. 112120. ISSN: 0010-2180. DOI: 10.1016/j.combustflame.2022.112120. URL: <https://www.sciencedirect.com/science/article/pii/S0010218022001390> (visited on 03/05/2024).
- [105] Pasquale W. Agostinelli et al. “Large eddy simulations of mean pressure and H<sub>2</sub> addition effects on the stabilization and dynamics of a partially-premixed swirled-stabilized methane flame”. In: *Combustion and Flame* 249 (Mar. 2023), p. 112592. ISSN: 0010-2180. DOI: 10.1016/j.combustflame.2022.112592. URL: <https://www.sciencedirect.com/science/article/pii/S0010218022006009> (visited on 03/05/2024).
- [106] Daniel Fredrich, W. P. Jones, and Andrew J. Marquis. “The stochastic fields method applied to a partially premixed swirl flame with wall heat transfer”. In: *Combustion and Flame* 205 (July 2019), pp. 446–456. ISSN: 0010-2180. DOI: 10.1016/j.combustflame.2019.04.012. URL: <https://www.sciencedirect.com/science/article/pii/S0010218019301579> (visited on 03/05/2024).
- [107] Michael F. Modest and Sandip Mazumder. *Radiative Heat Transfer*. en. Google-Books-ID: j2Q0EAAAQBAJ. Academic Press, Oct. 2021. ISBN: 978-0-323-98407-2.
- [108] William Lytle Grosshandler. *RADCAL – a narrow-band model for radiation calculations in a combustion environment*. en. Tech. rep. NBS TN 1402. Edition: 0. Gaithersburg, MD: National Bureau of Standards, 1993, NBS TN 1402. DOI: 10.6028/NIST.TN.1402. URL: <https://nvlpubs.nist.gov/nistpubs/Legacy/TN/nbstechnicalnote1402.pdf> (visited on 03/05/2024).
- [109] D. Mira et al. “Numerical Characterization of a Premixed Hydrogen Flame Under Conditions Close to Flashback”. en. In: *Flow, Turbulence and Combustion* 104.2 (Mar. 2020), pp. 479–507. ISSN: 1573-1987. DOI: 10.1007/s10494-019-00106-z. URL: <https://doi.org/10.1007/s10494-019-00106-z> (visited on 03/07/2024).
- [110] Steffen Terhaar et al. “Vortex Breakdown Types and Global Modes in Swirling Combustor Flows with Axial Injection”. en. In: *Journal of Propulsion and Power* 31.1 (Jan. 2015), pp. 219–229. ISSN: 0748-4658, 1533-3876. DOI: 10.2514/1.B35217. URL: <https://arc.aiaa.org/doi/10.2514/1.B35217> (visited on 03/08/2024).
- [111] T. Capurso et al. “NO<sub>x</sub> pathways in lean partially premixed swirling H<sub>2</sub>-air turbulent flame”. In: *Combustion and Flame* 248 (Feb. 2023), p. 112581. ISSN: 0010-2180. DOI: 10.1016/j.combustflame.2022.112581. URL: <https://www.sciencedirect.com/science/article/pii/S0010218022005892> (visited on 03/08/2024).



- [112] Lukas Berger, Antonio Attili, and Heinz Pitsch. “Synergistic interactions of thermodiffusive instabilities and turbulence in lean hydrogen flames”. In: *Combustion and Flame* 244 (Oct. 2022), p. 112254. ISSN: 0010-2180. DOI: 10.1016/j.combustflame.2022.112254. URL: <https://www.sciencedirect.com/science/article/pii/S0010218022002693> (visited on 03/10/2024).
- [113] Gioele Ferrante et al. “LES of Hydrogen-Enriched Methane Flames in a Lean-Burn Combustor With Axial Air Injection”. en. In: American Society of Mechanical Engineers Digital Collection, Sept. 2023. DOI: 10.1115/GT2023-103006. URL: <https://dx.doi.org/10.1115/GT2023-103006> (visited on 03/05/2024).
- [114] A. Chem1D. *one-dimensional laminar flame code*, Eindhoven University of Technology. 2016.
- [115] James C. Massey, Zhi X. Chen, and Nedunchezian Swaminathan. “Modelling Heat Loss Effects in the Large Eddy Simulation of a Lean Swirl-Stabilised Flame”. en. In: *Flow, Turbulence and Combustion* 106.4 (Apr. 2021), pp. 1355–1378. ISSN: 1573-1987. DOI: 10.1007/s10494-020-00192-4. URL: <https://doi.org/10.1007/s10494-020-00192-4> (visited on 03/05/2024).
- [116] Sarah Link et al. “The Influence of the Confinement Ratio on the Precessing Vortex Core Dynamics in a Counter-Rotating Dual Swirler”. en. In: American Society of Mechanical Engineers Digital Collection, Sept. 2023. DOI: 10.1115/GT2023-101678. URL: <https://dx.doi.org/10.1115/GT2023-101678> (visited on 03/05/2024).
- [117] Richards, Keith J Senecal, Peter K Pomraning, Eric. “CONVERGE 3.0”. In: *Convergent Science*, Madison, WI (2021).
- [118] Suhas Patankar. *Numerical Heat Transfer and Fluid Flow*. en. Google-Books-ID: Y2G1DwAAQBAJ. Taylor & Francis, Oct. 2018. ISBN: 978-1-4822-3421-3.
- [119] R. I Issa. “Solution of the implicitly discretised fluid flow equations by operator-splitting”. In: *Journal of Computational Physics* 62.1 (Jan. 1986), pp. 40–65. ISSN: 0021-9991. DOI: 10.1016/0021-9991(86)90099-9. URL: <https://www.sciencedirect.com/science/article/pii/0021999186900999> (visited on 03/08/2024).
- [120] *GRI-Mech Home Page*. URL: <http://combustion.berkeley.edu/gri-mech/> (visited on 03/08/2024).
- [121] Charles Francis Curtiss and Robert Byron Bird. *Molecular theory of gases and liquids*. J. Wiley, 1954.
- [122] T. P. Coffee and J. M. Heimerl. “Transport algorithms for premixed, laminar steady-state flames”. In: *Combustion and Flame* 43 (1981). Publisher: Elsevier, pp. 273–289. URL: <https://www.sciencedirect.com/science/article/pii/0010218081900274> (visited on 03/08/2024).
- [123] Pierre Sagaut. *Large eddy simulation for incompressible flows: an introduction*. Springer Science & Business Media, 2005. URL: <https://books.google.com/books?hl=it&lr=&id=SH90vyraAT0C&oi=fnd&pg=PA14&dq=Large+Eddy+Simulation+for+Incompressible+Flows&ots=Tzyrf39eSB&sig=gVhV5iQqnkYScPL8o40e8W2ASig> (visited on 08/21/2024).
- [124] S. Ghosal and P. Moin. “The Basic Equations for the Large Eddy Simulation of Turbulent Flows in Complex Geometry”. In: *Journal of Computational Physics* 118.1 (Apr. 1995), pp. 24–37. ISSN: 0021-9991. DOI: 10.1006/jcph.1995.1077. URL: <https://www.sciencedirect.com/science/article/pii/S0021999185710777> (visited on 03/10/2024).
- [125] Jean Boussinesq. *Essai sur la theorie des eaux courantes*. fr. Google-Books-ID: dOSb4mC6UtsC. Imprimerie nationale, 1877.

- [126] Stephen B. Pope. “Turbulent flows”. In: *Measurement Science and Technology* 12.11 (2001), pp. 2020–2021. URL: <https://iopscience.iop.org/article/10.1088/0957-0233/12/11/705/meta> (visited on 03/10/2024).
- [127] D. K. Lilly. “A proposed modification of the germano sugrid-scale closure method”. In: *Phys Fluids A* 4 (1992), pp. 633–635. URL: [https://cfd.spbstu.ru/agarbaruk/doc/1992\\_Lilly\\_A%20proposed%20modification%20of%20the%20Germano%20closure%20meth od.pdf](https://cfd.spbstu.ru/agarbaruk/doc/1992_Lilly_A%20proposed%20modification%20of%20the%20Germano%20closure%20method.pdf) (visited on 08/21/2024).
- [128] P. J O’Rourke and F. V Bracco. “Two scaling transformations for the numerical computation of multidimensional unsteady laminar flames”. In: *Journal of Computational Physics* 33.2 (Nov. 1979), pp. 185–203. ISSN: 0021-9991. DOI: 10.1016/0021-9991(79)90015-9. URL: <https://www.sciencedirect.com/science/article/pii/0021999179900159> (visited on 03/11/2024).
- [129] C. Meneveau and T. Poinso. “Stretching and quenching of flamelets in premixed turbulent combustion”. In: *Combustion and Flame* 86.4 (Sept. 1991), pp. 311–332. ISSN: 0010-2180. DOI: 10.1016/0010-2180(91)90126-V. URL: <https://www.sciencedirect.com/science/article/pii/001021809190126V> (visited on 03/11/2024).
- [130] O. Colin et al. “A thickened flame model for large eddy simulations of turbulent premixed combustion”. In: *Physics of Fluids* 12.7 (July 2000), pp. 1843–1863. ISSN: 1070-6631. DOI: 10.1063/1.870436. URL: <https://doi.org/10.1063/1.870436> (visited on 03/11/2024).
- [131] Fabrice Charlette, Charles Meneveau, and Denis Veynante. “A power-law flame wrinkling model for LES of premixed turbulent combustion Part I: non-dynamic formulation and initial tests”. In: *Combustion and Flame* 131.1 (Oct. 2002), pp. 159–180. ISSN: 0010-2180. DOI: 10.1016/S0010-2180(02)00400-5. URL: <https://www.sciencedirect.com/science/article/pii/S0010218002004005> (visited on 03/11/2024).
- [132] Fabrice Charlette, Charles Meneveau, and Denis Veynante. “A power-law flame wrinkling model for LES of premixed turbulent combustion Part II: dynamic formulation”. In: *Combustion and Flame* 131.1 (Oct. 2002), pp. 181–197. ISSN: 0010-2180. DOI: 10.1016/S0010-2180(02)00401-7. URL: <https://www.sciencedirect.com/science/article/pii/S0010218002004017> (visited on 03/11/2024).
- [133] Thomas Jaravel. “Prediction of pollutants in gas turbines using large eddy simulation”. PhD Thesis. Institut National Polytechnique de Toulouse-INPT, 2016. URL: <https://theses.hal.science/tel-04244436/> (visited on 03/11/2024).
- [134] Jean-Philippe Legier, Thierry Poinso, and Denis Veynante. “Dynamically thickened flame LES model for premixed and non-premixed turbulent combustion”. In: *Proceedings of the summer program*. Vol. 12. Citeseer, 2000, pp. 157–168. URL: <https://citeseerx.ist.psu.edu/document?repid=rep1&type=pdf&doi=4fc2a9c88ebad2c394b7e68017d7a63362547502> (visited on 03/11/2024).
- [135] Halit Kutkan et al. “Modeling of Turbulent Premixed CH<sub>4</sub>/H<sub>2</sub>/Air Flames Including the Influence of Stretch and Heat Losses”. In: *Journal of Engineering for Gas Turbines and Power* 144.011020 (Oct. 2021). ISSN: 0742-4795. DOI: 10.1115/1.4051989. URL: <https://doi.org/10.1115/1.4051989> (visited on 02/21/2024).
- [136] Thoralf G. Reichel and Christian Oliver Paschereit. “Interaction mechanisms of fuel momentum with flashback limits in lean-premixed combustion of hydrogen”. In: *International Journal of Hydrogen Energy* 42.7 (Feb. 2017), pp. 4518–4529. ISSN: 0360-3199. DOI: 10.1016/j.ijhydene.2016.11.018. URL: <https://www.sciencedirect.com/science/article/pii/S0360319916333109> (visited on 08/12/2024).

- [137] Fengshan Liu et al. “The impact of radiative heat transfer in combustion processes and its modeling – with a focus on turbulent flames”. In: *Fuel* 281 (Dec. 2020), p. 118555. ISSN: 0016-2361. DOI: 10.1016/j.fuel.2020.118555. URL: <https://www.sciencedirect.com/science/article/pii/S0016236120315519> (visited on 08/11/2024).
- [138] *Thermophysical properties of quartz glass | Journal of Engineering Physics and Thermophysics*. URL: <https://link.springer.com/article/10.1007/BF00824797> (visited on 08/11/2024).
- [139] Anthony F. Mills. “Basic heat and mass transfer”. In: (*No Title*) (1999). URL: <https://cir.nii.ac.jp/crid/1130000796140292864> (visited on 08/11/2024).
- [140] Roland Span. “D2. 2 Properties of Dry Air”. In: *VDI-GVC, Ed. VDI Heat Atlas* (2010), pp. 172–191. URL: [https://books.google.com/books?hl=it&lr=&id=0t-HrUf1aHEC&oi=fnd&pg=PA172&dq=VDI+Heat+Atlas+air+properties&ots=tGKBQ7g\\_L&sig=poTe9V1FVa\\_2WQt-Aqo0FMxRU1c](https://books.google.com/books?hl=it&lr=&id=0t-HrUf1aHEC&oi=fnd&pg=PA172&dq=VDI+Heat+Atlas+air+properties&ots=tGKBQ7g_L&sig=poTe9V1FVa_2WQt-Aqo0FMxRU1c) (visited on 08/11/2024).
- [141] Julien Weiss. “A Tutorial on the Proper Orthogonal Decomposition”. en. In: (2019). URL: <https://depositonce.tu-berlin.de/handle/11303/9456> (visited on 08/11/2024).
- [142] A. Montorfano, F. Piscaglia, and G. Ferrari. “Inlet boundary conditions for incompressible LES: A comparative study”. In: *Mathematical and Computer Modelling*. Public Key Services and Infrastructures EUROPKI-2010-Mathematical Modelling in Engineering & Human Behaviour 2011 57.7 (Apr. 2013), pp. 1640–1647. ISSN: 0895-7177. DOI: 10.1016/j.mcm.2011.10.077. URL: <https://www.sciencedirect.com/science/article/pii/S0895717711006820> (visited on 08/28/2024).
- [143] Steffen Terhaar. “Identification and modeling of coherent structures in swirl-stabilized combustors at dry and steam-diluted conditions”. PhD Thesis. Berlin, Technische Universität Berlin, Diss., 2015, 2015. URL: <https://d-nb.info/106856962X/34> (visited on 08/13/2024).
- [144] Kilian Oberleithner et al. “Why Nonuniform Density Suppresses the Precessing Vortex Core”. In: *Journal of Engineering for Gas Turbines and Power* 135.121506 (Sept. 2013). ISSN: 0742-4795. DOI: 10.1115/1.4025130. URL: <https://doi.org/10.1115/1.4025130> (visited on 08/13/2024).
- [145] *Vortex Breakdown Types and Global Modes in Swirling Combustor Flows with Axial Injection | Journal of Propulsion and Power*. URL: <https://arc.aiaa.org/doi/10.2514/1.B35217> (visited on 08/14/2024).
- [146] ANSYS Fluent. “Ansys fluent theory guide”. In: *Ansys Inc., USA* 15317 (2011), pp. 724–746.
- [147] Daniel Silva. “Modeling the transient response of thermal circuits”. In: *Applied Sciences* 12.24 (2022). Publisher: MDPI, p. 12555. URL: <https://www.mdpi.com/2076-3417/12/24/12555> (visited on 08/29/2024).
- [148] Gregory P. Smith. “GRI-Mech 3.0”. In: [http://www.me.berkeley.edu/gri\\_mech/](http://www.me.berkeley.edu/gri_mech/) (1999). URL: <https://cir.nii.ac.jp/crid/1570572700799977728> (visited on 08/25/2024).
- [149] ANSYS Chemkin. “17.0 (15151)”. In: *ANSYS Reaction Design: San Diego* 20 (2016).
- [150] Tianfeng Lu and Chung K. Law. “A directed relation graph method for mechanism reduction”. In: *Proceedings of the Combustion Institute* 30.1 (2005). Publisher: Elsevier, pp. 1333–1341. URL: [https://www.sciencedirect.com/science/article/pii/S0082078404001973?casa\\_token=BK\\_sX4GGwmkAAAAA:l\\_Tc901GG9LM4PG4hhuhDduh3qVQ4uQqxzLBHIDb9hVj1-dV8HerdmcZp8RthJ3rcq51yvKc8A](https://www.sciencedirect.com/science/article/pii/S0082078404001973?casa_token=BK_sX4GGwmkAAAAA:l_Tc901GG9LM4PG4hhuhDduh3qVQ4uQqxzLBHIDb9hVj1-dV8HerdmcZp8RthJ3rcq51yvKc8A) (visited on 08/25/2024).

- [151] Kyle E. Niemeyer, Chih-Jen Sung, and Mandhapati P. Raju. “Skeletal mechanism generation for surrogate fuels using directed relation graph with error propagation and sensitivity analysis”. In: *Combustion and flame* 157.9 (2010). Publisher: Elsevier, pp. 1760–1770. URL: [https://www.sciencedirect.com/science/article/pii/S0010218010000039?casa\\_token=MEBilyu7MmQAAAAA:hUdh0fEUqLy1ZQ47TTFeuGCqZv0YBGEL7rq7PVrF0hTWwUET0ezSJKVNT93YhPlkHznwU2Jc0g](https://www.sciencedirect.com/science/article/pii/S0010218010000039?casa_token=MEBilyu7MmQAAAAA:hUdh0fEUqLy1ZQ47TTFeuGCqZv0YBGEL7rq7PVrF0hTWwUET0ezSJKVNT93YhPlkHznwU2Jc0g) (visited on 08/25/2024).
- [152] Tianfeng Lu and Chung K. Law. “On the applicability of directed relation graphs to the reduction of reaction mechanisms”. In: *Combustion and Flame* 146.3 (2006). Publisher: Elsevier, pp. 472–483. URL: [https://www.sciencedirect.com/science/article/pii/S0010218006001398?casa\\_token=nyDFXPx49xQAAAAA:z6CXMMYFqI4CT0bj\\_Nhixg62ePtLcr-iuq31C\\_o4DxhQMPd0si0o3bPRfY3nD2m6yZ4sS840UQ](https://www.sciencedirect.com/science/article/pii/S0010218006001398?casa_token=nyDFXPx49xQAAAAA:z6CXMMYFqI4CT0bj_Nhixg62ePtLcr-iuq31C_o4DxhQMPd0si0o3bPRfY3nD2m6yZ4sS840UQ) (visited on 08/25/2024).